

TABLE OF CONTENTS

<u>Section</u>	<u>Title</u>	<u>Page</u>
FOREWORD	iii	1/A6
LIST OF FIGURES	vii	1/A10
SUMMARY	1	1/B7
1.0 INTRODUCTION	1	1/B7
2.0 SYMBOLS	3	1/B9
3.0 PROGRAM DEFINITION - TASK I	5	1/B11
4.0 CRUISE PERFORMANCE DATA BASE - TASK II	7	1/C1
4.1 Exploratory Wind-Tunnel Tests	7	1/C1
4.1.1 Experimental models	8	1/C2
4.1.2 Test facilities	16	1/D2
4.1.3 Experimental data analysis	16	1/D2
4.1.3.1 Pressure-test results	19	1/D7
4.1.3.2 Force-test results	34	1/E8
4.1.3.3 Geometric "effects" data	93	2/D2
4.2 Math Model Development	114	2/E10
4.2.1 Representation of wing, nacelle and power unit .	114	2/E10
4.2.2 Surface pressure	119	2/F3
4.2.3 Lift	122	2/F8
4.2.4 Drag prediction methods	122	2/F8
4.2.5 Drag correlation	127	2/F13
5.0 COMPATIBILITY STUDIES - TASK III	127	2/F13
5.1 Design and Feasibility Studies	130	2/G2
5.1.1 Perturbation studies	133	2/G7
5.1.2 Final design	133	2/G7
5.2 Supplementary Low-Speed Tests	137	2/G14
5.2.1 Model description		
5.2.1.1 Leading-edge device	142	3/A9
5.2.1.2 Trailing-edge flaps	142	3/A9
5.2.1.3 Nacelles	142	3/A9
5.2.1.4 Instrumentation	142	3/A9

TABLE OF CONTENTS (CONT'D)

<u>Section</u>	<u>Title</u>	<u>Page</u>
	5.2.2 Test results	147 3/B2
	5.2.2.1 Static performance	147 3/B2
	5.2.2.2 Wind-on performance	147 3/B2
	5.2.3 Discussion	147 3/B2
	5.2.3.1 Experimental data comparisons	147 3/B2
	5.3 Powered-Lift Analytical Synthesis	157 3/B14
6.0	RECOMMENDATIONS FOR ADDITIONAL DEVELOPMENT - TASK IV	160 3/C3
7.0	PROGRAM CONCLUSIONS	167 3/C13
	7.1 Cruise Performance Data Base - Task II	167 3/C13
	7.1.1 Experimental program	167 3/C13
	7.1.2 Theoretical program	169 3/D1
	7.1.2.1 Vortex lattice studies	169 3/D1
	7.1.2.2 Applications of jet flap theory	171 3/D3
	7.2 Compatibility Studies - Task III	171 3/D3
	7.2.1 Design feasibility studies	172 3/D4
	7.2.2 Supplementary tests	173 3/D5
8.0	REFERENCES	174 3/D6

JUL 2 1 1980

Ref. No. 130-31-19

NAS 1.26: 3193

NASA Contractor Report 3193

COMPLETED

ORIGINAL

Exploratory Studies of the Cruise
Performance of Upper Surface
Blown Configurations

Summary Report

J. A. Braden, J. P. Hancock, J. E. Hackett,
K. P. Burdges, and V. Lyman

CONTRACT NAS1-13871
JULY 1980

NASA

193

**Exploratory Studies of the Cruise
Performance of Upper Surface
Blown Configurations**

Summary Report

J. A. Braden, J. P. Hancock, ¹⁹⁷⁷ J. E. Hackett,
K. P. Burdges, and V. Lyman
Lockheed-Georgia Company
Marietta, Georgia

Prepared for
Langley Research Center
under Contract NAS1-13871



National Aeronautics
and Space Administration

**Scientific and Technical
Information Office**

BLANK PAGE

FOREWORD

This document is submitted in accordance with the requirements of NASA Contract NAS1-13871, Exploratory Studies of the Cruise Performance of Upper Surface Blown Configurations. W. C. Sleeman, Jr. is the NASA-Langley Contract Monitor and J. A. Braden is the Lockheed-Georgia Project Manager.

The technical results under this contract are presented in five reports. For convenience, the overall program documentation is summarized below:

DOCUMENTATION SUMMARY

<u>CR-Number</u>	<u>Title</u>
CR-3193	Summary Report
CR-3192	Experimental Program - Test Facilities, Model Design, Instrumentation, and Low-Speed, High-Lift Tests
CR-159134	Experimental Program - High-Speed Force Tests
CR-159135	Experimental Program - High-Speed Pressure Tests
CR-159136	Program Analysis and Conclusions

BLANK PAGE

TABLE OF CONTENTS

<u>Section</u>	<u>Title</u>	<u>Page</u>
	FOREWORD	iii
	LIST OF FIGURES	xi
	SUMMARY	1
1.0	INTRODUCTION	1
2.0	SYMBOLS	3
3.0	PROGRAM DEFINITION - TASK I	5
4.0	CRUISE PERFORMANCE DATA BASE - TASK II	7
	4.1 Exploratory Wind-Tunnel Tests	7
	4.1.1 Experimental models	8
	4.1.2 Test facilities	16
	4.1.3 Experimental data analysis	16
	4.1.3.1 Pressure-test results	19
	4.1.3.2 Force-test results	34
	4.1.3.3 Geometric "effects" data	93
	4.2 Math Model Development	114
	4.2.1 Representation of wing, nacelle and power unit	114
	4.2.2 Surface pressure	119
	4.2.3 Lift	122
	4.2.4 Drag prediction methods	122
	4.2.5 Drag correlation	127
5.0	COMPATIBILITY STUDIES - TASK III	127
	5.1 Design and Feasibility Studies	130
	5.1.1 Perturbation studies	133
	5.1.2 Final design	133
	5.2 Supplementary Low-Speed Tests	137
	5.2.1 Model description	
	5.2.1.1 Leading-edge device	142
	5.2.1.2 Trailing-edge flaps	142
	5.2.1.3 Nacelles	142
	5.2.1.4 Instrumentation	142

TABLE OF CONTENTS (CONT'D)

<u>Section</u>	<u>Title</u>	<u>Page</u>
	5.2.2 Test results	147
	5.2.2.1 Static performance	147
	5.2.2.2 Wind-on performance	147
	5.2.3 Discussion	147
	5.2.3.1 Experimental data comparisons	147
	5.3 Powered-Lift Analytical Synthesis	157
6.0	RECOMMENDATIONS FOR ADDITIONAL DEVELOPMENT - TASK IV	160
7.0	PROGRAM CONCLUSIONS	167
	7.1 Cruise Performance Data Base - Task II	167
	7.1.1 Experimental program	167
	7.1.2 Theoretical program	169
	7.1.2.1 Vortex lattice studies	169
	7.1.2.2 Applications of jet flap theory	171
	7.2 Compatibility Studies - Task III	171
	7.2.1 Design feasibility studies	172
	7.2.2 Supplementary tests	173
8.0	REFERENCES	174

LIST OF FIGURES

<u>Figure</u>	<u>Title</u>	<u>Page</u>
1	Major elements of USB Cruise Program	6
2	Exploded view of basic test model arrangement	10
3	USB experimental program - matrix of nozzle geometric parameters	11
4	Key dimensions for nozzles in test matrix	12
5	Typical nozzle design	14
6	Nacelle general arrangement for straight wing	15
7	Dual D-duct installation on 3-D swept wing force model in CFF	17
8	AR4 nozzle installation on 3-D straight wing force model in 4' x 4' tunnel	17
9	Lockheed Compressible Flow Facility (CFF)	18
10	Jet centerline pressure distributions, "D-duct" noz (N_6), $H_j/p_\infty \approx 2.6$, $\alpha \approx 2.6^\circ$	20
11	Comparison of static and wind-on jet isobars one chord length behind straight wing, $H_j/p_\infty \approx 2.2$, $\alpha \approx 2.6^\circ$	22
12	LV measurements of spanwise distribution of trailing-edge flow singularity, small "D-duct" nacelle, $\alpha = 0^\circ$	23
13	Effect of nozzle exit shape on jet centerline pressures, $\alpha = 2^\circ$, $M_\infty \approx 0.60$, $H_j/p_\infty \approx 1.4$	24

LIST OF FIGURES (CONT'D)

<u>Figure</u>	<u>Title</u>	<u>Page</u>
14	Effect of nozzle pressure ratio on jet centerline pressures, $\alpha = 3^0$, $M_{\infty} = 0.70$	26
15	Variation of scrubbed area pressure drag with pressure ratio, $\alpha = 2^0$, $M_{\infty} = 0.68$	28
16	Variation of scrubbed area pressure drag with pressure ratio, $\alpha = 2^0$, $M_{\infty} = 0.68$	29
17	Comparison of pressure drag developed in scrubbed area	31
18	Lift developed in scrubbed area with blowing, $\alpha = 2^0$, $M_{\infty} = 0.70$	32
19	Lift developed in scrubbed area with blowing, $\alpha = 2^0$, $M_{\infty} = 0.70$	33
20	Effect of lift coefficient on nacelle drag, $M_{\infty} = 0.68$	36
21	Effect of lift coefficient on nacelle drag, $M_{\infty} = 0.68$	38
22	Effect of lift coefficient on nacelle drag, $M_{\infty} = 0.68$	39
23	Effect of lift coefficient on nacelle drag, $M_{\infty} = 0.73$	41
24	Effect of lift coefficient on nacelle drag, $M_{\infty} = 0.73$	42
25	Effect of nozzle pressure ratio on total lift, nozzle N_{3E} , $AR = 2.5$, $M_{\infty} = 0.68$	43
26	Effect of nozzle pressure ratio on total lift, nozzle N_2 , circular, $M_{\infty} = 0.68$	44

LIST OF FIGURES (CONT'D)

<u>Figure</u>	<u>Title</u>	<u>Page</u>
27	Effect of nozzle pressure ratio on total lift, nozzle N_4 , AR = 4, $M_\infty = 0.68$	45
28	Effect of nozzle pressure ratio on total lift, nozzle N_5 , AR = 6.0, $M_\infty = 0.68$	46
29	Effect of nozzle pressure ratio on total lift, nozzle N_{11} , AR = circular, $M_\infty = 0.73$	48
30	Effect of nozzle pressure ratio on total lift, nozzle N_R^2 , AR = 2.5, $M_\infty = 0.73$	49
31	Effect of nozzle pressure ratio on total lift, nozzle N_{12} , AR = 4, $M_\infty = 0.73$	50
32	Effect of nozzle pressure ratio on total lift, nozzle N_{13} , AR = 6, $M_\infty = 0.73$	51
33	Effect of nozzle pressure ratio on pitching moment, nozzle N_2 , circular, $M_\infty = 0.68$	52
34	Effect of nozzle pressure ratio on pitching moment, nozzle N_{3E} , AR = 2.5, $M_\infty = 0.68$	53
35	Effect of nozzle pressure ratio on pitching moment, nozzle N_5 , AR = 6, $M_\infty = 0.68$	54
36	Effect of Mach number on nacelle drag coefficient, $C_{L_M} = 0.40$	55
37	Effect of Mach number on nacelle drag coefficient, $C_{L_M} = 0.40$	56

LIST OF FIGURES (CONT'D)

<u>Figure</u>	<u>Title</u>	<u>Page</u>
38	Effect of Mach number on nacelle drag coefficient, $C_{LM} = 0.40$	57
39	Effect of Mach number on nacelle drag coefficient, $C_{LM} = 0.40$	58
40	Effect of Mach number on nacelle drag coefficient, $C_{LM} = 0.40$	59
41	Variation of lift and moment increments due to blowing, nozzle N_2 , circular	61
42	Variation of lift increments due to blowing, nozzle N_{2E} , circular	62
43	Variation of lift increment due to blowing, nozzle N_{3B} , $AR = 2.5$	63
44	Variation of lift and moment increments due to blowing, nozzle N_{3E} , $AR = 2.5$	64
45	Variation of lift and moment increments due to blowing, nozzle N_4 , $AR = 4$	65
46	Variation of lift and moment increments due to blowing, nozzle N_{4E} , $AR = 4$	66
47	Variation of lift and moment increments due to blowing, nozzle N_5 , $AR = 6$	67
48	Tabulation of estimated skin friction drag of test nacelles	70

LIST OF FIGURES (CONT'D)

<u>Figure</u>	<u>Title</u>	<u>Page</u>
49	Tabulation of η_T (δ_{j_s}) for test nozzles; static data	71
50	Variation of effective drag-due-to-lift parameters with thrust and Mach number, nozzle N_{2E} , circular	73
51	Variation of effective drag-due-to-lift parameters, with thrust and Mach number, nozzle N_{3B} , AR = 2.5	74
52	Variation of effective drag-due-to-lift parameters with thrust and Mach number, nozzle N_5 , AR = 6	75
53	Variation of effective drag-due-to-lift parameter with thrust and Mach number, nozzle N_8 , AR = 2.5	76
54	Variation of effective drag-due-to-lift parameter with thrust and Mach number, nozzle N_{12} , AR = 4	77
55	Tabulation of effective wing/body efficiency factors, e_w , for clean wing-body configurations	78
56	Incremental nacelle drag and component buildup, nozzle N_{2E} , circular, $M_\infty = 0.68$, $C_{L_M} = 0.40$	81
57	Incremental nacelle drag and component buildup, nozzle N_{3B} , AR = 2.5, $M_\infty = 0.68$, $C_{L_M} = 0.40$	82
58	Incremental nacelle drag and component buildup, nozzle N_4 , AR = 4, $M_\infty = 0.68$, $C_{L_M} = 0.40$	83
59	Incremental nacelle drag and component buildup, nozzle N_5 , AR = 6.0, $M_\infty = 0.68$, $C_{L_M} = 0.40$	84

LIST OF FIGURES (CONT'D)

<u>Figure</u>	<u>Title</u>	<u>Page</u>
60	Incremental nacelle drag and component buildup, nozzle N_{11} , circular, $M_{\infty} = 0.73$, $C_{L_M} = 0.40$	85
61	Incremental nacelle drag and component buildup, nozzle N_8^2 , $AR = 2.5$, $M_{\infty} = 0.73$, $C_{L_M} = 0.40$	86
62	Incremental nacelle drag and component buildup, nozzle N_{12} , $AR = 4$, $M_{\infty} = 0.73$, $C_{L_M} = 0.40$	87
63	Incremental nacelle drag and component buildup, nozzle N_{13} , $AR = 6$, $M_{\infty} = 0.73$, $C_{L_M} = 0.40$	88
64	Incremental nacelle drag and component buildup, nozzle N_{3E} , $AR = 2.5$, $M_{\infty} = 0.68$, $C_{L_M} = 0.40$	89
65	Incremental nacelle drag and component buildup, nozzle N_{4E} , $AR = 4$, $M_{\infty} = 0.68$, $C_{L_M} = 0.40$	91
66	Oil-Flow Photograph of high-boattail nozzle (N_{4E}), $\beta = 36^{\circ}$, $M_{\infty} = 0.70$, $\alpha = 2.6^{\circ}$	92
67	Components of total lift coefficient, $M_{\infty} = 0.68$, $\alpha = +3^{\circ}$	94
68	Effect of nozzle aspect ratio on nacelle drag	96
69	Effect of nozzle exit aspect ratio on lift-dependent drag, $M_{\infty} = 0.68$	97
70	Effect of nozzle exit aspect ratio on lift-dependent drag, $M_{\infty} = 0.73$	98
71	Effect of nozzle exit aspect ratio on scrubbing drag, $M_{\infty} = 0.68$	100

LIST OF FIGURES (CONT'D)

<u>Figure</u>	<u>Title</u>	<u>Page</u>
72	Effect of nozzle exit aspect ratio on scrubbing drag, $M_\infty = 0.73$	101
73	Effect of nozzle exit aspect ratio on "effective" jet angle, $M_\infty = 0.68, \alpha = 3^\circ$	102
74	Effect of nozzle exit aspect ratio on "effective" jet angle, $M_\infty = 0.73, \alpha = 3^\circ$	104
75	Effect of nacelle installation and blowing on lift, $M_\infty = 0.68$	105
76	Comparison of streamlined and symmetrical nacelle drag, $C_{L_M} = 0.40$	107
77	Effect of nacelle boattail angle on nacelle drag	109
78	Effect of Mach number on drag for faired-over vs flow- through forebodies, straight wing with circular nozzle N_2	110
79	Effect of multiple engine installation on drag, $C_{L_M} = 0.40$, swept wing	112
80	Comparison of lift due to blowing for two-engine and four-engine configurations, D-duct nacelle, swept wing $M_\infty = 0.73$	113
81	Effect of Mach number on drag for pylon-mounted OTW vs integrated USB nacelles, straight wing with circular nozzle N_2	115

LIST OF FIGURES (CONT'D)

<u>Figure</u>	<u>Title</u>	<u>Page</u>
82	Panel details for D-duct nacelle and adjacent wing	117
83	Representation of jet spreading and entrainment by vortex ring polygons	117
84	Mathematical model of the USB jet efflux	118
85	Predicted nacelle-spline and wing surface pressure distribution as a function of jet pressure ratio: $\alpha = 2^{\circ}$, $M_{\infty} = 0.60$	120
86	Predicted and measured surface pressure increments aft of nacelle (Row A)	121
87	Comparison of USB test results with modified jet-flap theory, nozzle N_{3E} , AR = 2.5, $M_{\infty} = 0.68$	123
88	Computed drag count distribution along nacelle axis (Nacelle Surfaces Only)	125
89	Computed drag count distribution along semi-span (All surfaces)	126
90	Location of drag-producing and thrust-producing regions due to application of power	126
91	Comparison between predicted and measured drag increments for nacelle N_{3E} , $M_{\infty} = 0.60$, $H_j/p_{\infty} = 2.00$	128
92	Residual difference between experimental and predicted drag increments for nacelle N_{3E} at $M_{\infty} = 0.60$	129

LIST OF FIGURES (CONT'D)

<u>Figure</u>	<u>Title</u>	<u>Page</u>
93	USB study aircraft	131
94	Noise footprint and measurement point noise levels, USB study aircraft	132
95	General arrangement, baseline aircraft	134
96	Nacelle inboard profile	135
97	Flight path and noise footprints, final design aircraft	138
98	Spectra by source, final design aircraft, takeoff elevation angle = 90°, 152.4 M (500 ft) distance, no ground reflection	139
99	PNL directivity, final design aircraft, takeoff 152.4 M (500 ft) radius, no ground reflections	140
100	Low-speed, high-lift test model	141
101	Trailing edge flap system design details, low speed model	144
102	Nacelle installation on the wing	145
103	Nozzle design details	146
104	Low-speed model thrust coefficient, $q_{\infty} = 718.2 \text{ N/m}^2$ (15 lbs/ft ²)	148
105	Low-speed model static turning characteristics	149

LIST OF FIGURES (CONT'D)

<u>Figure</u>	<u>Title</u>	<u>Page</u>
106	USB low-speed model propulsion performance	150
107	Variation of low-speed model lift coefficient with angle of attack, $q_{\infty} = 718.2 \text{ N/m}^2$ (15 lbs/ft ²), $\delta_f = 25^\circ$, Coanda plate	151
108	Variation of low-speed model lift coefficient with drag coefficient, $q_{\infty} = 718.2 \text{ N/m}^2$ (15 lbs/ft ²), $\delta_f = 25^\circ$, Coanda plate	152
109	Variation of low-speed model lift coefficient with angle of attack, $q_{\infty} = 718.2 \text{ N/m}^2$ (15 lbs/ft ²), $\delta_f = 52^\circ$, Coanda plate	153
110	Variation of low-speed model lift coefficient with drag coefficient, $q_{\infty} = 718.2 \text{ N/m}^2$ (15 lbs/ft ²), $\delta_f = 52^\circ$, Coanda plate, tail-off	154
111	Oil flow photograph of nacelle-wing flow pattern, $\delta_f = 42.5^\circ$, $C_T = 0.82$, $\alpha = 10^\circ$	155
112	USB/EBF performance comparison, tail-off configuration, $C_{\mu} = 1.66$	156
113	USB performance comparison, two-engine configurations	158
114	Effect of thrust coefficient on USB performance comparisons, two-engine configurations	159
115	Correlation of theoretical and experimental longitudinal aerodynamic characteristics for a NASA-Ames tested high-wing EBF STOL configuration	161

LIST OF FIGURES (CONT'D)

<u>Figure</u>	<u>Title</u>	<u>Page</u>
116	Correlation of theoretical and experimental longitudinal aerodynamic characteristics for a NASA-Ames tested high-wing USB STOL configuration	162
117	Correlation of theoretical and experimental high-lift performance, USB low-speed model, tail-off	163
118	Comparison of Task III USB configuration performance with math model prediction, $\eta_t = 0.90$, $\delta_f = 45^0$	164
119	Pressure drag reduction through local modification of airfoil	166

TABLE

1	Model Dimensional Data	143
---	------------------------	-----

SUMMARY

This document summarizes the work performed under NASA Contract NAS1-13871, which had the objective of establishing an experimental/theoretical aerodynamic data base for upper-surface-blown (USB) configurations at cruise. The scope of the technical effort on the USB-Cruise Program has included extensive transonic wind-tunnel tests of a comprehensive array of nacelle/wing geometric combinations under simulated powered conditions. The experimental studies have been supported by a three-dimensional theoretical model of the system also inclusive of first-order power effects. The data obtained in the experimental/theoretical phase of the program are used to develop aerodynamic "effects" trends as indicative of the effects of variations in component design and placement. Such data have been utilized to aid in the definition of a typical USB-commercial transport suitable for a transonic cruise mission. Feasibility studies, conducted in cooperation with on-going USB acoustical work (NASA Contract NAS1-13870), evaluate the compatibility of the USB-system with current design criteria. Supplementary tests have assessed the high-lift capabilities of the selected study aircraft. As an outgrowth of this background work, recommendations have been formulated as to technical areas where additional USB development work would appear to be potentially beneficial.

1.0 INTRODUCTION

In early 1975, the NASA awarded a contract (NAS1-13871) to the Lockheed-Georgia Company for the acquisition of a high-speed, experimental data base for aircraft configurations featuring nacelles mounted on the wing upper-

surface. This design concept, known as USB (upper-surface blowing), had received earlier experimental endorsement as a viable means of achieving moderate-to-good powered lift performance along with beneficial noise reduction in the STOL environment. In the interest of further development of the USB-system, two related contracts were awarded by the NASA; the present (NAS1-13871) and the other, "Exploratory Studies of the Noise Characteristics of Upper-Surface Blown Configurations" (NAS1-13870). The contractual work performed under the present contract emphasizes exploratory investigations of USB transonic cruise characteristics. The companion contract had a similar objective as related to airport noise. In the present work, the fundamental nature of the experimental effort has been manifested in the use of interchangeable model parts employed in a build-up fashion. As such, the intent has been to primarily develop trends and aerodynamic "effects" as influenced by geometric variations in the nacelle configuration. The more-refined, low-drag designs could then evolve from the more favorable trends established by this base.

The five major elements comprising the cruise data base program are:

- o Program Definition - Task I
- o Experimental Data Base - Task II
- o Compatibility Studies - Task III
- o Recommendations for Additional Development - Task IV
- o Reporting - Task V

The present report summarizes the work performed and results obtained as pertaining to each of the foregoing tasks. The format used in these discussions is structured according to task as given above. In view of the comprehensive nature of the overall study, documentation has been extensive. For convenience, a documentation summary is provided in the Foreword.

Use of trade names or names of manufacturers in this report does not constitute an official endorsement of such products or manufacturers, either expressed or implied, by the National Aeronautics and Space Administration.

2.0 SYMBOLS

A	area, cross-sectional, cm^2 (in. 2)
AR	aspect ratio
c	local wing chord, cm (in.)
\bar{c}	mean aerodynamic chord, cm (in.)
C_D	model drag coefficient, $D/q_x S_W$
C_L	model lift coefficient, $L/q_x S_W$
C_p	pressure coefficient, $(p_1 - p_x)/q_x$
C_T	gross thrust coefficient, $T/q_x S_W$
D	drag force, N (lb)
e	wing efficiency factor
F or T	force or thrust, N (lb)
h	jet or nozzle height, cm (in.)
H	total pressure, N/m^2 (lb/in. 2)
H_j/p_∞	nozzle pressure ratio
L	lift force, N (lb)
L/D	lift-to-drag ratio
M	Mach number
p	static pressure, N/m^2 (lb/in. 2)
q	dynamic pressure, N/m^2 (lb/in. 2)
R_N \bar{c}	Reynolds number based on wing chord
w	nozzle width at wing surface, cm (in.)
x	chordwise dist
z	vertical dimension
δ_j	jet angle, deg

η	spanwise position
w/B	wing plus body
α_{l0}	angle from zero lift, deg
β	boattail angle (or roof angle), deg
δ_{AIL}	aileron deflection, deg

Subscripts:

\bar{c}	based on mean aerodynamic chord
install	installed
isol	isolated
jet	due to jet
l	local
M	measured
N	nacelle
NF	nacelle friction
TOT	total
w	wing
V/T	due to vectored thrust
∞	freestream conditions
η	due to scrubbing
Γ	due to aerodynamic circulation

3.0 PROGRAM DEFINITION - TASK I

The USB Cruise Program was primarily an experimental effort guided appropriately by analytical modeling of the aerodynamic/propulsive characteristics of the USB system. The requirements attendant to secondary program objectives, that is the selection of promising cruise configurations and the assurance of acceptable powered high-lift performance, were necessary elements of the program plan.

The purpose of Task I was to define a program framework in which the remaining tasks could be effectively accomplished. Preliminary studies were undertaken to identify basic needs of the experimental work in terms of key aerodynamic/propulsive phenomena to be evaluated. Secondly, a program concept was formulated, embracing both testing and analyses, which would provide the means of assessing typical USB-cruise performance in terms of wing/nacelle geometric variations. With this background, Task III (Compatibility Studies) and IV (Recommendations) could then flow accordingly. The major elements of the overall USB-Data Base Program, as resulting from these considerations, are shown in Figure 1.

Task II was the heart of the program with a two-phase wind tunnel test to explore transonically the gross effects of systematic geometric variations of the parameters selected in Task I. A powered model concept was selected based on a building block arrangement to take advantage of model components already in existence. Concurrently with the test program, an analytical model was developed to correlate and extend the test results.

In Task III, a Compatibility Study was performed to evaluate the installation, design, and structural implications associated with candidate configurations selected from Task II. This task was performed jointly with the related, on-going acoustical work being performed under contract NAS1-13870. The objective of this combined study was to perform a complete installation design of a competitive short-haul aircraft using guidance from both disciplines.

BLANK

PAGE

USB CRUISE PROGRAM

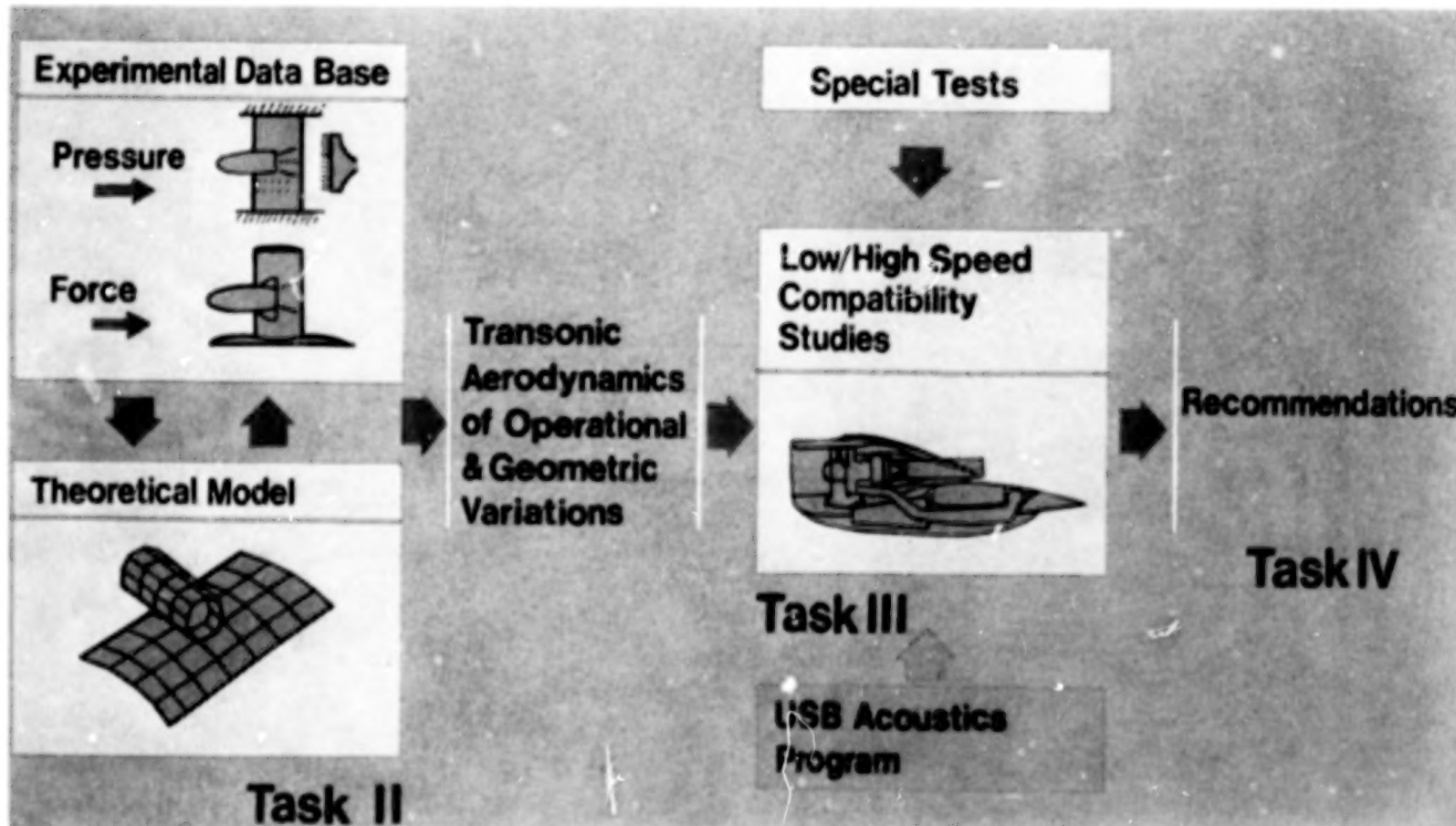


Figure 1. Major elements of USB Cruise Program.

Task IV consisted of organizing the recommendations for additional USB development which evolved from the previous tasks and documenting these recommendations as a separate report.

4.0 CRUISE PERFORMANCE DATA BASE - TASK II

The Task II effort had the objective of experimentally quantifying the effects of various nacelle geometric parameters on cruise lift and drag performance. The experimental phase of this task was supported where possible through guidance from the theoretical model of the system. The matrix of test configurations was selected to provide geometric "effects" data representing major variables such as nacelle size, location, shape, boattail angle and number of nacelles. The corresponding theoretical model was structured around a vortex-lattice representation of the wing-nacelle configuration with a simulated power-package providing first-order propulsive interactions. In the paragraphs which follow, Section 4.1 summarizes the scope and results off the experimental phase of Task II while Section 4.2 considers the capabilities and limitations of the theoretical model. Conclusions relative to the overall Task II effort, inclusive of both experimental and theoretical findings, are given in Section 4.3.

4.1 Exploratory Wind-Tunnel Tests

The major elements off the experimental program consisted of:

- o nozzle calibrations
- o static testing
- o high-speed testing

Static nozzle calibrations were performed on each test nozzle as isolated from the wing in terms of gross thrust coefficient versus nozzle pressure ratio. Initially, the nozzle calibrations were performed on a highly-accurate low-speed balance system. Later in the test program, calibrated thrust checks were made utilizing the several balance systems used in the high speed wind tunnel tests.

Each of the test nozzles was installed on the test wing and tested statically across the pressure ratio range. These tests provided information as to installation losses (i.e., jet scrubbing losses) in terms of the parameters' $\eta_T = T_{\text{INSTALL}}/T_{\text{ISOL}}$. Static jet deflection angles, δ_j , were also defined by these studies. Again a low-speed balance system, as well as high-speed balance systems, afforded cross-checks of the data obtained.

The high-speed testing surveyed the wing-nacelle configuration matrix utilizing both surface-pressure and force-measurement models. With the pressure models, fixed and traversing total-head rakes provided wake momentum profiles under both unpowered and powered test conditions. For the most part, the nominal range of test parameters considered for both force and pressure-testing were:

$$\begin{aligned} .60 &\leq M_\infty \leq 0.80 \\ 0^\circ &\leq \alpha \leq 5^\circ \\ 1.0 &\leq H_j/p_\infty \leq 3.0 \\ R_{N_c} &= 3.5 \times 10^6 \text{ (based on chord)} \end{aligned}$$

For most of the test configurations, flow-photographs were obtained at selected blowing levels and Mach numbers using oil mixed with titanium-oxide as a flow-visualization medium.

Prior to the acquisition of the high-speed force and pressure data, a series of preliminary investigations were conducted to assess the effects of utilizing relatively high-blockage (5 percent) powered models in a porous-walled, blowdown test facility. Physical and jet-blockage interference effects were evaluated by instrumenting the test-section walls with static pressure taps in the vicinity of the model. It was concluded from these preliminary investigations that the test facility was compatible with the sizes and types of models employed in the Data Base Program and that only minor corrections to pre-set freestream conditions would be required.

4.1.1 Experimental models. - The basic objective of the model design effort was to develop a wing-nacelle arrangement which could accommodate a wide range of USB nozzle types for comparative evaluation. To accomplish

this, the high-speed test configurations were developed around two semi-span wing-body combinations with untapered wings swept 0 and 25 degrees. These basic test vehicles could be combined in build-up fashion with a series of nacelle forebodies to form a wide range of powered or unpowered configurations. Figure 2 provides an exploded view of a typical example of the selected model design concept. The choice of a "piped-in" nozzle supply air as a powered simulator was made for simplicity and economy. The removable nozzle block, denoted as "mid-pylon" in Figure 2, provides for the substitution of other nozzle and forebody designs as well as for the conversions to the clean-wing configuration. As shown, the wing has two tangs for wall-mounting in the two-dimensional configuration. For three-dimensional testing, one tang is removed and replaced by the tip, also shown in the figure. Although not shown here, the addition of a fuselage half-body completes the conversion to the 3-D test installation. A remotely-controlled traversing wake rake is positioned one chord length downstream to provide for complete mapping of the model/jet wake pattern.

The nozzle configuration matrix employed in the experimental studies is summarized in Figure 3. As noted, the major geometric variables for which aerodynamic evaluations could be made consisted of nozzle exit aspect ratio, (w^2/A_N) , nozzle size (in terms of the parameter, C^2/A_N), nozzle boattail angle in the nozzle plane of symmetry) and chordwise position of the nozzle exit. Figure 4 provides additional dimensional data appropriate to each of the nozzle designs. As indicated in this table, the largest nacelles ($C^2/A_N = 12$ and 24) were utilized as straight wing installation whereas the smaller nacelles ($C^2/A_N = 48$) were mated with swept wing. A single exception to this was nozzle N_6 which was a small, streamlined nacelle tested as a straight wing installation. The wing-mounted nozzles, indicated in the last column of the table denote those nacelles which were supplied by the wing internal air supply system and therefore could be tested as 3-D force-measurement configurations. With many of these same nozzles, the chordwise exit position could be varied by mounting directly on an upstream-directed pipe which supplied the blowing air; these are also identified in Figure 4. As pipe-mounted installations, the nozzle/wing combination was tested as a 2-D surface-pressure model or as a wake-survey model. All of the nacelles and nozzles were symmetrical-shaped in planform with the single exception of the

BLANK

PAGE

Typical Test Model

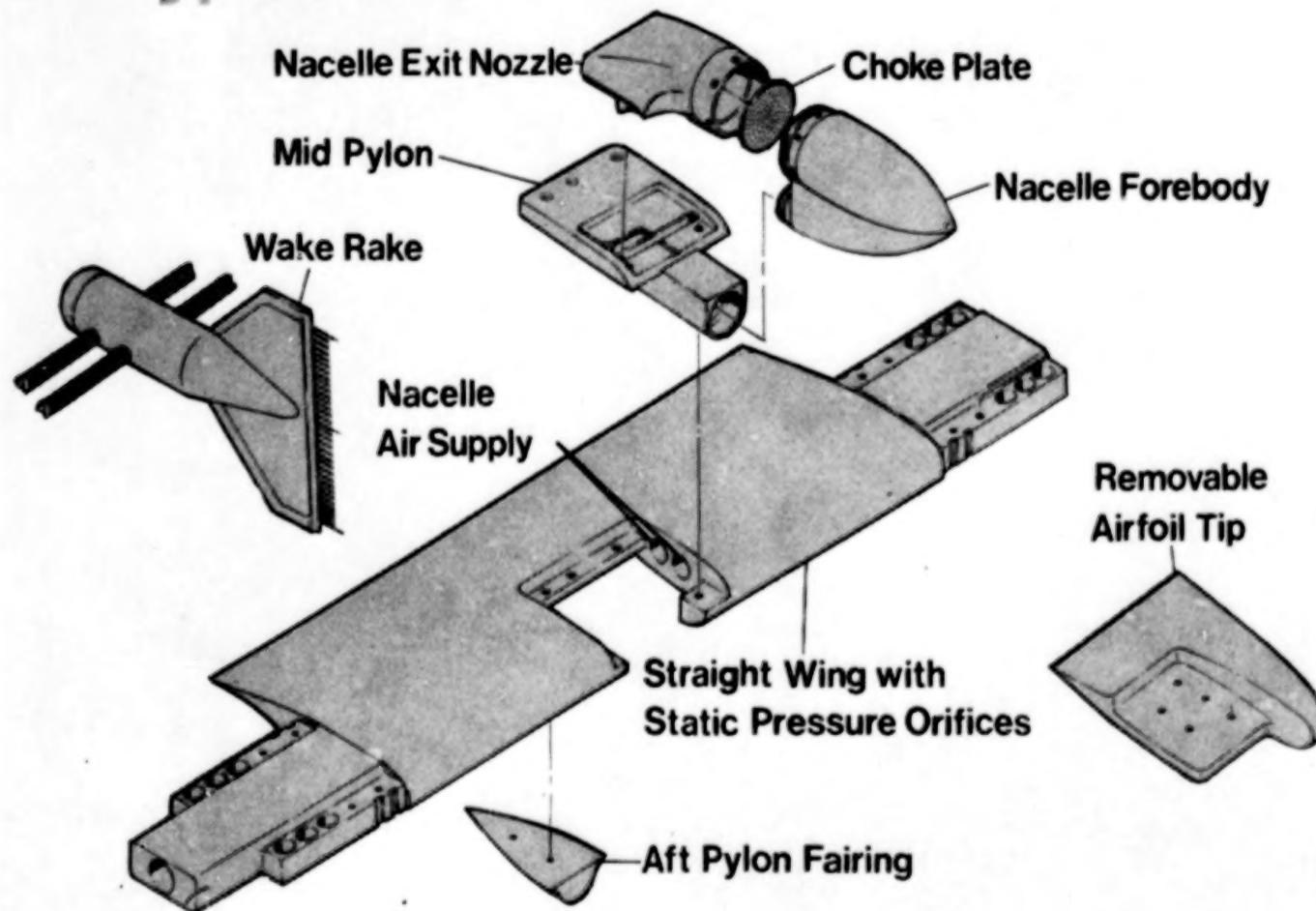


Figure 2. Exploded view of basic test model arrangement.

		NOZZLE BOATTAIL ANGLE *								
		6° - 12½°				12° - 32°				
		NOZZLE DISCHARGE POSITION								
		10%	20%	35%	50%	10%	20%	35%	50%	
** NOZZLE AREA PARAMETER, C^2/A_N	12	1.25					N_9^+	N_9^+	N_9^+	
		2.50	N_1^+	N_1^+	N_1^+	N_1^+				
		4.00								
		6.00	N_{10}^+	N_{10}^+	N_{10}^+	N_{10}^+				
		1.25	N_2^+	N_2^+	N_2^+	N_2^+		N_{1E}	N_{2E}	
	24	2.50	N_3^+	N_3^+	N_3^+	N_3^+			N_{3E}	
		4.00	N_4^+	N_4^+	N_4^+	N_4^+			N_{4E}	
		6.00	N_5^+	N_5^+	N_5^+	N_5^+			N_{4E}^+	
		1.25					N_{11}			
		2.50		N_8^1	N_8^2	N_6				
		4.00			N_{12}					
		6.00				N_{13}				

* Boattail angle dependent on aspect ratio

** Nacelle frontal area varies with nozzle area

† Indicates air supplied by upstream tunnel pipe

Subscript E : Existing hardware

Figure 3 . USB Experimental Program - Matrix of Nozzle Geometric Parameters

BLANK

PAGE

USB CRUISE PROGRAM



GEOMETRIC		RELATIVE SIZE	ASPECT RATIO	DISCHARGE LOCATION	BOATTAIL ANGLE	NOZZLE LENGTH	MAXIMUM DIAMETER	NOZZLE AREA	WINGS	MOUNTING		
NO.	NOZZLE DESCRIPTION	c^2/A_N	AR	x/c	$\theta - \text{DEG}$	cm (in)	cm (in)	cm^2 (in^2)	STRAIT	SWPT	PIPE	WING
N ₁	LARGE D-DUCT, LONG	12	2.5	0.1 - 0.5	9.0	28.915	11.384	9.088	3.578	26.923	4.173	X
N ₂	INTERMED. CIRCL., LONG	24	1.25	0.35	5.90	20.447	8.050	6.426	2.530	13.464	2.087	X X X X
N ₃	INTERMED. D-DUCT, LONG	24	2.5	0.35	9.0	20.447	8.050	6.426	2.530	12.935	2.005	X X
N ₄	INTERMED. HIGH AR, LONG	24	4.0 ¹	0.35	11.0	20.447	8.050	6.426	2.530	13.464	2.087	X X X
N ₅	INTERMED. VERY HI-AR, LONG	24	6.0 ¹	0.35	12.5	20.447	8.050	6.426	2.530	13.464	2.087	X X
N ₆	SM. STRMLN. D-DUCT, LONG	48	2.5	0.35	9.00 ²	14.408	5.692	4.544 ¹	1.789 ¹	6.729	1.043	X
N _{8¹}	SM. INBD. D-DUCT, LONG	48	2.5	0.20	9.90	11.791	4.642	4.544	1.789	6.729	1.043	X X
N _{8²}	SM. OUTBD. D-DUCT, LONG	48	2.5	0.20	9.90	11.791	4.642	4.544	1.789	6.729	1.043	X X
N ₉	LARGE CIRCULAR, SHORT	12	1.25	0.1 - 0.5	12.00	28.915	11.384	9.088	3.578	26.923	4.173	X X X
N ₁₀	LARGE VERY HI-AR, LONG	12	6.0 ¹	0.1 - 0.5	12.50	28.915	11.384	9.088	3.578	26.923	4.173	X X
N ₁₁	SMALL CIRCL., SHORT	48	1.25	0.10	12.00	10.013	3.942	4.544	1.789	6.729	1.043	X X
N ₁₂	SMALL HI-AR, LONG	48	4.0 ¹	0.35	11.00	14.458	5.692	4.544	1.789	6.729	1.043	X X
N ₁₃	SMALL VERY HI-AR, LONG	48	6.0 ¹	0.30	11.00	17.125	6.742	4.544	1.789	6.729	1.043	X X
N _{1E}	INTERMED. CIRCL., SHORT	24	1.25	0.20	16.78	9.629	3.791	6.426	2.530	12.813	1.986	X X
N _{2E}	INTERMED. CIRCL., SHORT	24	1.25	0.35	16.78	12.296	4.841	6.426	2.530	12.813	1.986	X X
N _{3E}	INTERMED. D-DUCT, SHORT	24	2.5	0.35	24.52	12.296	4.841	6.426	2.530	13.464	2.087	X X
N _{4E}	INTERMED. HI-AR, SHORT	24	4.0 ¹	0.35	35.88	12.296	4.841	6.426	2.530	13.464	2.087	X X

² THESE ASPECT RATIOS ARE EXPRESSED FOR EQUIVALENT RECTANGULAR NOZZLE CROSSECTIONS

¹ APPROXIMATELY EQUIVALENT DIMENSIONS FOR NON-CIRCULAR, NON-SYMMETRIC NACELLES

Figure 4. Key dimensions for nozzles in test matrix

aforementioned nozzle N_6 . Exit shapes appropriate to each of the exit aspect ratios listed are also shown in Figure 4.

Design details of a typical nozzle are shown in Figure 5. The internal rake was used for setting nozzle thrust in terms of the H_j/P vs C_T data generated during the nozzle static calibrations. The short, straight section noted in Figure 5 just forward of the nozzle exit, was a design feature incorporated in some nozzles to minimize the impingement angle between wing and jet. As the nozzle exit aspect ratio increases, the nozzle boattail (or impingement) angle tends to become larger resulting in increased jet spreading and a greater degree of jet-attachment to the wing surface. In the use of the straight section, the intent was to minimize these effects when evaluating the aerodynamics attendant to varying nozzle width or exit aspect ratio. Nozzles denoted with an "E" subscript in Figure 5 did not utilize this feature and thus the boattail and impingement angles increased progressively with exit aspect ratio.

The method for combining the wing, nacelle forebody and nozzle for force testing is shown in Figure 6. High-pressure blowing air was supplied through the wing ducts, into an underwing pylon and then into the faired-over nacelle forebody. It is then exhausted through the nozzle after passing through a choke plate. For a fixed exit aspect ratio, nozzle boattail angle could be varied by changing the overall length of the nacelle/forebody combination; a long nozzle design is illustrated in the figure.

The total test matrix available with the model hardware included several supplementary configurations not shown in Figures 3 or 4. These were the upper-surface pylon configurations used for representing over-the-wing (OTW) installations as contrasting with the surface-mounted, USB, arrangements. Several pylon lengths permitted positioning of the circular nacelle, N_2 (see Figures 3 or 4) at 0.5 and 1.0 nozzle exit diameters above the wing (surface-to-surface) on either the straight or swept wings. For straight wing installation, the pylons were constant chord, symmetrical airfoils while for the swept wing application, the pylons were twisted and cambered to conform with theoretically-derived streamlines above the wing-surface. A thickness ratio of $t/c = 0.06$ was employed for both sets of pylons.

BLANK

PAGE

USB CRUISE PROGRAM

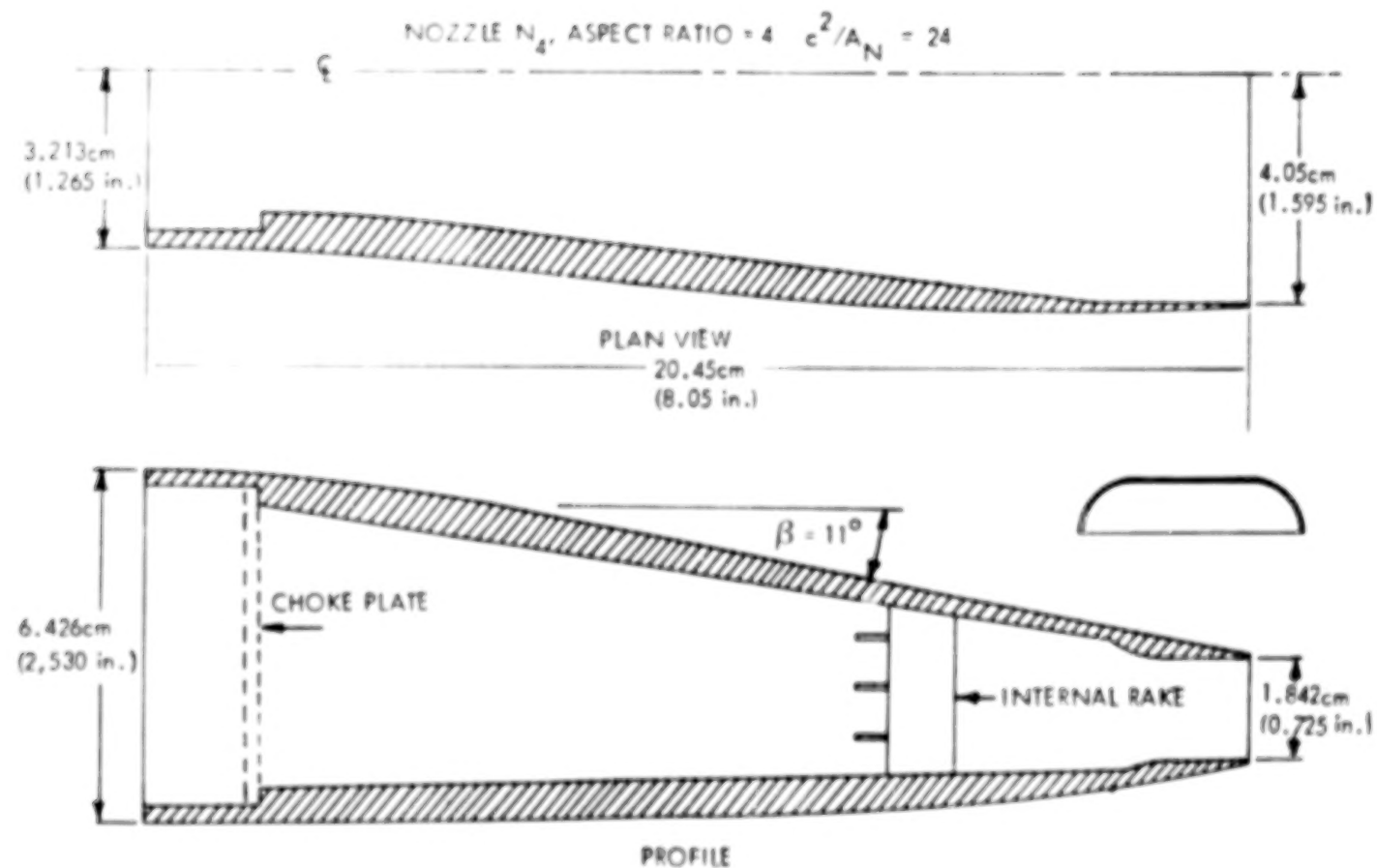


Figure 5. Typical nozzle design

USB CRUISE PROGRAM

*NACA 1-SERIES CONTOUR

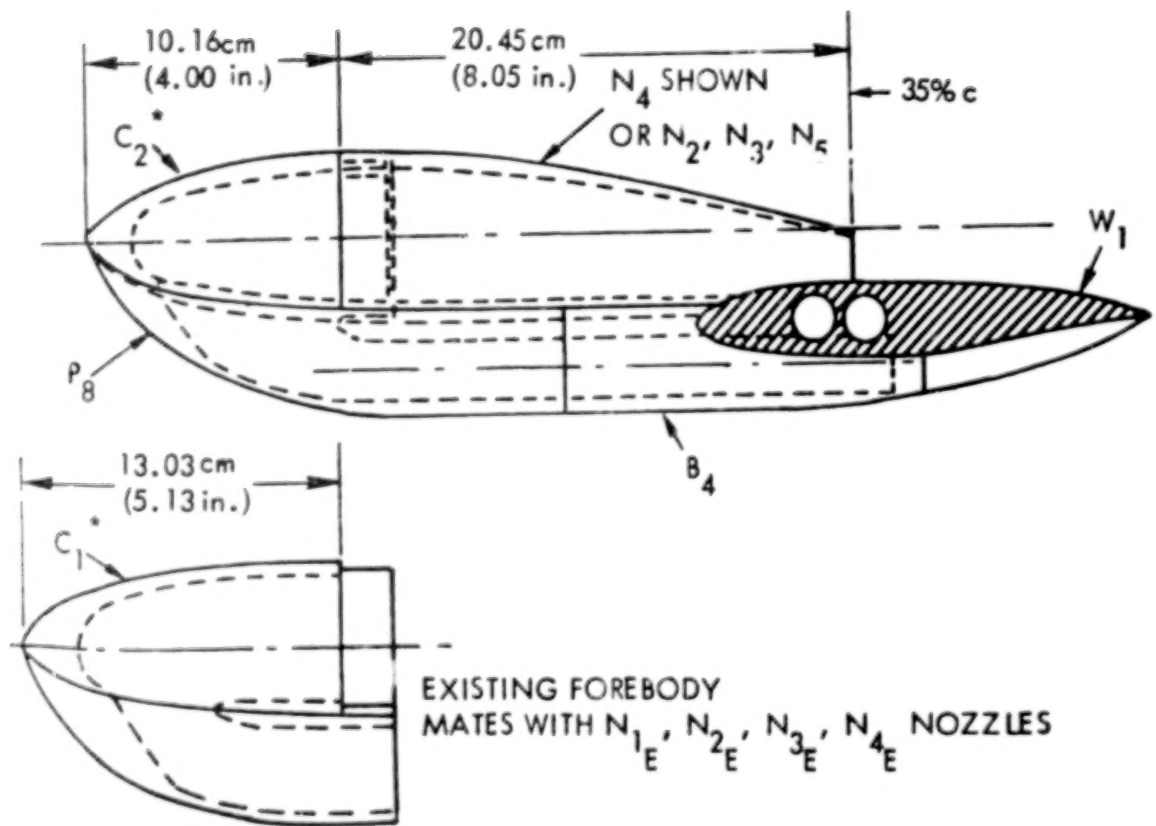


Figure 6. Nacelle general arrangement for straight wing

Figure 7 shows an example of the small "D-Duct" nacelles (N_8) mounted as a 3-D force model in the Compressible Flow Facility (CFF). Extensive filleting used to "soften" the nacelle-wing junction is evident in the photograph. A typical 3-D, straight wing force model is shown in Figure 8. A medium-sized ($c^2/A_N = 24$), aspect ratio 4 nozzle (N_4) is pictured in this configuration. Although not in evidence here, leading-edge filleting, similar to that of the swept wing, was employed for all such straight wing installations.

4.1.2 Test facilities. - The experimental phase of the USB-Cruise Program was formulated around the use of minimum-cost, powered models in several porous-wall blow-down test facilities - the Lockheed Compressible Flow and 4' x 4' tunnels. This combination permitted a test program covering a comprehensive series of test configurations and parameter variations over an extensive range of test conditions. The Lockheed Compressible Flow Facility (CFF), shown in Figure 9 is a specialized, exploratory test facility capable of conducting transonic investigations at Reynolds numbers up to $164 \times 10^6 / M$ ($50 \times 10^6 / \text{ft}$). The tunnel is of the blow-down type, exhausting directly to the atmosphere. The test section is 50.8 cm (20.0 in.) wide by 71.2 cm (28.0 in.) high by 183 cm (72.0 in.) long and is enclosed in a 3.7 m (12.0 ft) diameter plenum chamber. The top and bottom walls of the two-dimensional test section have variable-porosity capability (from 0 to 10 percent), obtained by sliding two parallel plates with 0.635 cm (0.250 in.) diameter holes slanted 60 degrees from the vertical. The 2-D test section side walls are not porous. The three-dimensional test section has variable-porosity top and side walls while the bottom wall, where the balance is located, is not porous. The 5-component semispan balance used in these tests is located in the floor of the tunnel. High-pressure air is passed through the balance to the model nacelles via two opposing bellows arrangements.

The Lockheed-California 4 x 4 ft. tunnel is similar to the CFF except that it has a much larger test section flow area. For this test, a 6-component wall-mounted balance was employed. The basic design and air ducting arrangement was essentially the same as for the balance system used in the CFF.

4.1.3 Experimental data analysis. - The format for presenting the more significant test results of Task II is first a summary of the aerodynamic wake

USB CRUISE PROGRAM

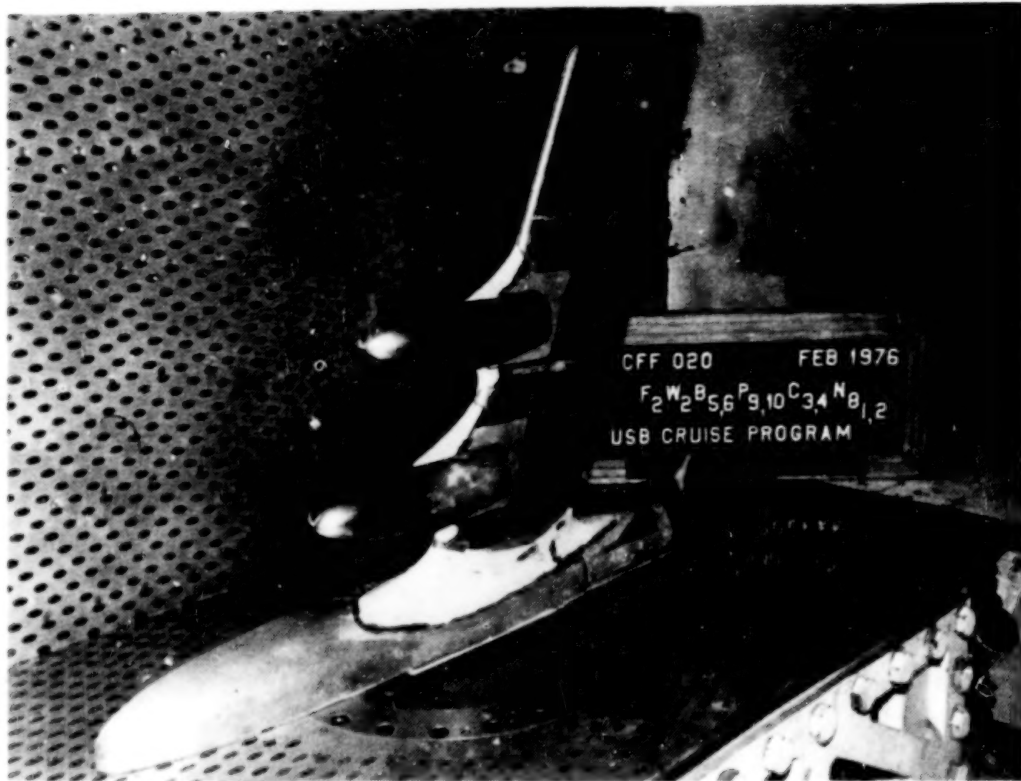


Figure 7. Dual D-Duct installation on 3-D swept wing force model in CFF.

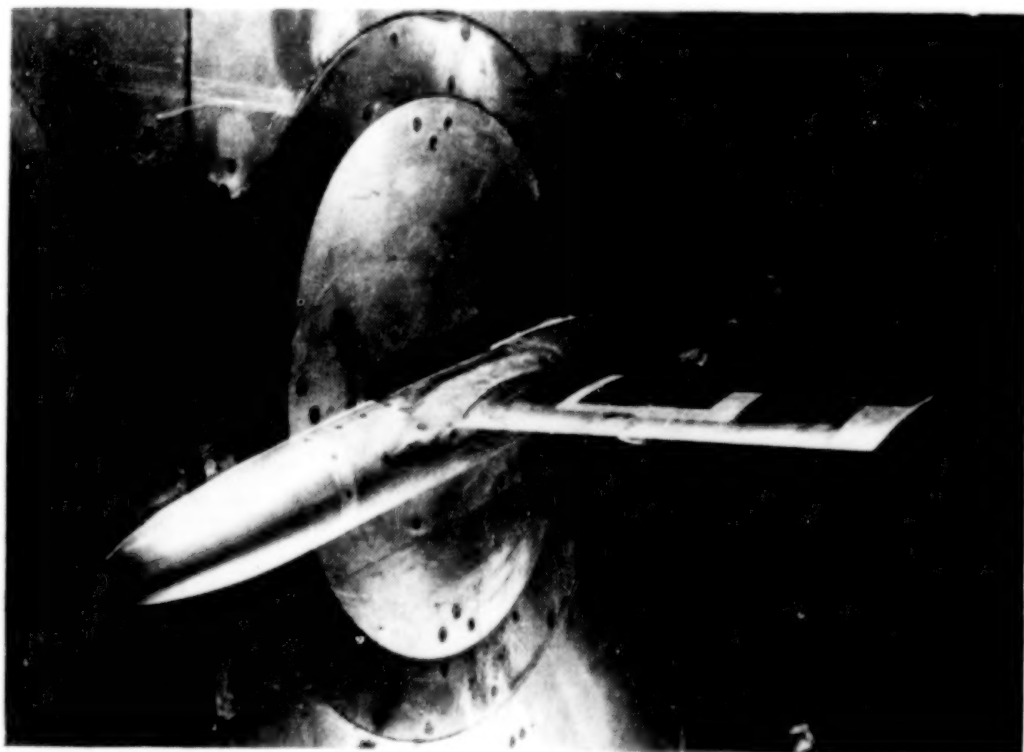


Figure 8. AR 4 nozzle installation on 3-D straight wing force model in 4' x 4' tunnel.

BLANK

PAGE

Lockheed Compressible Flow Facility

- Transonic Blowdown Tunnel $0.2 \leq M \leq 1.2$
- High Reynolds Number Capability $50 \times 10^6 / \text{Ft}$
- Variable Wall Porosity
- Model Blowing Capability 300PSI

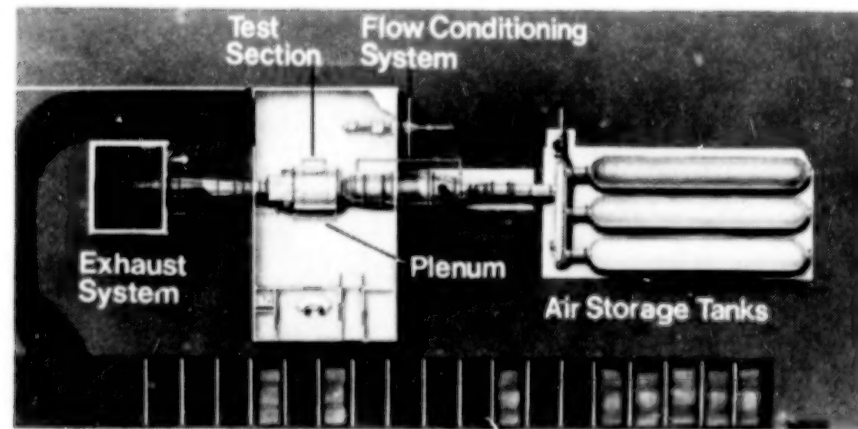


Figure 9. Lockheed Compressible Flow Facility (CFF). NOTE: $164 \times 10^6 / \text{m} = 50 \times 10^6 / \text{FT}$,
 $207 \text{ N/CM}^2 = 300 \text{ PSI}$

surveys. This discussion is followed by presentation of force-measurements results typifying the basic aerodynamic features of the USB-cruise configurations as tested.

4.1.3.1 Pressure-test results:

o Static versus wind-on - In the Data Base Program, it was necessary that the composition of the measured performance changes nominally associated with typical USB-installations be quantified in order to identify causative or particularly sensitive parameters. At cruise conditions, the highly interactive nature of the aerodynamic and propulsion flow-fields can greatly hinder identification of the sources of observed lift or drag changes. As a aid to this end, static tests of the installed nacelle are of value in assessing, to the first-order, parameters such as jet-deflection angles and jet-scrubbing losses. Since, in many instances, the assumption is made that these parameters vary little in going from the static to wind-on condition, surface-pressure measurements within the jet are particularly useful in studying the comparative behavior of the deflecting jet as such ambient changes occur.

Figure 10 shows typical chordwise variations of wing-surface pressures along the jet centerline of a small "D-Duct" - shaped nozzle. The figure compares pressures at both static and wind-on test conditions to those existing on the straight wing at $M = 0.68$. The pressure coefficients have been normalized on the basis of jet dynamic pressure, q_j , rather than q_∞ for convenience. At the pressure ratio selected, $H_j/p \approx 2.6$, the jet efflux is supersonic and the associated ~~shock~~ pattern generates rapid fluctuations in the measured pressures. It is apparent from these data that a basic difference in centerline pressure level exists between those measured statically and those in the wind-on condition. Moreover, the mean (negative) pressure level generated by the jet at wind-on conditions can exceed that existing on the clean wing at the same freestream conditions. These differences within the jet-scrubbing area are reflected as an increase in lift due to the jet turning over the wing surface and a corresponding increase in wing pressure-drag. Additionally, the data would suggest that, between static and wind-on conditions, a basic difference can exist in the angle at which the jet leaves the wing trailing-edge. This wind-on interaction of the jet and

USB CRUISE PROGRAM

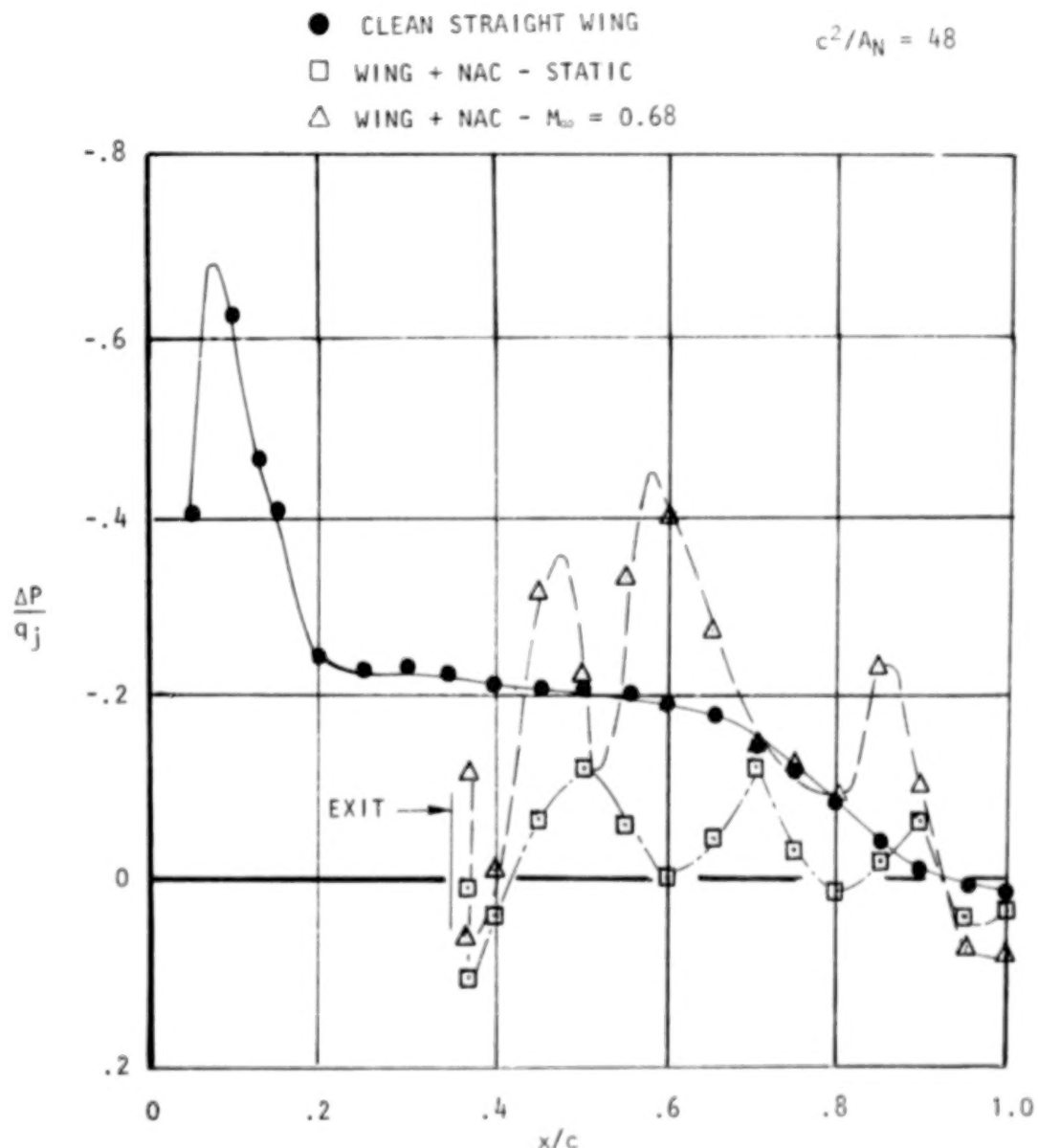


Figure 10. Jet centerline pressure distributions,
 "D-Duct", noz N_6 , $H_j/p_\infty = 2.6$, $\alpha = 2.6^\circ$.

wing flow-field is such as to generally increase the jet deflection angle with a subsequent increase in wing-surface pressure load (i.e., increased lift and pressure drag). These conclusions are supported by the wake-rake data provided in Figure 11 which compares total pressure measurements within the jet at both static and wind-on conditions. The comparison shows that at one chord-length aft of the wing trailing-edge, the jet is more concentrated and appears to be more highly deflected at the wind-on condition.

Figure 12 compares results obtained from several laser velocimeter surveys made spanwise near and slightly above the wing trailing-edge at both static and wind-on conditions. The nozzle configuration is a small "D-duct" design with exit at $x/c = 0.35$. The data are presented in terms of flow angularity relative to the wing chord-line; angle-of-attack is therefore subtracted out. The increase in inclination or vectoring of the jet flow-field ($\approx 8^\circ$) as a result of wind-on wing lift is readily apparent. Of interest also is the even greater flow inclination at the outer edges of the jet ($\frac{\Delta Y}{D_N}/2 > \pm 1.0$) induced by the strong vortices shed by the nacelle at angle-of-attack.

The primary conclusion drawn from the foregoing data is that the apparent or effective angle through which the jet is vectored by the wing under static conditions is substantially increased when the wing/nacelle is immersed in a freestream flow field. Therefore, static testing to quantify the trailing-edge jet angle may not necessarily be meaningful to the wind-on case.

o Effect of nozzle shape - Evaluation of the effects of geometric variations in the nozzle exit shape on aft-wing pressure at Mach number are provided in Figure 13; a relatively low nozzle pressure ratio is employed to minimize shock-induced pressure fluctuations in the comparison. From these as well as similar data, the pressure load generated within the scrubbed area appears to be generally dependent on nozzle height (nozzle aspect ratio in the figure) and on the boattail angle or jet-impingement angle. In this figure, the wide nozzle, (aspect ratio = 4) characterizes a high boattail angle configuration ($\beta = 36^\circ$). The resulting impingement of the jet creates a comparatively high-pressure region just aft of the nozzle exit thus tending to suppress the lift generated at least along the jet centerline. The high impinge-

USB CRUISE PROGRAM

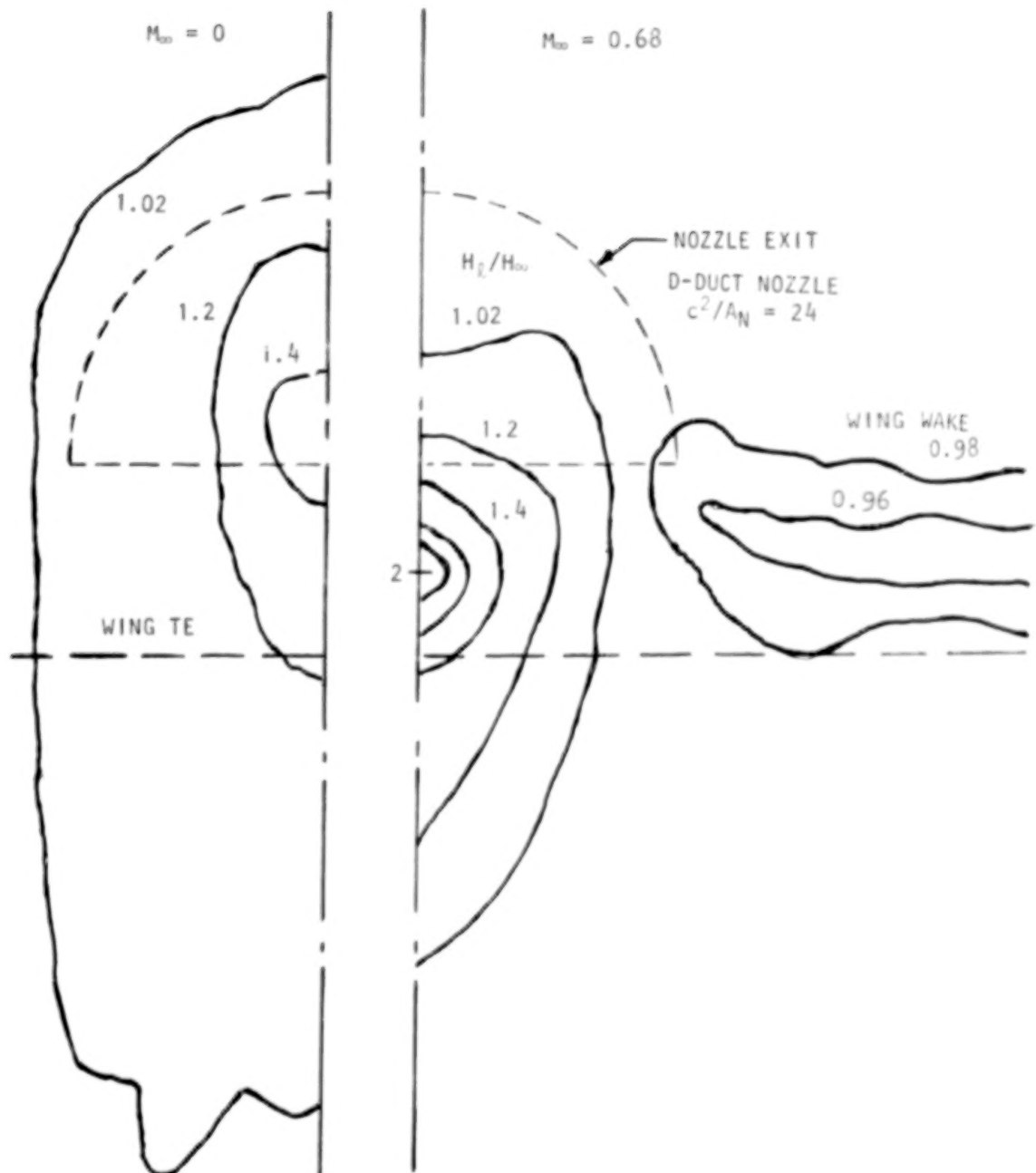


Figure 11. Comparison of static and wind-on jet isobars one chord length behind straight wing, $H_j/p_{\infty} = 2.2$, $\alpha = 2.6^\circ$.

USB CRUISE PROGRAM

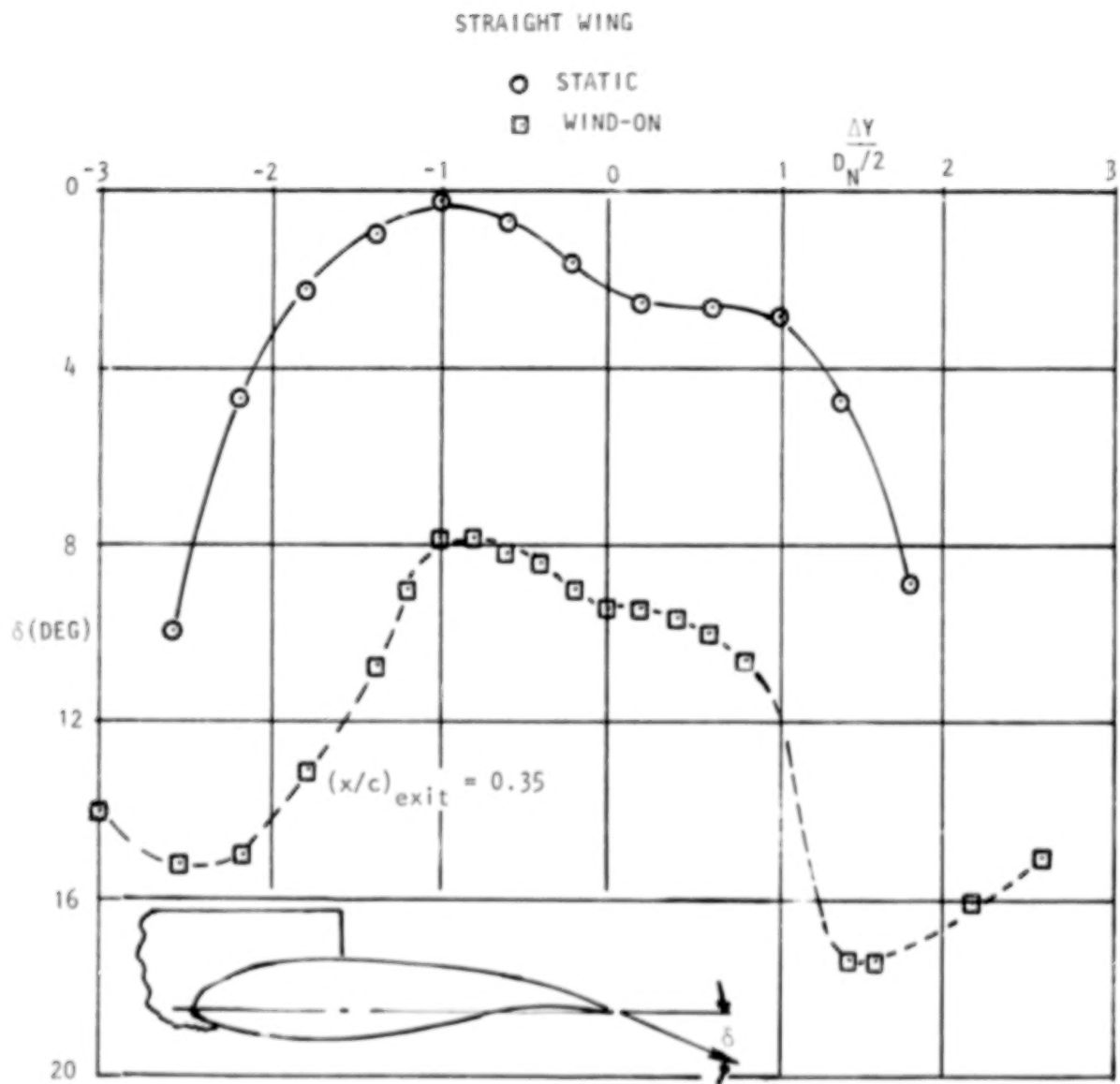


Figure 12. LV measurements of spanwise distribution of trailing-edge flow angularity, small "D-duct" nacelle $\alpha = 0^\circ$

USB CRUISE PROGRAM

NOZ	AR	β (DEG)	
\circ N_{2E}	1.25	16	$c^2/A_N = 24$
\square N_{3E}	2.5	25	
\triangle N_{4E}	4	36	
● CLEAN STRAIGHT WING			

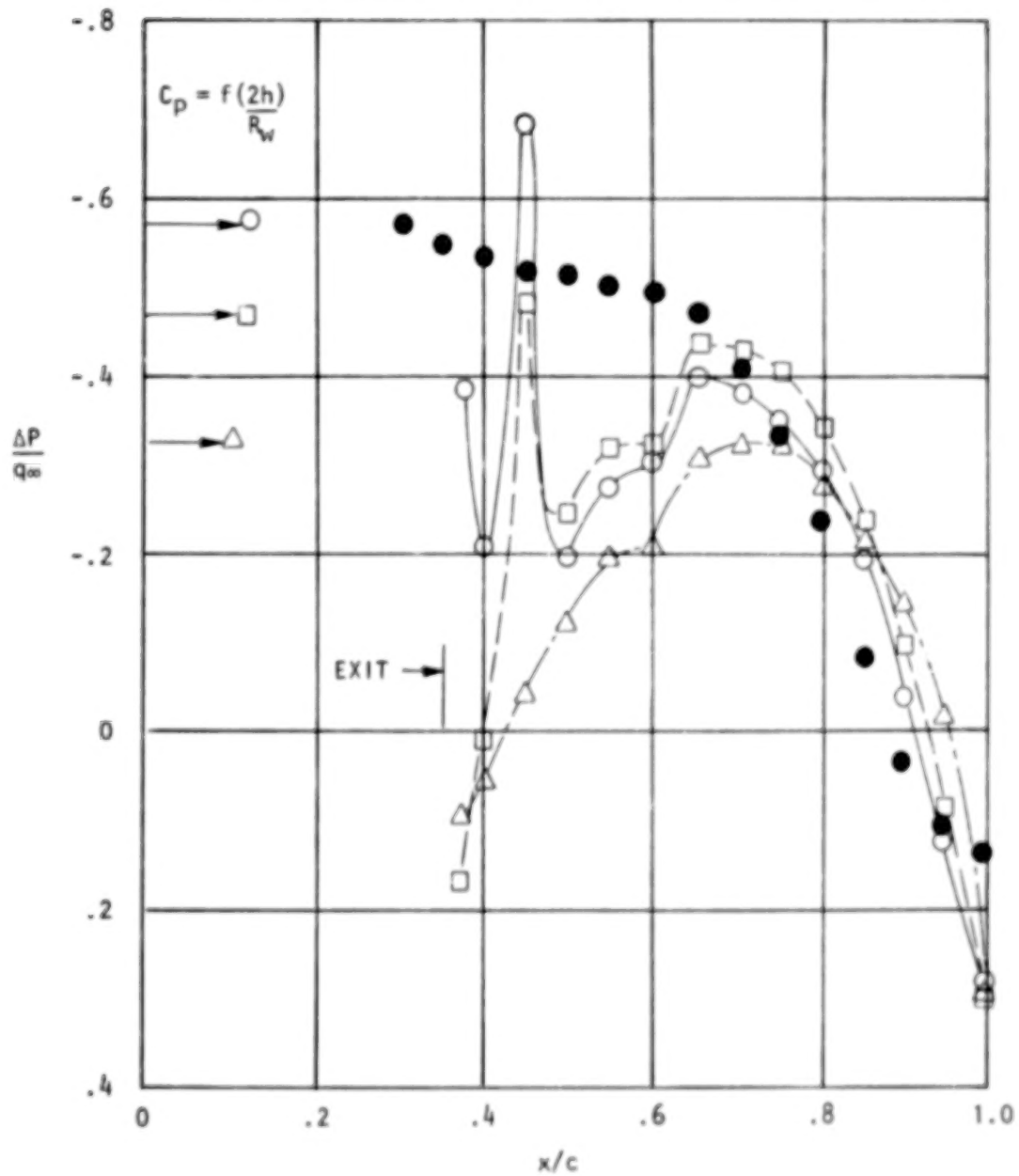


Figure 13. Effect of nozzle exit shape on jet center-line pressures, $\alpha = 2^\circ$, $M_\infty = 0.60$, $H_j/p_\infty = 1.4$.

ment angle would also cause a thinning and spreading of the jet with closer adherence to the wing surface forward of the trailing-edge. The increase in jet-vectoring due to jet-thinning would also tend to produce a more negative pressure level forward of the wing trailing-edge as evidenced in the figure by the data for the aspect ratio 4 nozzle. This increase in section aft-loading produces a pressure drag component relative to the drag of the clean wing. As the nozzle aspect ratio is reduced and the jet thickness is increased (nozzles N_{3E} and N_{2E}), both the extent of the high pressure region and the pressure drag diminish, with the latter indicative of a lower jet-deflection angle. Shown also on Figure 13 are values of the pressure coefficient as calculated from the statically-derived Coanda expression (Reference 1):

$$C_p = \frac{2h}{R} \left(\frac{q_j}{q_\infty} \right) \quad (1)$$

which relates maximum centerline pressure for an attached jet to jet-height, (h), aft-wing radius of curvature (R) and jet-dynamic pressure ratio (q_j/q_∞). The jets from the two wide nozzles more closely follow the wing upper surface and therefore show trends corresponding to the calculated pressure coefficient. The thick circular jet, unable to follow the wing surface, separates thereby generating a less negative pressure level which implies less jet-induced lift and less section pressure drag.

- o Effect of pressure ratio - As indicated in Figure 14, the general effect of nozzle pressure ratio on jet-centerline pressures is a gradual increase in the negative pressure level over the airfoil aft-surface. Thus, these changes would be manifested as an increase in lift generated within the area scrubbed by the jet and a similar change in aft-wing pressure drag when comparing these pressure levels to those of the clean wing. The aft-wing pressure drag appears to be generally increasing with pressure ratio; evaluation of the lift changes requires integration of the pressures to properly assess the trend.

- o Integrated pressure data - As an aid to force-data interpretation, pressure data within the jet-scrubbed area were integrated in both the lift and drag directions. The basic assumption made was that the measured centerline pressures were essentially sustained across the exit width of the nozzle.

USB CRUISE PROGRAM

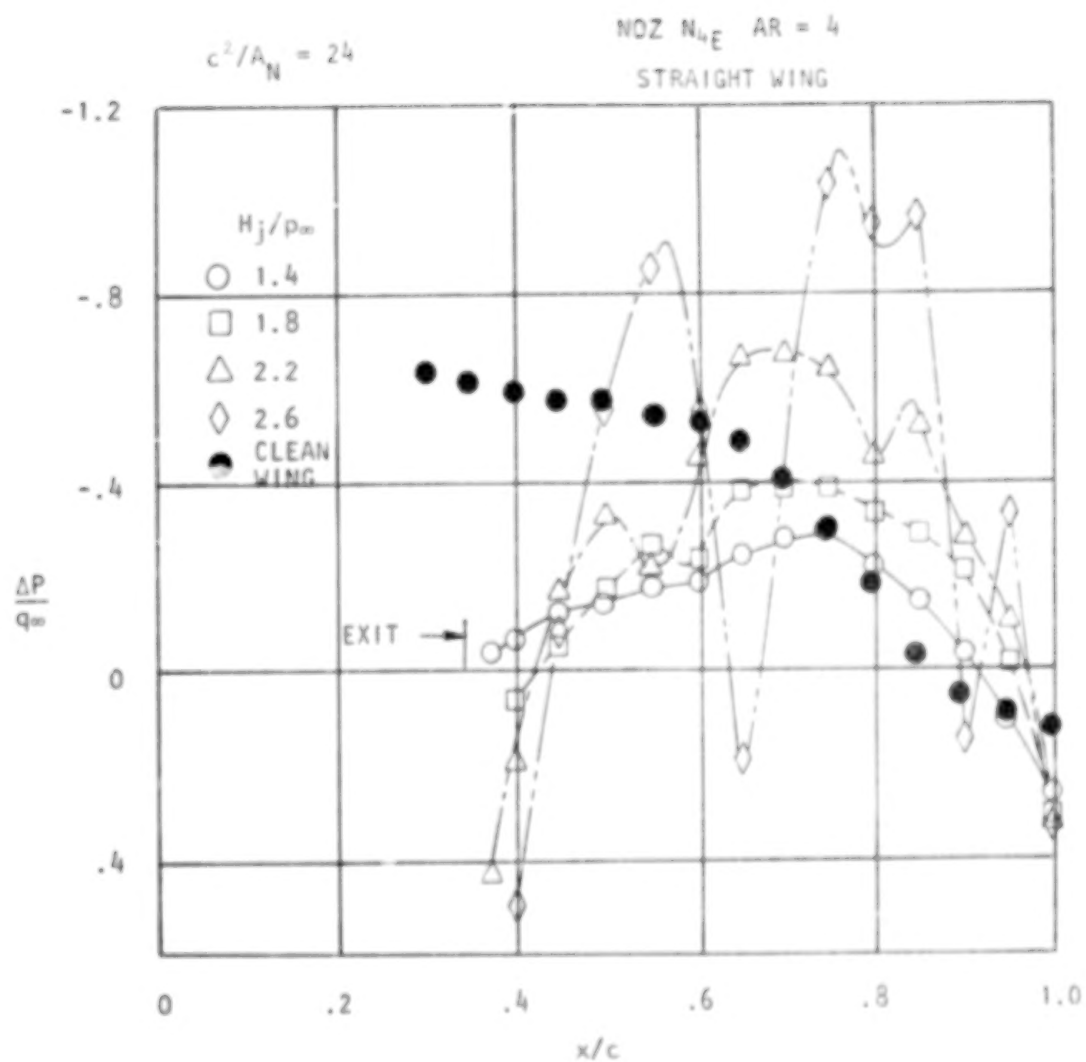


Figure 14. Effect of nozzle pressure ratio on jet centerline pressures, $\alpha = 3^\circ$, $M_\infty = 0.70$.

The validity of this assumption has an obvious dependency on the spreading rate of the jet or the degree of jet attachment to the surface. However, flow visualization photographs, along with evaluation of multiple rows of surface pressures behind the wide nozzles, indicated this assumption to be reasonable.

The pressure integration was carried out chordwise from the nozzle exit to the wing trailing-edge. Incremental lift and drag coefficients, based on wing area, could then be evaluated from:

$$\Delta C_L = \left| \int_{(x/c)_{\text{Exit}}}^{1.0} C_p \frac{d(x/c)}{c} \right| \Delta \eta \quad (2a)$$

$$\Delta C_D = \left| \int_{(z/c)_{\text{Exit}}}^{(z/c)_{\text{TE}}} C_p \frac{d(z/c)}{c} \right| \Delta \eta \quad (2b)$$

where $\Delta \eta$ represents the exit width of the nozzle. Use of a similar procedure for the clean wings provided comparative data such as shown in Figures 15 and 16. The data show typical variations of the integrated pressure drag coefficient as a function of nozzle pressure ratio. For the two wide nozzles, Figure 15, the pressure drag increases almost linearly with nozzle pressure ratio starting at a level corresponding to that of the clean wing. Also shown on the Figure are the pressure drags calculated by the function:

$$\Delta C_L = \eta_T C_T \sin(\alpha + \delta_j) \quad (3)$$

which is derived from simple momentum relationships associated with a deflecting jet. The deflection angle, δ_j , (see Force Data Analysis for static δ_j and η_T evaluations) as used herein, represent either the static value or an angle approximating the wing upper-surface angle at the trailing-edge ($\approx 17^\circ$); both values are represented in the Figure. For both nozzles, the integrated pressure drags indicate that the jets are turning through approximately the full trailing-edge angle of the wing and are thus capable of generating a high pressure drag penalty. Figure 16, prepared for the "D-duct" and circular nozzles, shows a progressive reduction in pressure drag relative to that potentially possible under fully attached conditions as the jet thickness increases.

USB CRUISE PROGRAM

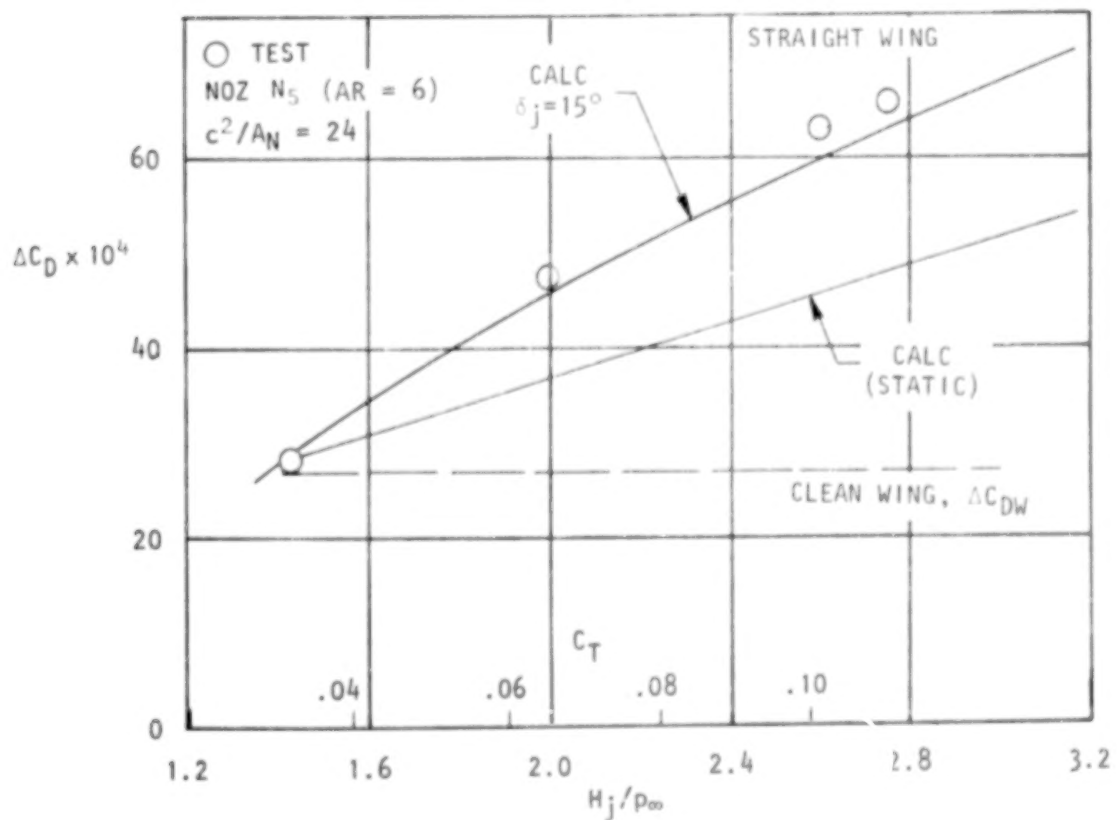
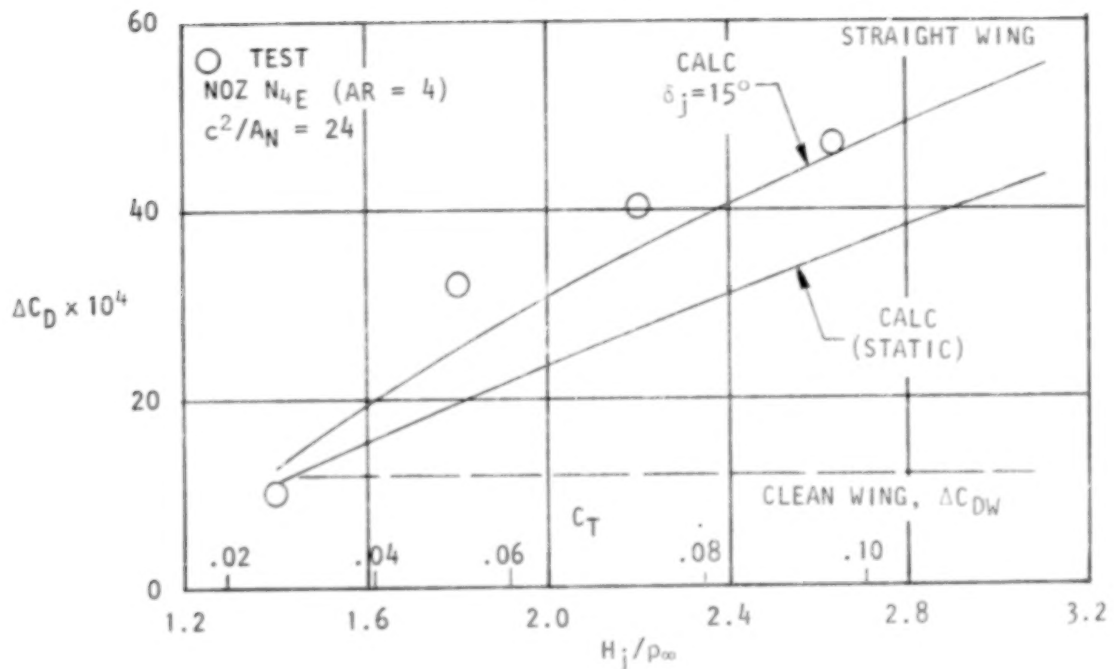


Figure 15. Variation of scrubbed area pressure drag with pressure ratio, $\alpha = 2^\circ$, $M_\infty = 0.68$.

USB CRUISE PROGRAM

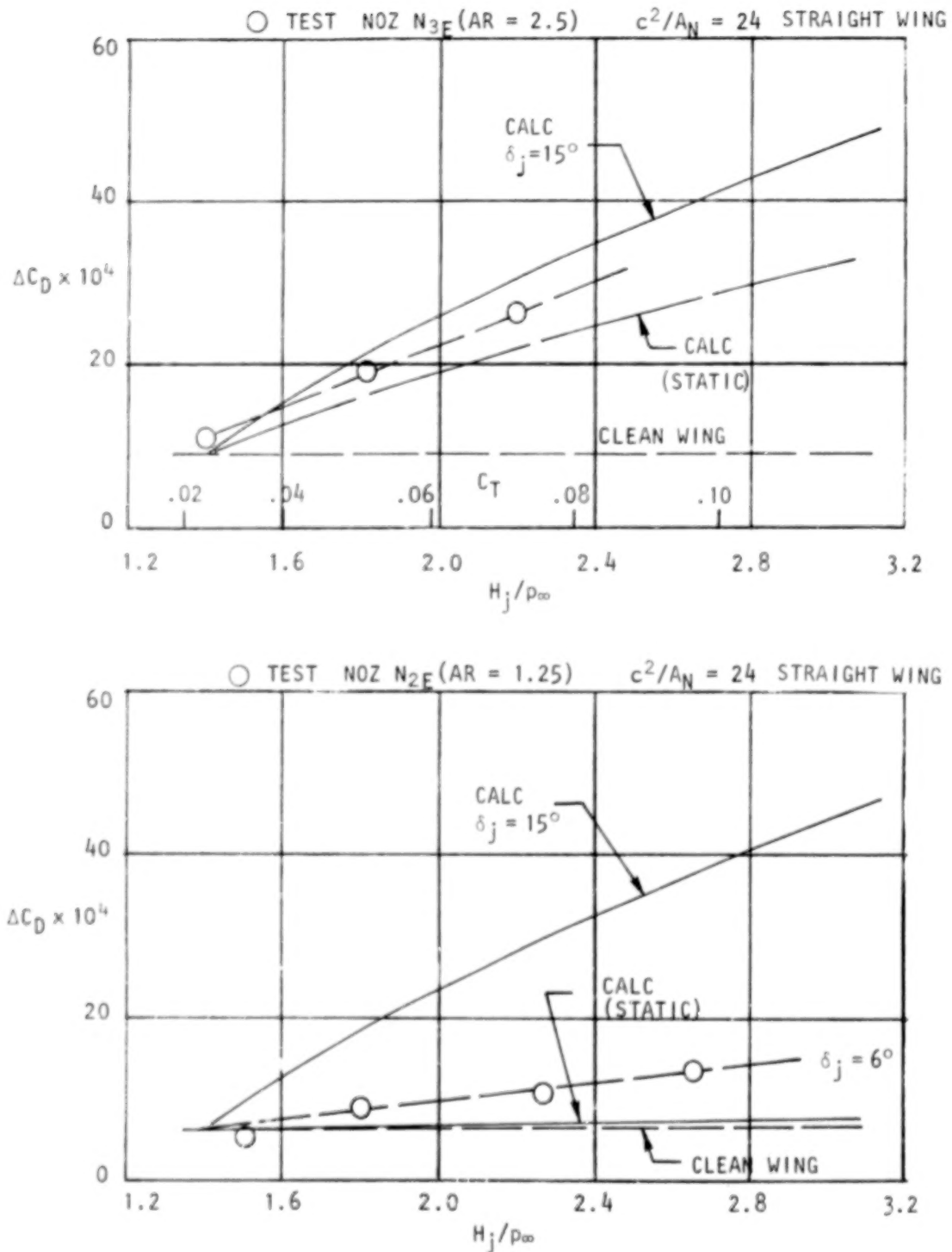


Figure 16. Variation of scrubbed area pressure drag with pressure ratio, $\alpha = 2^\circ$, $M_\infty = 0.68$.

Integrated pressure drags as obtained from the present model are compared in Figure 17 to those obtained in a similar fashion from a rectangular (exit) nozzle configuration, Reference (2). The comparison is made in terms of the ratio of increase in drag of the nacelle with blowing to that of the nacelle at flow-through conditions. As noted, the trends and magnitude of the drag variations are similar for the two tests. Since the foregoing pressure integrations have been based on only that segment of wing area immediately aft of the nozzle exit, the possibility exists for full or partial recovery of the scrubbed area pressure drag via increased leading-edge suction on adjacent wing sections. Additionally, the suction lost over that span of wing covered by the nacelle forebody should also be accounted for by this mechanism. While modest reductions in adjacent leading-edge pressure were noted as nozzle pressure ratio was advanced, these regions generally culminated in increasingly strong shocks at the forward wing/nacelle-forebody junctures. It is believed, therefore, that due to the freestream Mach conditions, coupled with displacement effects of the nacelle forebody, a sufficient increase in leading-edge suction such as to overcome these accrued pressure drag components would be highly unlikely. It is believed reasonable also, that the loss in suction over that portion of the leading-edge covered by the nacelle could be so recovered. As will be indicated in a later section, this rationale appears to be warranted by the breakdown of the force data.

Corresponding integrated lift increments are presented in Figures 18 and 19 as a function of nozzle pressure ratio. The data show that, when considering only the prescribed scrubbed area downstream of the nozzle exit, lift is reduced, upon nozzle installation, below that carried by the clean wing. This is particularly true of the high boattail angle configuration (N_4 _E, Figure 18) which, as mentioned previously, incurs a high-pressure region near the nozzle exit thus suppressing the section lift. As the pressure ratio is increased, the integrated lift increment recovers toward the clean wing values.

Also shown on Figures 18 and 19 are values of the lift increment derived from the expression:

$$\Delta C_L = n C_T \sin (\alpha + \delta_j) \quad (4)$$

USB CRUISE PROGRAM

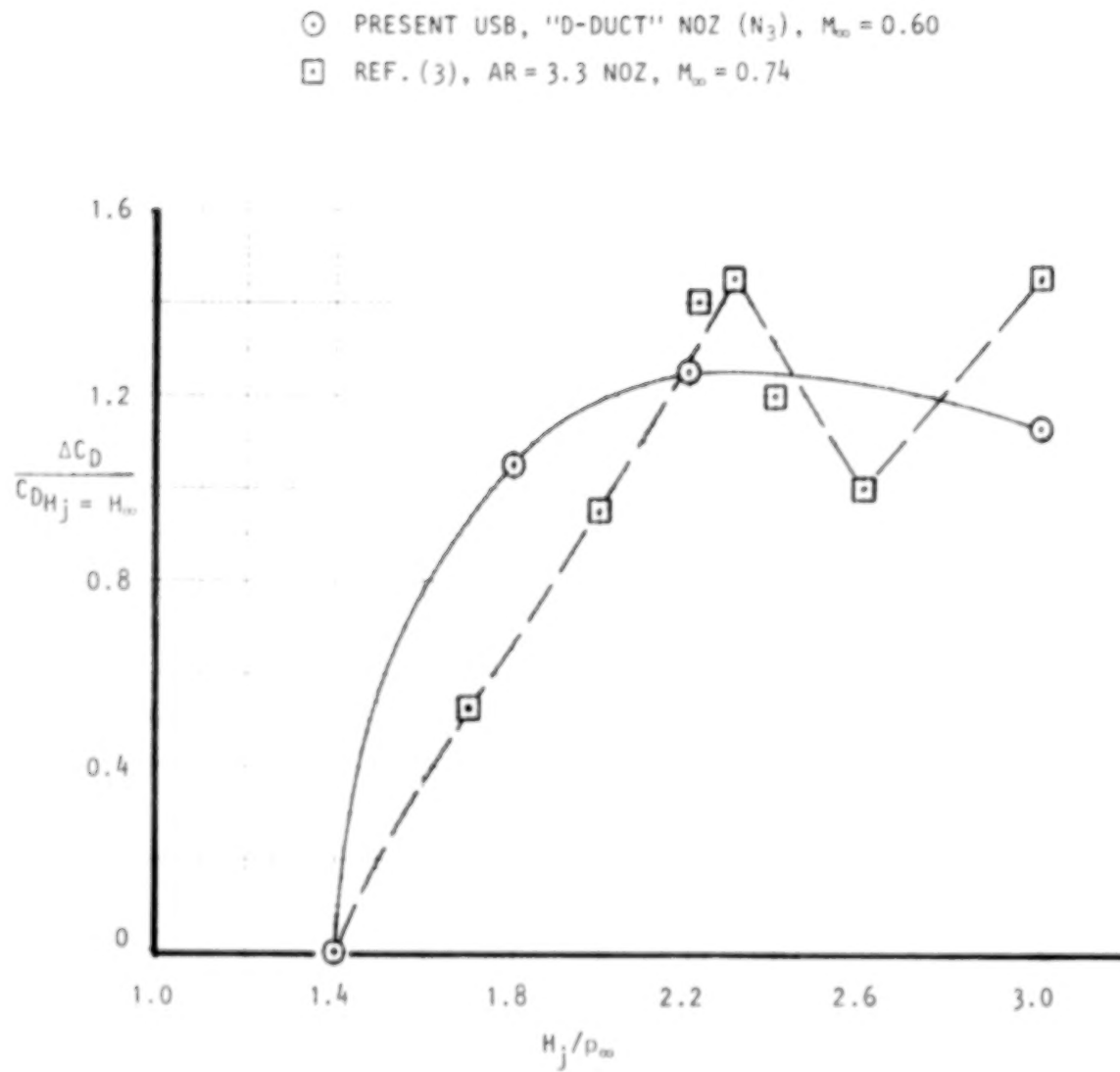


Figure 17. Comparison of pressure drag developed in scrubbed area.

USB CRUISE PROGRAM

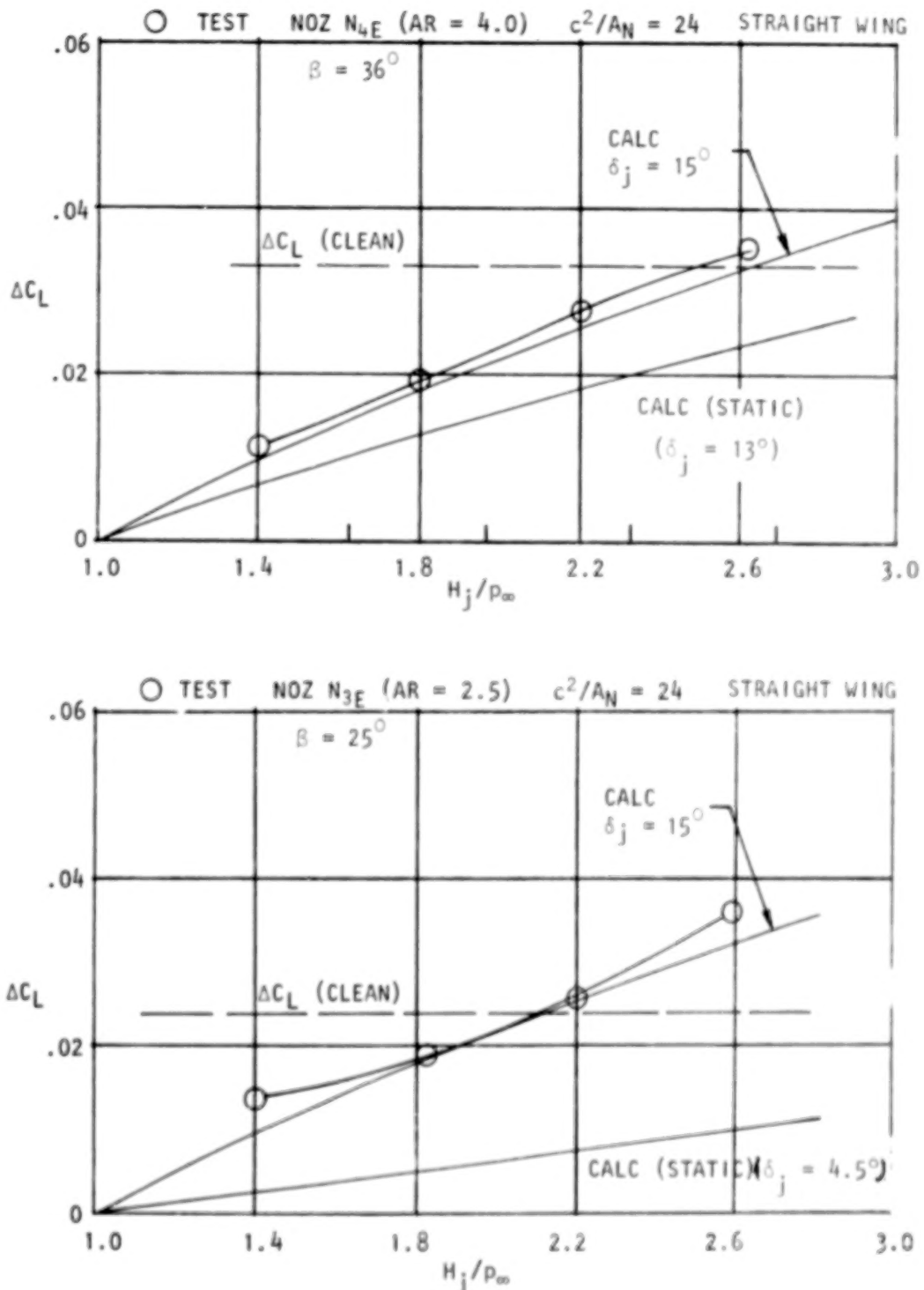


Figure 18. Lift developed in scrubbed area with blowing, $\alpha = 2^\circ$, $M_\infty = 0.70$.

USB CRUISE PROGRAM

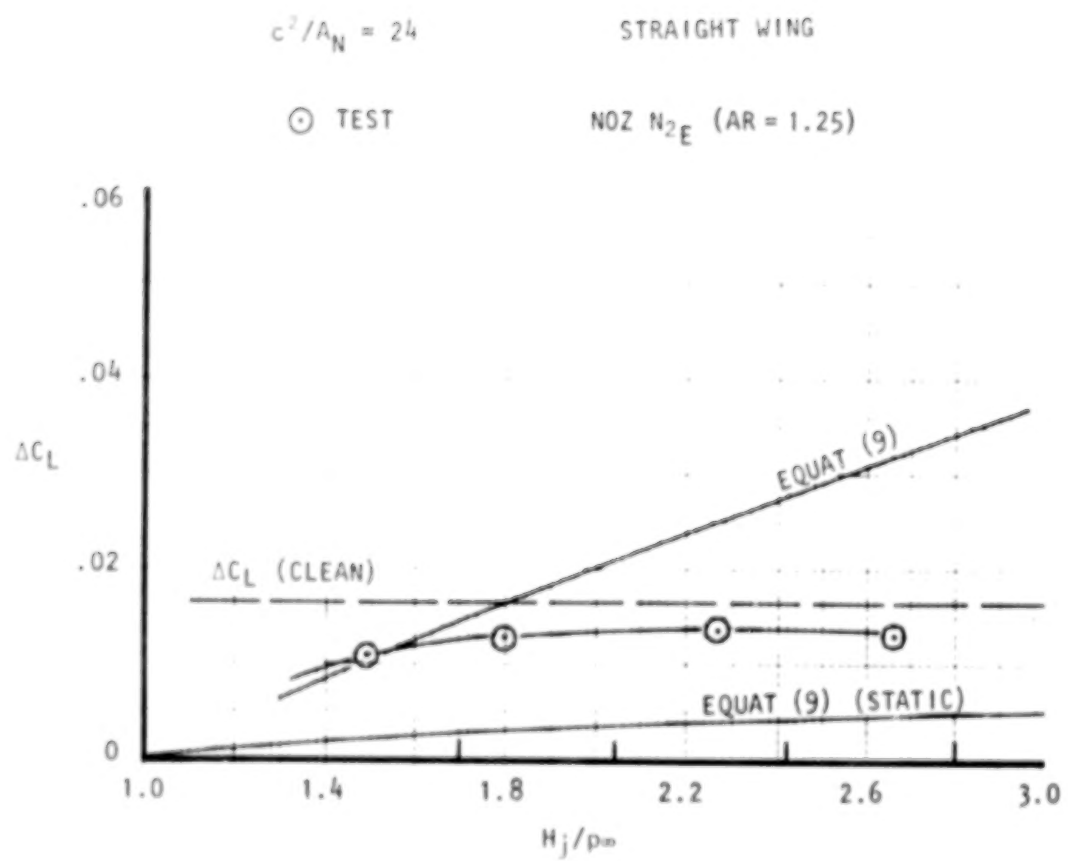


Figure 19. Lift developed in scrubbed area with blowing, $\alpha = 2^\circ$, $M_\infty = 0.70$.

which is the lift component corresponding to the aforementioned momentum-derived drag expression, (equation 3). As indicated in Figure 18, the calculated values agree more closely with the integrated lift increments when the wing trailing-edge angle of 17° is used in the calculations rather than the lower, statically-determined values of δ_j .

As will be shown later in discussions of force data, total lift increments due to blowing are substantially higher than those indicated in Figure 18 and 19. This would indicate that a substantial amount of jet-induced lift is carried by adjacent sections. As indicated in the spanwise survey of Figure 12, the maximum trailing-edge injection angles occur just beyond the boundary defined by the projected nozzle width. The lift on these sections should be increased accordingly. This effect, coupled with jet-entrainment of the boundary-layer from adjacent sections, is believed responsible for the additional lift of the system evidenced in the force data.

As preliminary to force-test analysis, it was concluded from the pressure test results that an unrefined USB-configuration can potentially sustain a high pressure drag penalty dependent upon the shape or two-dimensionality of the jet and operating pressure ratio. High boattail angles, employed to enhance jet attachment, can increase the aft-wing pressure loading, and thereby lift and pressure drag, as the thinned jet becomes more strongly attached to the wing. At least within the scrubbed area, the net lift can also be suppressed by high impingement or boattail angles due to high pressure near the nozzle exit. Other conclusions drawn were that static testing could not be relied upon as an indication of effective wind-on jet deflection angles and that at cruise conditions, the influence of the jet on adjacent wing pressures was confined to a span of several nozzle half-widths of the jet centerline.

4.1.3.2 Force-test results: Results of the force tests are considered in terms of incremental drag and lift due to installation of the blowing nacelle on the clean wing. With particular reference to the nacelle drag penalties at cruise, such penalties are always derived herein as the balance-measured drag (or accelerating) force less the thrust produced by the isolated nozzle. The total drag penalty then consists of all losses inclusive of in-

stallation as well as cruise interference effects. Major results and typical trends from the force tests are summarized below.

o Total cruise drag penalty - The increment in drag coefficient due to the installation of several medium-sized ($c^2/A_N = 24$), "D-duct" nacelles (N_{3B} and N_{3E}) on the straight wing is shown in Figure 20 as a function of nozzle gross thrust and lift coefficients. The Mach number represents a typical straight-wing cruise point of $M = 0.68$. The trend of the drag data with thrust coefficient at $C_{LM} = 0.4$ shows a minimum drag point at $C_T = 0.05$, or a nozzle pressure ratio of 1.8 - 1.9. At greater values of C_T , the drag of these installations gradually increases with a slight drop-off indicated at the maximum test C_T - value ($H_j/p_\infty = 3.0$). It is believed that these trends are primarily a reflection of the changing jet-flow characteristics as the pressure ratio is advanced. Between H_j/p_∞ - values of 1.4 and 1.8 (i.e. approaching sonic conditions at $H_j/p_\infty = 1.89$), the interactive effects of the jet are primarily viscous in nature with a favorable boundary-layer control effect exerted on adjacent wing sections (entrainment) and within the wing scrubbed area. With further advances in pressure ratio, a pressure drag, induced by the jet deflecting over the aft-wing surface, increases in accordance with the conclusions drawn in the pressure test discussions. At, or near, the maximum test pressure ratio ($2.6 \leq H_j/p_\infty \leq 3.0$), the "hard-choke" condition at the nozzle exit, along with the associated shock structure within the jet, sets up unstable flow conditions such that the jet tends to separate from the aft-wing surface. Under these conditions, the jet deflection angle, and the attendant pressure drag, would be suppressed or reduced. A similar trend was noted earlier in regard to the evaluation of the integrated pressure data. With nozzle N_{3B} , an increase in lift coefficient has little effect on the drag trend with C_T ; the magnitude of drag coefficient does show a progressive increase with C_L as reflecting a greater drag-due-to-lift penalty. The effect of lift coefficient on the drag performance of the companion nozzle (N_{3E} , Figure 20) shows a rather abrupt increase in drag at $C_L \approx 0.5$. This configuration was designed with a relatively high boattail angle ($\beta = 25^\circ$) which would promote flow separation on the nozzle just ahead of the exit in the higher α -range. At a typical cruise lift coefficient of 0.4, the boattail flow is marginally attached on this configuration with a slightly higher drag

USB CRUISE PROGRAM
STRAIGHT WING

C_{LM}

○ 0.3

□ 0.4

△ 0.5

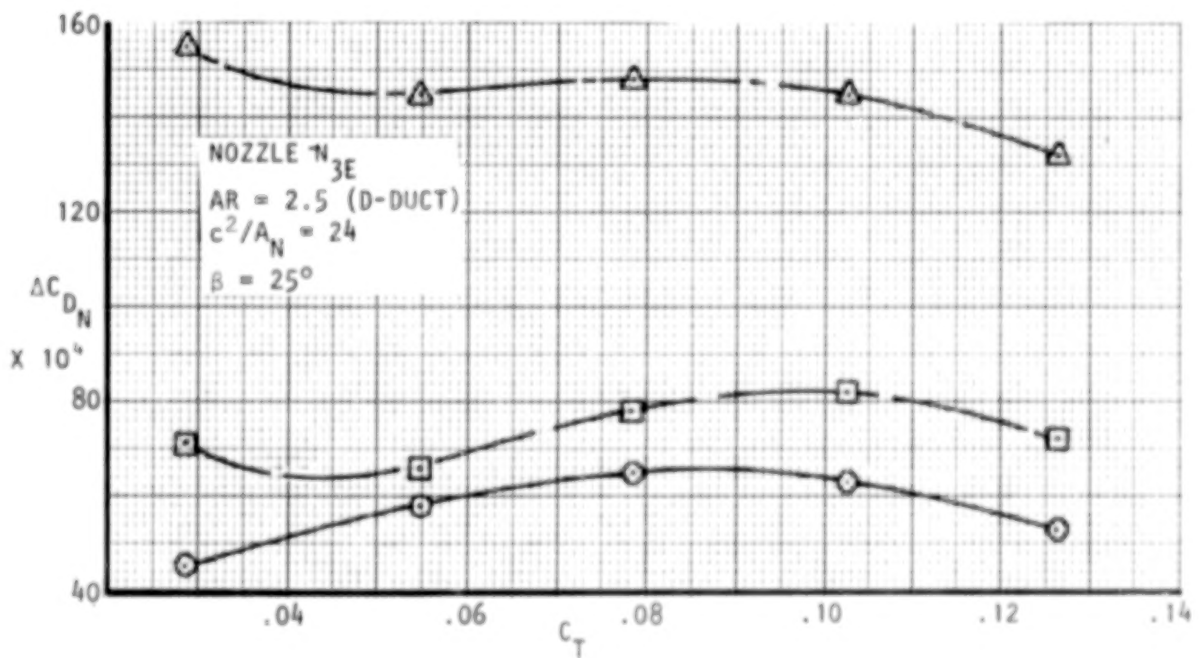
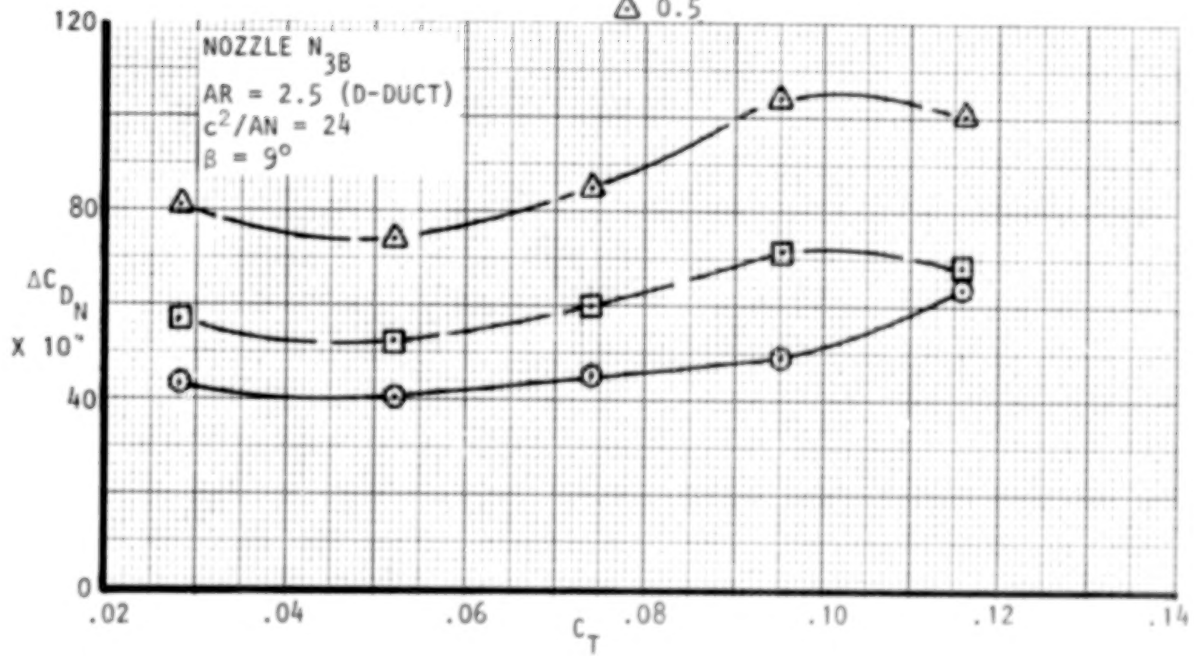


Figure 20 . Effect of lift coefficient on nacelle drag, $M_\infty = 0.68$

level and about the same trend with C_T , as its lower boattail angle counterpart, nozzle N_{3B} .

Similar drag data are shown in Figure 21 for several circular nozzle configurations mounted on the straight wing. The geometric difference in these two nozzles is essentially one of nacelle length and boattail angle with N_{2E} being the shorter, high boattail angle configuration. In contrast to the "D-duct" arrangement (Figure 20), both circular nozzles portray a more linear variation of C_{D_N} with C_T in the low blowing range rather than an optimum blowing rate as noted earlier. It would be expected that any beneficial boundary-layer control exerted by the circular jet would be essentially via flow entrainment inasmuch as the degree of contact between jet and wing is limited (initially) to the point of tangency at the nozzle exit. Therefore, the influence of the jet on the viscous characteristics of adjacent wing sections and aft-wing surface would be similarly limited. Beyond $H_j/p_\infty = 1.89$, (choke), the jet shock formations delay a rapid build-up of pressure drag until the maximum blowing rate is reached. On some configurations, testing at pressure ratios in excess of $H_j/p > 3.0$ indicated an almost cyclic-drag trend above choke pressure ratio ($H_j/p_\infty = 1.89$); this effect would be consistent with progressive changes in the inclination and positions of the jet-shocks as the nozzle exit Mach number is increased.

Increasing the nozzle exit aspect ratio to 4.0 and 6.0 (Figure 22) provides drag data with somewhat the same trends with thrust coefficient as were noted for the "D-duct" designs. With the thin, wide jet, a strong viscous interaction would be expected at the lower blowing rate. However, a greater tendency for jet-attachment would tend to offset this beneficial effect due to a corresponding increase in pressure drag. These combined effects would tend to delay the appearance of an "optimum" blowing condition (i.e. minimum drag point) to the higher lift-range where viscous effects on the basic wing are more pronounced. Thus, aspect ratio 4 nozzle (N_4) shows a pronounced "drag bucket" at $C_T = .05$ and $C_L = 0.5$ rather than $C_L = 0.4$ as for the "D-duct" arrangement. The aspect ratio 6 nozzle (N_5) shows a minimum drag point at $C_T \approx 0.10$ and $C_L = 0.5$. A more important observation in the case of the high-aspect ratio nozzles of Figure 22 is that the magnitude of the nacelle drag penalties at all lift levels is significantly higher than for the circular or

USB CRUISE PROGRAM
STRAIGHT WING

C_{LM}

- 0.3
- 0.4
- △ 0.5

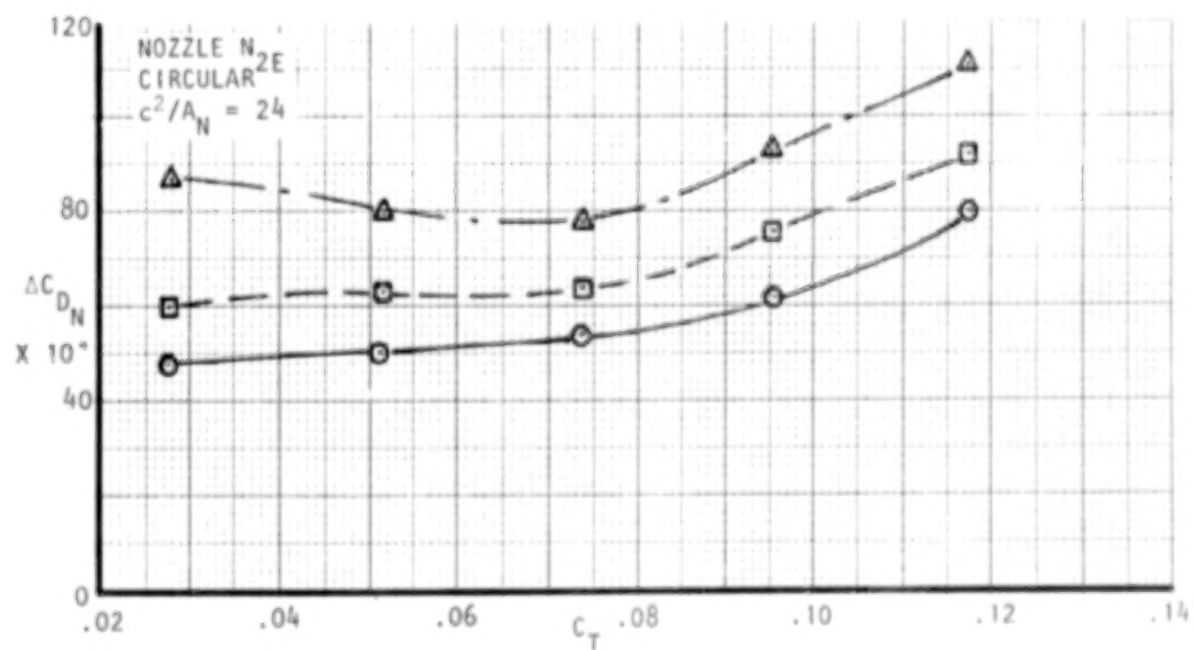
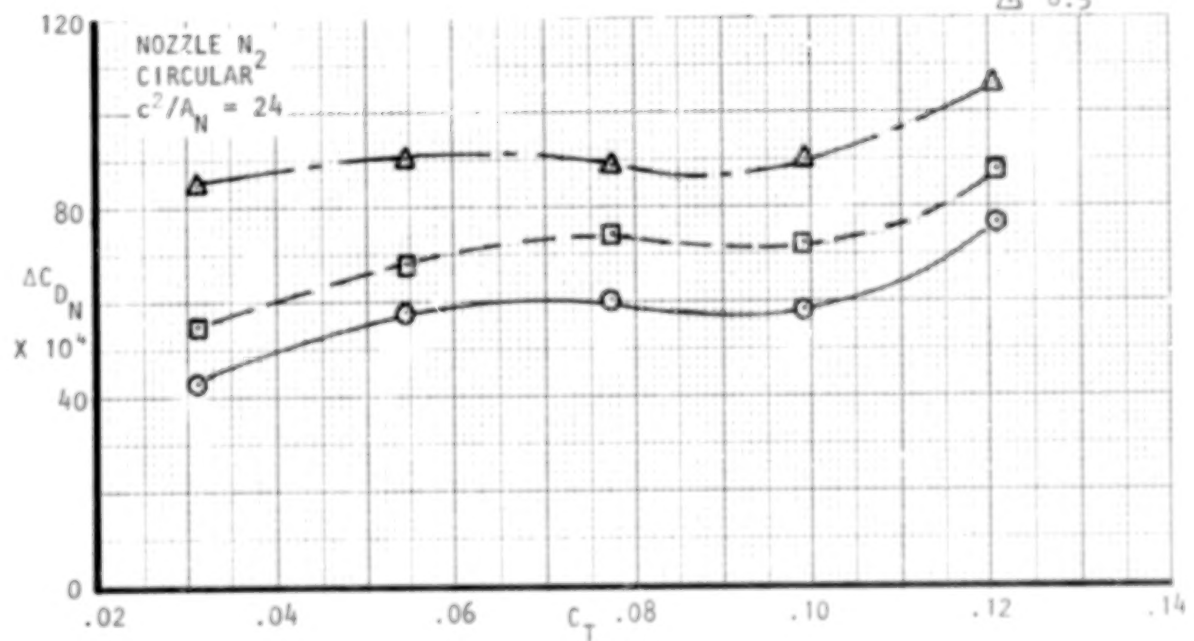


Figure 21 . Effect of lift coefficient on nacelle drag, $M_\infty = 0.68$

USB CRUISE PROGRAM
STRAIGHT WING

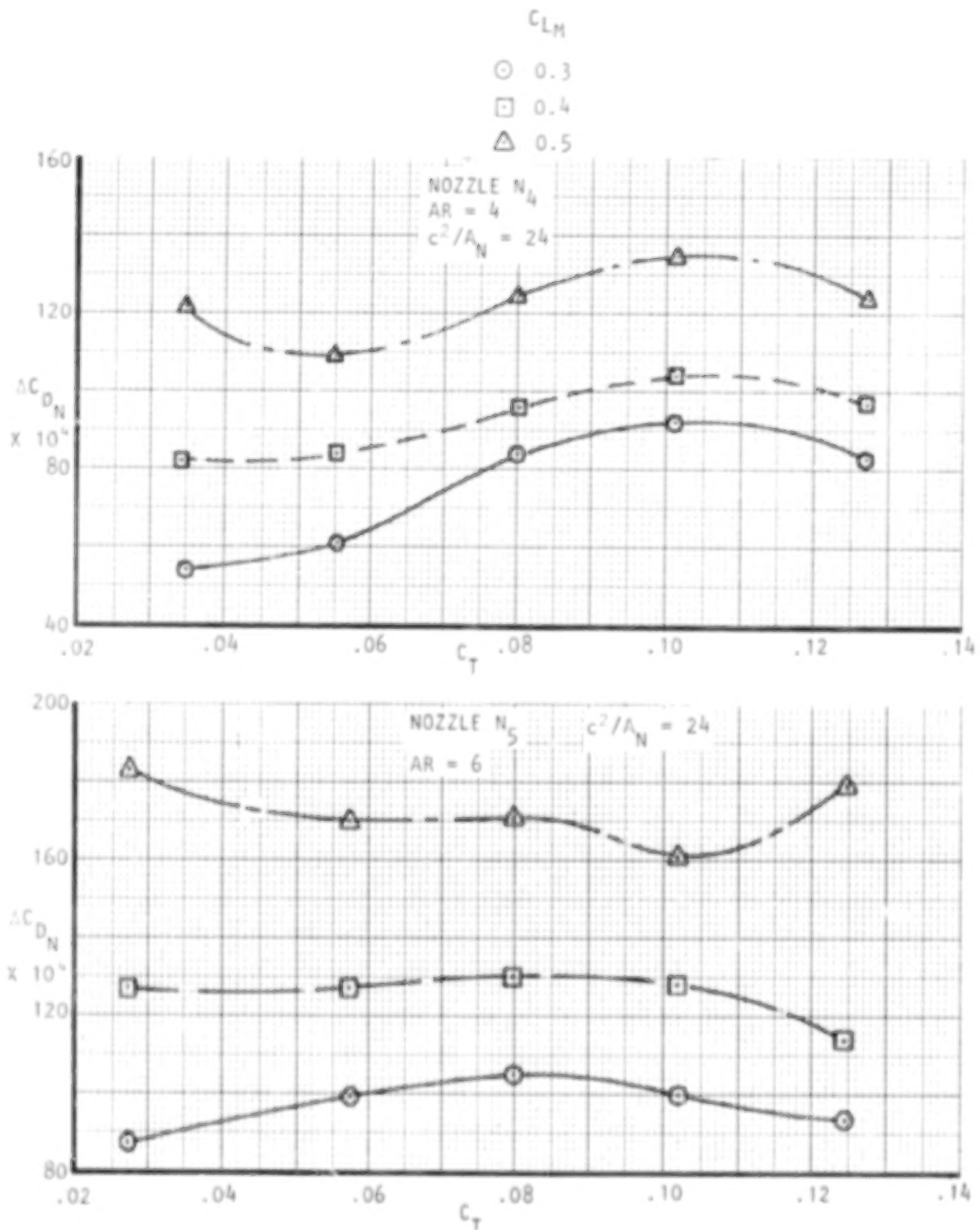


Figure 22 . Effect of lift coefficient on nacelle drag, $M_\infty = 0.68$

"D-duct" designs. As will be discussed, this drag increase with nozzle width is associated with a much higher drag-due-to-lift penalty.

Nacelle drag data representing swept-wing installations at a drag-rise Mach number of 0.73 are provided in Figures 23 and 24. The nacelle size is half that of the straight wing designs ($c^2/A_N = 48$ as opposed to $c^2/A_N = 24$) but similarly, range in exit aspect ratio from circular (N_{11}) to aspect ratio 6 (N_{13}). While, in general, the drag trends with C_T resemble those noted for straight wing installations, drag excursions for a specified nozzle and lift coefficient are smaller. The latter effect is principally due to the much reduced level of thrust produced by the small nozzles when operating at pressure ratios between 1.4 and 3.0. It is also noted that, relative to the medium-sized, straight wing nozzles, the magnitude of the drag increments with the swept wing installations are not reduced in proportion to the nozzle size. This, in part, is due to the sensitivity of the swept wing design at the higher Mach number. Additionally, difficulties in providing swept wing/nacelle fillets of "equivalent effectiveness" to those of the straight wing installations could be involved in this comparison.

o Effect of Thrust (H_j/p) on Total Lift - Typical levels of cruise total measured lift developed at various nozzle pressure ratios and angles-of-attack are shown in Figure 25. The installation represented is a medium-sized ($c^2/A_N = 24$) "D-duct" configuration (N_{3E}); clean wing lift values are also shown for comparison. In contrast with the integrated pressure results, (Section 4.1.3.1), which considered only the lift generated within the jet-scrub area, these data show that the clean wing lift is essentially recovered at the flow-through pressure ratio ($H_j/p_\infty \approx 1.4$) rather than at $H_j/p_\infty \approx 2.2$ (Figure 18). This difference supports the view that substantial lift is promoted on the wing sections adjacent to the jet via flow entrainment and highly localized trailing-edge jet angles such as illustrated in Figure 12. Figures 26 through 28 show similar lift data for straight wing installations spanning the nozzle aspect ratio range from circular to $AR = 6.0$. As would be expected, increments of lift-due-to-blowing with the circular nozzle are small due to reduced jet vectoring angles and the limited spanwise influence of the jet. Correspondingly, lift-due-to-blowing improves rapidly as the width or aspect ratio of the nozzle increases (Figure 27 and 28). The lift increments due to

USB CRUISE PROGRAM
SWEPT WING

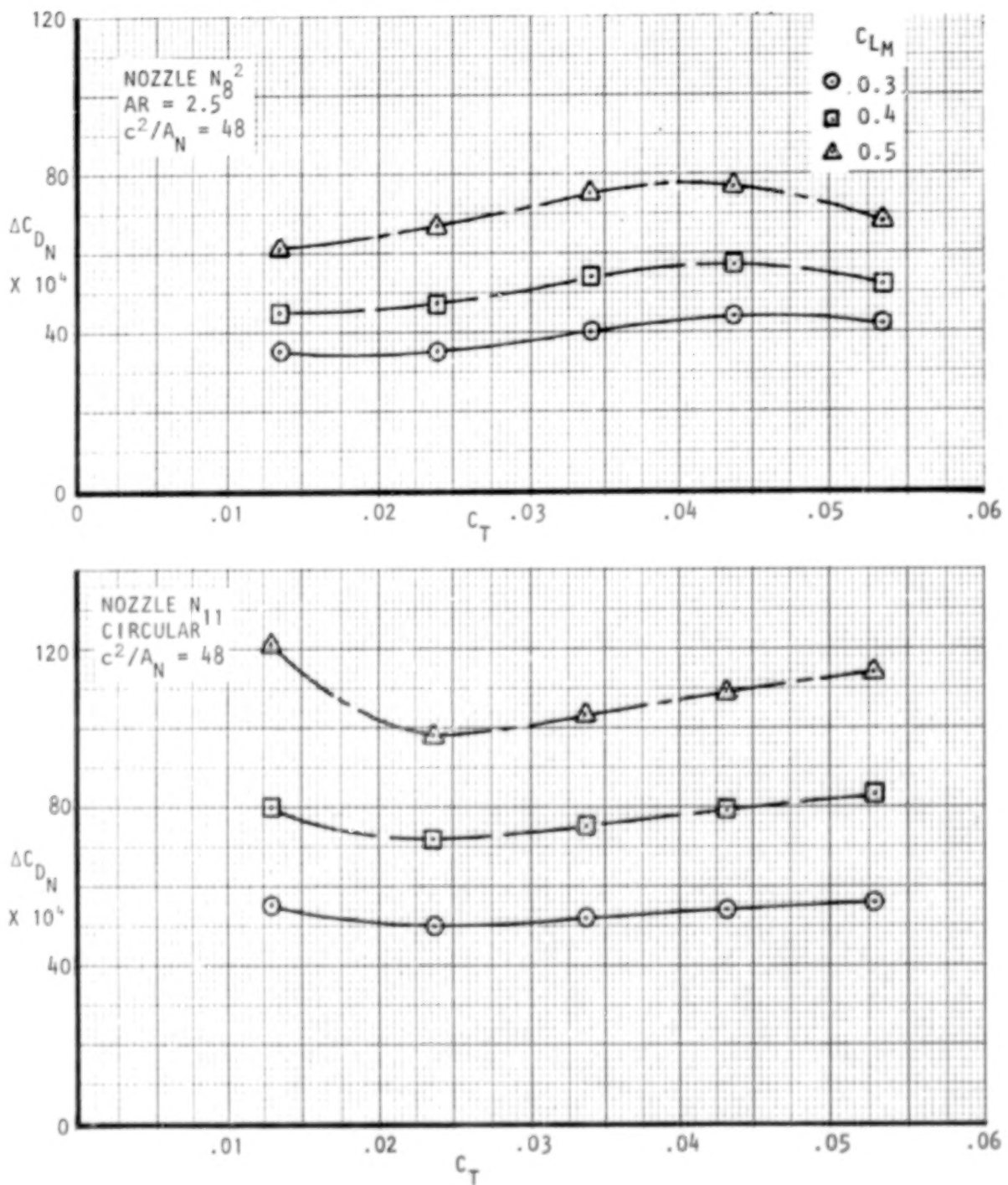


Figure 23. Effect of lift coefficient on nacelle drag, $M_\infty = 0.73$

USB CRUISE PROGRAM
SWEPT WING

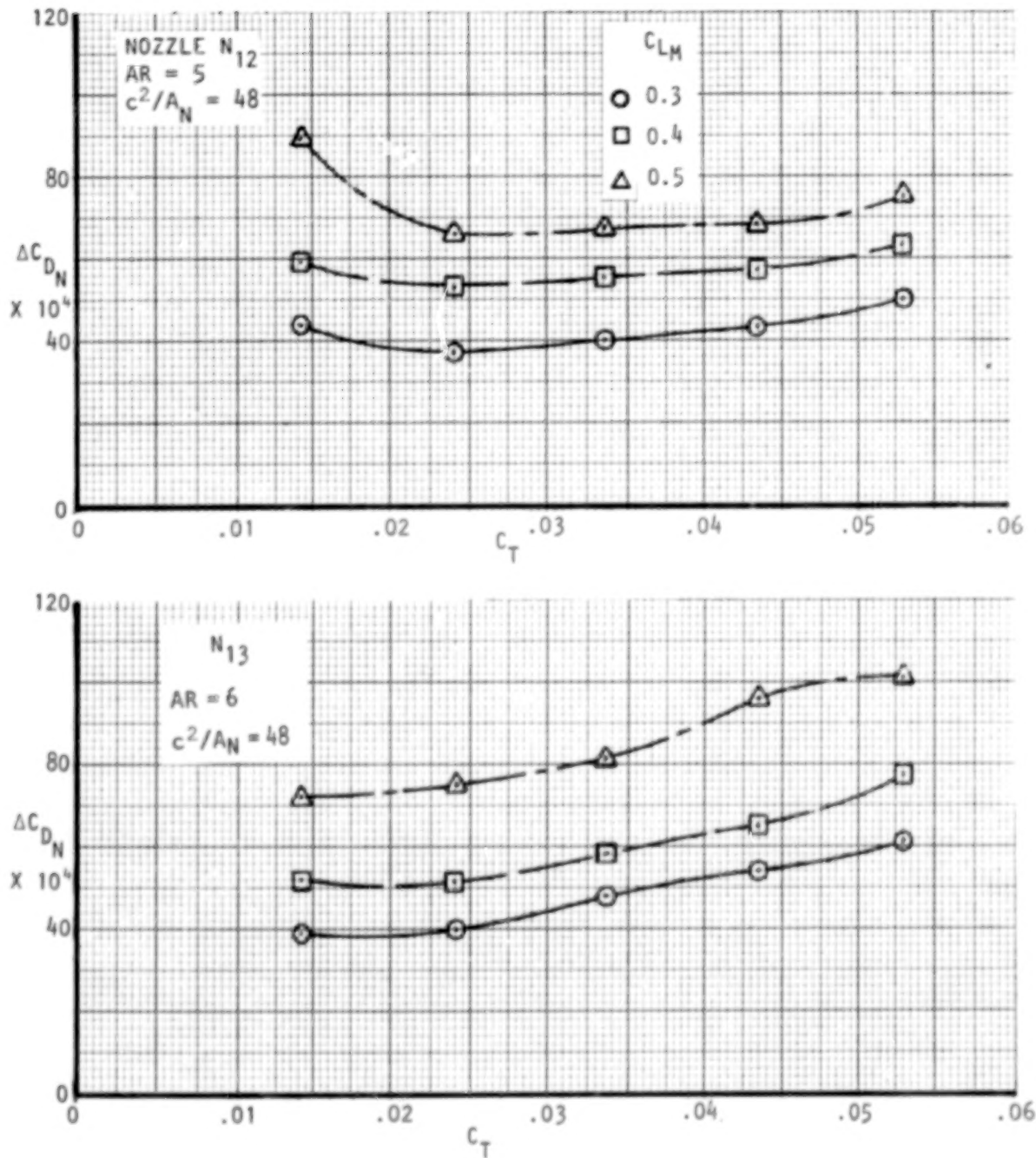


Figure 24 . Effect of lift coefficient on nacelle drag, $M_\infty = 0.73$

USB CRUISE PROGRAM

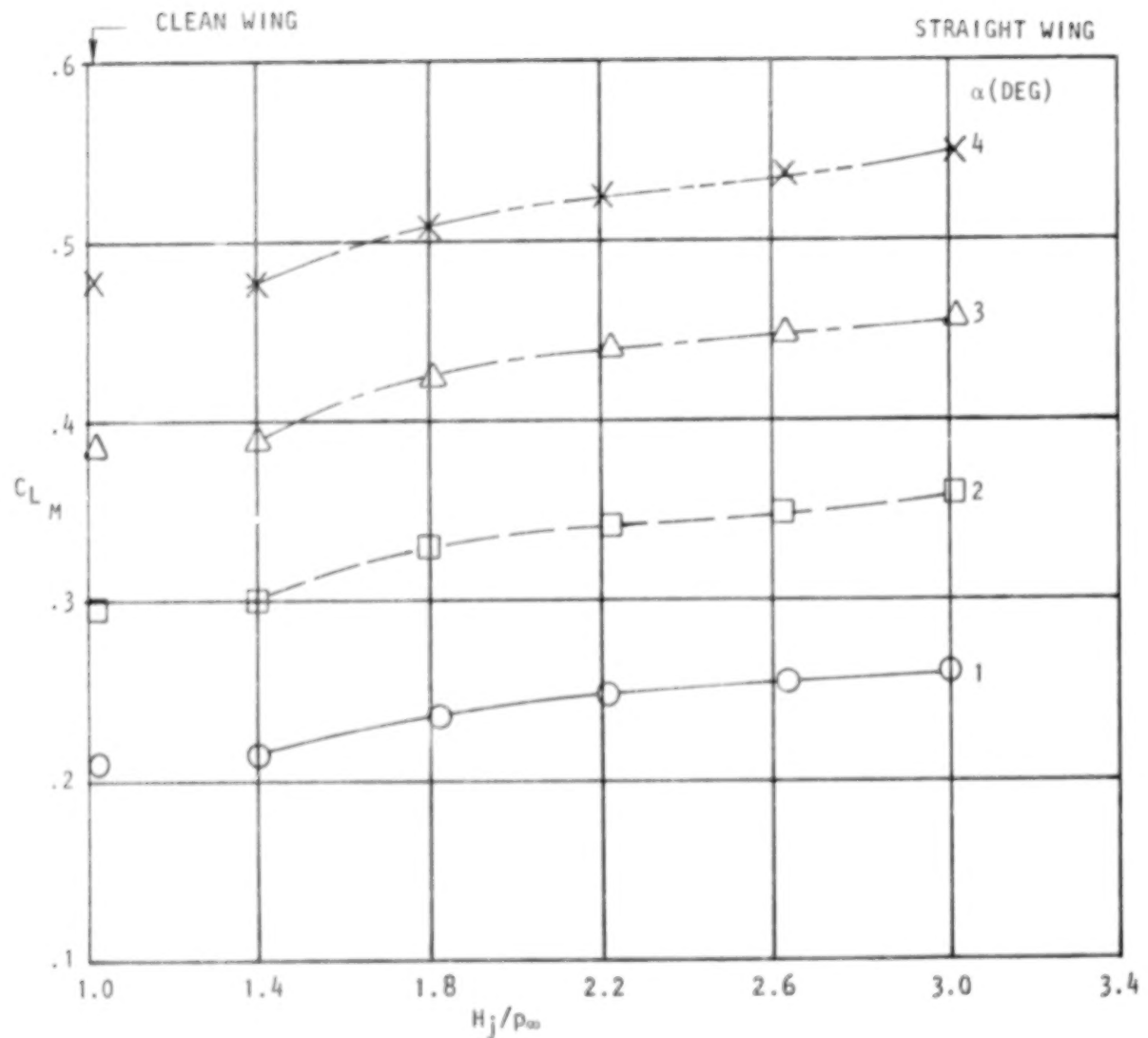


Figure 25. Effect of nozzle pressure ratio on total lift,
noz N_{3E} , AR = 2.5, $M_{\infty} = 0.68$.

USB CRUISE PROGRAM

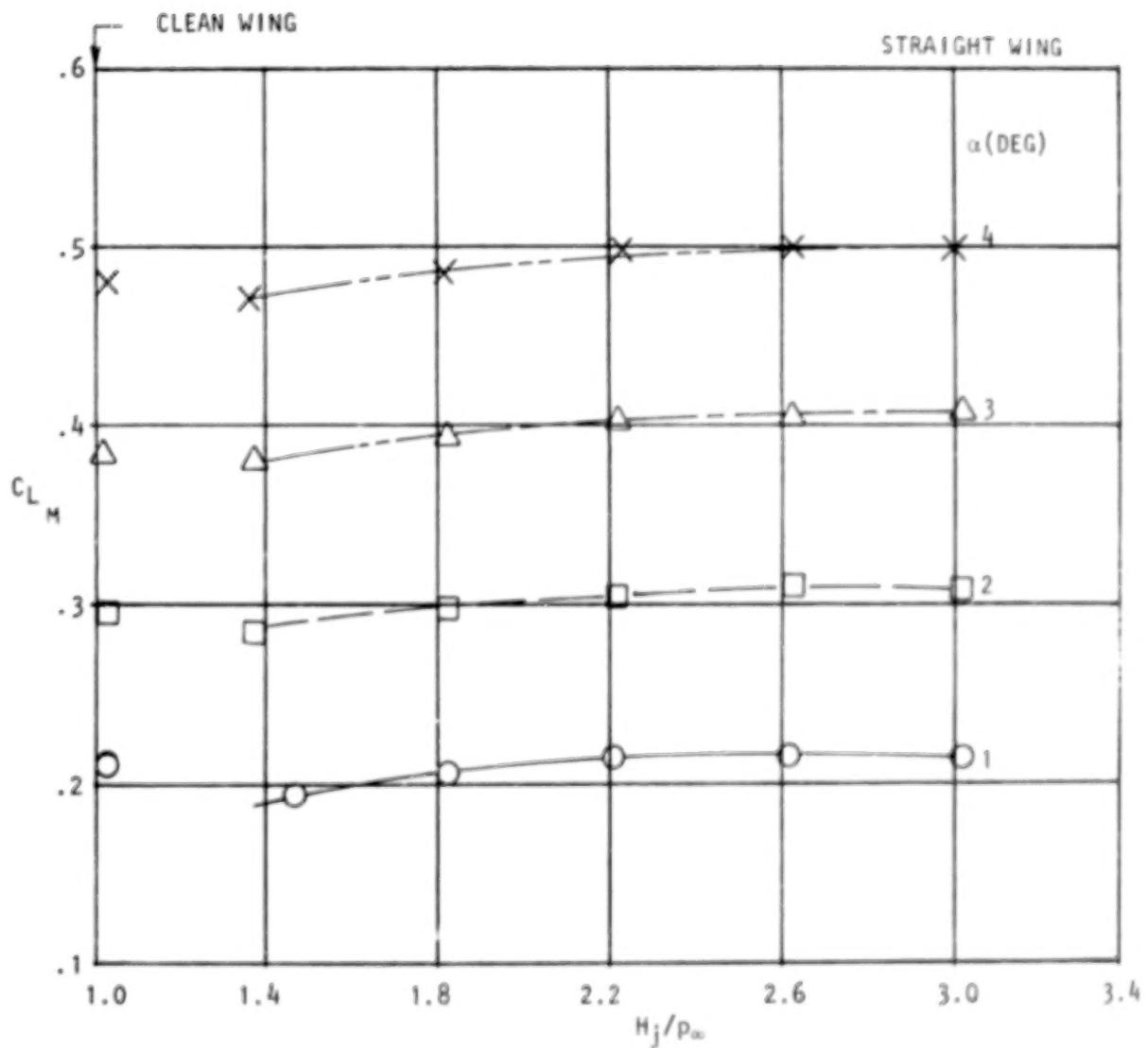


Figure 26. Effect of nozzle pressure ratio on total lift, noz N_2 , circular, $M_\infty = 0.68$.

USB CRUISE PROGRAM
STRAIGHT WING

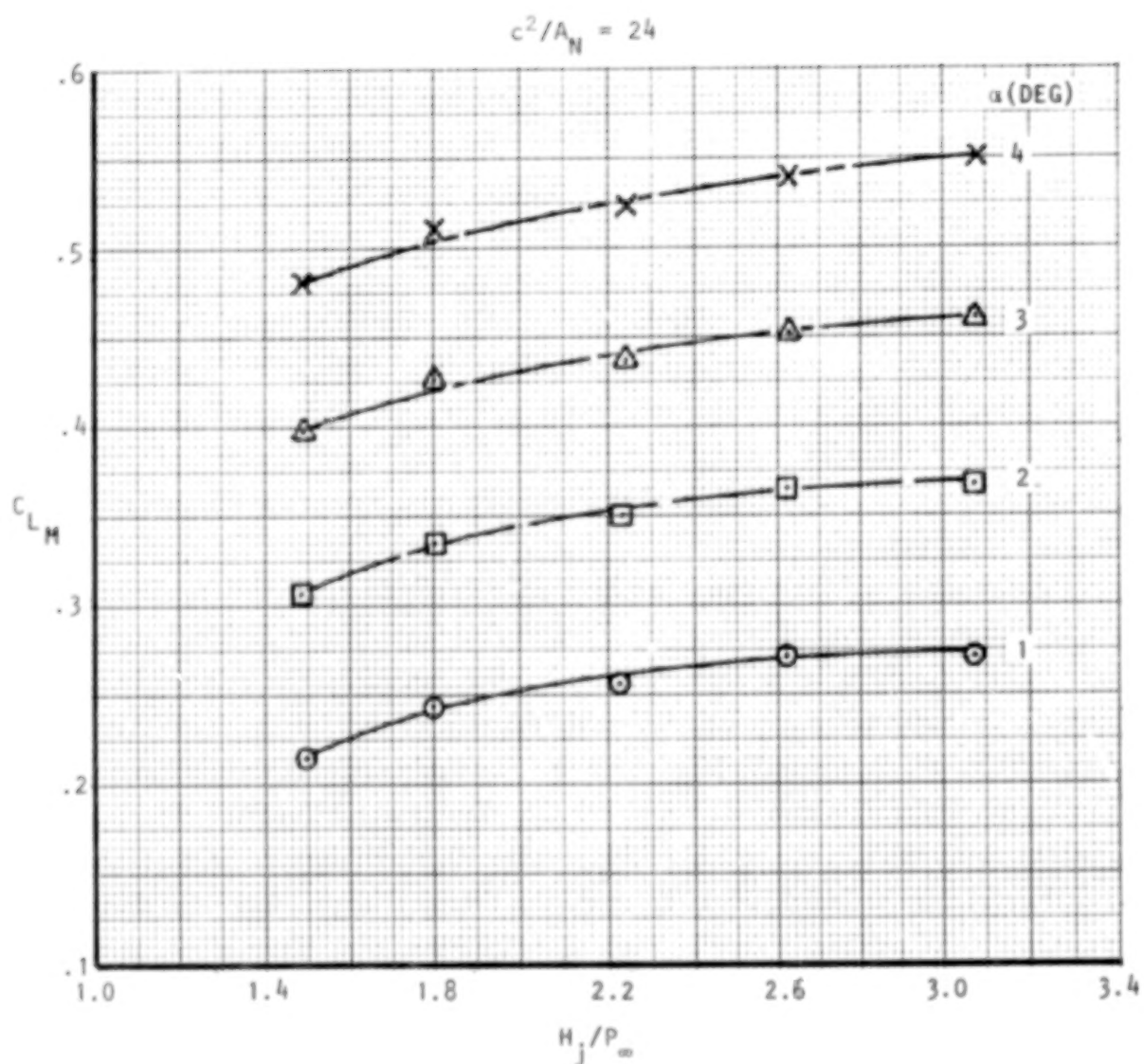


Figure 27. Effect of nozzle pressure ratio on total lift,
noz N_4 , AR = 4, $M_\infty = 0.68$

USB CRUISE PROGRAM
STRAIGHT WING

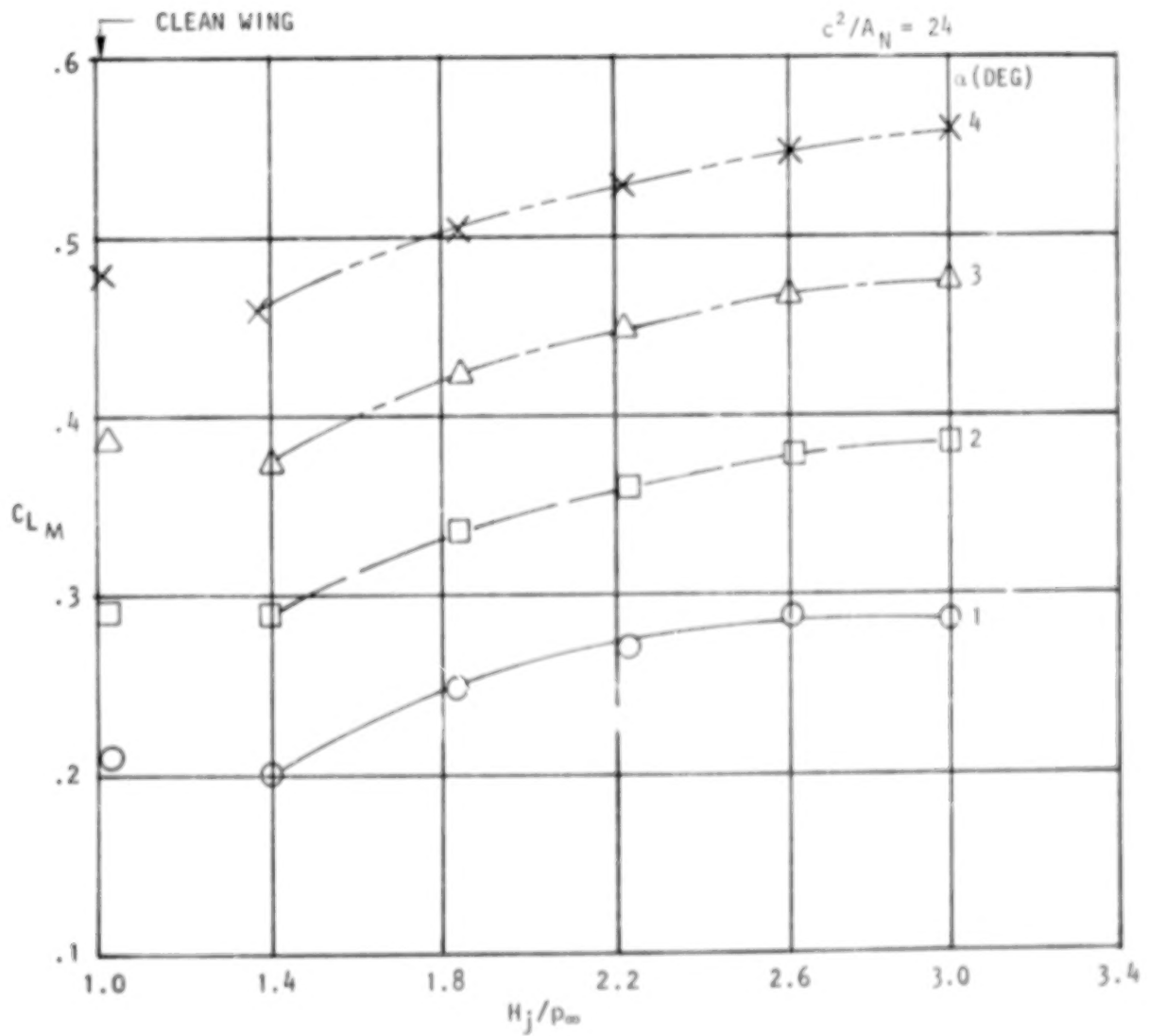


Figure 28. Effect of nozzle pressure ratio on total lift,
noz N_5 , AR = 6.0, $M_\infty = 0.68$.

blowing are seen to be reasonably constant with angle-of-attack as the latter is increased. In general, however, a slightly higher lift increment is obtained in the upper α -range as the blowing tends to counteract increased viscous losses (or uncambering effects) on the unblown wing.

Lift performance of several swept wing nozzle installations are shown in Figures 29 through 32. The trends in lift with pressure ratio are similar but somewhat reduced in level from those of the straight wing. This difference reflects the relative sizes of the nozzles with the small ($c^2/A_N = 48$) nacelles on the swept wing producing only half of the thrust, for a given pressure ratio, as for the straight wing installations.

o Effect of Thrust (H_j/p_∞) on Pitching Moment - Pitching moments about the wing quarter chord are shown in Figures 33 through 35 for several representative nozzles as a function of angle-of-attack and pressure ratio. With the thrust vector above the wing, pitching-moment becomes increasingly negative as the pressure ratio, or thrust, is increased. Relative to the clean wing moments, also shown on the figure, local interference with the basic wing flow-field plus the drag of the nacelle installation itself creates a positive increment initially; this is recovered at maximum blowing. Of interest also, is the trend in moment with pressure ratio for the wide, $AR = 6$ nozzle (Figure 35). At the higher blowing rate, the direction of the slope change of the data supports the view that the jet tends to separate from the aft-wing surface under supercritical blowing conditions.

o Effect of Mach number on Nacelle Drag - The effect of Mach number on the nacelle drag increments are portrayed in Figure 36 through 38 for representative straight wing installations and in Figures 39 and 40 for swept wing configurations. These data are provided at constant levels of thrust coefficient and for a typical cruise lift coefficient of $C_{L_M} = 0.4$. For the most part, the straight wing nacelle drag increments show substantial increases in level between $M_\infty = .60$ and the selected drag-rise condition of 0.68. This is particularly characteristic of the circular or very wide nozzles ($AR = 4$ or 6), whereas the "D-duct" configurations (Figure 37) show generally smaller Mach-related changes. These differences could well reflect the effectiveness achieved by adapting a given fillet design to a wide variety

USB CRUISE PROGRAM
SWEPT WING

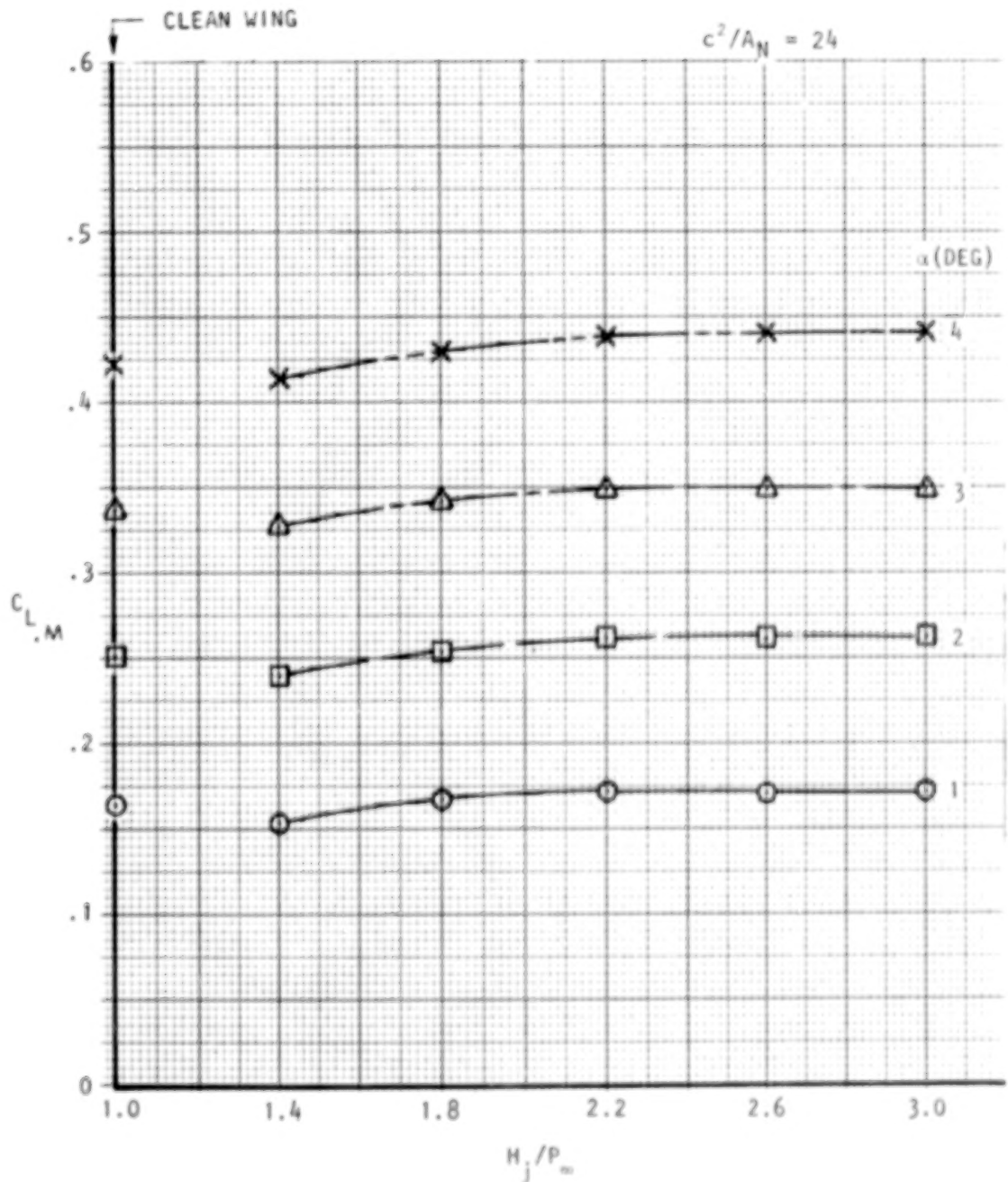


Figure 29 . Effect of nozzle pressure ratio on total lift,
noz N₁₁, AR = circular, M_∞ = 0.73

USB CRUISE PROGRAM
SWEPT WING

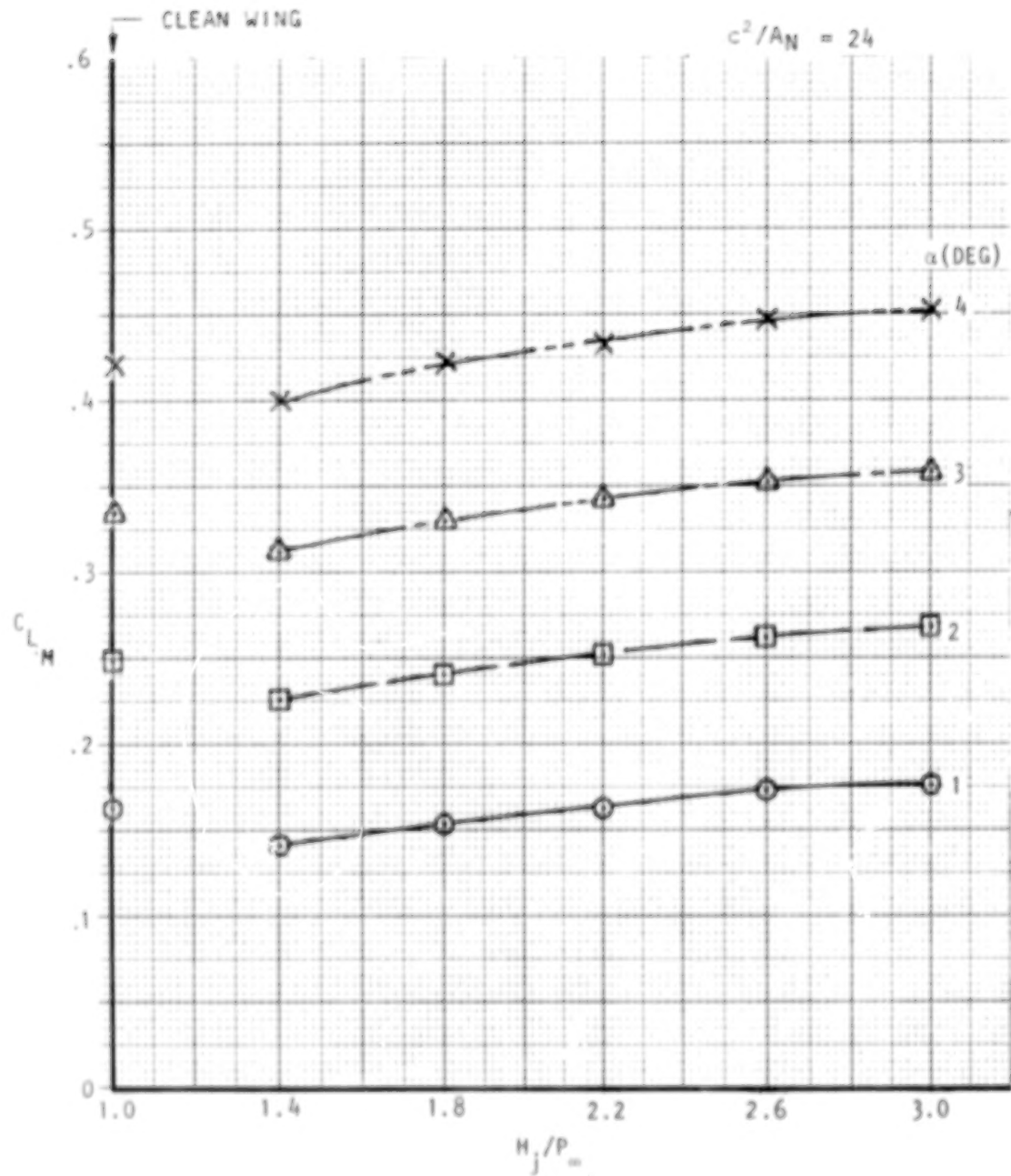


Figure 30. Effect of nozzle pressure ratio on total lift,
noz N_8^2 , AR = 2.5, $M_\infty = 0.73$

USB CRUISE PROGRAM
SWEPT WING

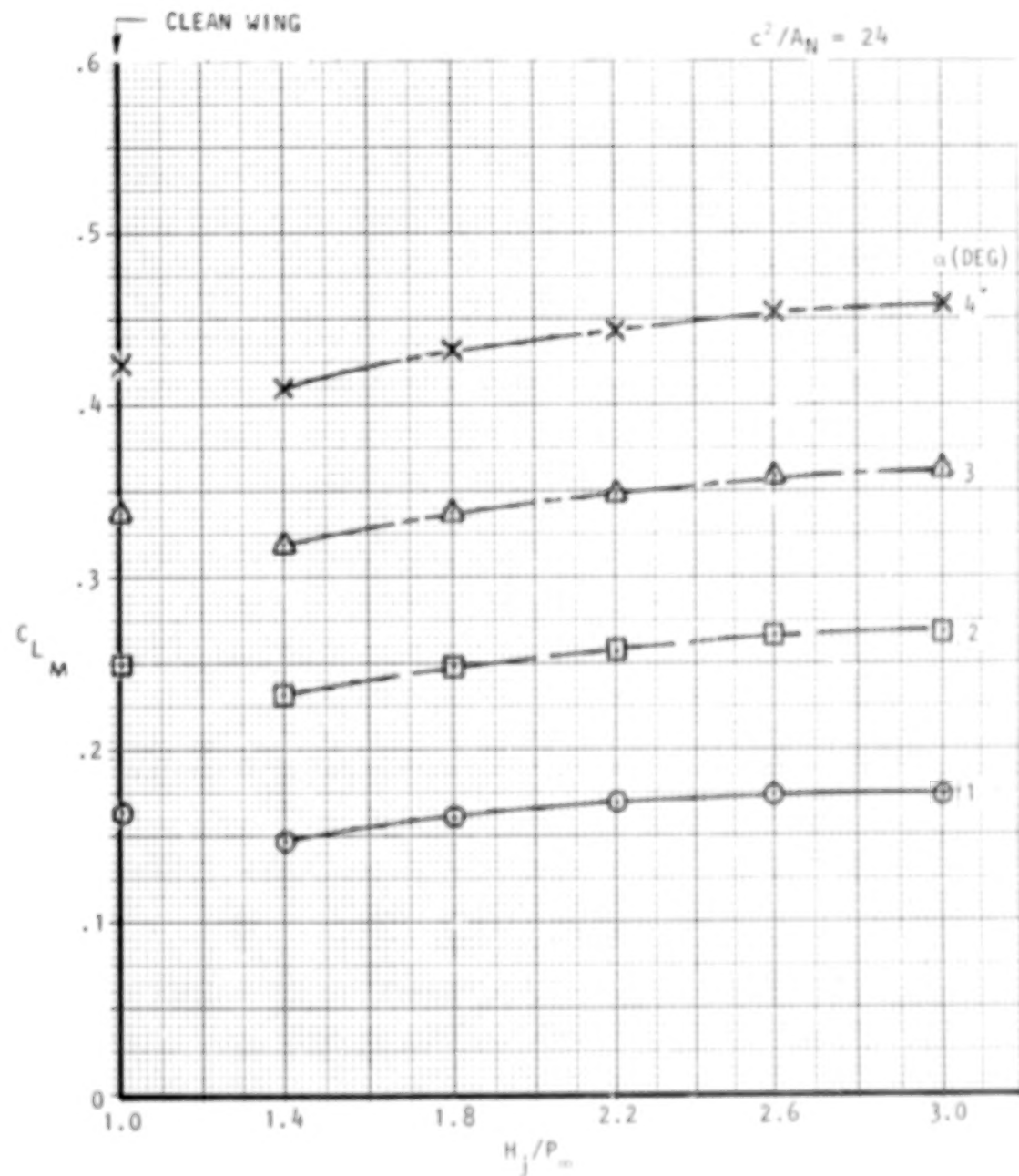


Figure 31. Effect of nozzle pressure ratio on total lift
noz N₁₂, AR = 4, $M_{\infty} = 0.73$

USB CRUISE PROGRAM
SWEPT WING

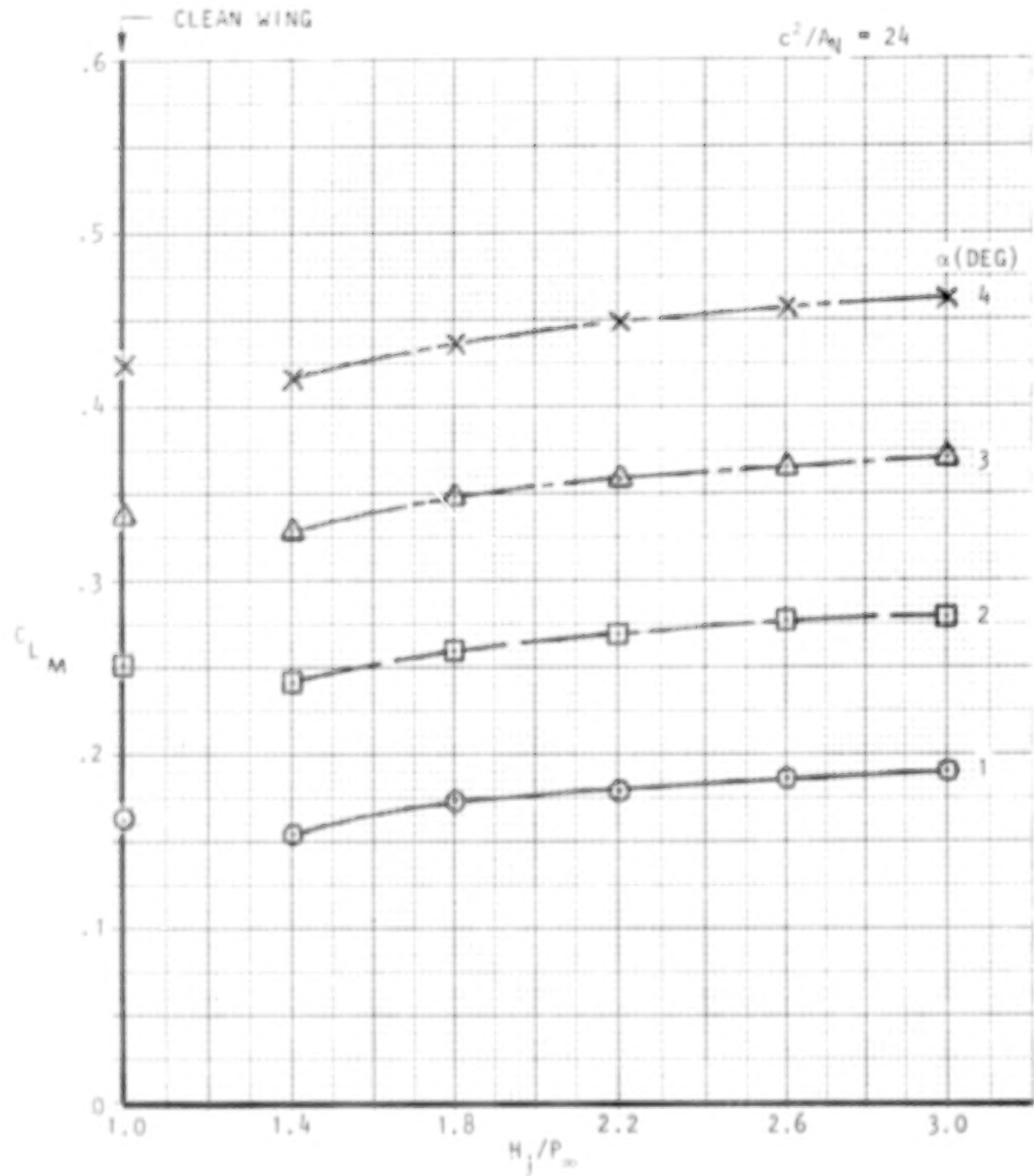


Figure 32. Effect of nozzle pressure ratio on total lift,
noz N_{13} , AR = 6, $M_\infty = 0.73$

USB CRUISE PROGRAM

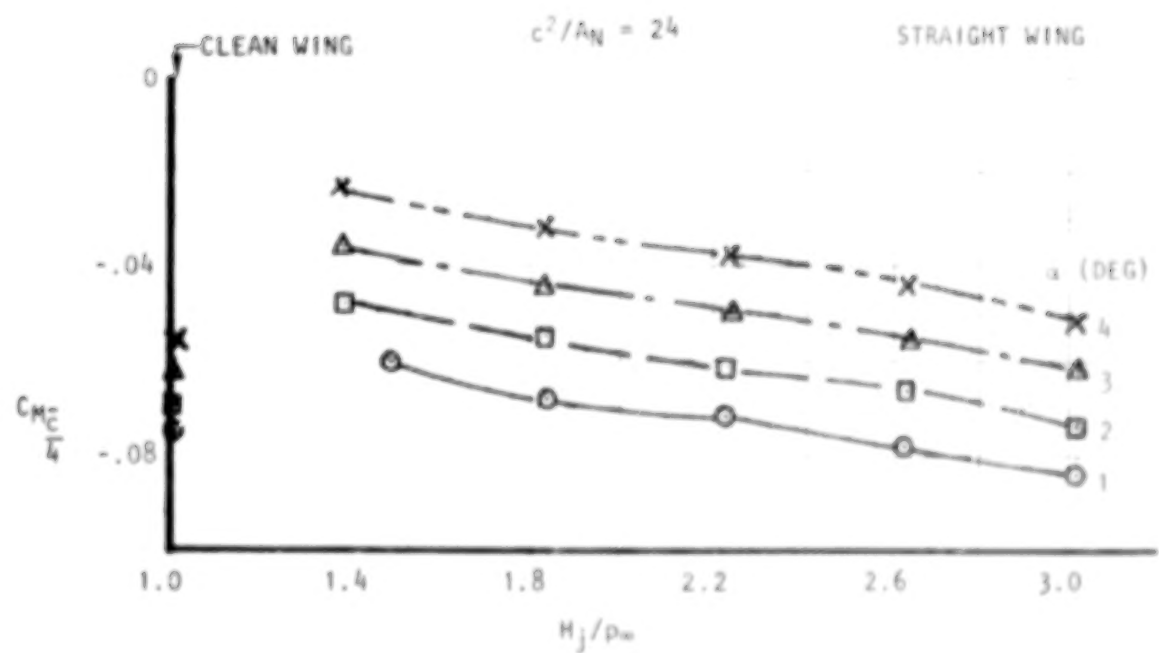


Figure 33. Effect of nozzle pressure ratio on pitching-moment, noz N_2 , circular, $M_\infty = 0.68$.

USB CRUISE PROGRAM

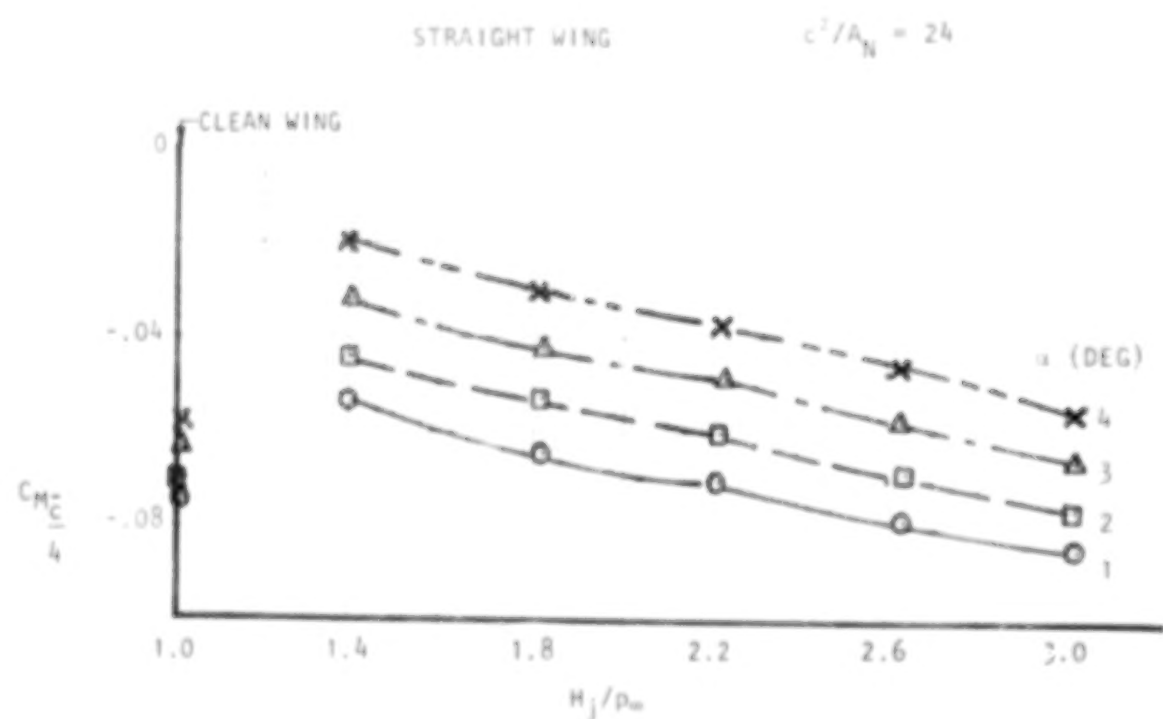


Figure 34. Effect of nozzle pressure ratio on pitching-moment, noz N_{JE}, AR = 2.5, $M_\infty = 0.68$.

USB CRUISE PROGRAM

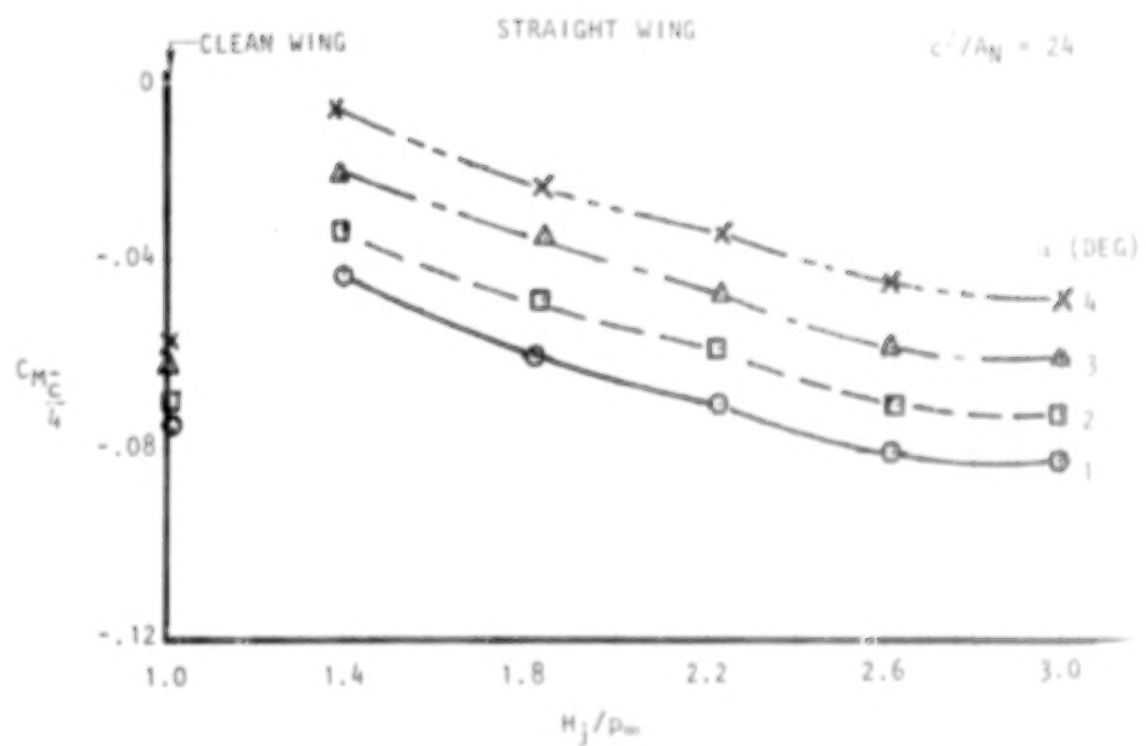


Figure 35 . Effect of nozzle pressure ratio on pitching-moment, noz N₅, AR = 6, $M_\infty = 0.68$.

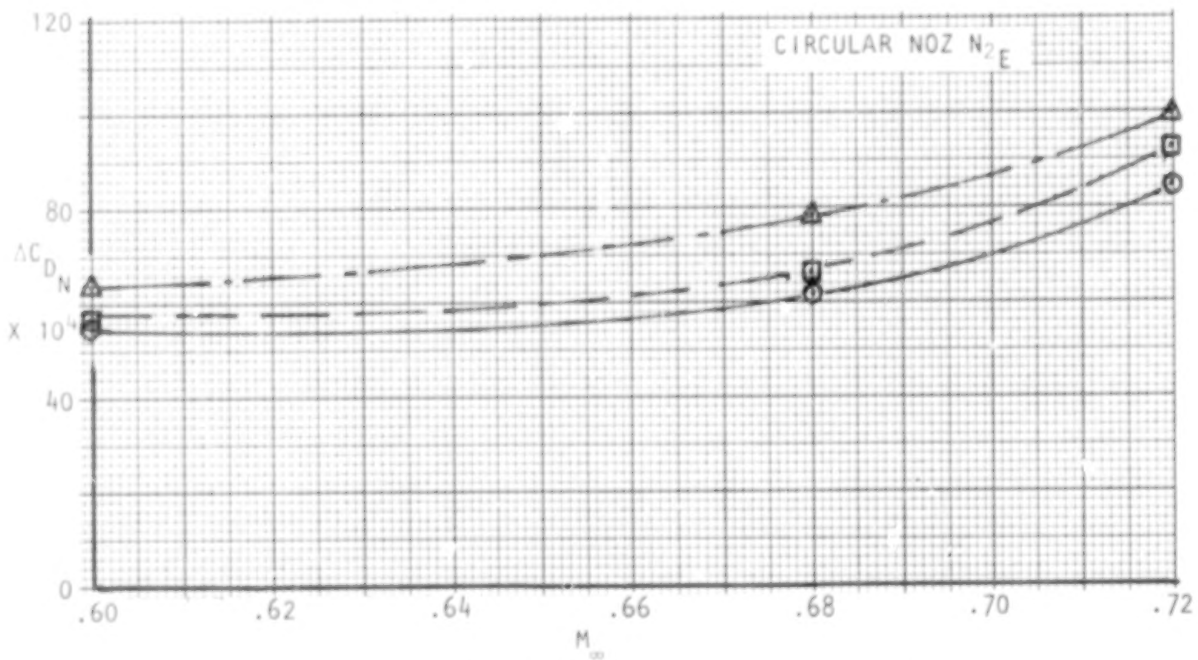
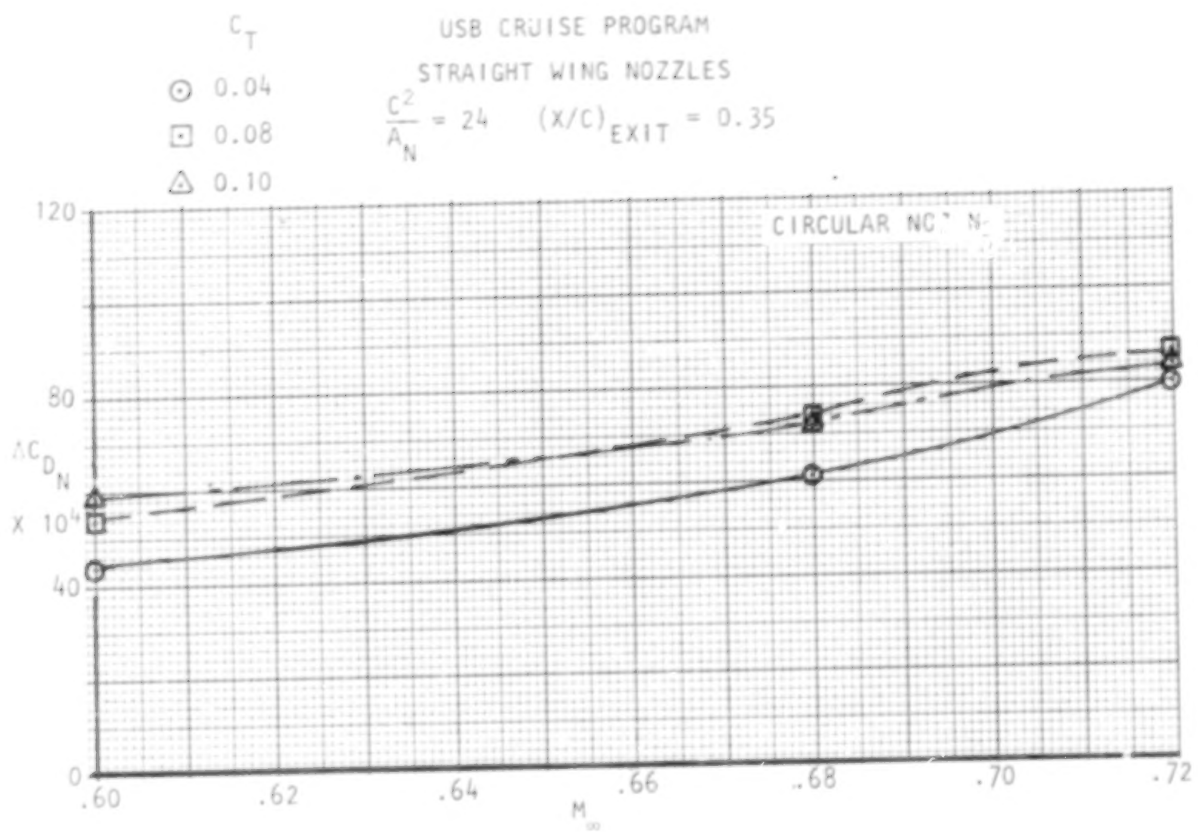


Figure 36. Effect of Mach number on nacelle drag coefficient, $C_{L_M} = 0.40$

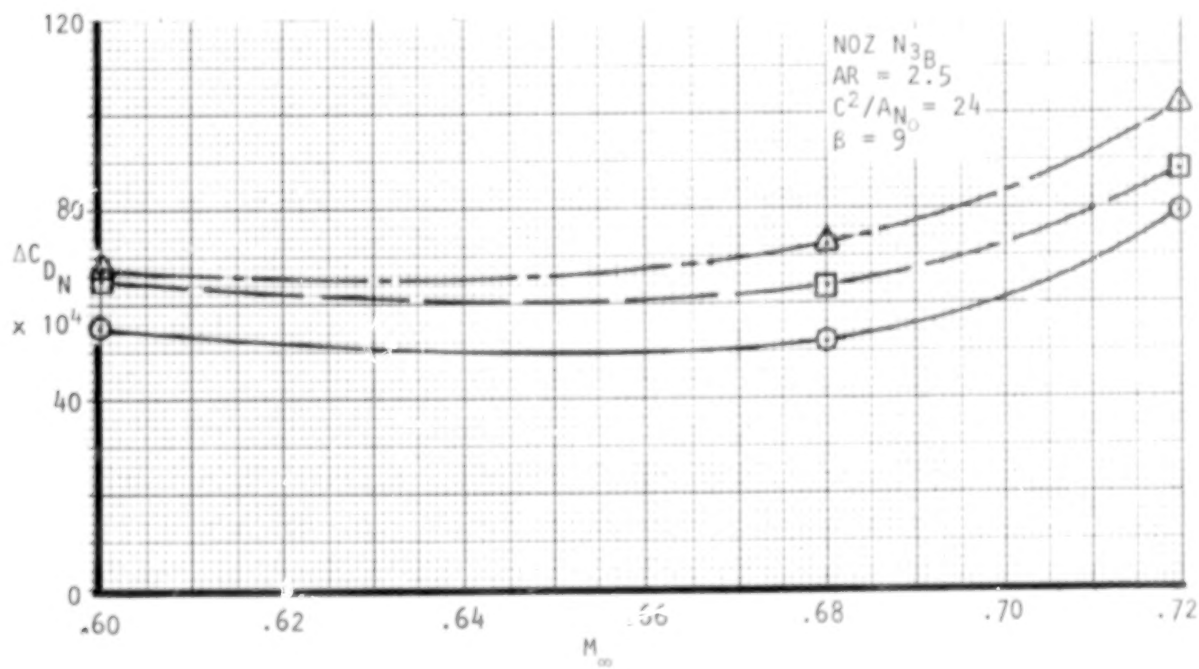
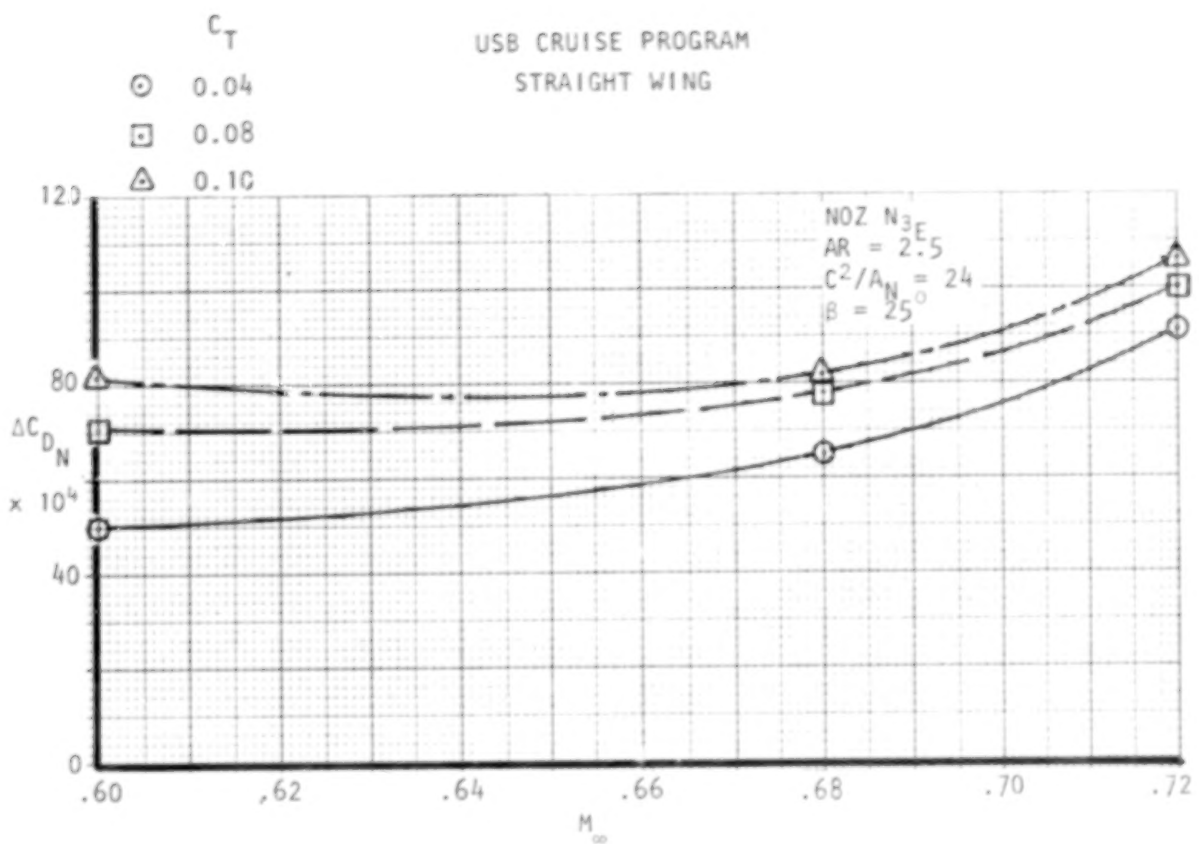


Figure 37. Effect of Mach number on nacelle drag coefficient, $C_{LM} = 0.40$

USB CRUISE PROGRAM

STRAIGHT WING

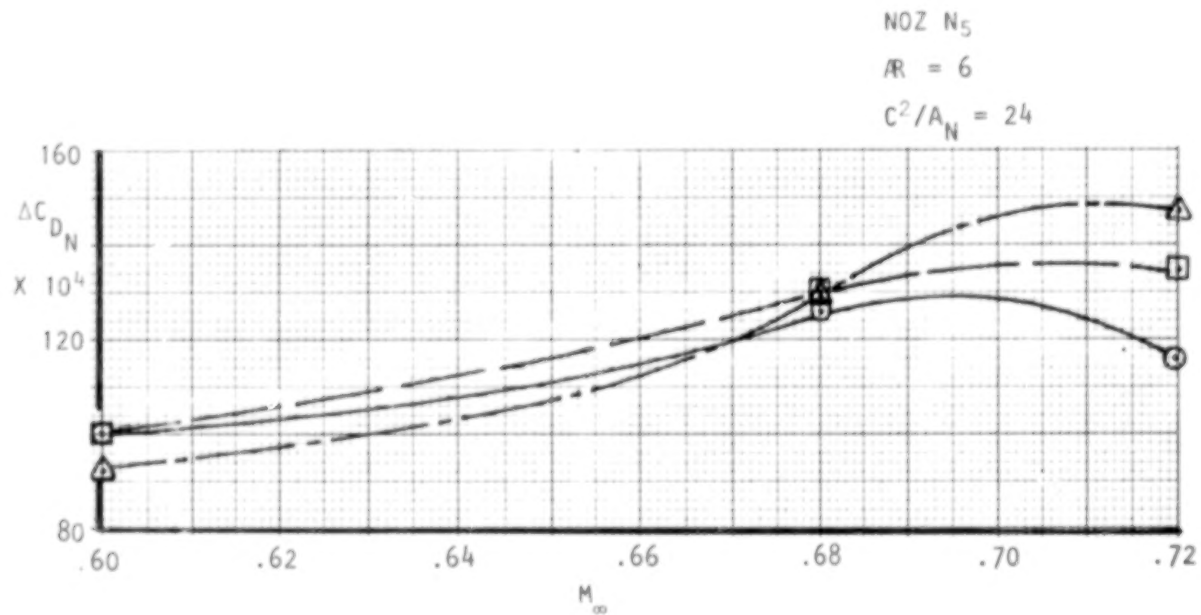
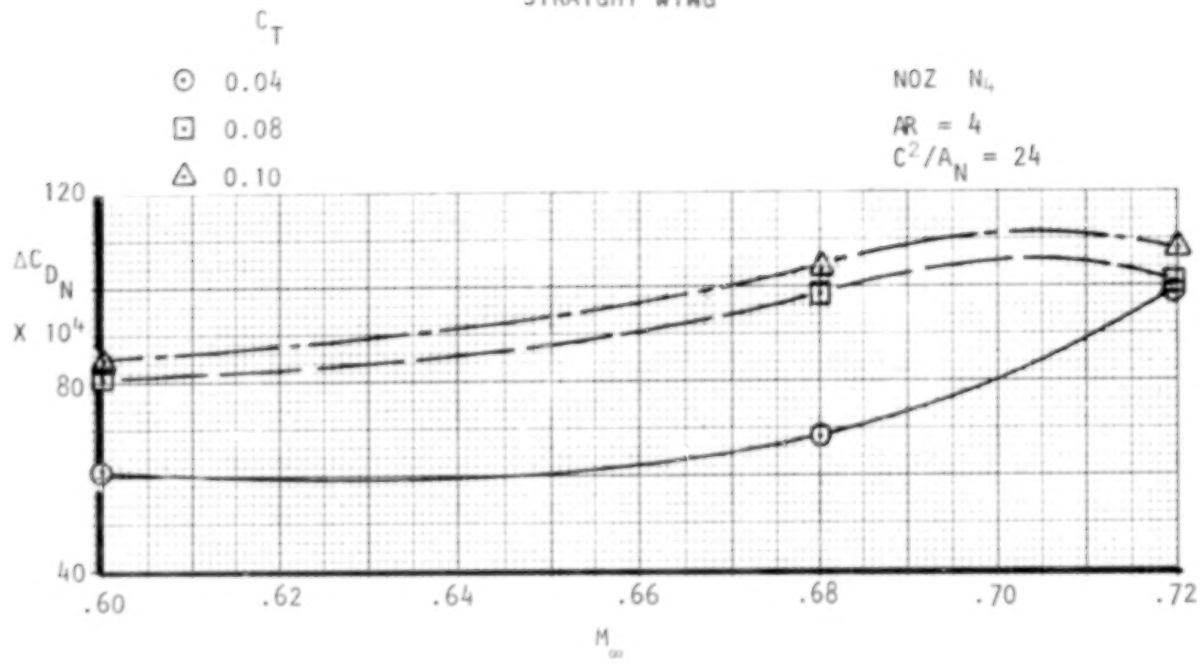


Figure 38. Effect of Mach number on nacelle drag coefficient, $C_{L_M} = 0.40$

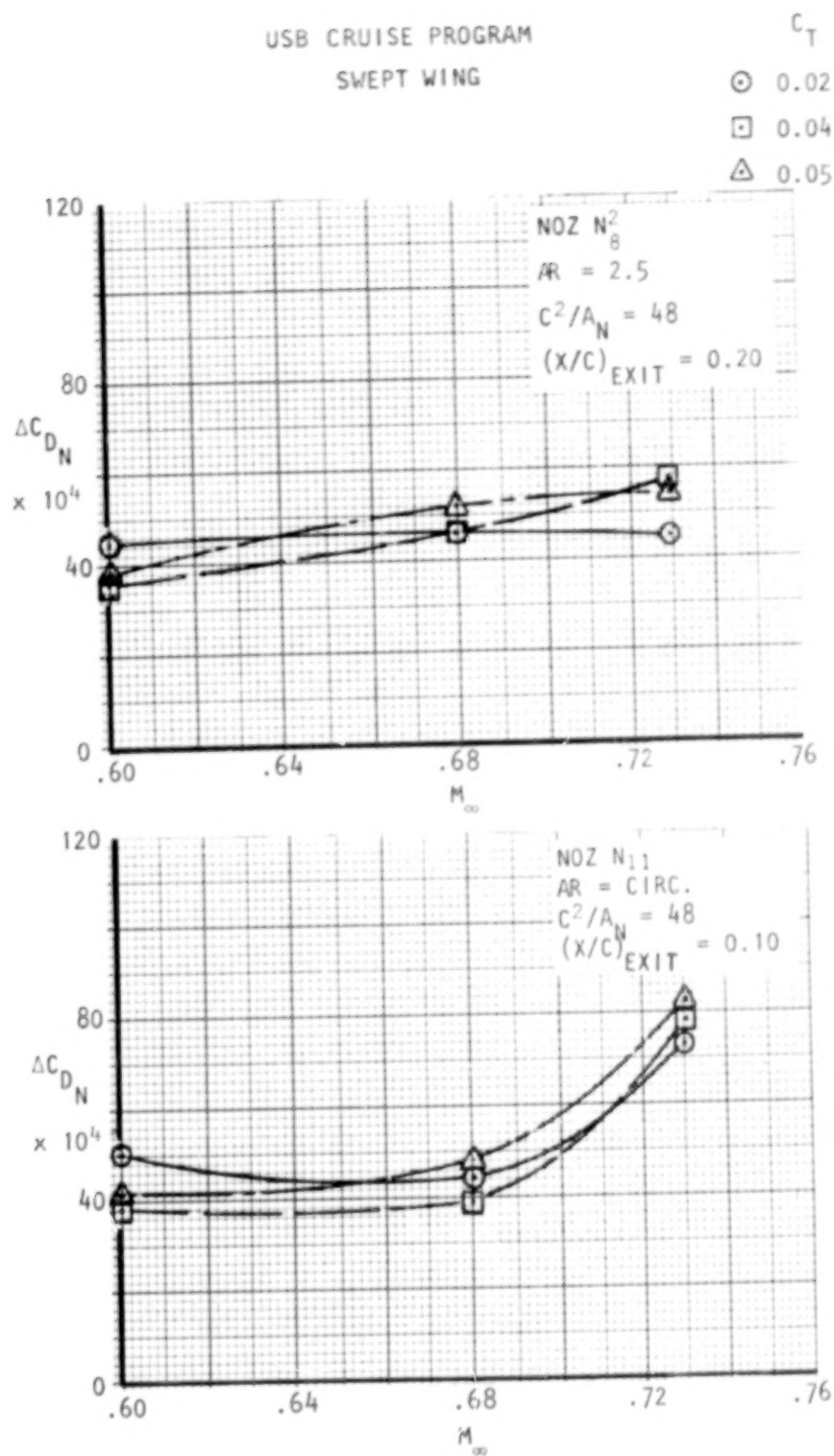


Figure 39. Effect of Mach number on nacelle drag coefficient, $C_{L_M} = 0.40$

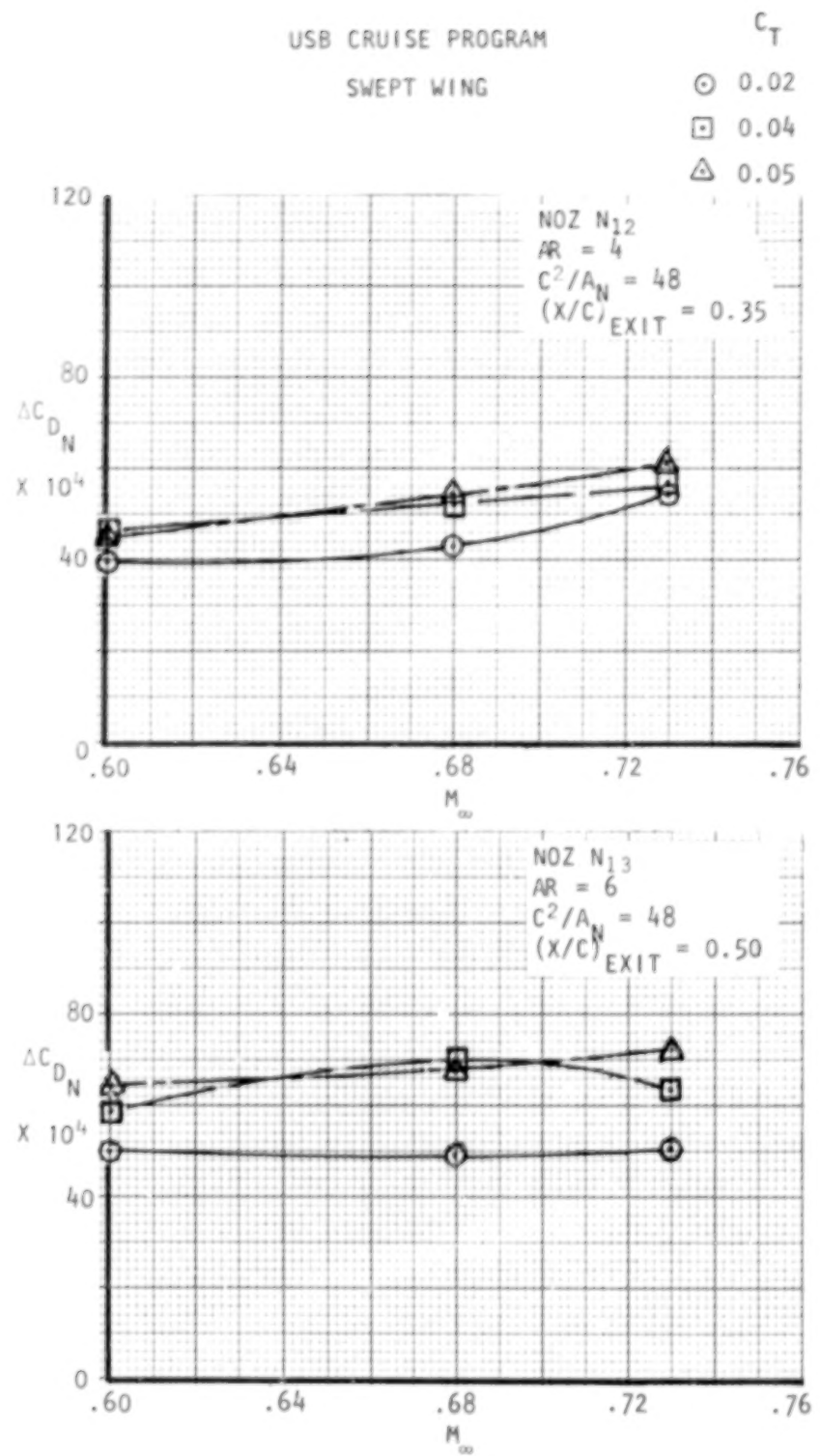


Figure 40. Effect of Mach number on nacelle drag coefficient, $C_{L_M} = 0.40$

of nozzle planform shapes. The circular, boattailed nozzles and the wider, flaring nozzle shapes were not as amenable to this filleting process as were the more straight-sided "D-duct" designs.

The effect of Mach number on the swept wing nacelle drag coefficients (Figures 39 and 40), where more extensive filleting was employed, show moderate drag creep up to the critical Mach number of 0.73. An exception to this is the data from the circular nozzle (N_{11}) for which $M = 0.73$ is well beyond the effective drag-rise Mach number of the wing-nacelle combination. As noted in the configuration matrix off Figure 3, swept-wing nozzles varied chordwise exit position simultaneously with nozzle aspect ratio. The exit position of the circular nozzle (N_{11}) is at $x/c = 0.10$, as noted on Figure 39, and represents the most forward position tested. A study of surface pressures showed that, under supercritical flow conditions, combined nozzle and jet displacement effects positioned a shock just ahead of the nozzle exit; in effect, the shock is "locked" in this forward region. With the subject nozzle (N_{11}), the shock remains essentially at the wing leading-edge and grows in strength with angle-of-attack and pressure ratio. Increased shock losses and the resulting adverse effects on local boundary-layer and leading-edge suction produces the exceptionally high drag noted for this configuration. These effects tend to highlight the difficulty of appropriately filleting the symmetrical nacelles with exits positioned well-forward on the wing.

o Effect of Mach number on Lift and Moment Due-to-Blowing - The variation of lift-due-to-blowing with Mach number and thrust coefficient is shown in Figures 41 through 47 for selected straight wing nacelles. Since the lift increments varied little with angle of attack, the data are provided for $\alpha = 3^\circ$ only. In some instances, the moment-due-to-blowing is also included as typical of the complete range of configurations tested. Lift and moment increments portrayed have been derived from the expressions:

$$\Delta C_{LM} = \left[C_{LM} \right]_{\frac{H_j}{P_\infty}} - \left[C_{LM} \right]_{\frac{H_j}{P_\infty}} = FLO-THRU \quad (5a)$$

$$\Delta C_{MM} = \left[C_{MM} \right]_{\frac{H_j}{P_\infty}} - \left[C_{MM} \right]_{\frac{H_j}{P_\infty}} = FLO-THRU \quad (5b)$$

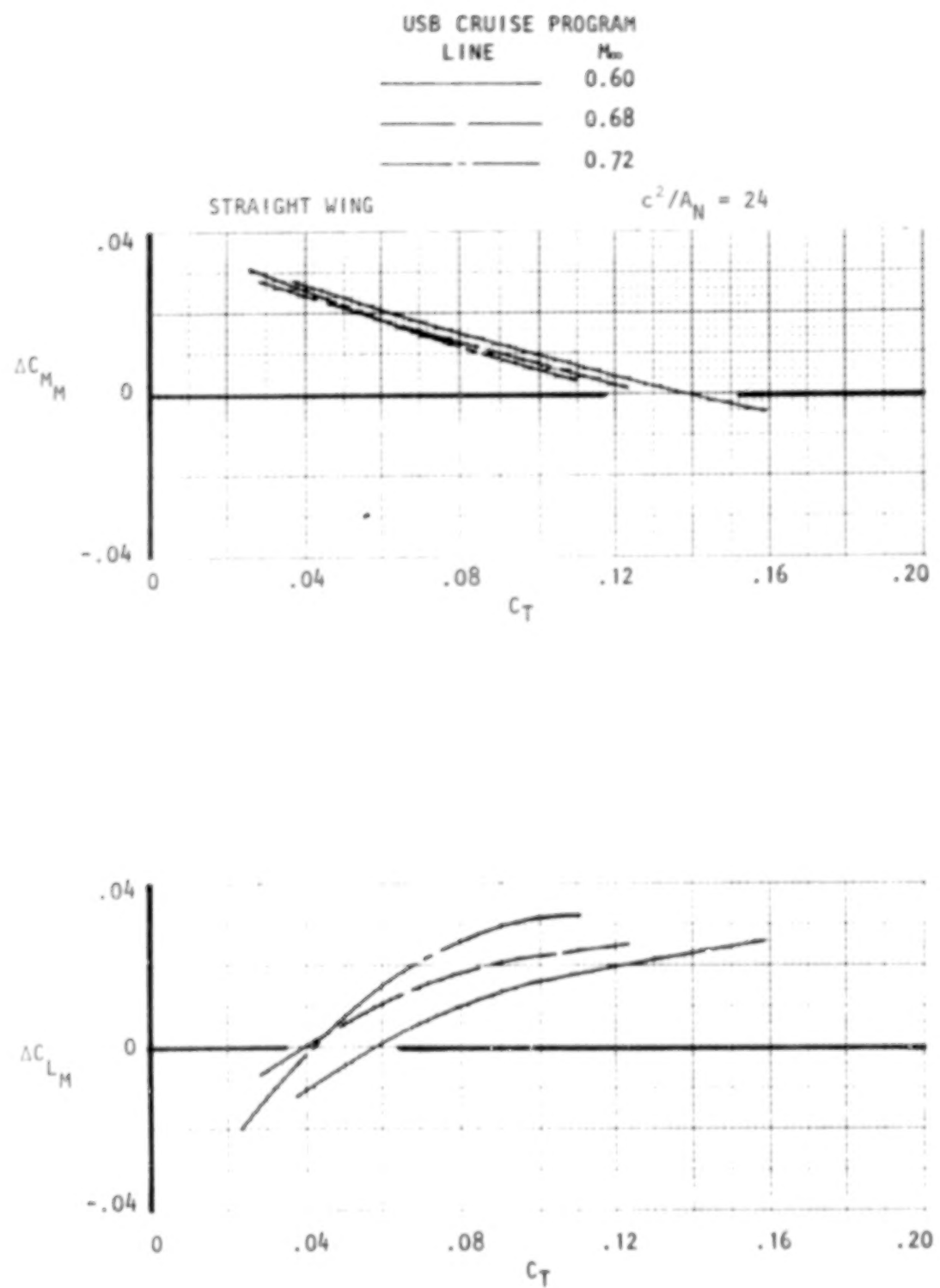


Figure 41. Variation of lift and moment increments due to blowing, noz N_2 , circular.

USB CRUISE PROGRAM

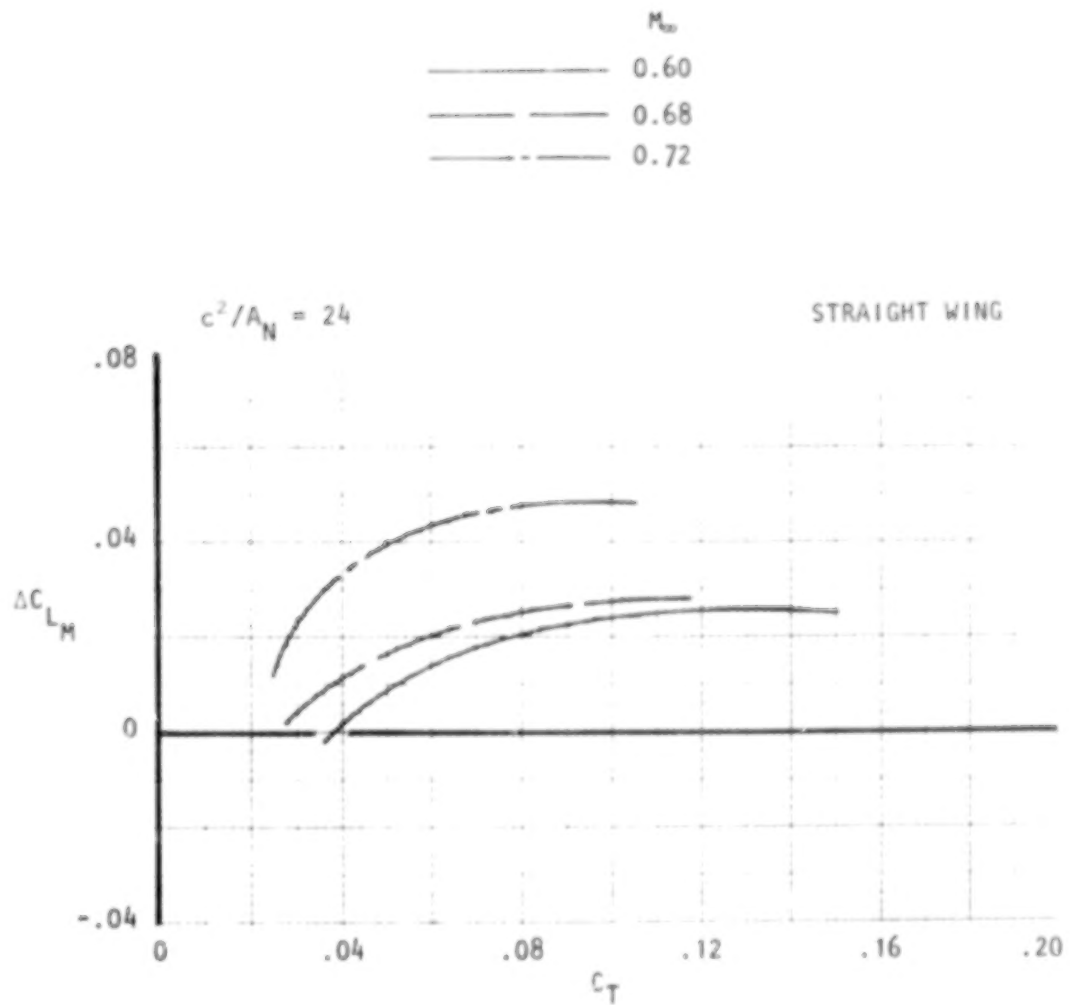


Figure 42. Variation of lift increments due to blowing, noz N_{2E} , circular.

USB CRUISE PROGRAM

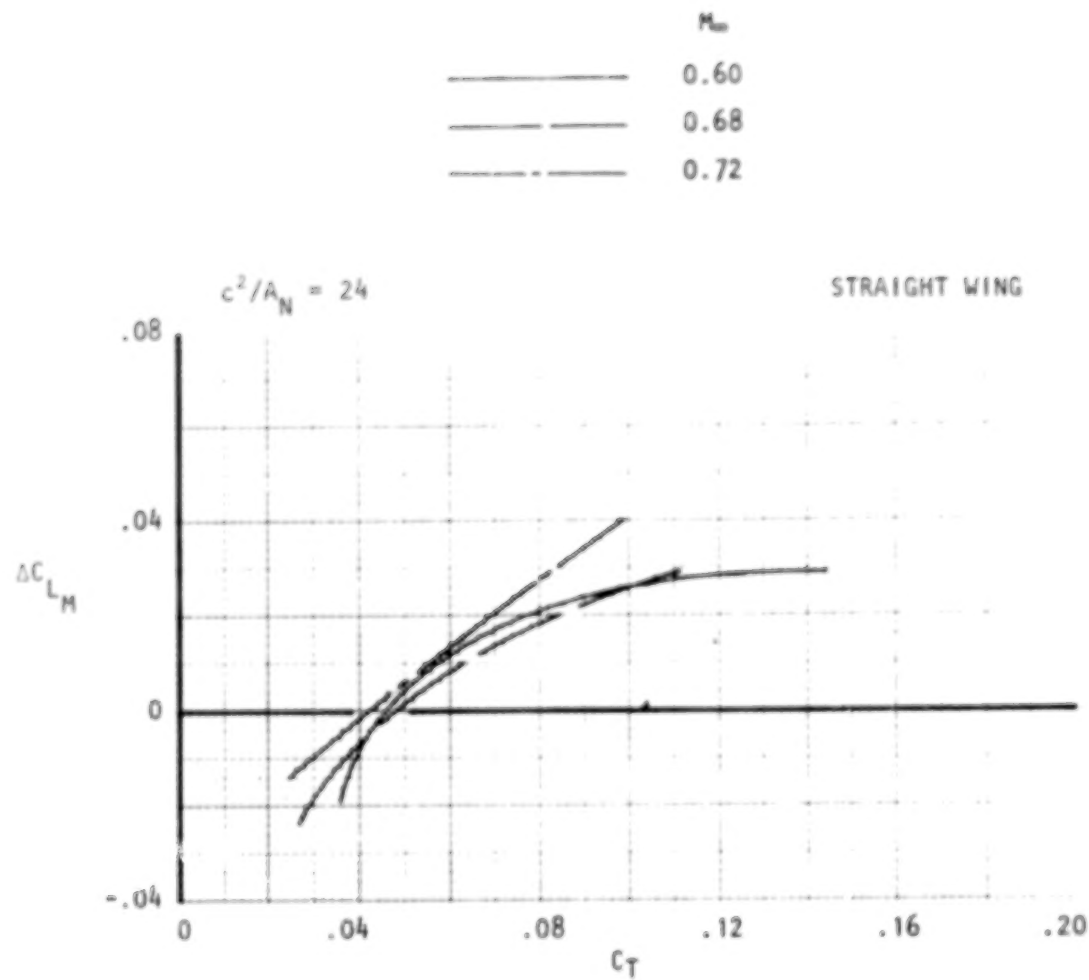


Figure 43

Variation of lift increment due to blowing,
noz N_{38} , AR = 2.5.

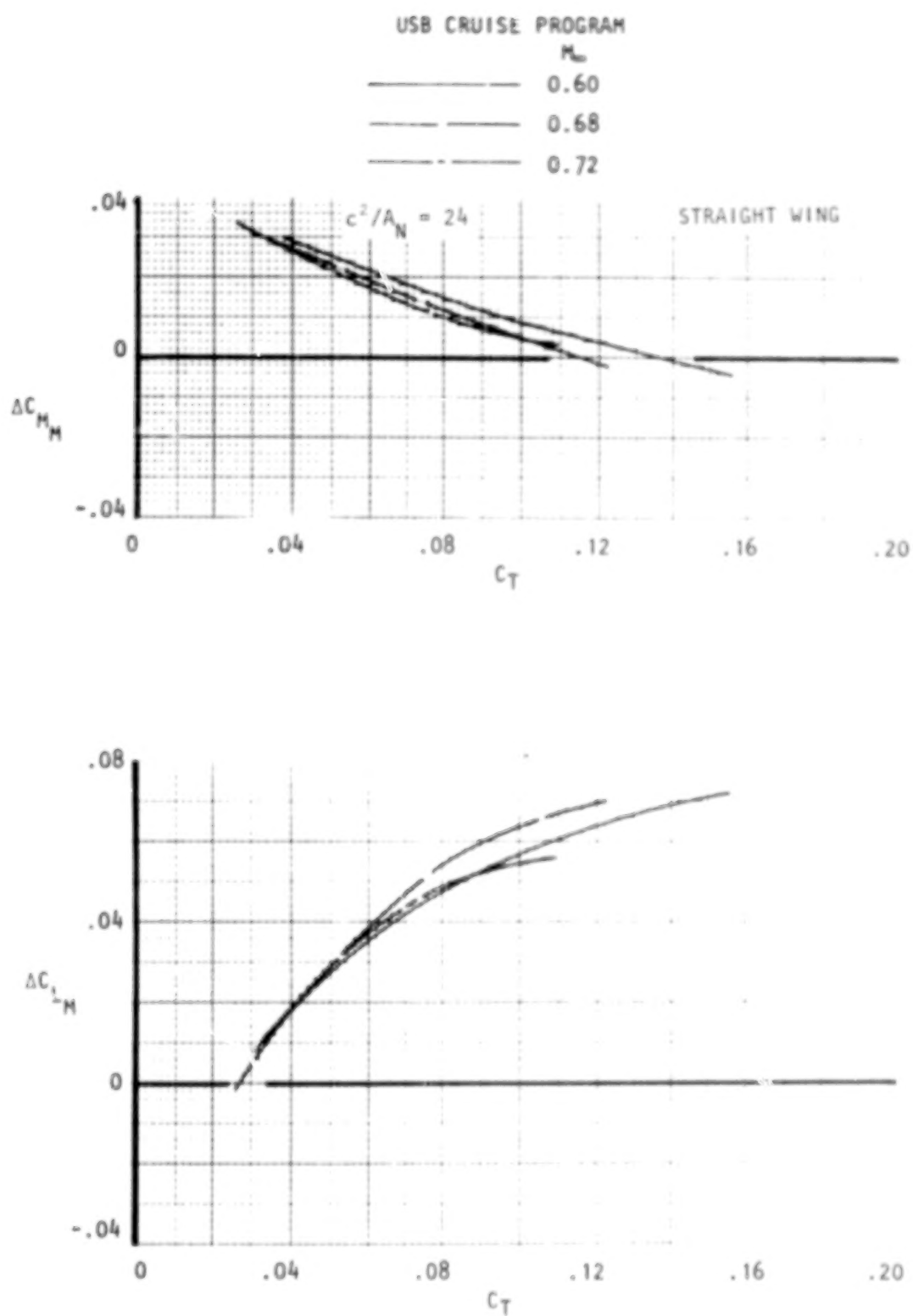


Figure 44. Variation of lift and moment increments due to blowing, noz N_{3E}, AR = 2.5.

USB CRUISE PROGRAM

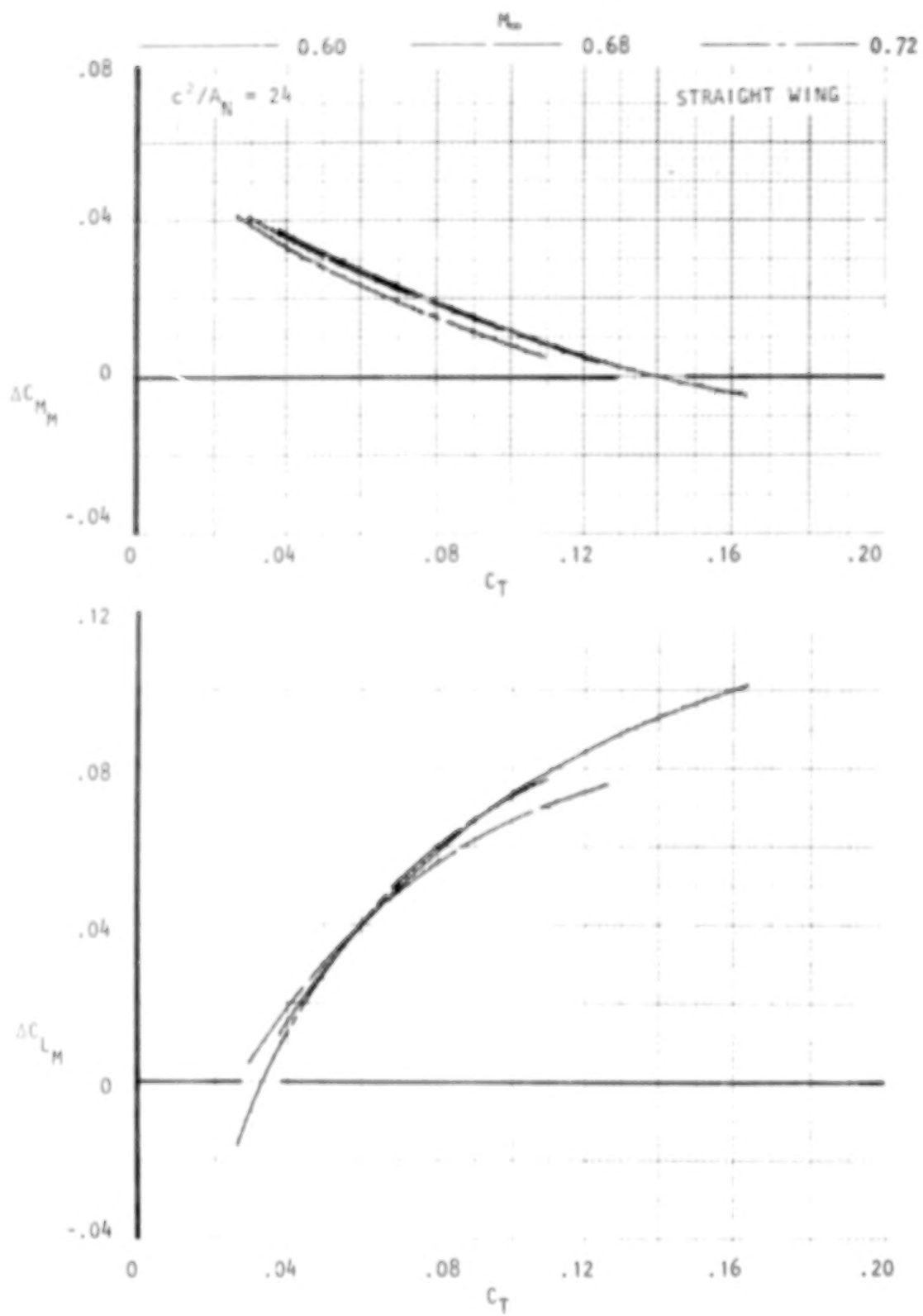


Figure 45. Variation of lift and moment increments due to blowing, noz N_4 , AR = 4.

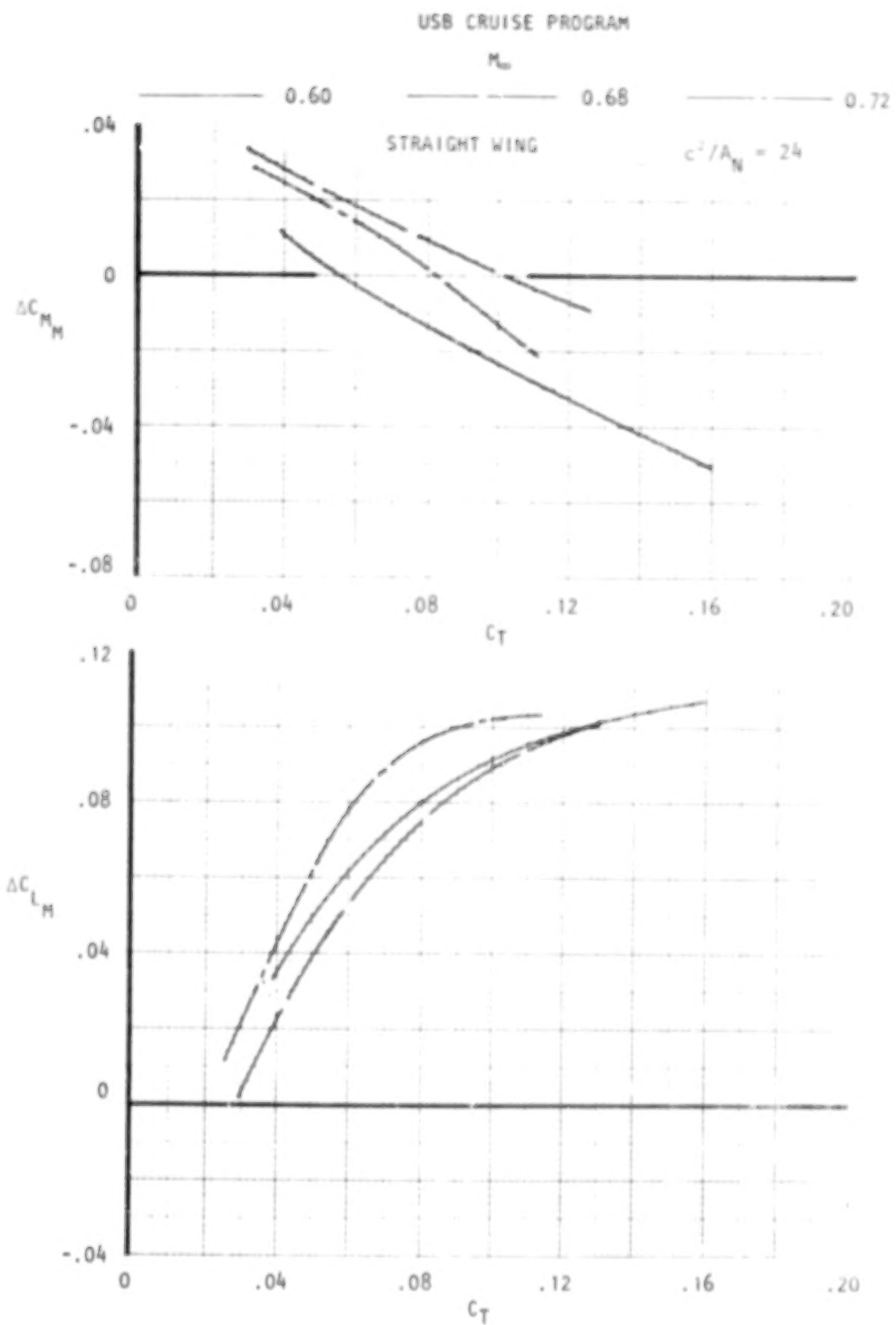


Figure 46. Variation of lift and moment increments due to blowing, noz N_{4E} , AR = 4.

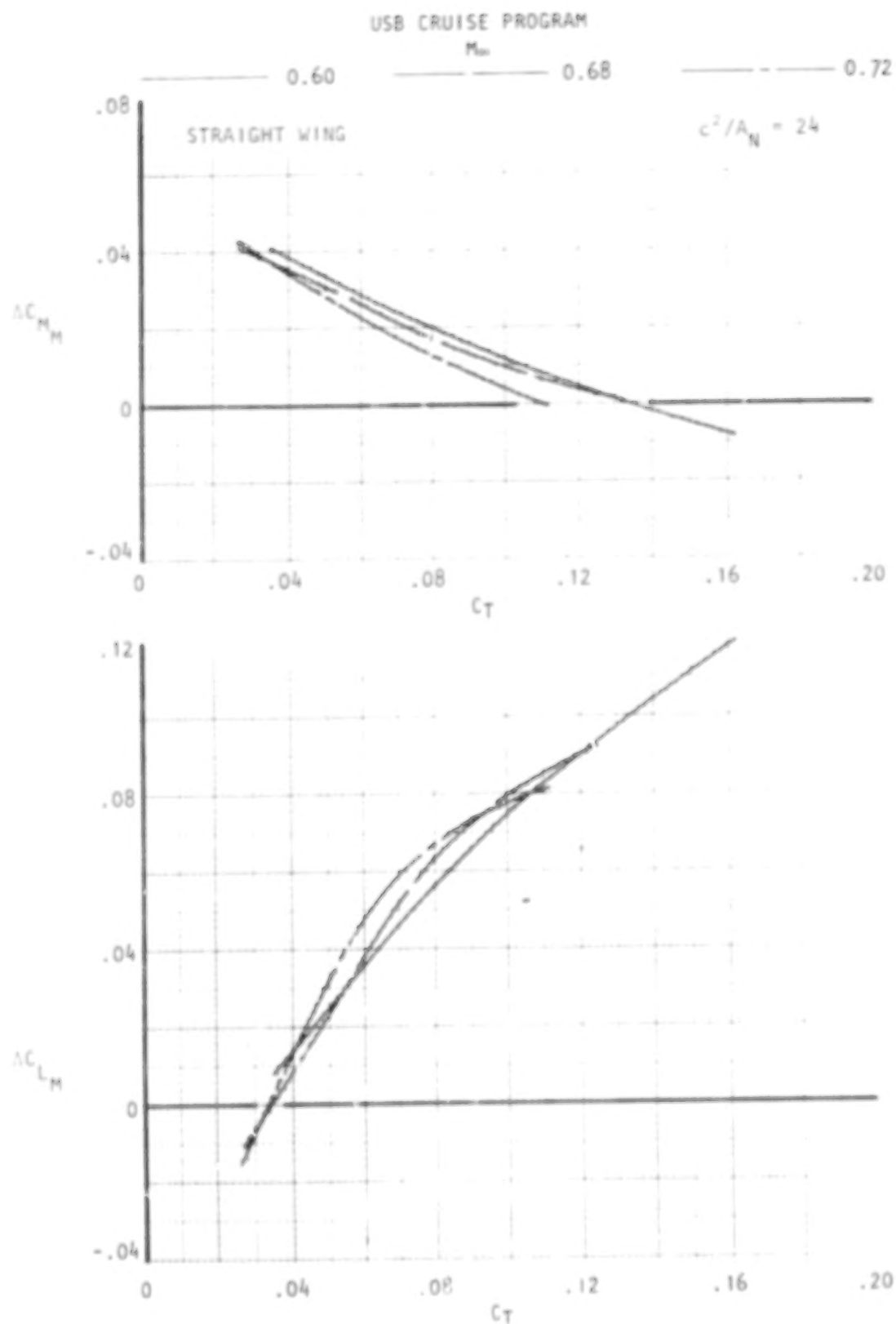


Figure 47. variation of lift and moment increments due to blowing, noz N₅, AR = 6.

In general, these data show the effect of Mach number on lift- and moment-due-to-blowing is relatively small and that the largest lift increments usually occur at the higher Mach numbers. Additionally, trends of these increments with C_T change little with Mach number with the more three-dimensional shapes, in particular, leveling off in the higher blowing range. As noted in Section 4.1.1, some of the nozzle designs incorporated a straight-section at the nozzle exit to minimize the impingement angle between jet and wing. It was expected that this feature would influence jet impingement more with the wide, thin jets than with the circular or "D-duct" nozzles. Within the subject figures, nozzles denoted with the "E" subscript do not contain the straight section having been designed with boattail angles geometrically increasing with the nozzle aspect ratio; nozzles without the subscript employed the short straight section. A comparison of the data between Figures 43 (N_3^B) and 44 (N_3^E), for example, indicate that the straight-section designs do generally show a lower lift-due-to-blowing than the more conventionally designed counterparts. This would imply that jet impingement and thereby, jet-spreading and jet-attachment were suppressed by this design change.

o Build-Up of Cruise Drag Components - In an effort to identify the sources of the nacelle drag components accruing to the total measured penalty, a build-up procedure was undertaken. For this procedure, it was assumed that most of the total nacelle drag increment is composed of at least four major components. These are:

- o nacelle skin friction drag
- o jet-scrubbing drag
- o drag-due-to-lift
- o jet-induced pressure drag

There are obvious additional losses which would be incurred at some points in the test matrix; flow separation on nacelles with extremely high boattail angles would be an example. Additionally, adverse shock-boundary-layer interactions and other Mach-related penalties would be expected from the test conditions. It was anticipated, however, that where unidentified drag penalties or favorable flow interactions are large, this fact would be highlighted by the disparity between built-up drag increments and those obtained

TABLE OF CONTENTS

<u>Section</u>	<u>Title</u>	<u>Page</u>
	FOREWORD	iii 1/A6
	LIST OF FIGURES	vii 1/A10
	SUMMARY	1 1/B7
1.0	INTRODUCTION	1 1/B7
2.0	SYMBOLS	3 1/B9
3.0	PROGRAM DEFINITION - TASK I	5 1/B11
4.0	CRUISE PERFORMANCE DATA BASE - TASK II	7 1/C1
4.1	Exploratory Wind-Tunnel Tests	7 1/C1
4.1.1	Experimental models	8 1/C2
4.1.2	Test facilities	16 1/D2
4.1.3	Experimental data analysis	16 1/D2
4.1.3.1	Pressure-test results	19 1/D7
4.1.3.2	Force-test results	34 1/E8
4.1.3.3	Geometric "effects" data	93 2/D2
4.2	Math Model Development	114 2/E10
4.2.1	Representation of wing, nacelle and power unit .	114 2/E10
4.2.2	Surface pressure	119 2/F3
4.2.3	Lift	122 2/F8
4.2.4	Drag prediction methods	122 2/F8
4.2.5	Drag correlation	127 2/F13
5.0	COMPATIBILITY STUDIES - TASK III	127 2/F13
5.1	Design and Feasibility Studies	130 2/G2
5.1.1	Perturbation studies	133 2/G7
5.1.2	Final design	133 2/G7
5.2	Supplementary Low-Speed Tests	137 2/G14
5.2.1	Model description	
5.2.1.1	Leading-edge device	142 3/A9
5.2.1.2	Trailing-edge flaps	142 3/A9
5.2.1.3	Nacelles	142 3/A9
5.2.1.4	Instrumentation	142 3/A9

TABLE OF CONTENTS (CONT'D)

<u>Section</u>	<u>Title</u>	<u>Page</u>
	5.2.2 Test results	147 3/B2
	5.2.2.1 Static performance	147 3/B2
	5.2.2.2 Wind-on performance	147 3/B2
	5.2.3 Discussion	147 3/B2
	5.2.3.1 Experimental data comparisons	147 3/B2
	5.3 Powered-Lift Analytical Synthesis	157 3/B14
6.0	RECOMMENDATIONS FOR ADDITIONAL DEVELOPMENT - TASK IV	160 3/C3
7.0	PROGRAM CONCLUSIONS	167 3/C13
	7.1 Cruise Performance Data Base - Task II	167 3/C13
	7.1.1 Experimental program	167 3/C13
	7.1.2 Theoretical program	169 3/D1
	7.1.2.1 Vortex lattice studies	169 3/D1
	7.1.2.2 Applications of jet flap theory	171 3/D3
	7.2 Compatibility Studies - Task III	171 3/D3
	7.2.1 Design feasibility studies	172 3/D4
	7.2.2 Supplementary tests	173 3/D5
8.0	REFERENCES	174 3/D6

from the tests. Results from supporting tests (i.e. pressure, rake surveys, flow-visualization) could also be employed to further identify or isolate such effects. The assumptions made in quantifying the above four components are discussed in the following paragraphs.

- o Nacelle Skin Friction Drag - The skin friction drag of each nacelle was estimated using conventional prediction techniques. These increments were appropriately corrected for the drag of the mating surfaces between nacelle and wing. A tabulation of the corrected drag increments for each of the tested nacelle configurations is provided in Figure 48. These increments include the drag of the nacelle forebody, nozzle and air supply ducting where appropriate.

- o Jet-Scrubbing Drag - The assumption made in quantifying cruise scrubbing losses was that the statically-derived thrust losses due to nacelle installation on the wing remained invariant in the wind-on condition. The static thrust losses were obtained by a comparison of a vectorial summation of balance-measured forces on the wing-nacelle combination to the thrust produced by the isolated nacelle. This process defines the thrust efficiency ratio or:

$$\eta_T = \frac{\text{Installed Thrust}}{\text{Isolated Nacelle Thrust}} \quad (\text{for a specified } \frac{H_j}{P_\infty}) \quad (6)$$

The static, jet-deflection angle (δ_{j_s}) is also obtained in this process. A tabulation of both η_T and (δ_{j_s}) is given in Figure 49 for each of the tested nacelles. Under the foregoing assumption, the cruise drag penalty due to jet scrubbing would then be:

$$\Delta C_{D_n} = \Delta C_T (1 - \eta_T) \quad (7a)$$

where

$$\Delta C_T = (C_T)_{\frac{H_j}{P_\infty}} - (C_T)_{\frac{H_j}{P_\infty}} \quad \frac{H_j}{P_\infty} = \text{FLOW THROUGH} \quad (7b)$$

USB CRUISE PROGRAM

<u>NOZZLE</u>	<u>WING INSTALL.</u>	<u>ΔC_DNF</u>
N_2	STRAIGHT WING	0.0022
N_{2E}		0.0023
N_3		0.0025
N_{3E}		0.0021
N_4		0.0024
N_{4E}		0.0020
N_5		0.0024
N_6		0.0010
$N_2 + OTW PYLON$		0.0023 (FLOW-THROUGH FOREBODY)
↓		
N_8	25° SWEPT WING	0.0012
N_{11}		0.0013
N_{12}		0.0014
N_{13}		0.0013
$N_8^1 + N_8^2$ (DUAL)		0.0024
↓		

Figure 48.

Tabulation of estimated skin friction drag of test nacelles.

USB CRUISE PROGRAM

NOZZLE	<u>$H_j/p_{\infty} = 1.6$</u>	<u>2.0</u>	<u>2.6</u>	<u>3.2</u>
N_2	1.0 (1.0)	1.0 (0)	1.0 (.6)	1.0 (1.3)
N_{2E}	.990 (1.2)	.984 (1.0)	.989 (1.0)	.989 (1.0)
N_3	1.0 (5.2)	1.0 (5.0)	.994 (6)	.990 (6.1)
N_{3E}	.993 (4.5)	.988 (3.2)	.978 (3.0)	.975 (4.0)
N_4	.933 (8.6)	.966 (9.2)	.968 (9.8)	.970 (10)
N_{4E}	.964 (13)	.975 (13)	.969 (13)	.975 (13)
N_5	.971 (12)	.993 (12)	.977 (12.5)	.985 (11)
N_6	.946 (2)	.972 (2.0)	.982 (2.8)	.978 (3.3)
N_8	.946 (2)	.972 (2.0)	.982 (2.8)	.978 (3.3)
N_{11}	1.0 (2.3)	1.0 (2.8)	1.0 (2.5)	1.0 (2.0)
N_{12}	.966 (0.5)	.968 (2.5)	.972 (4.7)	.964 (4.8)
N_{13}	1.0 (7)	.962 (7.5)	.963 (7.3)	.966 (7)
$N_8^1 + N_8^2$ (DUAL)	.941 (1.5)	.967 (1.5)	.977 (2.1)	.973 (2.4)

NOTE: $n_{TS} = \frac{\text{INSTALL. THRUST}}{\text{ISOLAT. THRUST}}$

δ_{js} IN DEG.

Figure 49. Tabulation of n_{TS} (δ_{js}) for test nozzles; static data.

It is noted in the tabulated data that the jet scrubbing losses vary in value from 0 to 4 percent of the thrust with the wider nacelles showing the higher losses as expected. Except for the very high boattail angle configuration (N_4^E , $\beta = 36^\circ$) the static, jet-deflection angles are all well below the trailing-edge angle of the wing upper-surface ($\approx 16^\circ$); the circular nozzles (N_2 , N_2^E), in particular, show essentially no jet-deflection at static conditions with corresponding η_T -values approaching 1.0.

o Drag-Due-to-Lift - The terminology "drag-due-to-lift" is used herein in lieu of "induced-drag" inasmuch as this component combines any α - (or C_L -) dependent drag term with the potential flow induced drag. Thus, viscous effects, changes in shock position or strength along with associated boundary-layer interactions which vary with α are included in the drag-due-to-lift component. To quantify this term, plots of $C_{L_{TOT}}^2$ vs. $C_{D_{TOT}}$ were constructed for each nacelle at fixed pressure ratio and Mach number. The slopes of these polars defined an equivalent wing efficiency factor, "e", which could be compared directly to that of the basic, clean wing. Typical results obtained from this analysis are provided in Figures 50 through 54 for both straight and swept wing nacelle installations. The ordinate in these plots, $\Delta e/e_w$, is derived from:

$$\frac{\Delta e}{e_w} = \frac{(e)_{Hj}}{\frac{P_\infty}{e_w}} - 1 \quad (8)$$

The effective, clean wing efficiency factors, e_w , are given in Figure 55 for the two clean wing/body combinations. Drag-due-to-lift at a specified lift and pressure ratio would then be:

$$\Delta C_{D_l} = \frac{C_{L_{TOT}}^2}{\pi (AR)_w} \left| \frac{1}{(e)_{Hj}} - \frac{1}{e_w} \right| \frac{P_\infty}{P_\infty} \quad (9)$$

USB CRUISE PROGRAM

SYM M_∞

- 0.60
- 0.68
- △ 0.72

$$c^2/A_N = 24$$

STRAIGHT WING

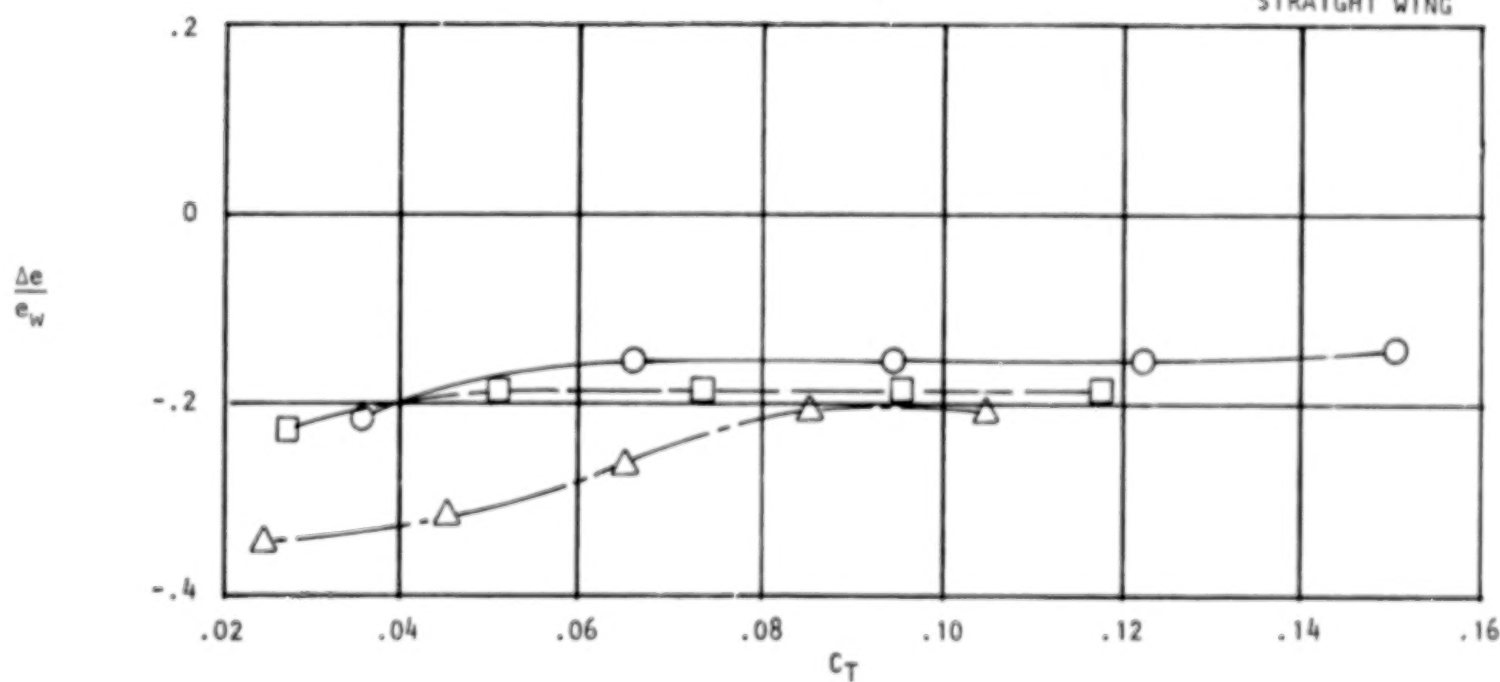


Figure 50. Variation of effective drag-due-to-lift parameter with thrust and Mach no., nozzle N_2E , circular.

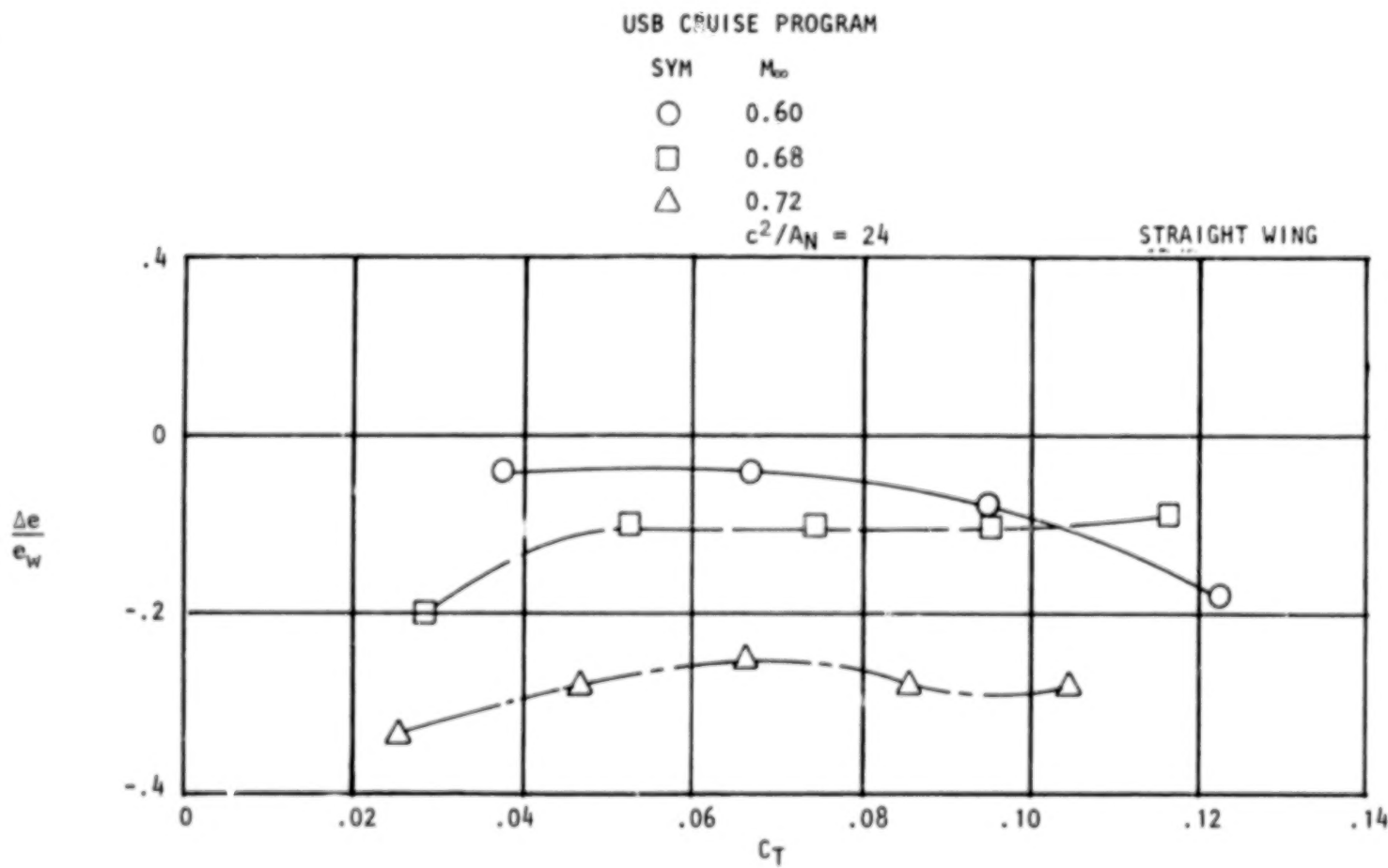


Figure 51. Variation of effective drag due-to-lift parameter with thrust and Mach no., nozzle N_{3B} , AR = 2.5.

USB CRUISE PROFILE

SYM M_∞

○ 0.60

□ 0.68

△ 0.72

 $c^2/A_N = 24$

STRAIGHT WING

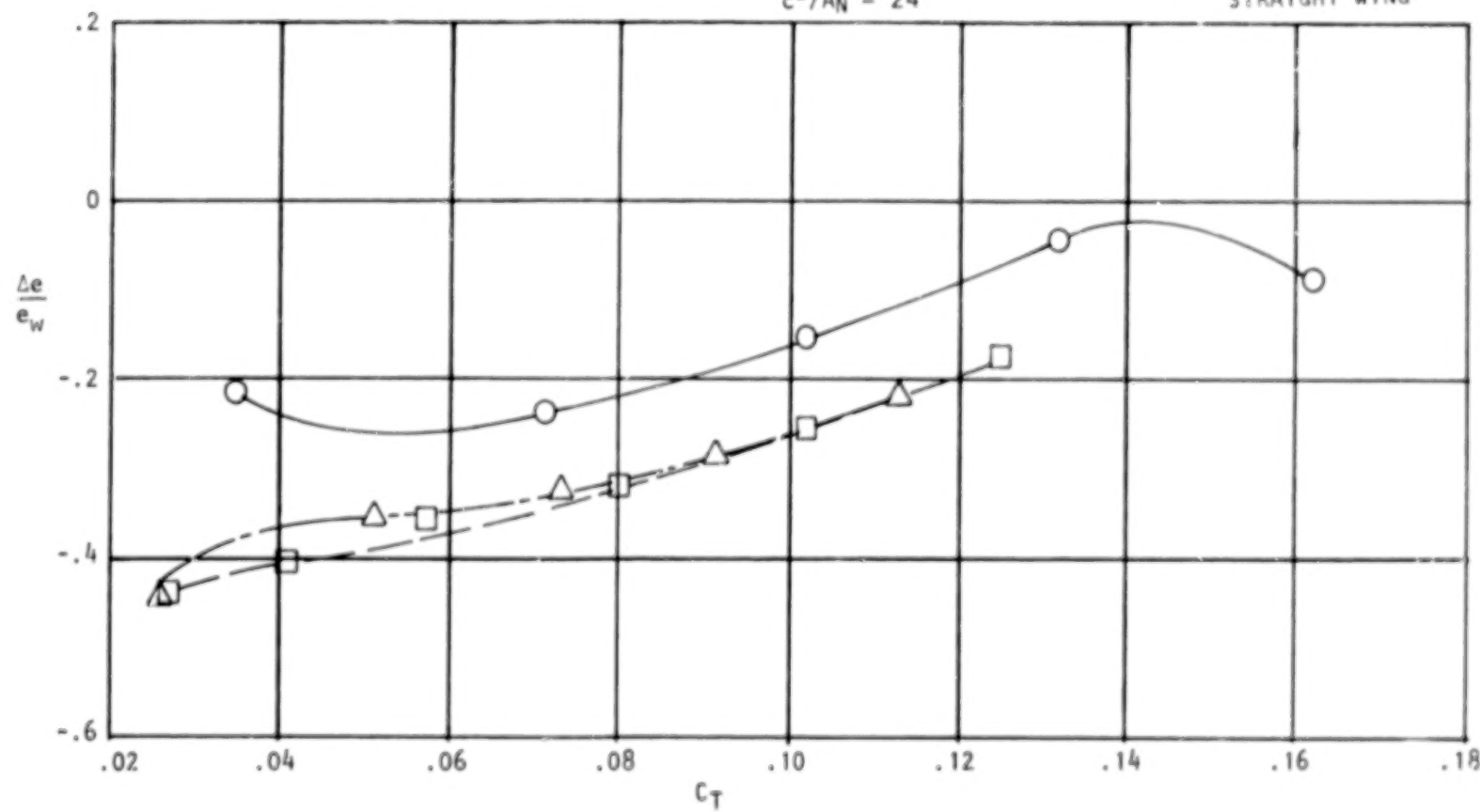


Figure 52. Variation of effective drag-due-to-lift parameter with thrust and Mach no., nozzle N_5 , AR = 6.

USB CRUISE PROGRAM

SYM	M_{∞}
○	0.60
□	0.68
△	0.73

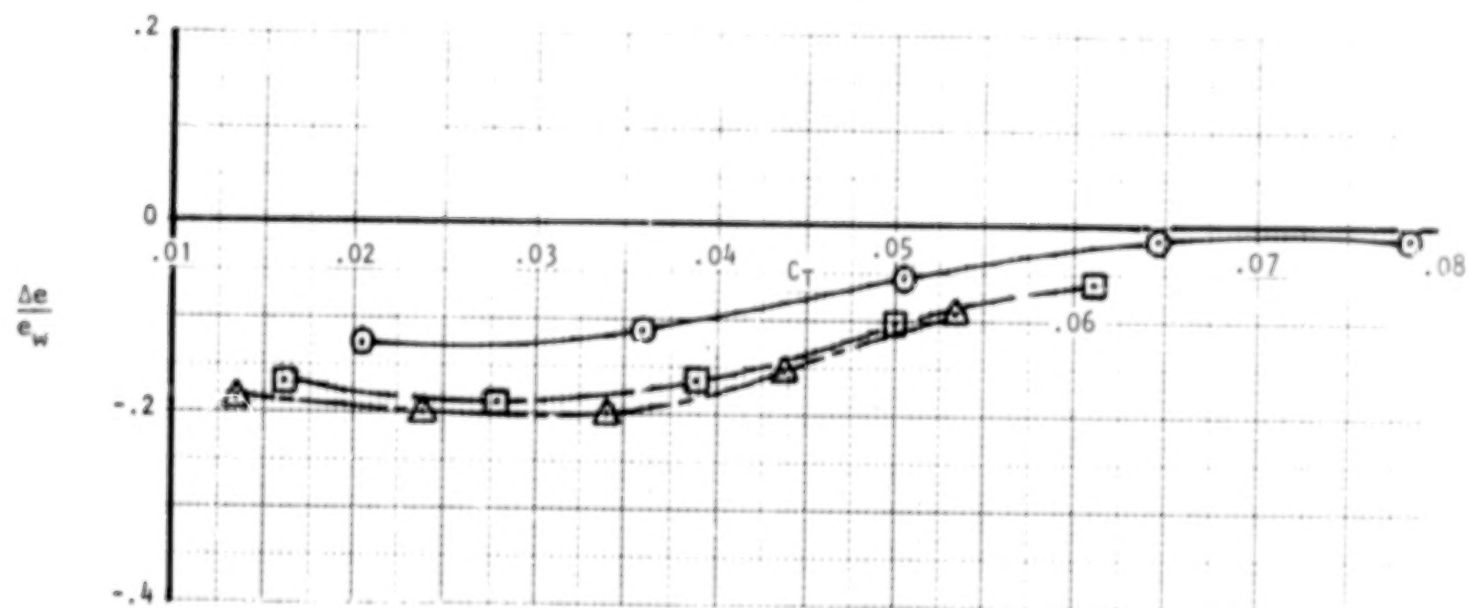
SWEPT WING $c^2/A_N = 48$ 

Figure 53.

Variation of effective drag-due-to-lift parameter with thrust and Mach no., nozzle N_B^2 , AR = 2.5.

USB CRUISE PROGRAM

SYM M_∞

○ 0.60

□ 0.68 •

△ 0.73

SWEPT WING $c^2/A_N = 48$

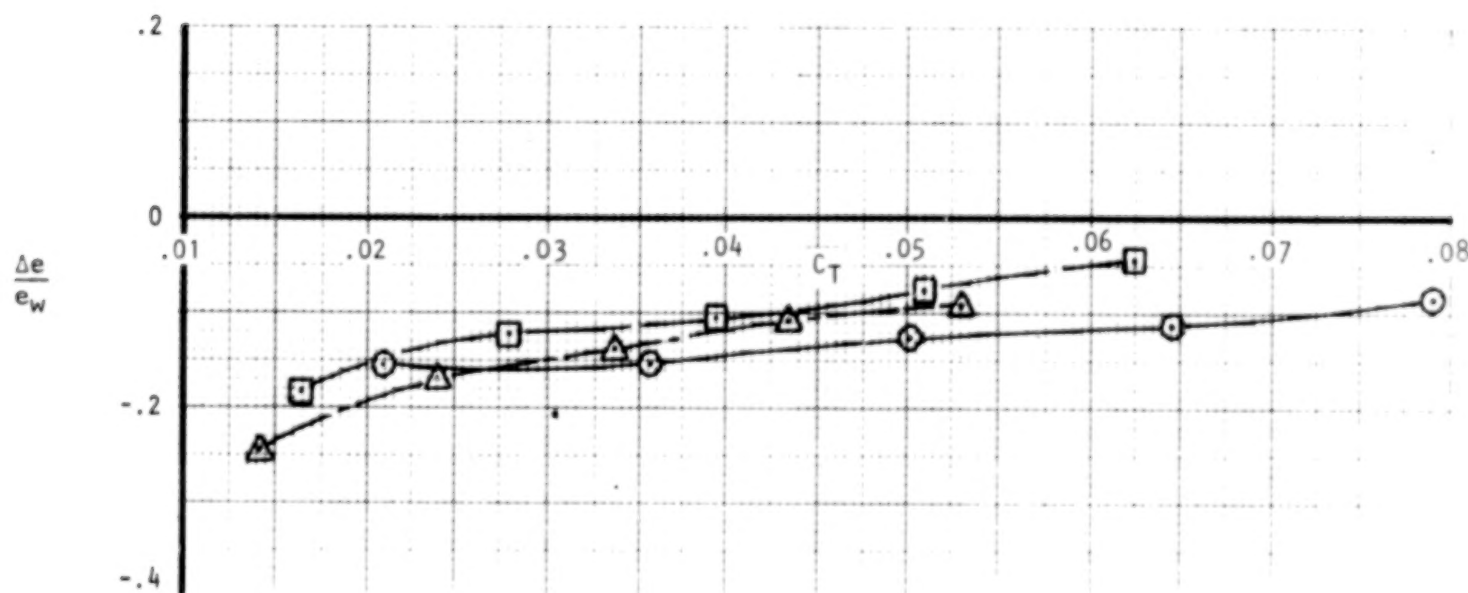


Figure 54. Variation of effective drag-due-to-lift parameter with thrust and Mach no., nozzle N_{12} , AR = 4.

M_{∞}	e_w , STRAIGHT WING	e_w , SWEPT WING
0.60	0.80	0.71
0.68	0.71	0.66
0.72	0.73	0.71
0.73	--	0.65

Figure 55. Tabulation of effective wing/body efficiency factors, e_w , for clean wing-body configurations.

As noted in Figures 50 through 54, and as typical of all force-measurements made, the effective nacelle-installed efficiency factors are less than those of the wing/body alone. The largest losses in equivalent "e" occur generally in the lower C_T -range, such as the flow-through condition, where a mutual interference between the symmetrical nacelle and wing-flow-fields would be expected. As nozzle blowing increases, local boundary-layer control via jet-scrubbing and entrainment provides a limited clean-up of local flow disturbances such that $\Delta e/e_w$ tends toward the clean-wing value ($\Delta e/e_w = 0$); this effect is most pronounced for the wide, high aspect ratio nozzles which influence a greater span of the wing (Figure 52). In no instance, however, was full recovery to the clean wing level in evidence for the models employed in the test program. The generally unfavorable trend of $\Delta e/e_w$ as indicated with Mach number would be anticipated due to the increased sensitivity of the combined wing/nacelle flow-fields to lift-related compressibility effects.

- o Jet-Induced Pressure Drag - Analysis of the surface-pressure test results indicated that the deflection of the jet over the aft-wing surface could give rise to a pressure drag component which acts, at least, over the jet-scrubbed area. Additionally, the analysis showed that this component could be approximated by the momentum expression

$$\Delta C_{Dj} = \eta \Delta C_T [1 - \cos (\alpha + \delta_j)] \quad (10)$$

if the trailing-edge injection, or jet-angle, δ_j , is known. In an earlier discussion of the measured nacelle drag increments (Figures 20 through 24), it was further postulated that the almost cyclic trend of ΔC_{DN} vs. C_T was a consequence of variations in the jet-angle with nozzle pressure-ratio. Under this rationale, the parameter δ_j could then be a constantly-changing variable. In an effort to predict such variations, use was made of the correlations between the foregoing momentum expression and the dragwise integrations of scrubbed area pressures at wind-on conditions. This roughly defined a range of jet-angles as characterizing a given nozzle exit shape for various pressure-ratios and Mach numbers. The upper limit of these angles was the 16^0 trailing-edge angle of the wing upper-surface. Use of these nominal angles, along with

appropriate values of α and ΔC_T , provided a first-order quantification of the jet-induced pressure drag, ΔC_{D_j} .

o Summation of Drag Components - The four major drag components, calculated by the foregoing methods, were summed for comparison to the measured nacelle drag increments. Figures 56 through 63 show the individual, calculated components, along with the total, for fixed cruise conditions of $C_{L_M} = 0.4$ and drag-rise Mach number ($M_\infty = 0.68$ and 0.73). Also shown on these figures are the nominal values of δ_j used in the approximation of ΔC_{D_j} . The "choke" pressure ratio of $H_j/p_\infty = 1.89$ generally defined conditions where rapid changes in δ_j occur; the assumed δ_j -values above and below "choke" onset are shown.

For a majority of the configurations, the built-up drag increments were in reasonable agreement in magnitude and trend with the wind-tunnel-measured drag increments as indicated in Figures 56 through 63. Most of the differences in drag (amounting to about $\Delta C_{D_N} \pm .0010-.0015$) could readily be accounted by assuming slightly different values of δ_j in the build-up process. The swept-wing nozzles generally did not provide as good a correlation as did the straight-wing installations. All of the swept-wing nozzles (Figures 60 through 63) contained the short straight section just ahead of the nozzle exit as mentioned in association with Figure 5. It is believed that this feature, effective with the small, swept-wing jets, suppressed jet-attachment and thus promoted excursions in effective jet angle.

Several cases are shown where significant differences between measured and built-up drag components are in evidence. Figure 60, providing data for the small, circular nozzle N_{11} , shows an unidentified drag component of about

$(\Delta C_{D_N}) \approx 0.0010$ across the blowing range. This has been labeled as a miscellaneous drag component and is believed to be Mach number-related interference reflecting the need for a more refined wing/nacelle fillet; this need was mentioned earlier in discussions of this configuration. Figure 64, portraying data for a high-boattail angle "D-duct" installation ($N_{3E}, \beta = 25^\circ$), shows a higher measured drag increment than could be accounted for in the build-up process in the lower blowing range. Surface pressure data and flow-visualiza-tion photographs suggested local flow separation along the nozzle boattail

BLANK

PAGE

USB CRUISE PROGRAM

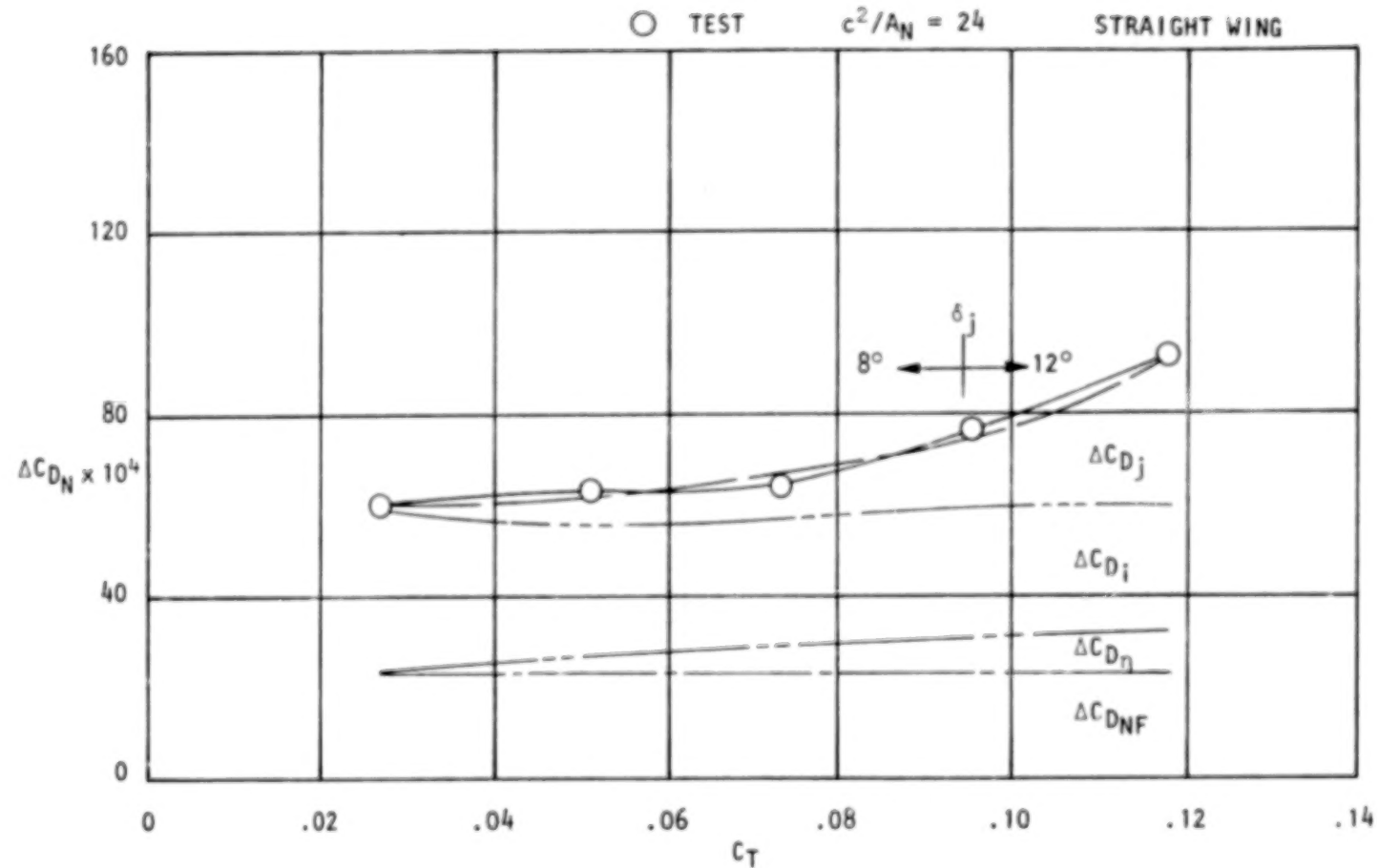


Figure 56. Incremental nacelle drag and component build-up,
noz N_2E , circular, $M_\infty = 0.68$, $C_{LM} = 0.40$.

USB CRUISE PROGRAM

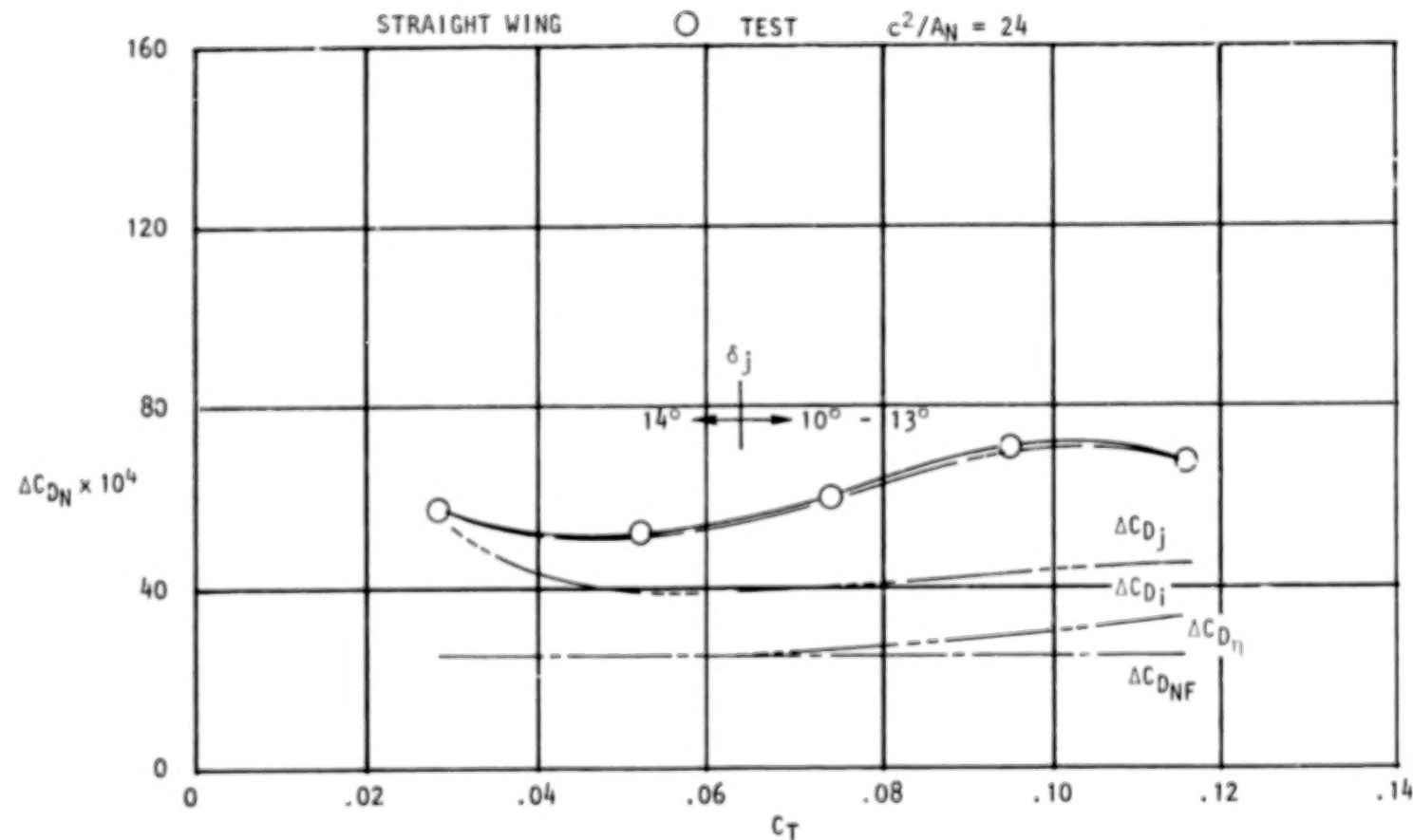


Figure 57. Incremental nacelle drag and component build-up,
noz N_{3B}, AR = 2.5, $M_\infty = 0.68$, $C_{LH} = 0.40$.

USB CRUISE PROGRAM

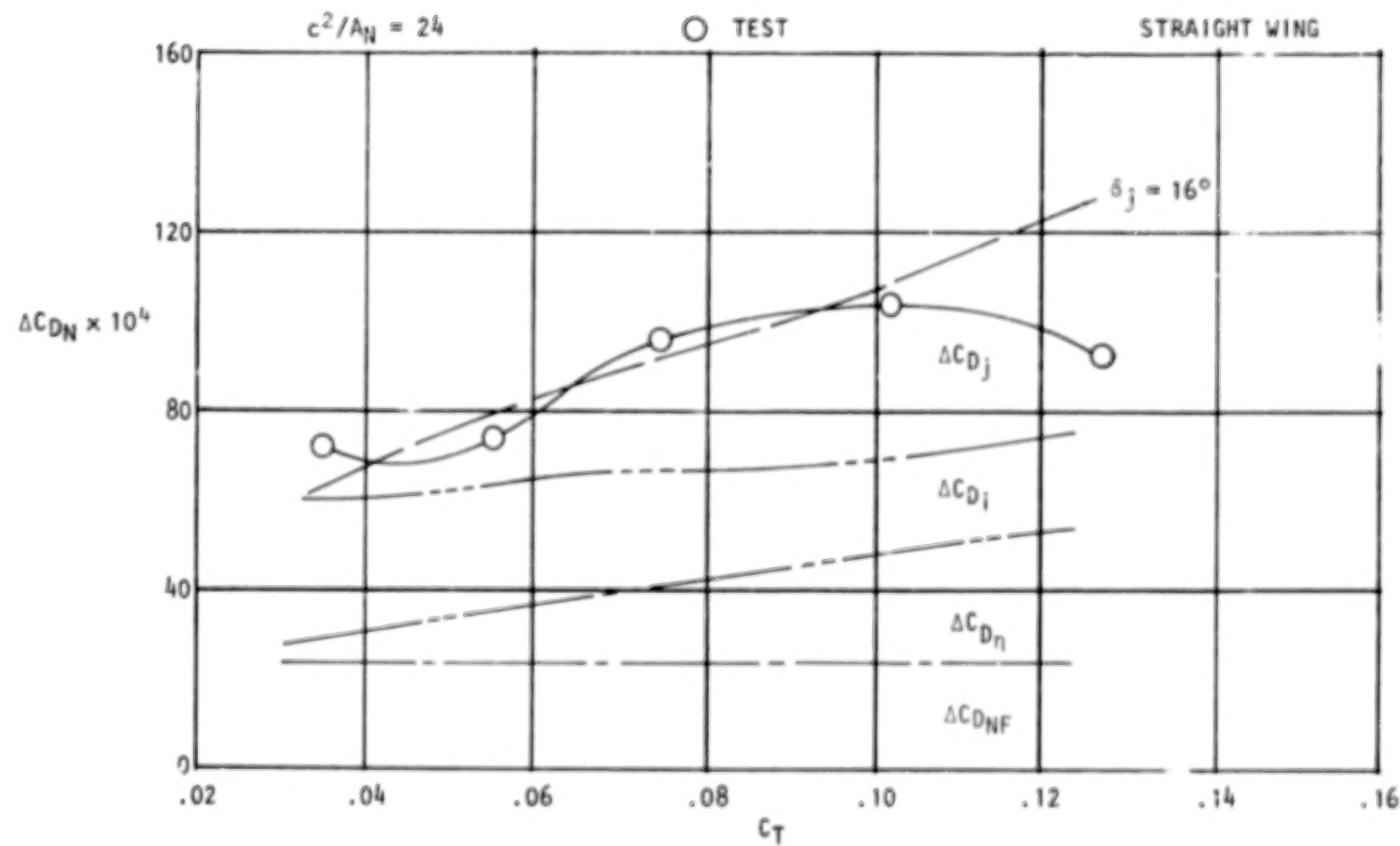


Figure 58. Incremental nacelle drag and component build-up,
noz N_4 , AR = 4, $M_\infty = 0.68$, $C_{LM} = 0.40$.

USB CRUISE PROGRAM

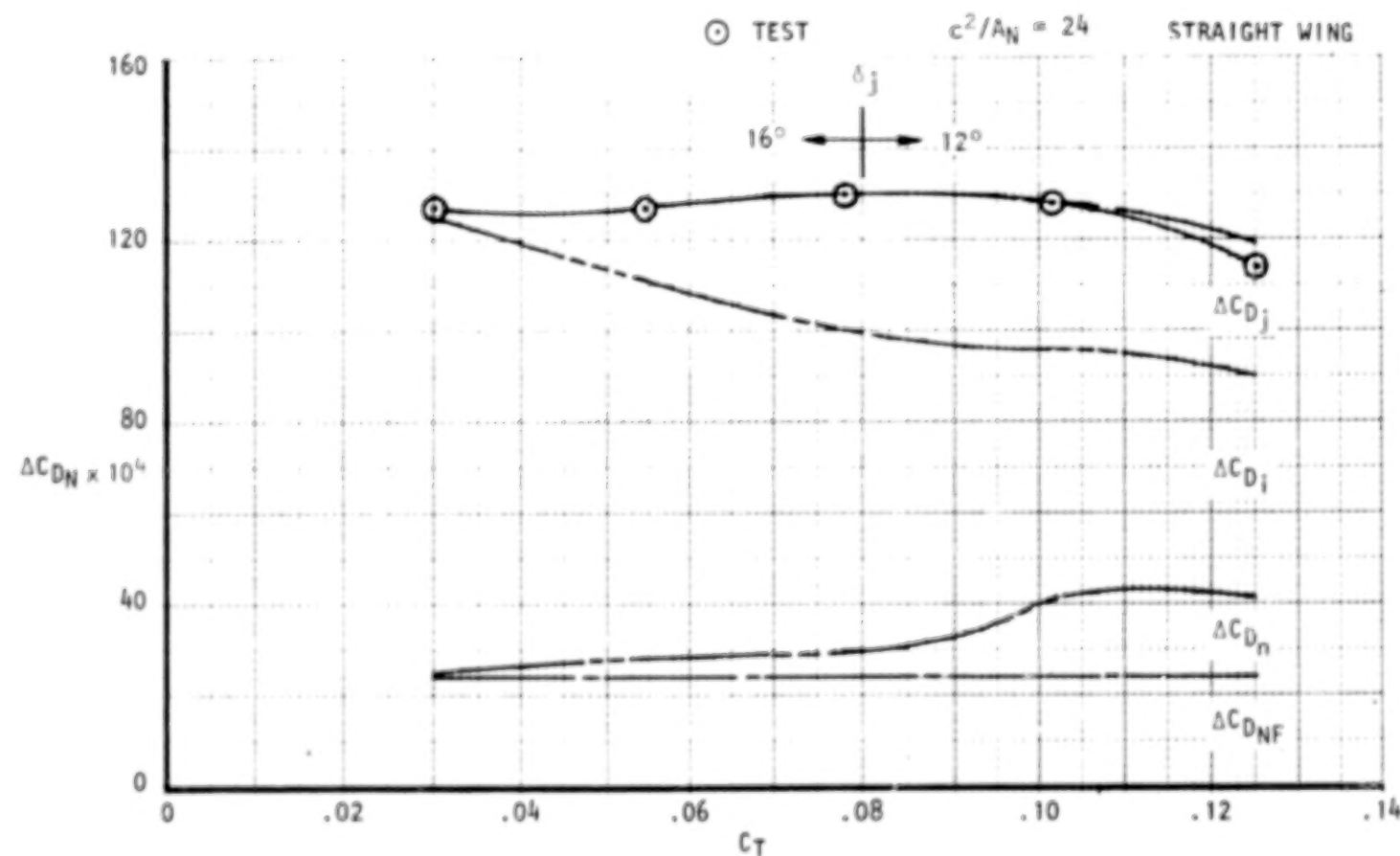


Figure 59. Incremental nacelle drag and component build-up
 noz N_S , AR = 6, $M_\infty = 0.68$, $C_{LH} = 0.40$

USB CRUISE PROGRAM

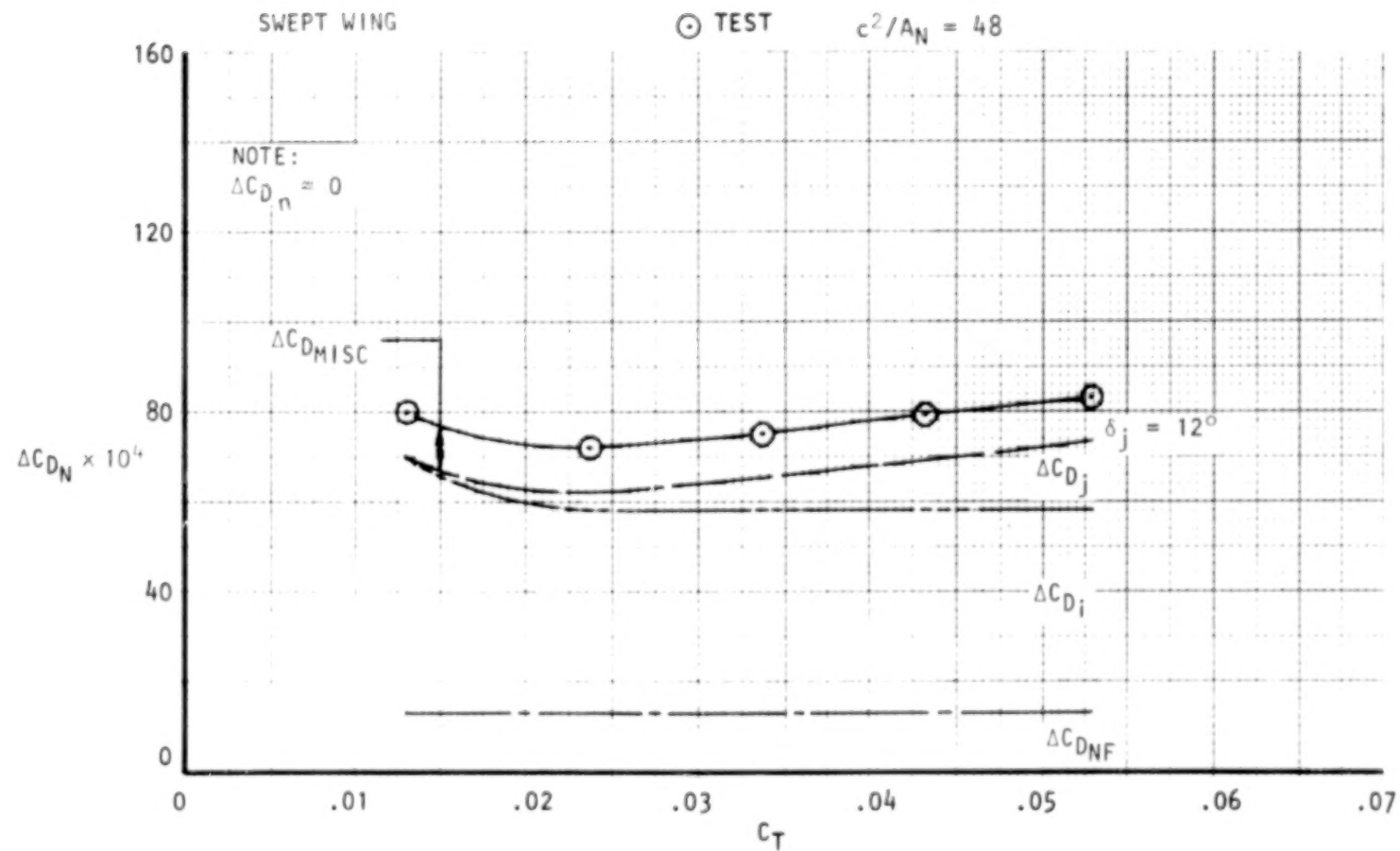


Figure 60. Incremental nacelle drag and component build-up, noz N₁₁, circular, $M_\infty = 0.73$, $C_{LM} = 0.40$.

86

USB CRUISE PROGRAM

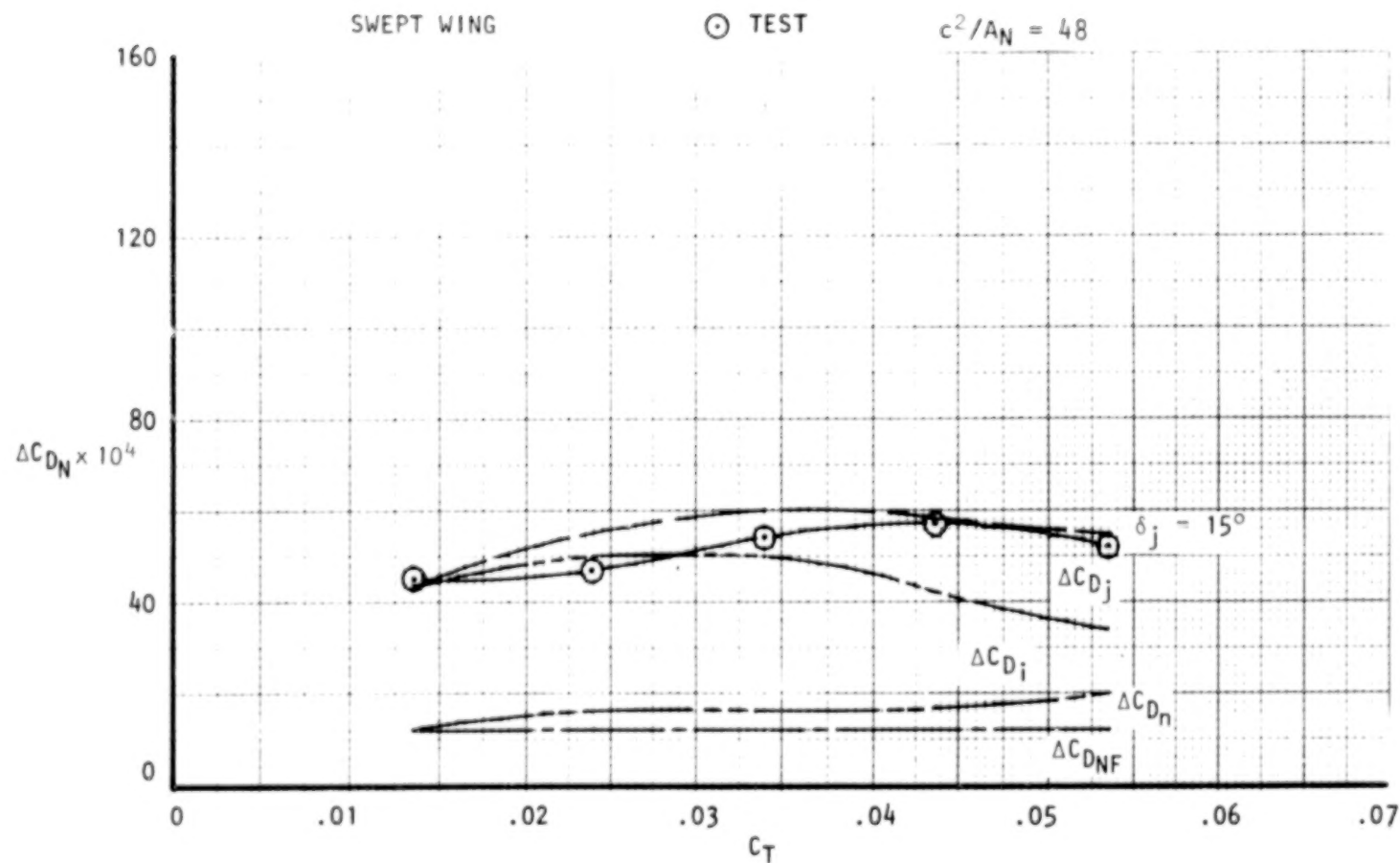


Figure 61. Incremental nacelle drag and component build-up,
 $\text{noz } N_b^2$, $\text{AR} = 2.5$, $M_\infty = 0.73$, $C_{LM} = 0.40$.

USB CRUISE PROGRAM

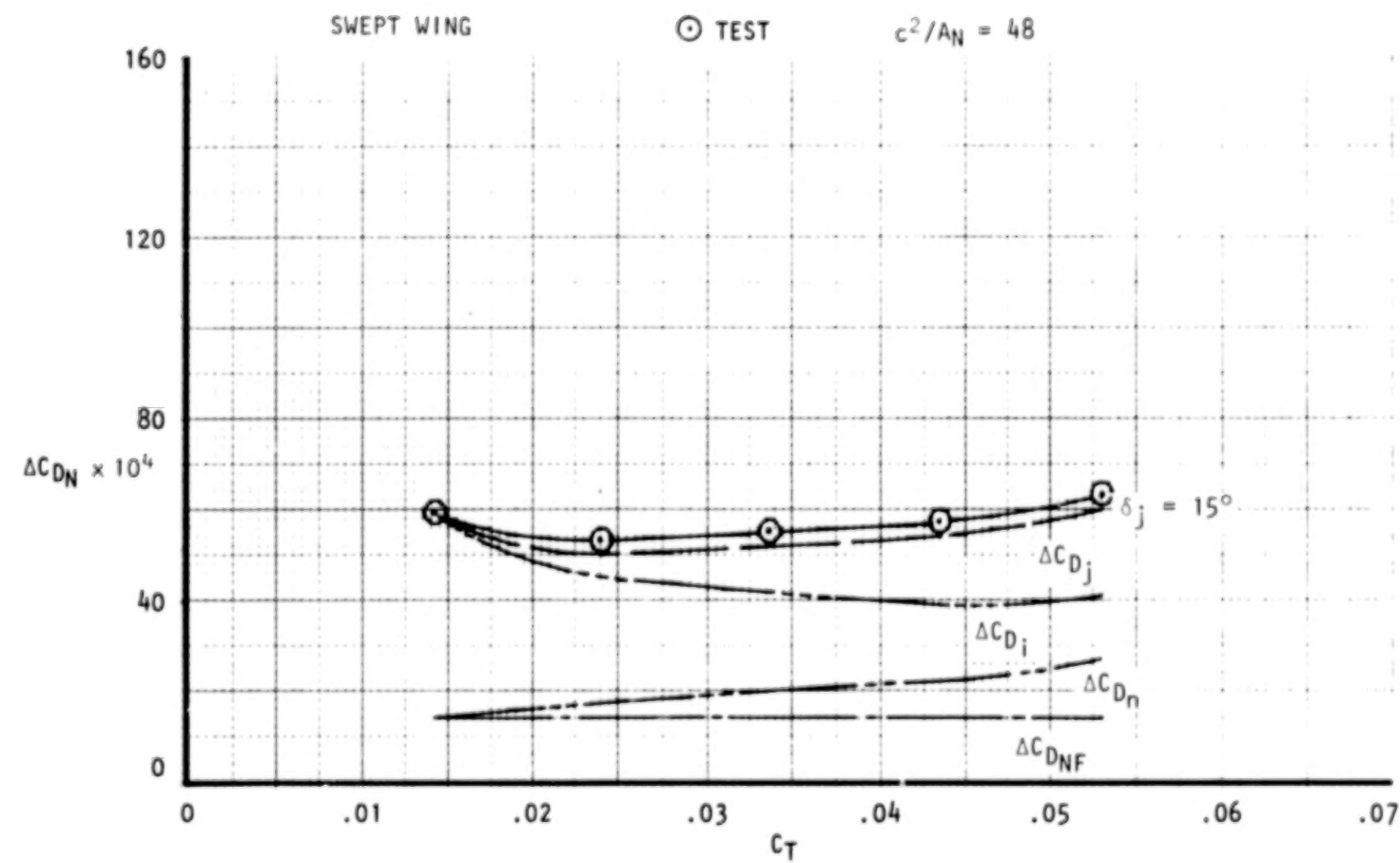


Figure 62. Incremental nacelle drag and component build-up,
noz N₁₂, AR = 4, $M_\infty = 0.73$, $C_{LM} = 0.40$.

88

USB CRUISE PROGRAM

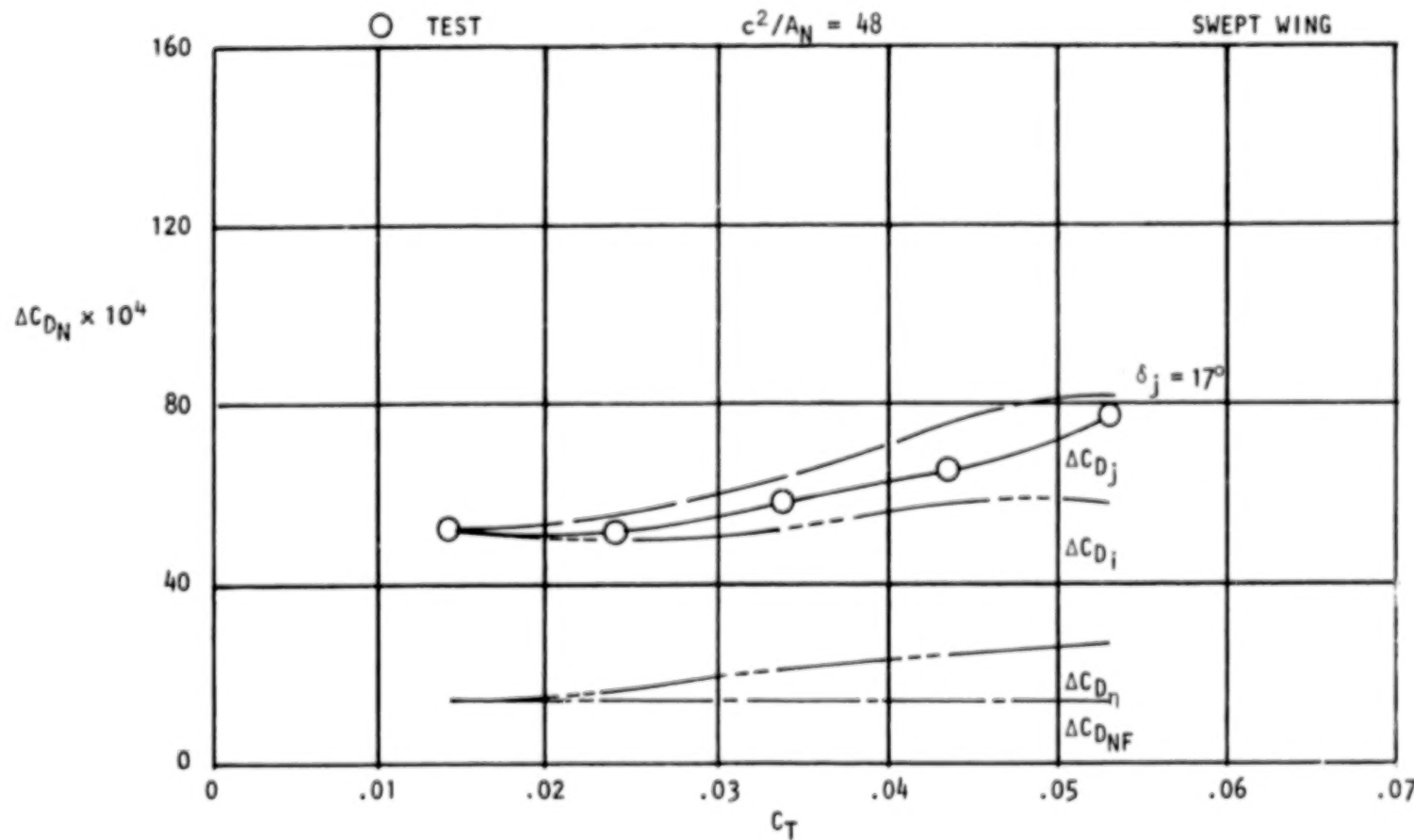


Figure 63. Incremental nacelle drag and component build-up, noz N₁₃, AR = 6, M_∞ = 0.73, C_{LM} = 0.40.

USB CRUISE PROGRAM

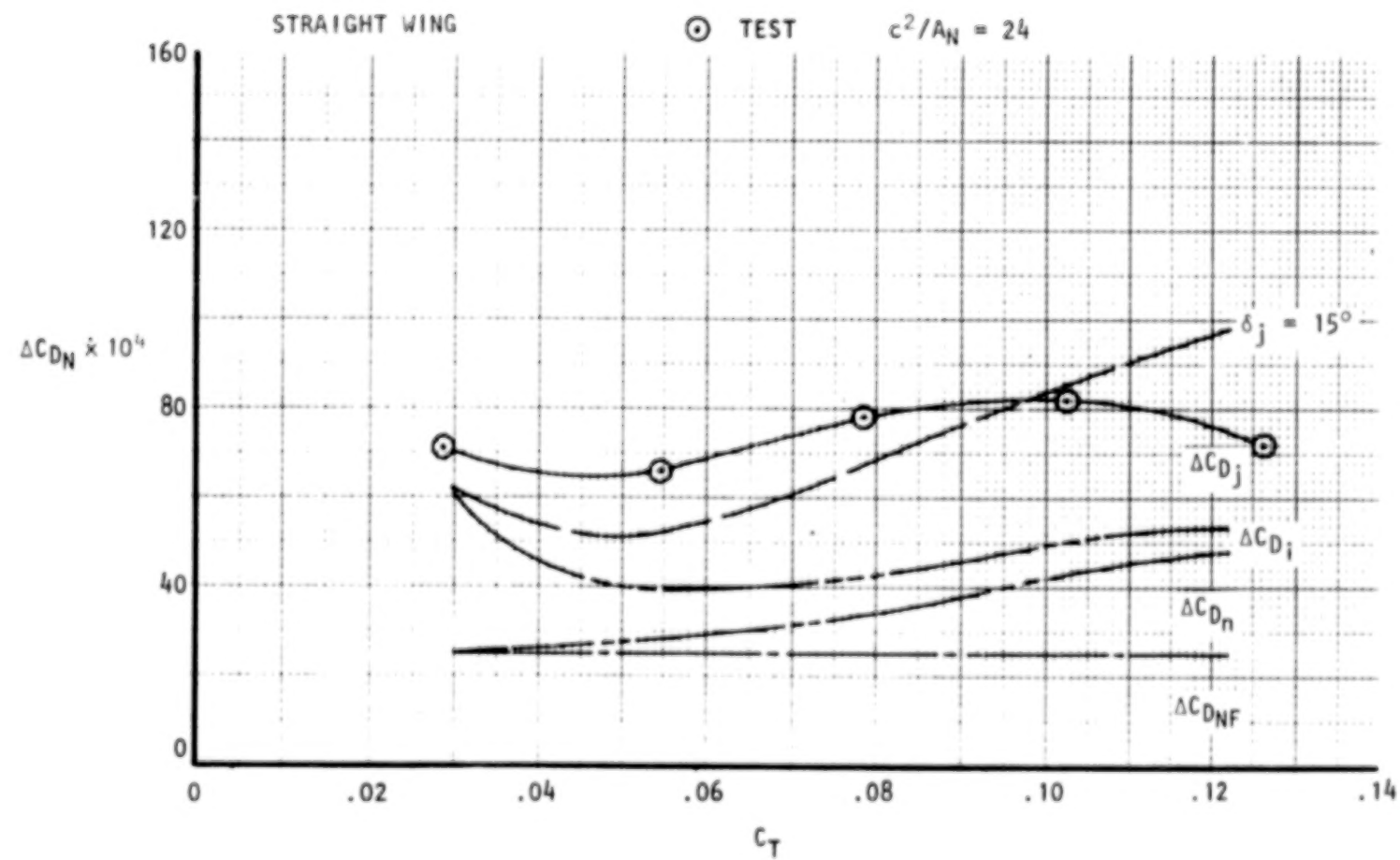


Figure 64. Incremental nacelle drag and component build-up
 noz N_{3E} , AR = 2.5, $M_\infty = 0.68$, $C_{LM} = 0.40$.

centerline just ahead of the exit. As the blowing increases, this separation diminishes as the pumping action of the jet provides a suppression effect. The effects of more extensive boattail flow separation is represented in Figure 65 wherein data for an extreme boattail angle of $\beta = 36^\circ$ is shown (nozzle N_4). That drag component believed to reflect primarily boattail separation is denoted as $\Delta C_{D\beta}$ on this figure. While the effect of C_T on the separation is shown to be favorable, the blowing rate reaches $C_T \approx 0.12$ ($H_j/p_\infty \approx 3.0$) before effective suppression occurs. Figures 66 provides an oil-flow photograph for this nozzle at a nozzle pressure-ratio of about 2.0.

o Build-Up of Total Cruise Lift - The total cruise lift coefficient can be componentized for source identification as was the nacelle drag. The total lift would be composed of:

- o wing/body lift, $C_{L_{W/B}}$
- o Lift increment due to the nacelle installation at flow-through pressure ratio, ΔC_{L_N}
- o power-induced lift, ΔC_{L_T}

The last increment ΔC_{L_T} can be further sub-divided into a vectored-thrust lift increment, $\Delta C_{L_{V/T}}$, and that due to increased circulation lift on the wing, ΔC_{L_j} . The total lift can therefore be represented by:

$$C_{L_{TOT}} = C_{L_{W/B}} + \Delta C_{L_N} + \Delta C_{L_{V/T}} + \Delta C_{L_j} \quad (11)$$

Of the foregoing components, the direct thrust term, $\Delta C_{L_{V/T}}$, can be quantified as

$$\Delta C_{L_{V/T}} = n \Delta C_T [\sin (\alpha + \delta_j)] \quad (12)$$

BLANK

PAGE

USB CRUISE PROGRAM

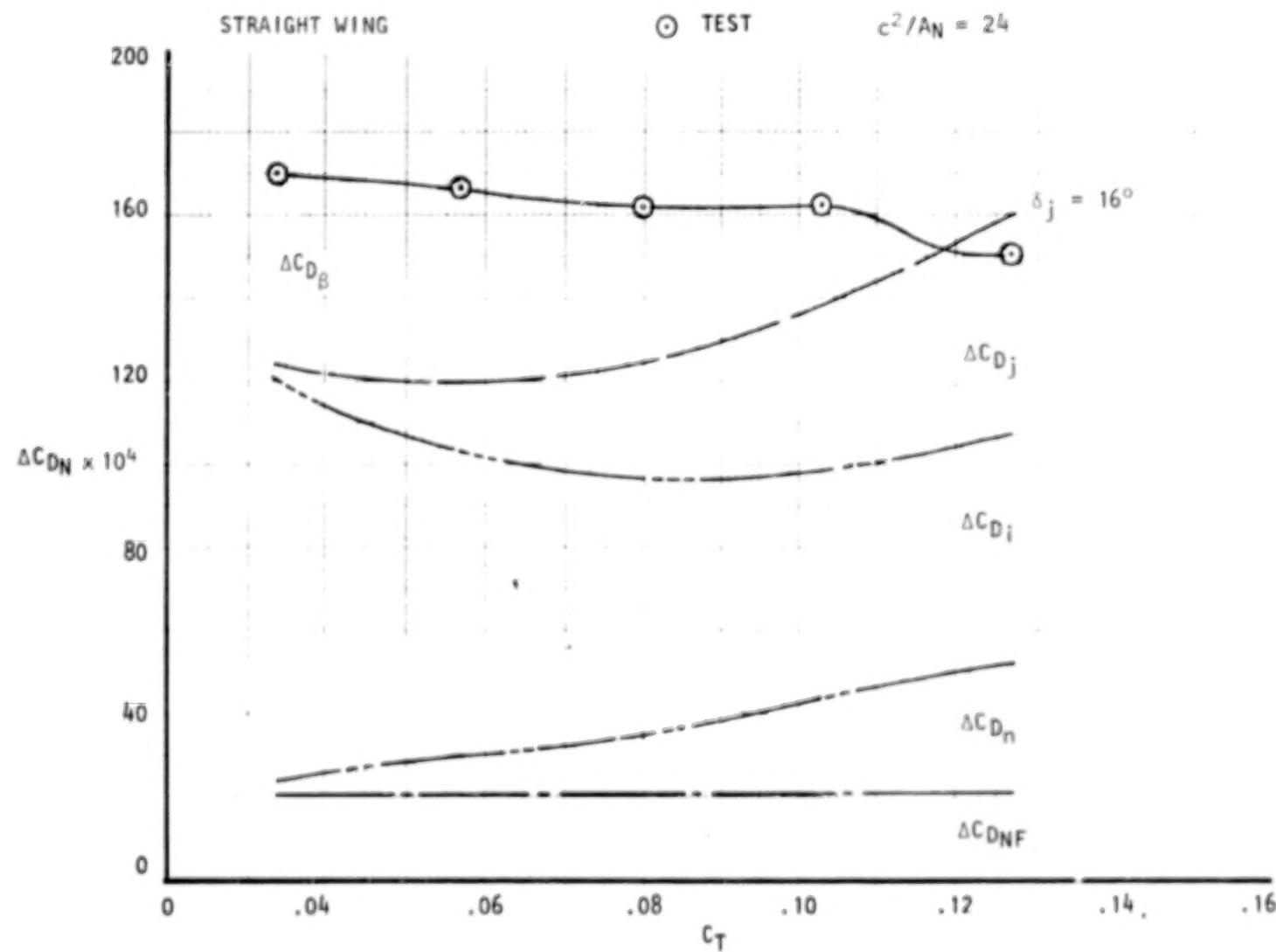


Figure 65. Incremental nacelle drag and component build-up
noz N_{4E} , $AR = 4$, $M_\infty = 0.68$, $C_{LM} = 0.40$.

USB CRUISE PROGRAM



Figure 66. Oil-flow photograph of high-boattail nozzle ($N_{\text{deg}} = 36$), $M_\infty = 0.70$, $\gamma = 2.6$.

The identity of the other components requires experimental/analytical correlation to establish appropriate configurational relationships. Typical examples of magnitudes of these lift components can be seen in Figure 67 for a representative cruise condition. The wing/body lift, at the specified cruise- α , is shown on the left of the figure. Also shown is the lift change due to the installed nacelle at flow-through ($H_j/p_\infty \approx 1.4$) pressure ratio; these were normally small negative values for most of the tested nozzle installations. Also shown on the plots are the calculated direct-thrust lift increments, $\Delta C_{L_{V/T}}$, where δ_j has been assumed as 15 degrees. The remainder of the lift-due-to-thrust has been assigned to the circulation lift increment, ΔC_{L_f} . As would be expected, ΔC_{L_f} increases rapidly with the width of the nozzle and for the circular nozzle, represents a very small component of the total lift.

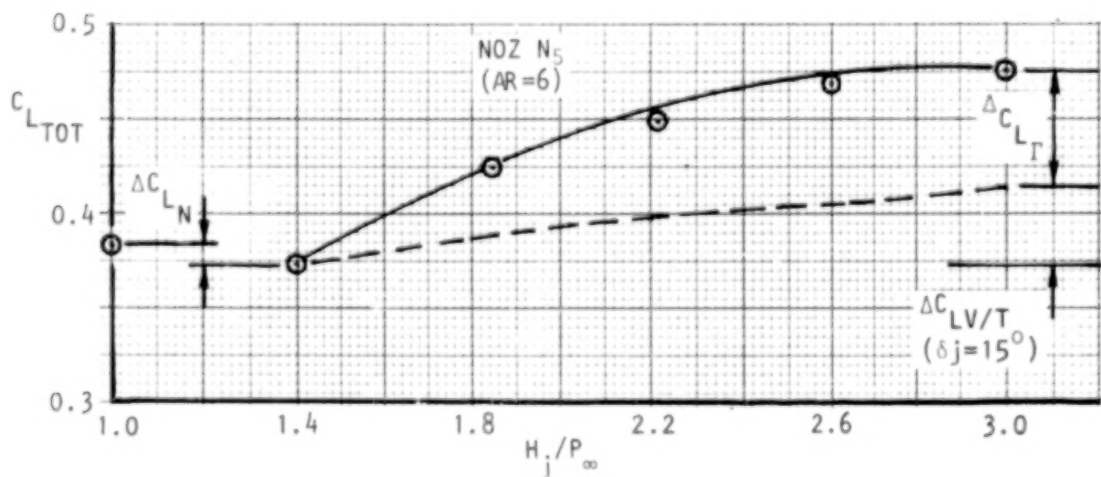
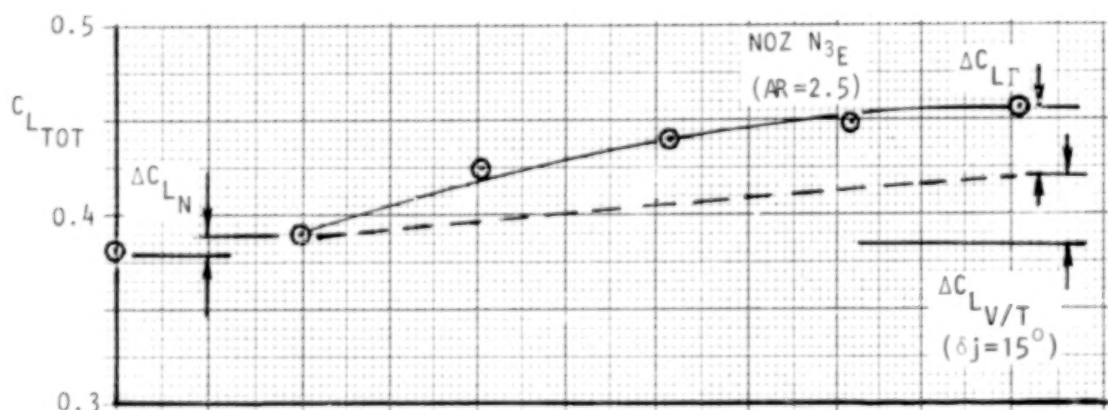
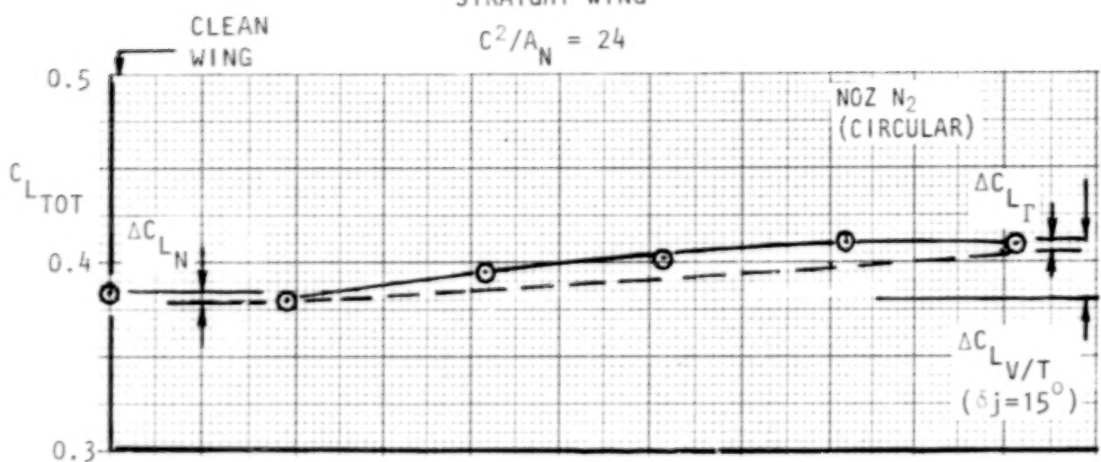
In support of the lift breakdown typified in Figure 67, a calculation method, discussed more fully in Section 4.2.3, has been evaluated for USB application. This method, based on limited span jet-flap theory, provides reliable predictions of lift-due-to-thrust, the major lift component of interest. In such calculations, the jet-angles required for reasonable correlation are found to be within several degrees of the wing trailing-edge angle or approximate the $\delta_j \approx 15$ degrees used in Figure 67. As a predictive technique, the part-span jet-flap analogy would be recommended as a simple but effective approach for USB synthesis.

4.1.3.3 Geometric "Effects": A primary objective of the USB Data Base Program has been the study of wing/nacelle geometric variables as related to cruise aerodynamics. The extensive experimental hardware matrix along with the foregoing attempt to identify "effected" aerodynamic quantities represent the means toward fulfilling this objective. In the paragraphs which follow, the major effects of various nacelle-wing geometric design variables are summarized.

o Effects of Nozzle Aspect Ratio - Because of the importance of nozzle exit aspect ratio as a meaningful variable for both high- and low-speed design, the aerodynamic affects of aspect ratio are presented in some detail.

USB CRUISE PROGRAM

STRAIGHT WING

Figure 67. Components of total lift coefficient, $M_\infty = 0.68$, $\alpha = 3^\circ$

- Total Drag - Figure 68 shows the effect of nozzle aspect ratio on the total nacelle drag increment over a range of thrust coefficients. The drag is given in ratio form normalized to the drag of the circular nozzle. While the general trend of drag increment is an increase with nozzle width, the design gross thrust would also be a consideration in selecting a candidate nacelle shape in the lower aspect ratio range. For the purposes of meeting Task III objectives in the Data Base Program, the "D-duct" (AR = 2.53) configuration was chosen for further study although, from cruise considerations, the circular nacelle shows a slightly lower drag. In making this selection, the need for providing a variable nozzle geometry in the low-speed, high-lift regime, as well as the potential for additional cruise refinements, were basic considerations in the nacelle selection.

- Drag-Due-to-Lift - A primary reason for the lower aspect ratio nozzles showing better cruise performance than the high aspect ratio installations is demonstrated in Figure 69. Drag-due-to-lift, for $CL_{TOT} = 0.4$, is plotted as a function of nozzle exit aspect ratio for the two boattail angle series of medium-sized nozzles. For the short, high boattail-angle configurations, there is a definite "bucket" in the lift-dependent drag at an aspect ratio approaching that of the "D-duct" installation at all blowing rates. The aspect ratio 4 nozzle (N_4), with an unrealistically high boattail angle of 36° , is penalized heavily by lift-dependent drag. A similar trend, but without a pronounced drag minimum, is shown for the low-boattail-angle nozzle series. As noted previously, the effectiveness of short, straight section ahead of the nozzle exit in reducing the jet impingement of the wide (AR = 6) nozzle probably accounts for the trend noted with pressure-ratio.

Similar lift-dependent drag data are shown in Figure 70 for the swept wing nozzles. It is noted that drag excursions, as influenced by both pressure ratio or nozzle aspect ratio, are comparatively small (i.e. relative to the straight wing data). The greatest difference is apparent in the high aspect ratio range where lift-dependent drag does not increase as rapidly as that shown for the straight wing cases. The major reason for this difference is that the swept-wing nacelles were designed with varying chordwise positions of the nozzle exit; this design change can influence jet-attachment. The circular nozzle (AR = 1.25) has an exit position at $x/c = 0.10$, as noted on

USB CRUISE PROGRAM

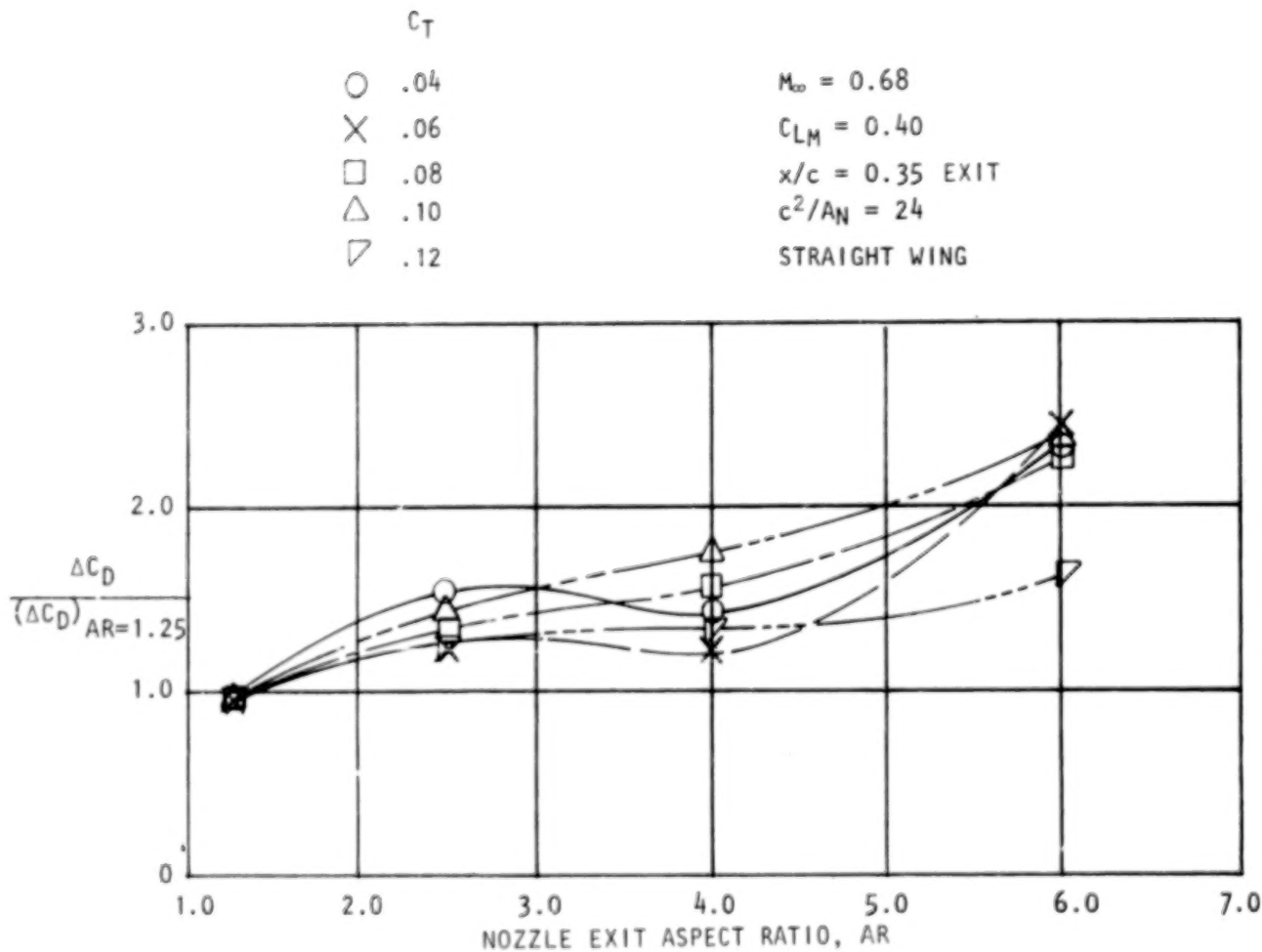


Figure 68. Effect of nozzle aspect ratio on nacelle drag.

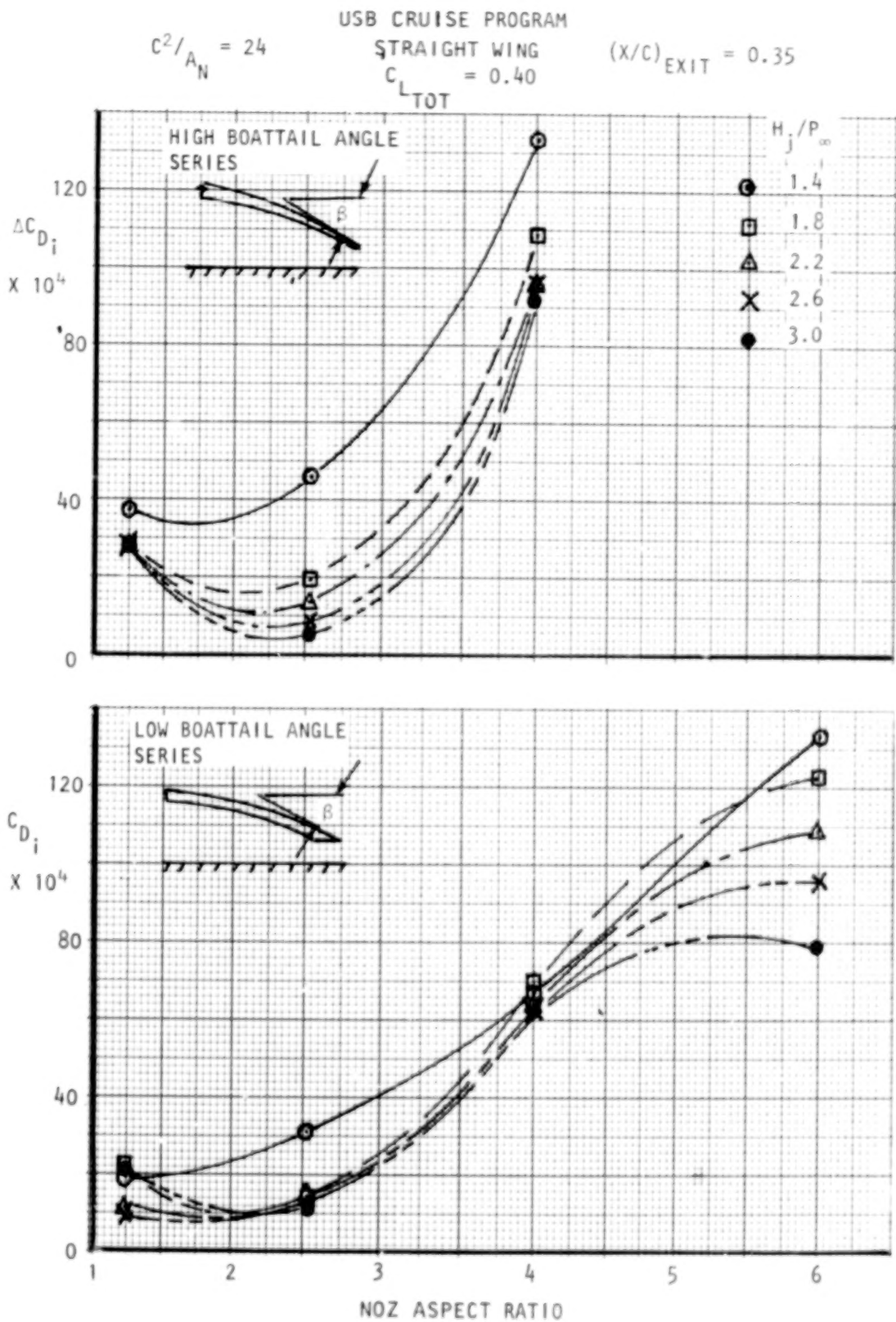


Figure 69. Effect of nozzle exit aspect ratio on lift-dependent drag, $M_{\infty} = 0.68$

USB CRUISE PROGRAM

SWEPT WING

$$C^2/A_N = 48 \quad C_{L_{TOT}} = 0.40$$

$$H_j/P_\infty$$

○ 1.4

□ 1.8

△ 2.2

× 2.6

● 3.0

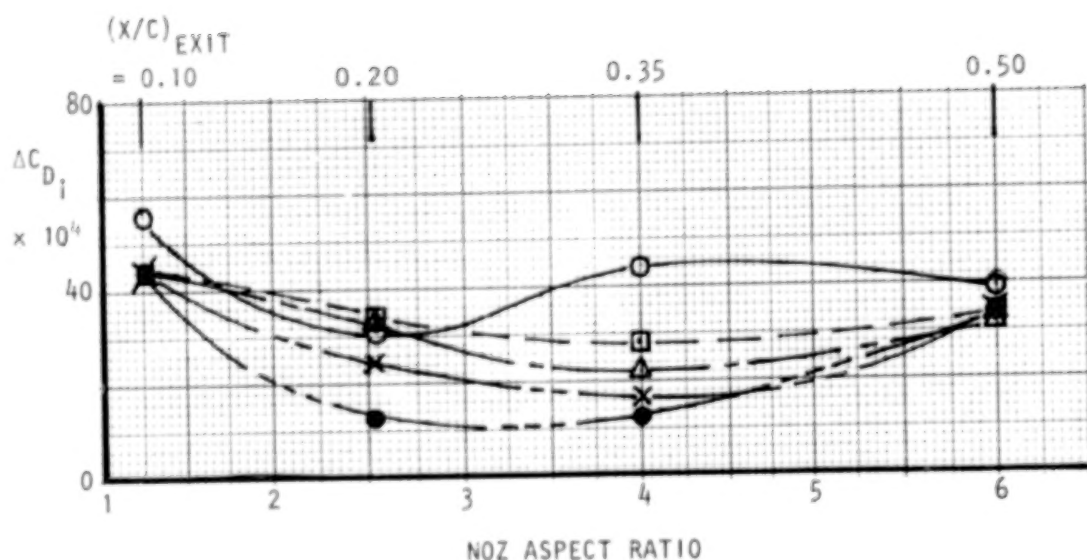


Figure 70. Effect of nozzle exit aspect ratio on lift-dependent drag, $M_\infty = 0.73$

the figure. This is well ahead of the airfoil crest at $x/c \approx 0.40$. Thus, an effective closure, or impingement angle between jet and airfoil crest results; this would generally promote jet-attachment and jet-spreading. At the upper end of the aspect ratio spectrum, jet-attachment is suppressed, due to placement of the nozzle exit aft of the airfoil crest. Therefore, it is believed that the trends shown in Figure 70 is the result of several counteracting effects. Jet-attachment is inhibited by the thick circular jet on the one hand, and is promoted by the airfoil exit position on the other. Under this rationale, it would be expected that both scrubbing drag and jet-deflection angles would show corresponding trends with a nozzle aspect ratio. Such agreement is demonstrated in the paragraphs which follow.

- Scrubbing Drag - Under the assumption that the statically-derived thrust efficiency ratio, η_T , is maintained at wind-on conditions, the variation of the scrubbing drag penalty due to nozzle aspect ratio would be as shown in Figures 71 and 72. Figure 71 prepared for the several straight wing series of nozzles, shows a constantly increasing drag penalty with nozzle aspect ratio for all nozzle pressure ratios. Comparing the two graphs at $AR = 2.5$ ("D-duct" design), the high-boattail angle series of nozzles show a substantially higher scrubbing drag penalty than do the low- β series. These trends would be expected, and have been demonstrated in low-speed, high-lift applications of the USB concept. Scrubbing drag penalties for the small, swept-wing nozzles are shown in Figure 72. Trends very similar to those noted for the straight-wing nozzles are evident although the nozzle exit position was varied simultaneously with nozzle aspect ratio for the swept-wing installations; exit positions are shown on the figure.

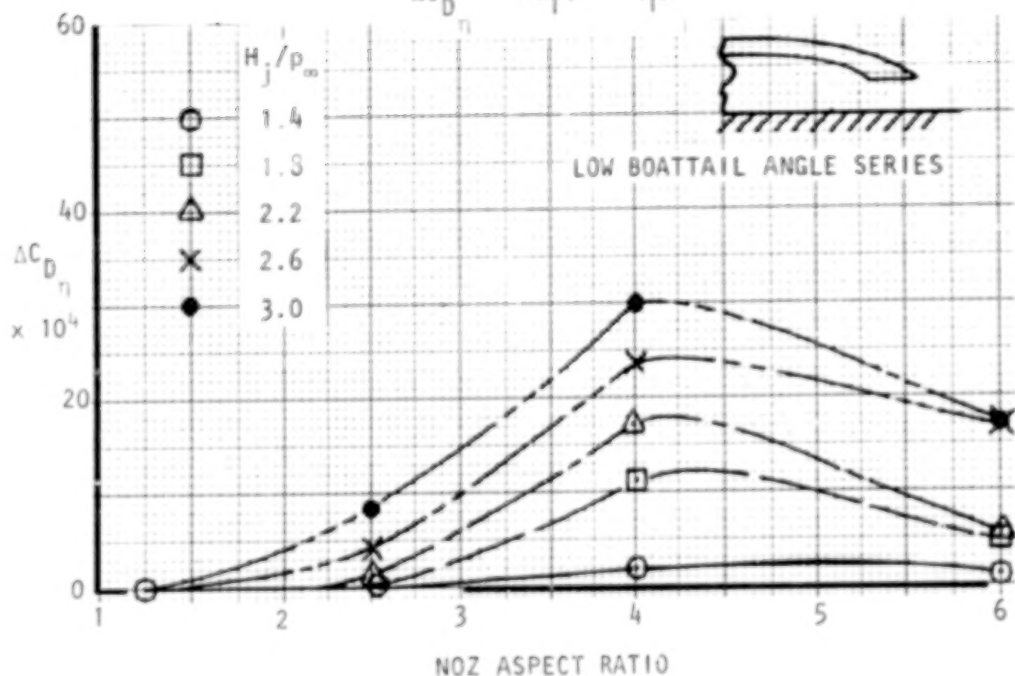
- Trailing-Edge Jet-Angle - As a measure of the jet-induced pressure drag penalties as affected by nozzle aspect ratio, the foregoing drag build-up results have been utilized. Under the assumption that the major difference between the built-up drag increments and those measured primarily reflect inaccuracies in the assumed δ_j -values, such differences can be used to recalculate δ_j . Typical results for straight wing nozzles are shown in Figure 73. As noted for all pressure ratios except $H_j/p_\infty = 3.0$, a consistent trend is developed as nozzle aspect ratio is increased. The wing upper-surface, trailing-edge angle of 16 degrees is rapidly approached by aspect ratio 4, and

USB CRUISE PROGRAM

STRAIGHT WING

$$C^2/A_N = 24 \quad (x/c)_{\text{EXIT}} = 0.35$$

$$\Delta C_{D_{\eta}} = \Delta C_T (1 - n_T)$$



HIGH BOATTAIL SERIES

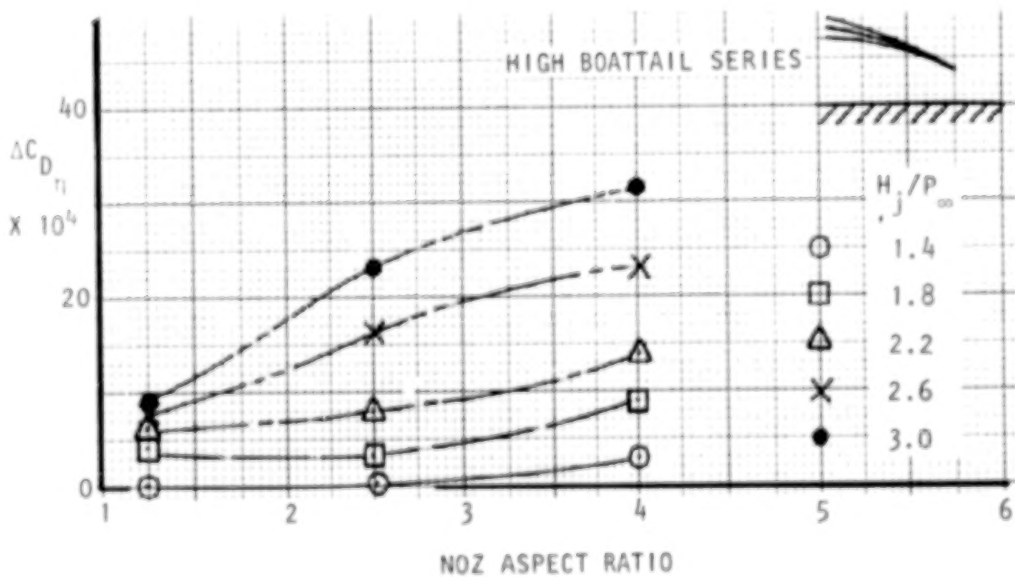


Figure 71. Effect of nozzle exit aspect ratio on scrubbing drag, $M_{\infty} = 0.68$

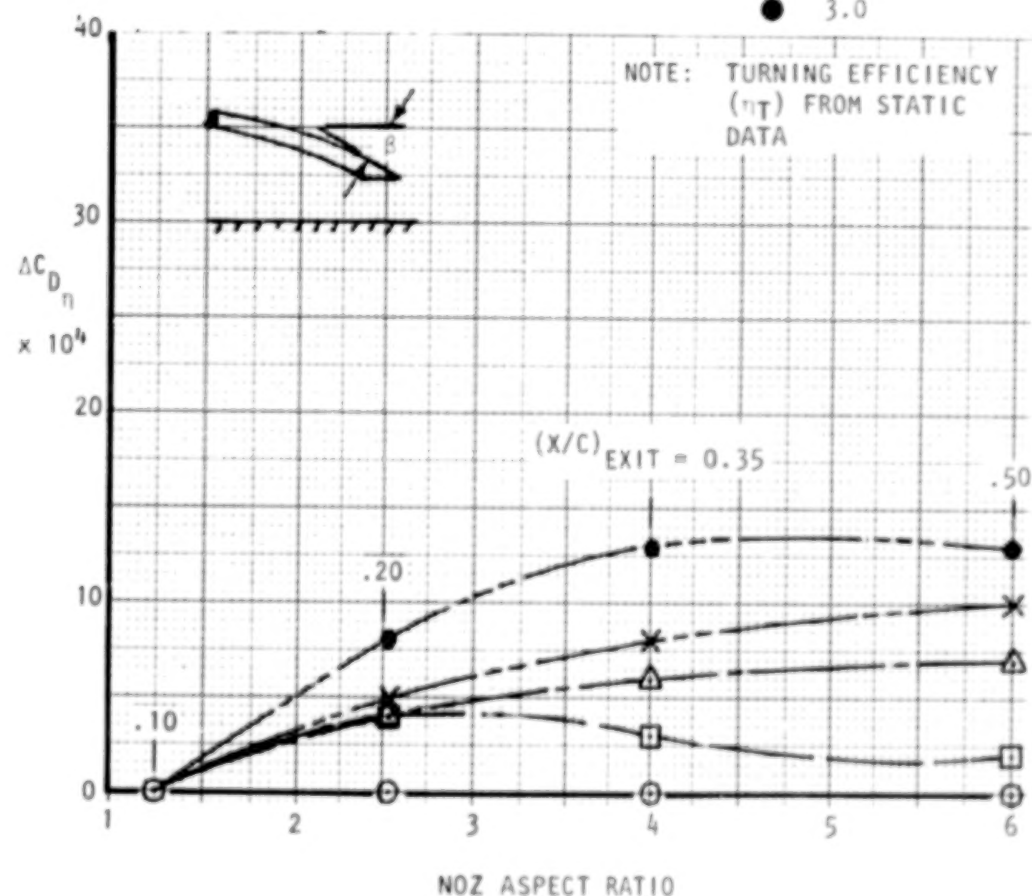
USB CRUISE PROGRAM

SWEPT WING

$C^2/A_N = 48$

H_J/P_∞

- 1.4
- 1.8
- △ 2.2
- × 2.6
- 3.0

Figure 72. Effect of nozzle exit aspect ratio on scrubbing drag, $M_\infty = 0.73$

USB CRUISE PROGRAM
STRAIGHT WING

$$c^2/A_N = 24 \quad (x/c)_{\text{EXIT}} = 0.35$$

	H_j/P_∞	C_T (APPROX)
○	1.4	0.03
□	1.8	0.054
△	2.2	0.078
×	2.6	0.102
●	3.0	0.120

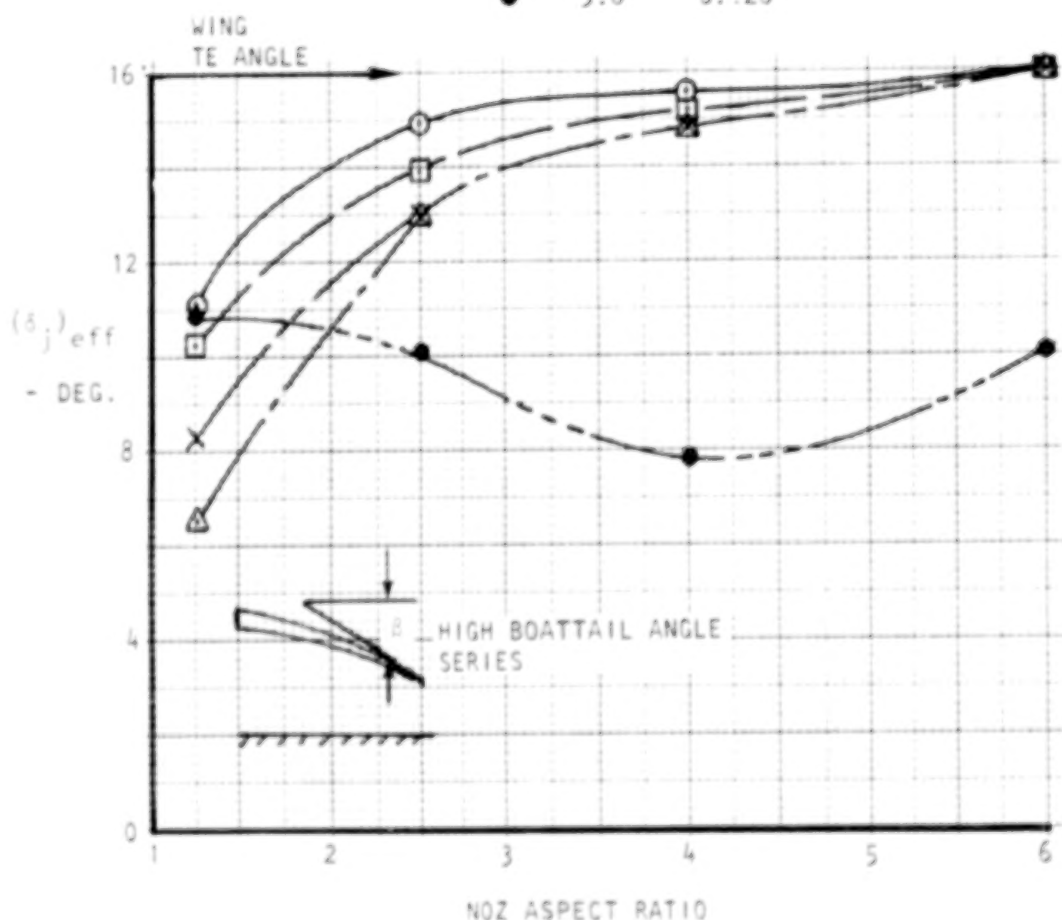


Figure 73. Effect of nozzle exit aspect ratio on "effective" jet angle, $M_\infty = 0.68$, $\alpha = 3^\circ$

higher, nozzle shapes. At the highest nozzle pressure ratio of $H_j/p_\infty = 3.0$, the jet-angle does not appear to be a strong function of nozzle aspect ratio. A similar set of data, constructed for the swept-wing nozzles, is shown in Figure 74. The obvious difference in trends with those of the straight wing are believed to stem from the aforementioned variation in nozzle exit position employed with the swept-wing installations. The trade-off between jet-thickness and exit chordwise position is such as to produce smaller variations in effective jet angle across the nozzle aspect ratio range.

- Lift - The effects of nozzle aspect ratio on lift-due-to-blowing are shown in the top-half of Figure 75. Two sets of data, representing "short" and "long" nacelle forebodies on medium-sized, straight wing nozzles, are plotted at cruise- α and the two extremes of nozzle pressure ratio ($H_j/p_\infty = 1.4$ and 3.0). The lift increments are derived from

$$\Delta C_L = [C_{L_{TOT}}]_{H_j/p} - [C_L]_{W/B} \quad (18)$$

The trends in lift increment with nozzle aspect ratio reflect the anticipated increase in lift as the nozzle becomes more two-dimensional, and influenced a greater span of wing. The short forebody configurations, designed with comparatively high boattail angles, provide a higher lift due to impingement induced spreading and jet-attachment. It is also of interest to note that at the flow-through pressure ratio ($H_j/p_\infty \approx 1.4$) the shape of the nozzle little influence on the lift increment (or decrement) due to nacelle installation.

o Effect of Nacelle Forebody Length - As implied by the data of Figure 75, the length of the faired-over forebody appears to have had some effect on the lift performance of the tested configurations. Forebody length was varied in the test program primarily in the interest of maintaining low nozzle boattail angles. Lift increments associated with both "long" and "short" faired forebody installations are compared in the previously presented Figure 75. The low-boattail-angle configurations (i.e. "long" forebody) show a consistent loss in lift when compared to the "short" forebody configurations in this

USB CRUISE PROGRAM

SWEPT WING

$$c^2/A_N = 48$$

$$H_J/P_\infty$$

- ◻ 1.8
- △ 2.2
- ✗ 2.6
- 3.0

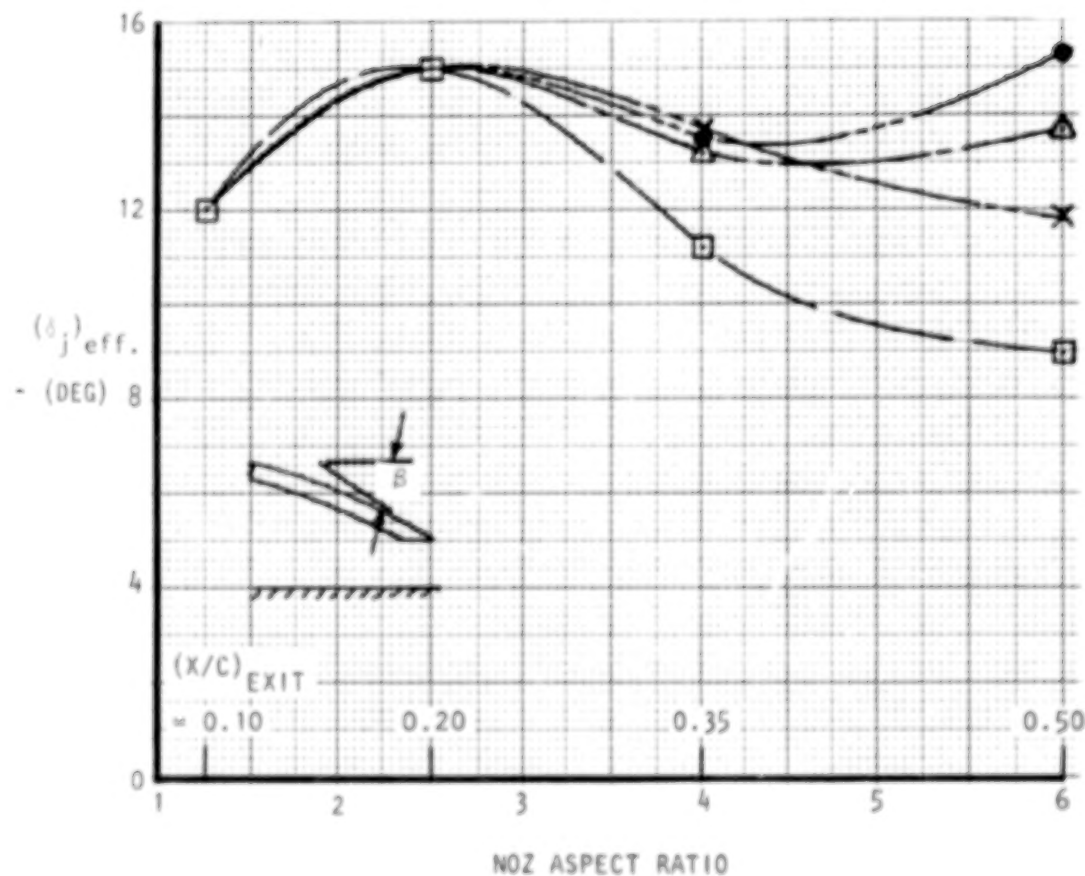


Figure 74. Effect of nozzle exit aspect ratio on "effective" jet angle, $M_\infty = 0.73$, $\alpha = 3^\circ$

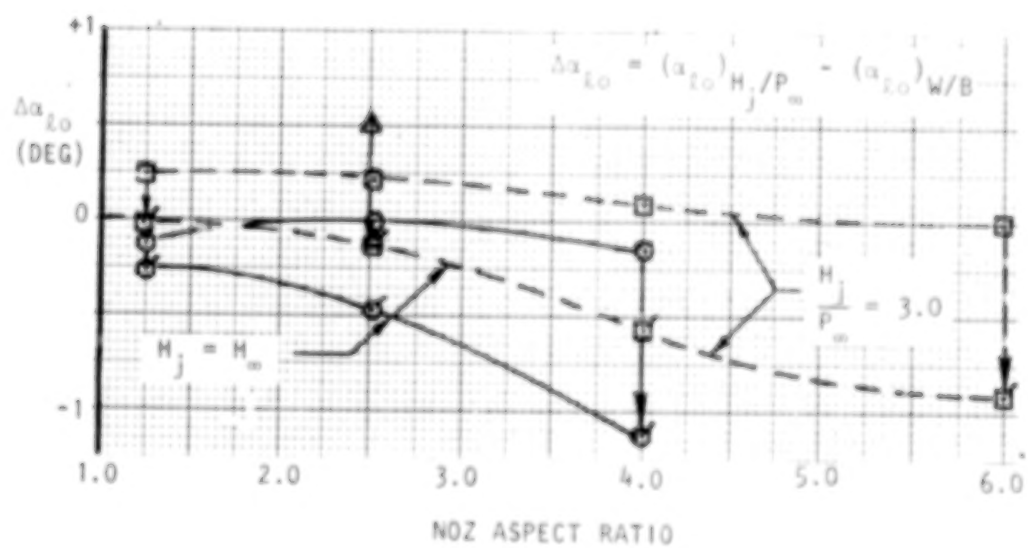
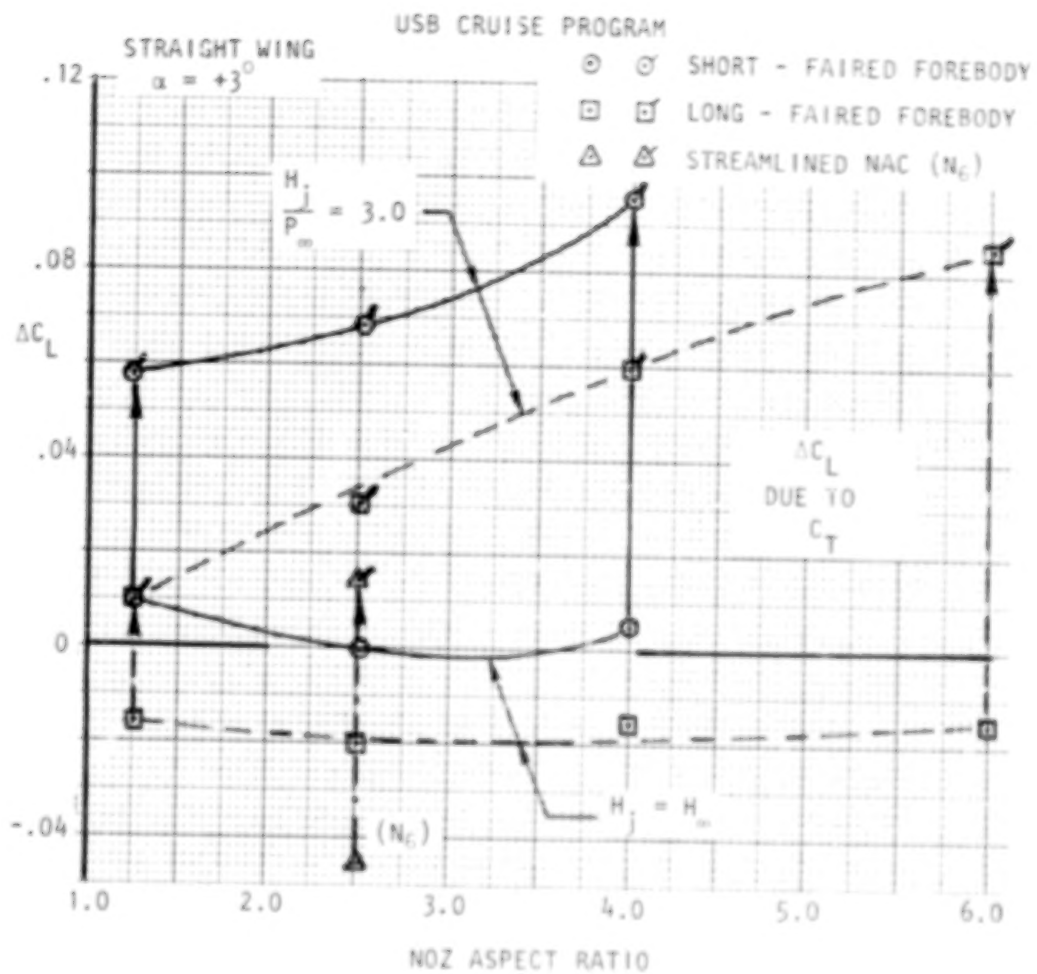


Figure 75. Effect of nacelle installation and blowing on lift, $M_\infty = 0.68$

figure; this effect is apparent at both the flow-through as well as the maximum nozzle pressure ratio. Only minor differences are noted in the lift increment generated by blowing. This difference in lift performance apparently stems from a greater uncambering effect produced by installation of the "long" forebody on the top-surface of the wing leading-edge. As noted in the bottom plot of Figure 75, the shift in the angle-of-zero-lift due to long forebody installation is consistently more positive than that associated with the "short" forebody designs. In correspondence with the aforementioned lift increments, this difference in α_{f0} is maintained even at the high blowing rate. It would appear, therefore, that while the differences in lift performance is relatively small, the manner in which blowing air is supplied to the nozzle (i.e. fan simulators vs faired forebody) can have some impact on overall performance.

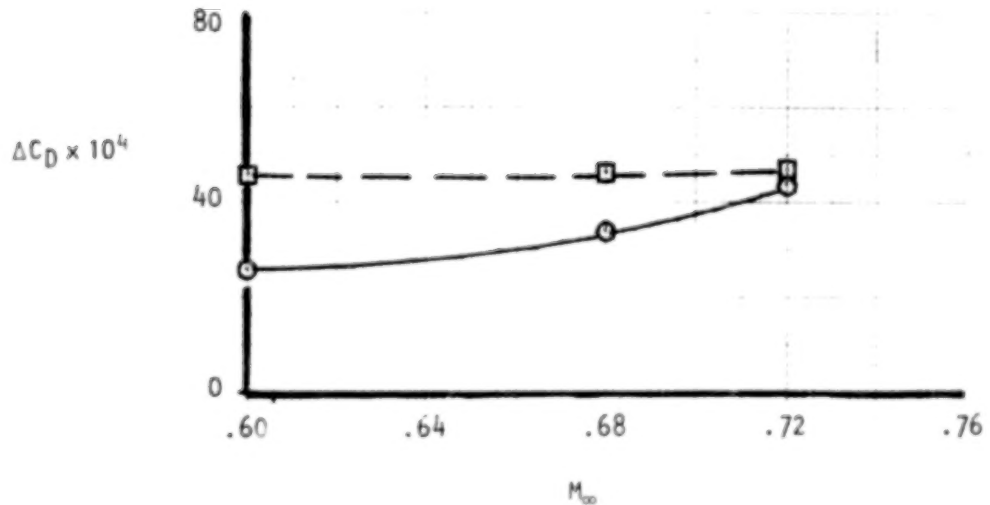
o Effect of Nacelle Streamlining - A small "D-duct" nozzle configuration (N_6) was analytically designed and tested on the straight wing in an attempt to quantify the merits of streamlining. The major difference between the streamline and symmetrical nacelles was a lowering and shaping of the forebody for alignment with the incoming streamlines. While streamlining the plan-view was also performed, the geometric differences from that of the symmetrical nacelles was very slight due to the unswept (straight) wing planform. A direct drag comparison of the streamlined nacelle versus the symmetrical nacelle is not available in the test data inasmuch as the straight wing nozzles were generally a larger size ($C^2/A_N = 24$ vs. $C^2/A_N = 48$ (N_6)); the smaller nacelle sizes were normally tested on the swept-wing configuration. However, in an attempt to provide such a comparison, Figure 76 shows the drag of the streamlined configuration compared to that of a symmetrical nacelle of the same size, but with the latter tested on the swept-wing. On this basis, the effects of sweep or relative adequacy of the wing-nacelle fillets may play a role in the comparison. As indicated in the figure, beneficial drag effects of streamlining are noted in the lower Mach-range and at the flow-through pressure ratio of $H_j/p_\infty = 1.4$. This difference is due primarily to the lower drag-due-to-lift penalty of the streamlined configuration which, of course, was a major design objective. At the higher pressure ratio and at cruise Mach numbers, the streamlined nacelle, which was designed with an almost non-existent boattail angle, shows only small drag benefits due generally to a

USB CRUISE PROGRAM

○ STREAMLINED (N_6) - STRAIGHT WING

□ SYMM (N_8^2) - SWEPT WING

$$c^2/A_N = 48 \quad H_j/p_\infty = 1.4$$



$$H_j/p_\infty = 2.2$$

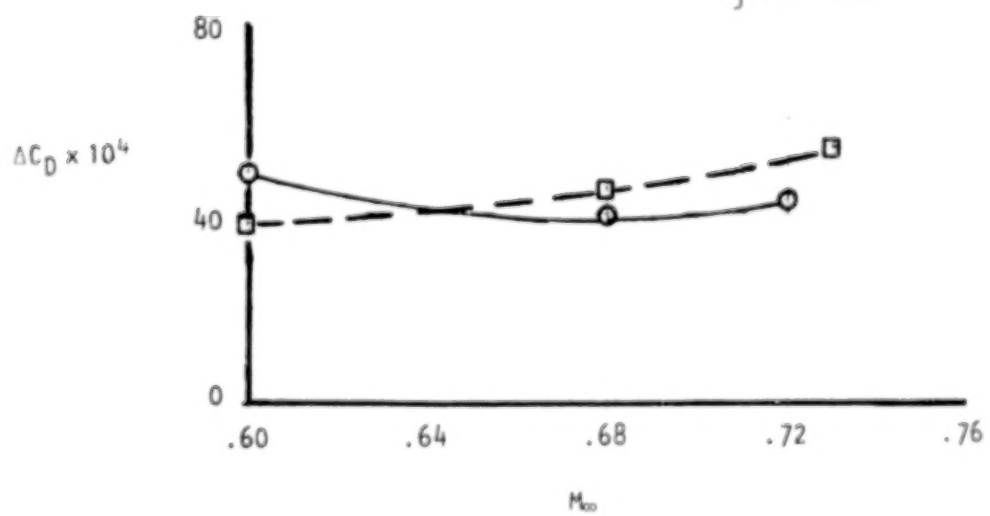


Figure 76. Comparison of streamlined and symmetrical nacelle drag,
 $C_{LM} = 0.40$.

slightly lower pressure drag increment. The lift increment due to the streamlined nacelle installation on the straight wing is included in the data of Figure 75. Since the streamlined nacelle is specifically designed to carry very little forebody loading, the lift penalty upon installation on the basic wing is the highest for any of the nacelles tested. The fact that this lift difference is due to a local uncambering effect on the wing is illustrated in the lower half of Figure 75. In this plot, the streamlined (N_6) nacelle data points show the largest positive change in angle-for-zero-lift of all nozzles tested. Since it is believed that the benefits of nacelle streamlining would become more pronounced as wing sweep increases, the present comparisons, based on straight wing results, should not be generalized. However, considering the present results for a single configuration, the rationale utilized for design of an effective streamlined nacelle merits some re-examination.

o Effect of Nacelle Boattail Angle - The angle between the nacelle upper-surface centerline at the exit and the wing chord plane, as used herein, is the boattail angle, β . Across the range of exit shapes tested, this angle varied from about 6° to a maximum of about 36° . In general, the lower angles represented circular nozzle designs with the higher angles required by the wider, high aspect ratio nacelles. For a given nozzle aspect ratio, this angle was also varied by changing the nacelle forebody length. In an attempt to define a limiting angle from a cruise standpoint, the data of Figure 77 has been prepared. Test results are shown in a drag ratio-form with the denominator representing a circular nozzle with $\beta = 6^\circ$. Below $\beta = 25^\circ$ the trends are not completely uniform due, it is believed, to variations in the effectiveness of the wing/nacelle filleting provided. Above 25° , however, the sharp increase in drag suggests that about 25° represents a maximum design value of β if severe boattail separation effects are to be avoided. It is also noted that as C_T increases, the drag ratio diminishes in value as the jet tends to suppress some of the boattail separation through a pumping effect.

o Effects of Forebody Fairing - The drag increment associated with an open or flow-through, type of forebody is compared in Figure 78 to that associated with a faired-over forebody with the latter operating at a flow-through nozzle pressure ratio. The nozzle in both cases is a circular configuration of intermediate size ($C^2/A_N = 24$). This study was made to de-

USB CRUISE PROGRAM

C_T

○ .04

$$M_{\odot} = 0.68$$

~~X~~ .06

$$C_{LM} = 0.40$$

.08

$x/\epsilon = 0.35$ EXIT

△ .10

$$c^2/A_N = 24$$

12

STRAIGHT WING

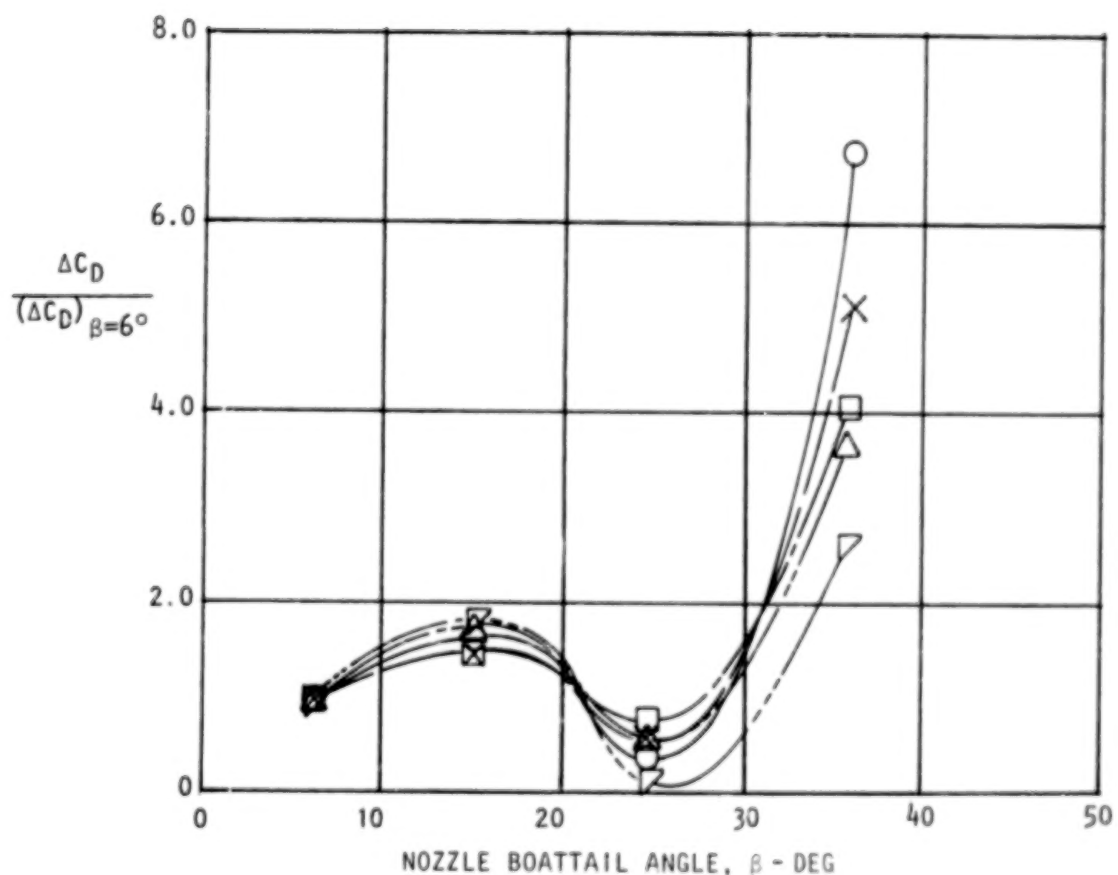


Figure 77. Effect of nacelle boattail angle on nacelle drag.

USB CRUISE PROGRAM

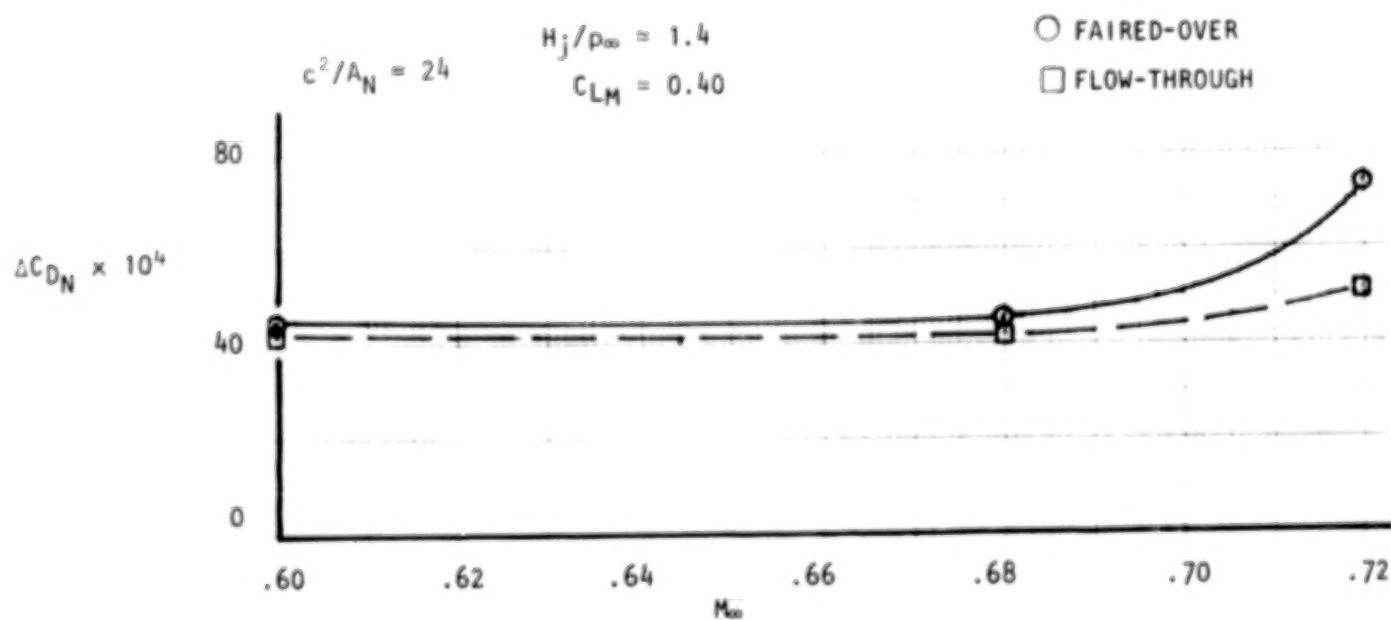


Figure 78. Effect of Mach number on drag for faired-over vs flow-through forebodies, straight wing with circular noz N₂.

termine if any significant drag differences were incurred when utilizing the two types of testing methods. Note also that in this comparison, the internal friction drag of the flow-through nacelle has been subtracted out. The drag difference noted in Figure 78 is only minor at speeds in the subcritical Mach range. Beyond the drag-rise of the straight-wing/nacelle combination ($M = 0.68$), the faired-forebody yields a substantially higher drag penalty possibly as a result of a difference in area-ruling effect on the wing-body combination. It is concluded from this portion of the study that, at least for the lower nozzle pressure ratios and at speeds up to the drag-rise Mach number, no major drag difference results when using the faired-forebody as a simple means of synthesizing powered nacelles.

o Effect of Multiple Nacelles - Figure 79 compares the nacelle drag increment of a 4-engine swept-wing configuration to that of a 2-engine design, both with small "D-duct" nozzles (N_8) at several nozzle pressure ratios. As presented, the friction drag ($\Delta C_{D_{NF}}$) of the nacelles has been removed from the drag increment. Also shown is a drag level derived by taking one-half of the 4-engine increment for comparison to the 2-engine version. At both of the representative pressure ratios, the data show that the drag does not scale proportionally with the number of engines with the 2-engine configuration showing a higher relative interference drag than does the 4-engine case. In the drag-due-to-lift analysis it was found that, while this penalty is larger for the 4-engine version, it is not doubly so. Additionally, the drag build-up showed that, in general, the 4-engine configuration reflects slightly lower turning angles than the 2-engine counterpart thus producing slightly less pressure drag. Further evidence of this difference is shown in Figure 80 where the lift-due-to-blowing is presented for the two cases at $M_\infty = 0.73$. Except at the highest pressure ratio, the total lift of the 4-engine configuration is less than that of the 2-engine with the lift trend of the former showing intermittent attachment of the jet in the lower blowing range. Note also in these data, that the 4-engine case is producing twice as much thrust as its 2-engine counterpart. Although the jets are widely spaced, it is believed that the two jets, operating in proximity to each other with both exits at a constant $x/c = 0.20$, produce a mutual interference which tends to suppress jet attachment. Oil flow photographs are not conclusive in this regard, although they generally show a slightly larger scrubbing footprint behind the single nacelle than

USB CRUISE PROGRAM

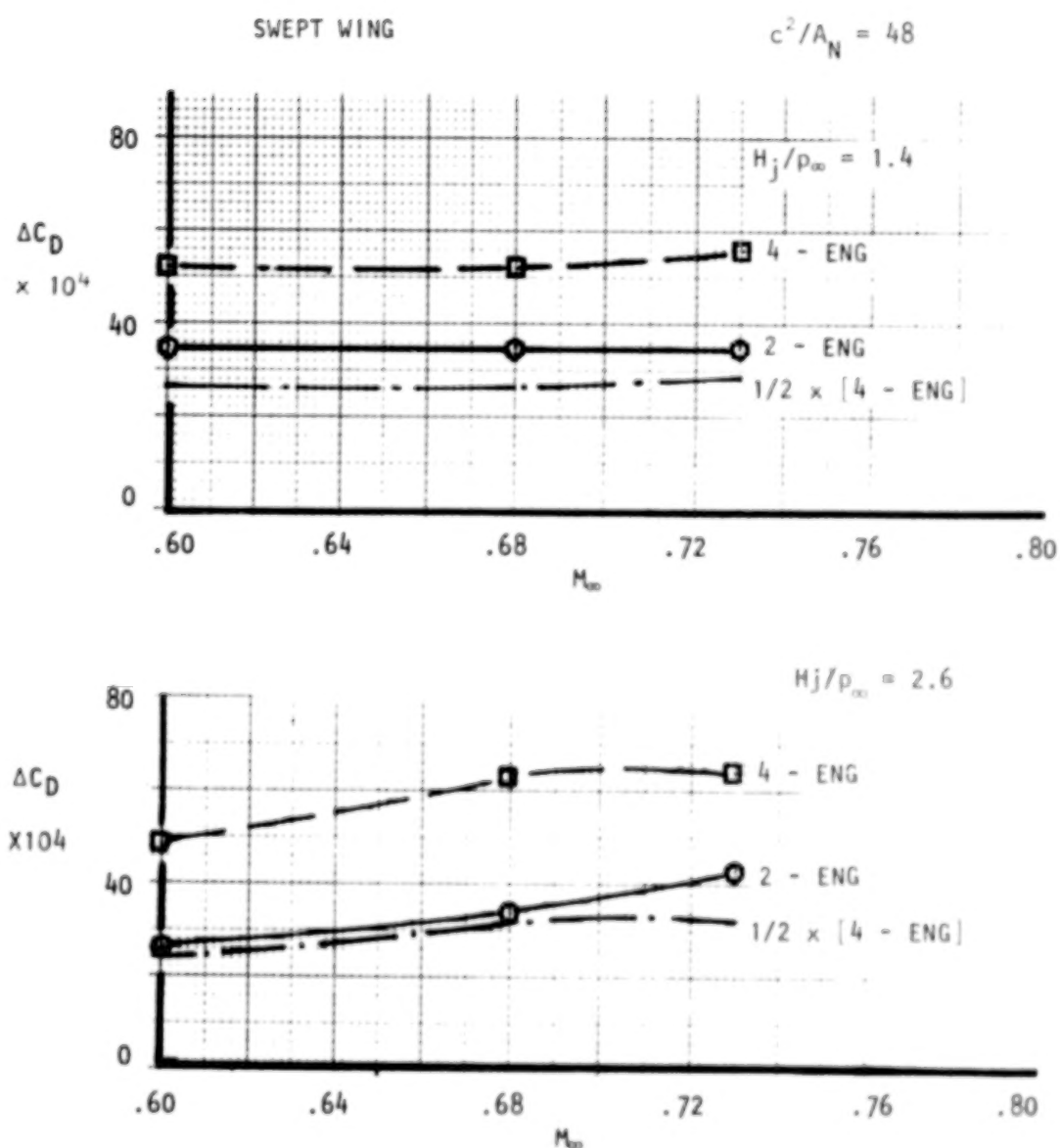


Figure 79. Effect of multiple engine installation on drag $C_{LM} = 0.40$, swept wing.

USB CRUISE PROGRAM

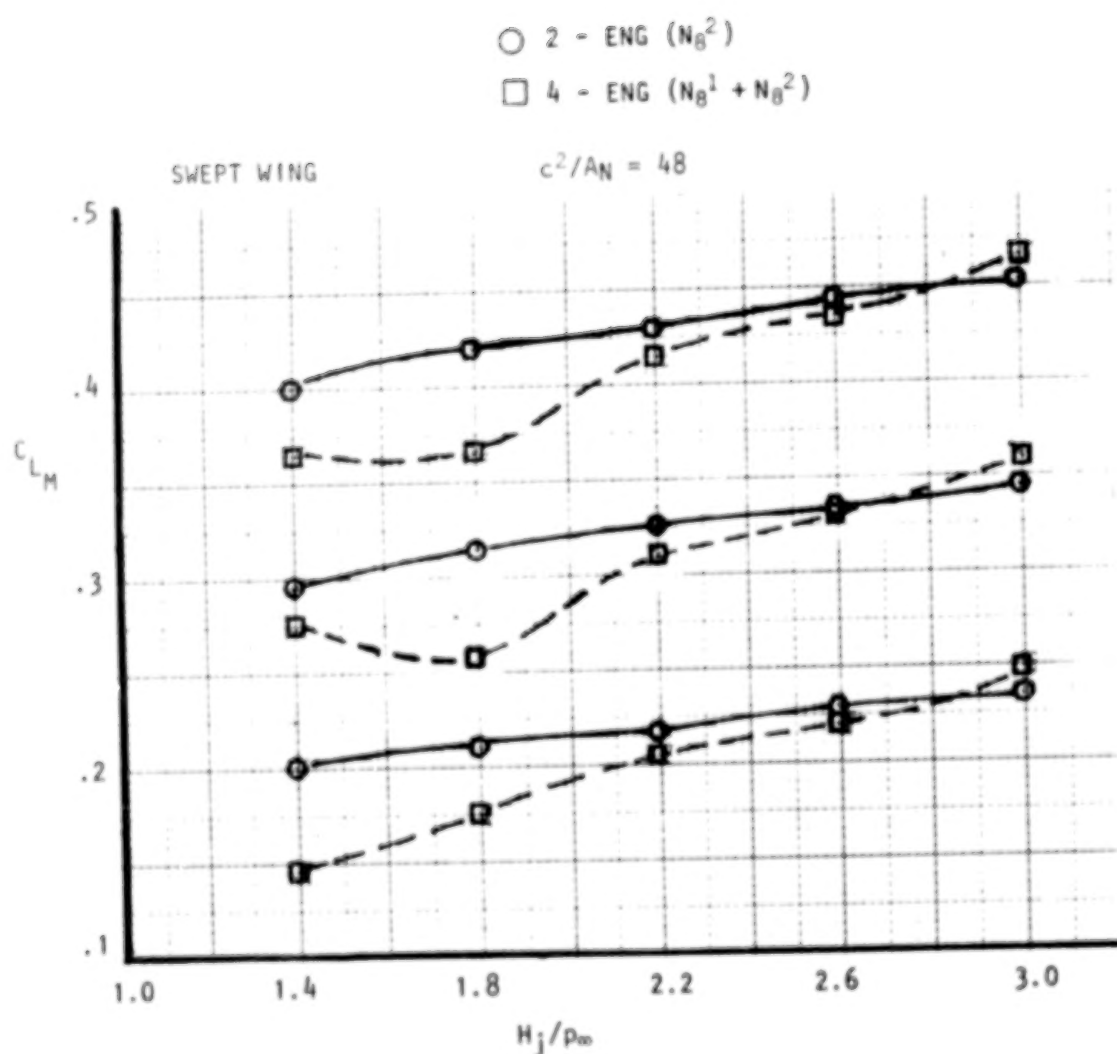


Figure 80.

Comparison of lift-due-to-blowing for 2-eng. and 4-eng. configurations "D-duct" nacelle, $M_\infty = 0.73$.

do the photographs of the twin-nacelle configuration. A conclusion basic to this study is that the interference drag does not necessarily scale in proportion to the number of USB-type engines and that any effective means of suppressing jet attachment will generally be beneficial to cruise performance drag.

o Effect of Nozzle Installation Height - In an effort to quantify drag trends as the nacelle is moved vertically from the wing surface, the circular nacelle was tested as both an integrated (USB) type model and a pylon-mounted (OTW) configuration. Results are shown in Figure 81 across the test speed range; both pylon and nacelle drags are represented in the data. The short- pylon configuration shows a lower drag coefficient than either the integrated (USB) or the long-pylon OTW configuration although the drag difference, in any case, is not large. Since these tests were conducted on the straight wing, camber variations designed into the pylons for minimum load, were slight. Oil-flow studies of the OTW designs indicated that the pylon intersection near the wing inboard leading-edge generated a vortex-type of flow which would obviously be detrimental to the drag of these configurations. While attempts to modify this flow pattern were made through the use of wax fairings it appeared that re-design of the pylon in both camber and, particularly, chordwise length, would be required to affect a major improvement in the flow. At the supercritical Mach number of 0.72, both pylon configurations show a favorable trend in drag reflecting a more moderate drag-rise for the nacelle-on case than for the basic wing-body. The drag differences shown at the lower speeds are due primarily to differences in drag-due-to-lift since scrubbing or jet pressure drag are essentially zero at the flow-through pressure ratio. At more realistic nozzle pressure ratios, these two drag components would need to be offset by a jet-induced improvement to the drag-due-to-lift component if the integrated nacelle is to remain the drag-equivalent of the OTW-design. These factors, together with the analytical and experimental results of References 3 and 4 indicate some merit in additional studies for optimizing the OTW design as a possible cruise configuration of interest.

4.2 Math Model Development

4.2.1 Representation of wing, nacelle and power unit. - The USB wing/nacelle/propulsive interactions are complex not only in their viscous

USB CRUISE PROGRAM

$$c^2/A_N = 24$$

$$C_{LM} = 0.40 \quad H_j/p_\infty = 1.4$$

○ SHORT PYLON (NOZ 0.5 D_N ABOVE WING SURFACE)

□ INTEGRATED (DISCHARGE ON SURFACE)

△ LONG PYLON (NOZ 1.0 D_N ABOVE WING SURFACE)

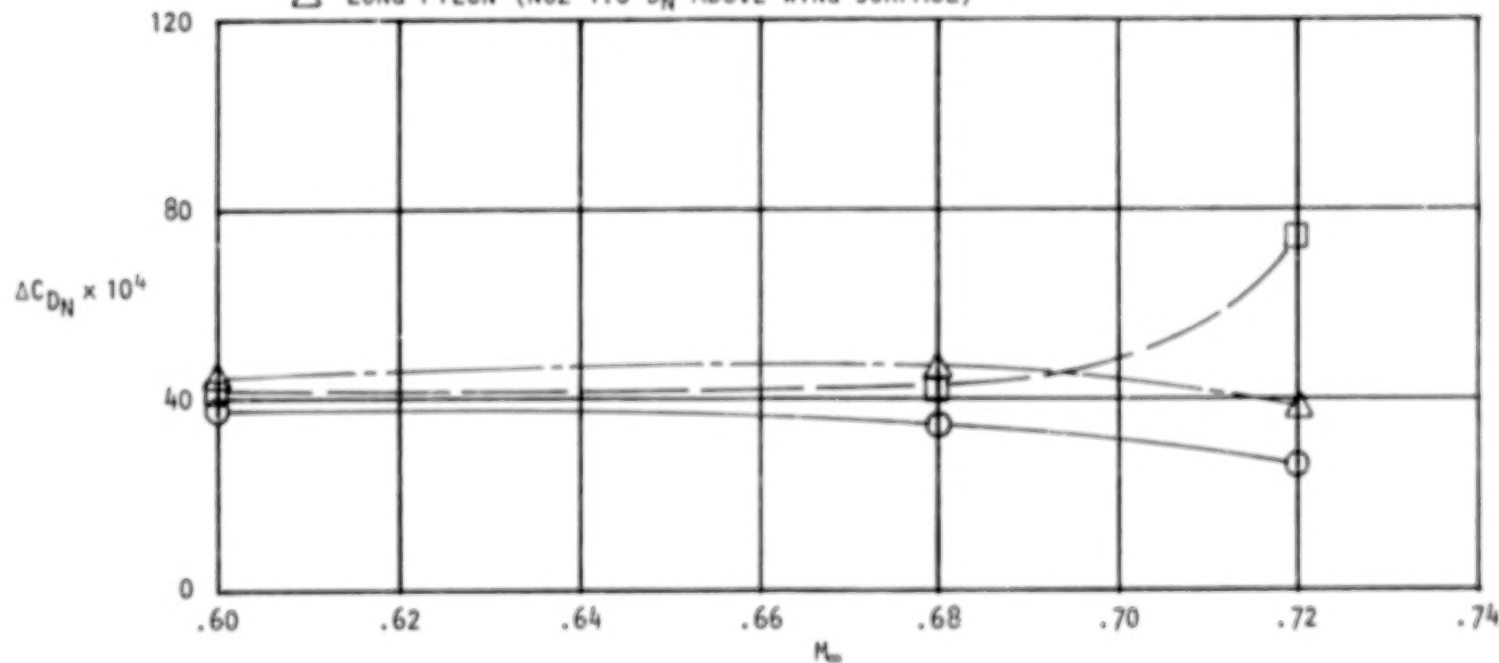


Figure 81. Effect of Mach number on drag for pylon-mounted OTW vs. integrated USB nacelles, straight wing with circular nozzle N₂.

aspects, but also regarding the potential flows involved. Theoretical studies have, therefore, been aimed at improving and understanding of the potential flows with minimal explicit representation of viscous effects. The latter thus appear as residual differences between the computed and experimental results.

The theoretical model employs vortex lattice techniques. The eventual panel layout used, typified by figure 82, represents the culmination of a series of method studies including sectional and finite-wing correlations, and several stages of nacelle paneling development.

In setting up the power-effects model, several established techniques had to be rejected. The 'hard-surface jet' approach is frequently used both experimentally and theoretically, but it is clearly inappropriate here because it fails to represent the jet properly in the scrubbed region aft of the nacelle exit. Discrete vortex rings centered on the jet axis have been used for Externally-Blown Systems (EBS) and other studies. Though these can represent the flow quite well when the jet exhausts into a relatively free environment, the ring singularities are incompatible with the lattice system in the present theoretical model. Accordingly, algorithms have been developed in which these rings are replaced by equivalent ring-vorticity sheets. These are wrapped around the jet axis in the form of an expanding tube and are graded in strength so as to approximate free-air spreading and entrainment effects while conserving axial momentum. Calculations for a quasi-axisymmetric model produced the streamline patterns shown in Figure 83.

Since no attempt is made to solve the free-jet surface problem in the present model, the choice of jet geometry is obviously very important. Early in the program, critical decisions were made concerning jet centerline direction and impingement effects. The jet mean line was inclined downward at half the boattail angle causing the jet tube to intersect the wing surface and expose it to jet supersonic velocities. The cross-sectional shape was flattened progressively towards the wing trailing edge (see Figure 84) in accordance with flow visualization and other observations of the impingement and spreading processes.

USB CRUISE PROGRAM

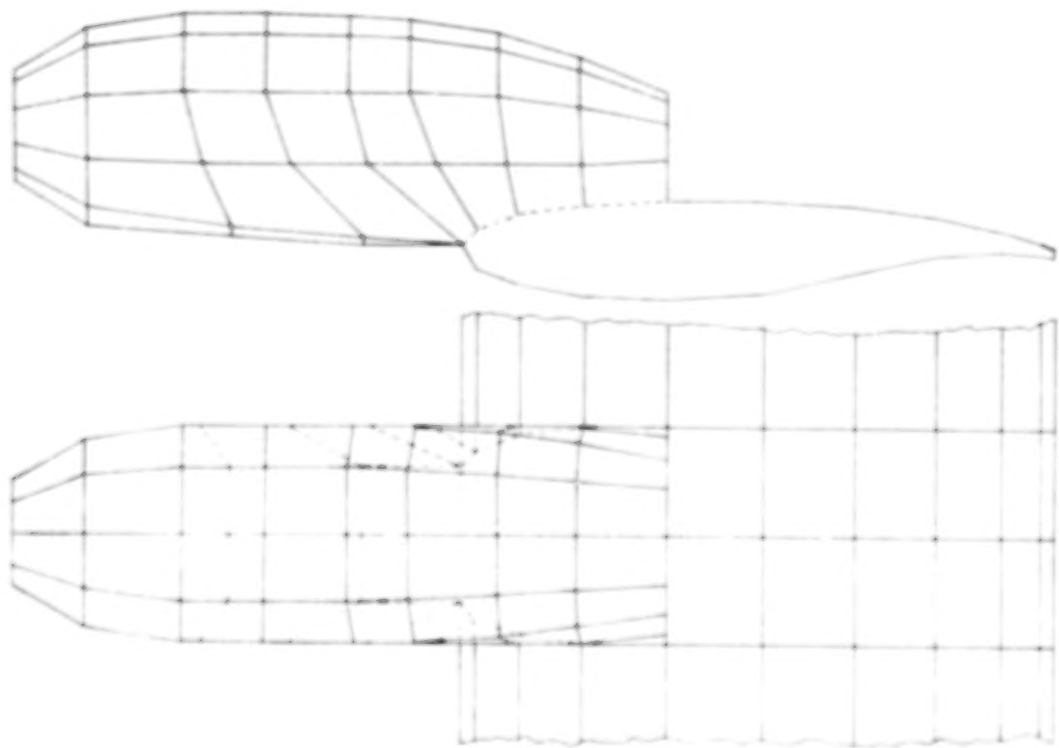


Figure 82. Panel details for D-duct nacelle and adjacent wing.

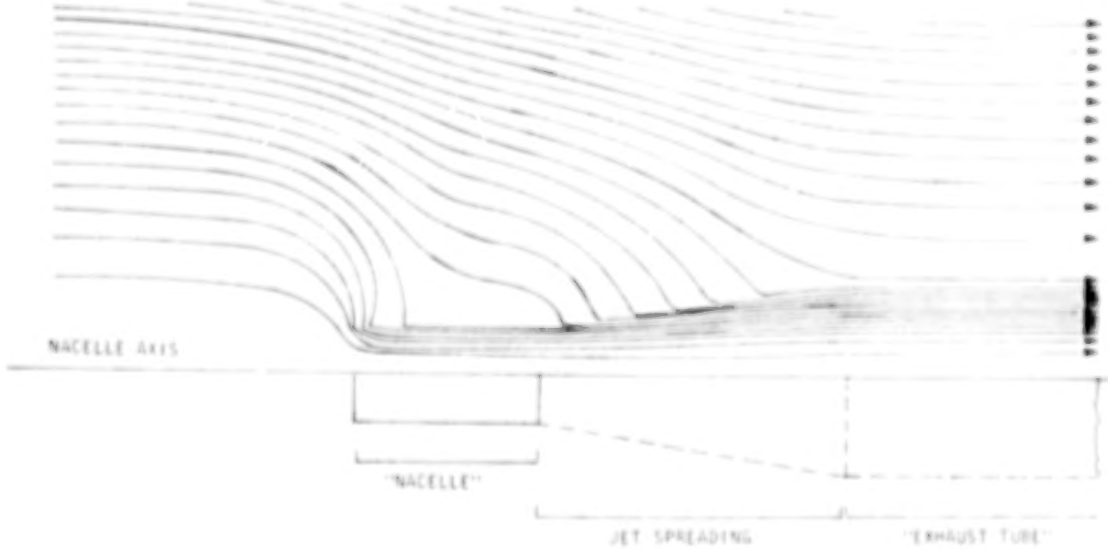


Figure 83. Representation of jet spreading and entrainment by vortex-ring polygons.

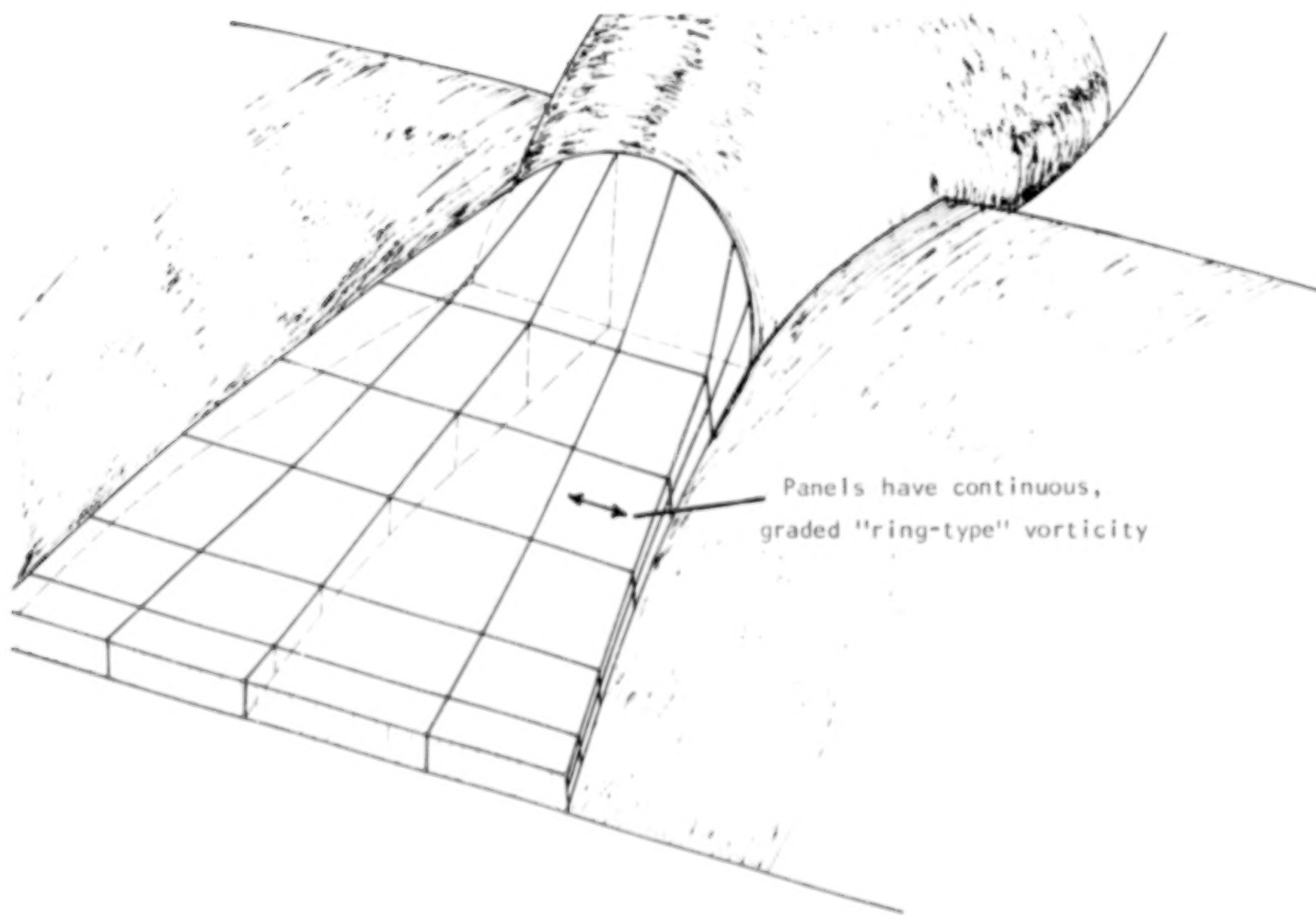


Figure 84. Mathematical model of the USB jet efflux.

4.2.2 Surface pressure. - Figure 85 shows the calculated pressure distribution on the wing and on the nacelle spine for several pressure ratios. Pressures on the nacelle itself are relatively insensitive to nozzle pressure ratio. After stagnating on the upper and lower lip centerlines, the flow accelerates over the nacelle forebody towards the barrel section. Due to angle-of-attack and wing-induced upwash, there is net lift in these regions. On approaching the wing leading edge, the lower surface flow accelerates to some degree, while the upper surface flow accelerates more rapidly over the boattail, giving an exit C_p of approximately -0.8 at the crest of the nozzle.

Even under flow-through conditions ($H_j/p_\infty = 1.25$), there is an upper surface suction peak toward the wing trailing edge. This is a characteristic of the wing section and may be attributed to aft camber. Figure 85 shows that the subsequent addition of power amplifies this peak significantly. It will be seen later that one consequence of this aft camber, in application to USB configurations, is a substantial drag penalty due to jet turning.

Just aft of the nozzle exit the jet is directed towards the wing upper surface and positive impingement pressures occur which increase with H_j/p_∞ . Though these pressures offset jet-turning lift effects substantially, the corresponding thrust effect is small because the wing surface is nearly horizontal in the impingement region.

At flow-through conditions, experience with wing-alone cases suggests that the lower surface pressure predictions in Figure 85 are probably not reasonable. Additionally, the variation with pressure ratio is believed to be spurious. These are most probably coarse-lattice effects.

Figure 86 shows comparisons between the above predictions and pressures measured on the wing surface aft of the nacelle exit, expressed as increments above the clean-wing condition. There is generally good agreement between predicted and measured results and the partial impingement and turning effects are well reproduced by the theory, despite the fact that there is no theoretical counterpart to shock cell effects which are evident at the highest pressure ratio.

BLANK

PAGE

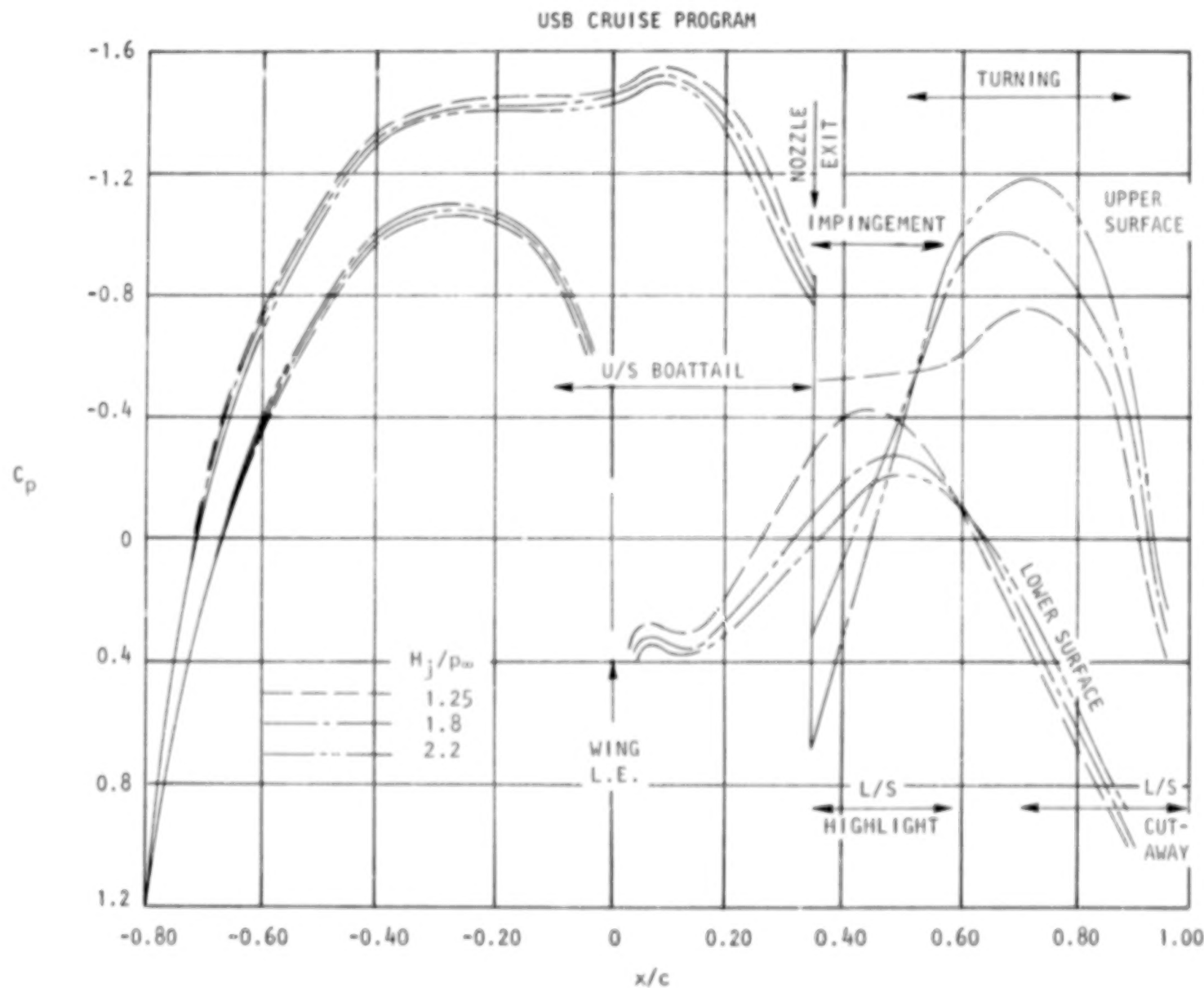


Figure 85. Predicted nacelle-spline and wing surface pressure distributions as a function of jet pressure ratio, $\alpha = 2^\circ$, $M_\infty = 0.60$.

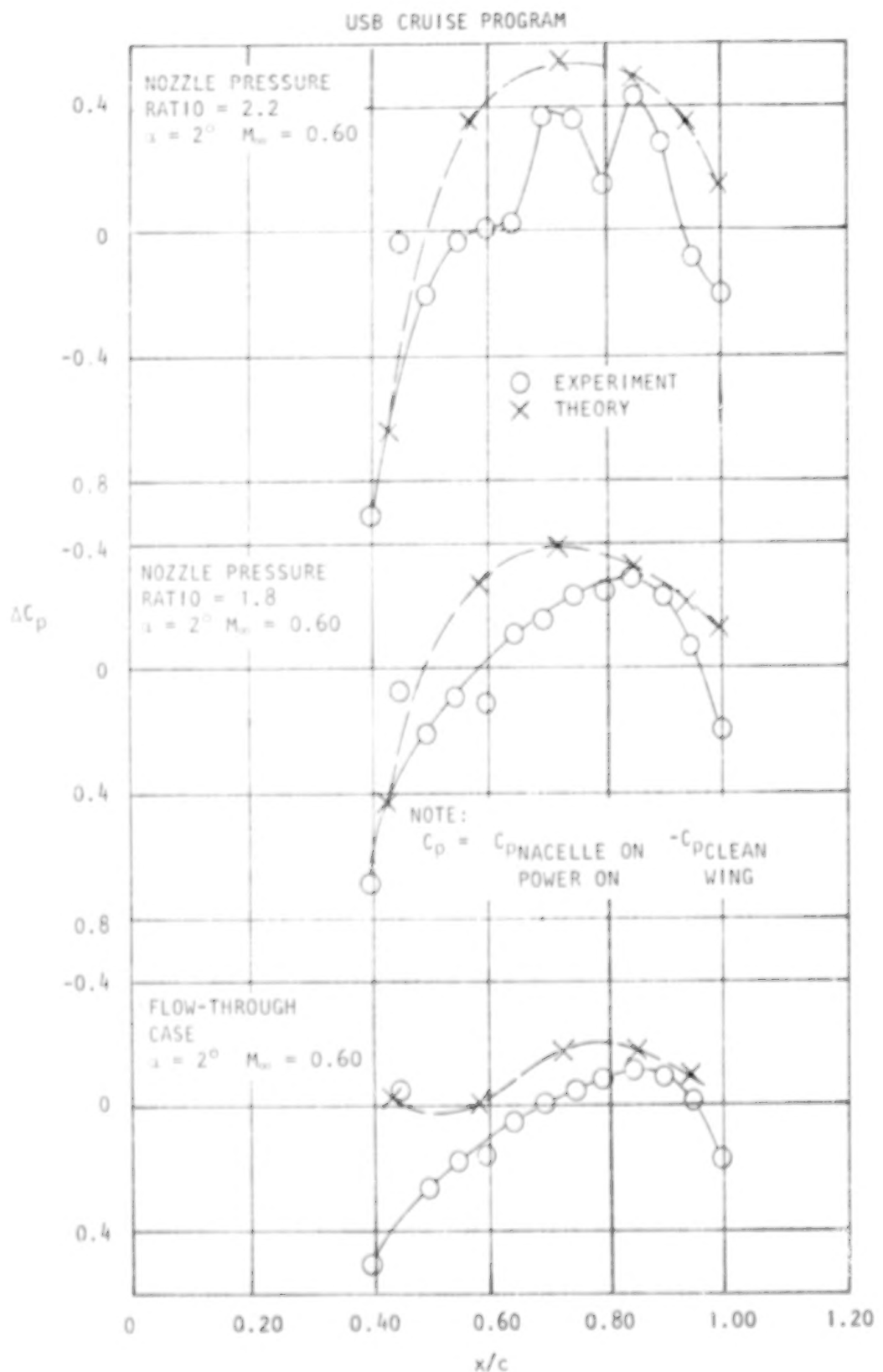


Figure 86. Predicted and measured surface pressure increments aft of nacelle (Row A).

Other comparisons included chordwise rows on each side of the nacelle and on the spine of the boattail. The former showed that the spreading angle of the theoretical model was a bit too large. In order to correlate in the boattail region, it was necessary to distinguish between internal and external pressures. This was accomplished by calculating velocity, and thence pressure, on the nacelle centerline and regarding this as a one-dimensional internal pressure. Corrected in this way, predicted external pressures correlated quite well with measurements.

4.2.3. Lift. - Lift increments arose as small differences between positive lift in the boattail and jet-turning regions, and download due to impingement just aft of the nacelle exit together with its lateral carry-over. Because the latter effect was over-predicted by the vortex lattice model, lift increments failed to increase with power setting (H_j/p_∞) in the manner shown by balance measurements. However, angle-of-attack effects were properly reproduced by the vortex lattice theory.

Application of simplified jet flap theory (see CR-159136) reproduced the effect of power on lift correctly, but the corresponding drag predictions were largely unsuccessful. Figure 87 shows that total lift predictions, based upon jet flap theory modified for finite-span and compressibility effects, agreed quite well with measured lift even for conditions well beyond critical jet pressure ratio. Equally good correlations were obtained for other nozzles ranging from circular to aspect ratio six rectangular shapes.

4.2.4 Drag prediction methods. - In consonance with the experimental program, drag estimation was emphasized strongly. As might be anticipated for such a complex flow as the present one, some quite formidable difficulties had to be overcome. Among these were (a) the correction from the true flow-through nacelle theory to that of the experimental, closed-nose configuration, (b) the fact that net drag invariably occurred as the difference between large thrust and drag forces, and (c) the failure of conventional vortex lattice methods to predict drag reliably in powered regions.

The initial approach to the closed-nose problem was to locate a source just inside the intake so sized and positioned as to pass a closing stream

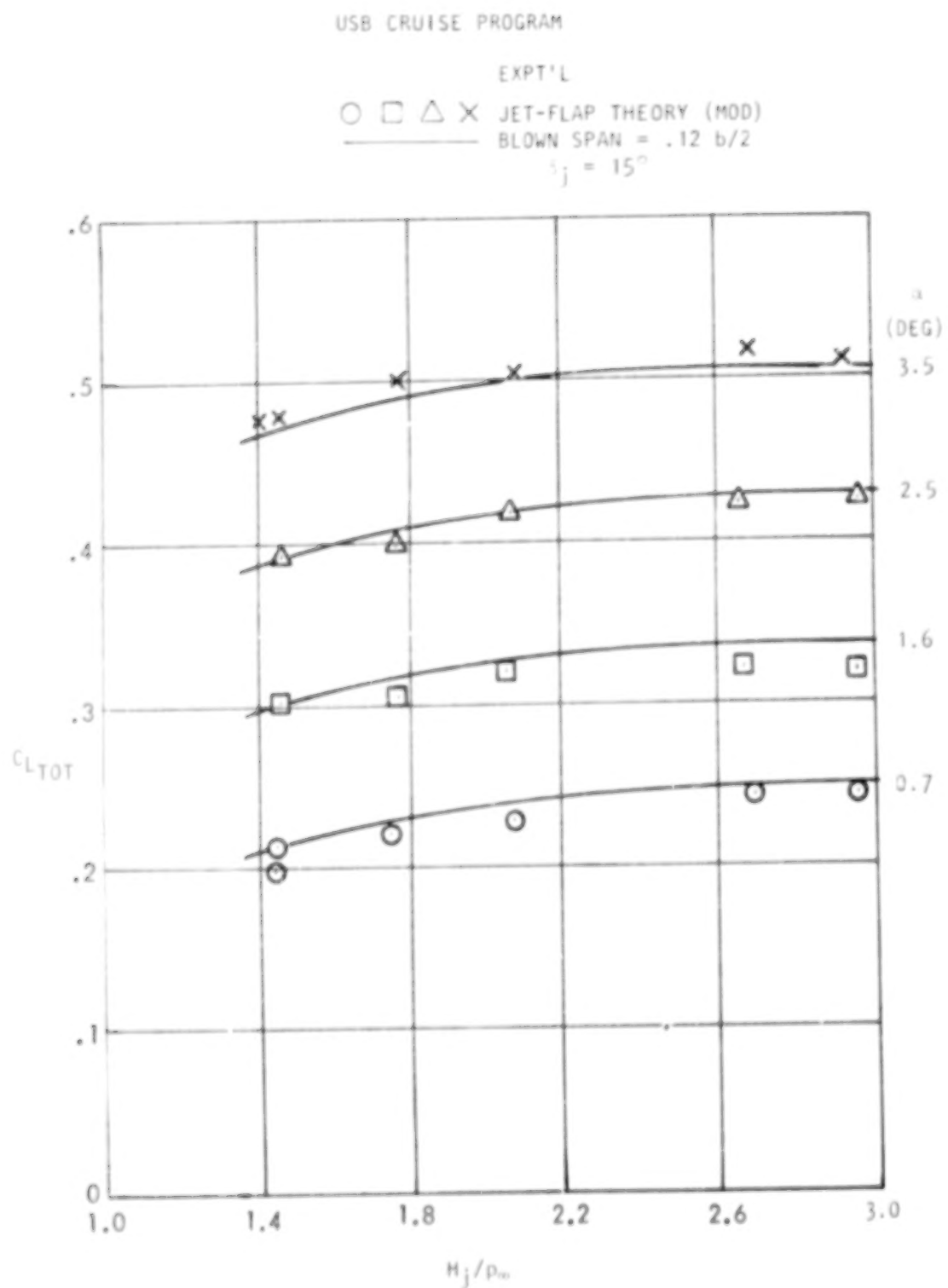


Figure 87. Comparison of USB test results with modified jet-flap theory, noz N₃E, AR = 2.5, $M_\infty = 0.68$.

surface tangentially through the first ring of collocation points. Forces on this surface were obtained explicitly. Both this approach and a subsequent momentum integration across the intake were unsuccessful. It was found that these failures were caused by "leakage" out of the nacelle in the first two bays. The final approach relied upon the fact that a long forebody - as generated by an axial row of sources, for example - has zero pressure drag in potential flow. Drag contributions forward of the barrel section were therefore discarded.

Figures 88 and 89 illustrate the second problem: differences between large numbers. With the nacelle at approximately zero lift, as shown by the broken line, (Figure 88), the net drag on it was very small. However, it was evident that this, almost-zero result occurred as the net of thrust and drag forces in excess of a hundred counts, on just the nacelle. Figure 89 shows a similar situation concerning the spanwise distribution of drag. Trailing vortices from the nacelle boattail produce downwash - and hence wing drag - between them and upwash (and thrust) to each side. Again, the desired result is the difference between large numbers. In flow-through cases, careful attention to detail in using standard vortex lattice procedures produced the desired results. Powered cases proved more difficult and are discussed in the following paragraph.

It was found that a straight forward extension of the previous, conventional vortex lattice methods to drag prediction simply did not work in powered cases. This was not unexpected, since it had already been determined in pressure distribution studies that it was necessary to replace the standard " ρV_i " approach by a "spread Γ " method in order to produce acceptable results. One reason for this was that the lattice surface aft of the nacelle exit was fully immersed in the jet efflux and was therefore subjected to unrepresentative velocities over the bound vortices. Various approaches were tried using surface velocities typical of the sheet edge, which corresponds to the real flow condition, but without success. The previous "spread Γ " C_p 's were, therefore, used to determine power-dependent drag increments. Because of the numerical problem mentioned above, it was necessary to plot ΔC_p due to power against y/c and integrate graphically, taking special care to be consistent when draw-

USB CRUISE PROGRAM

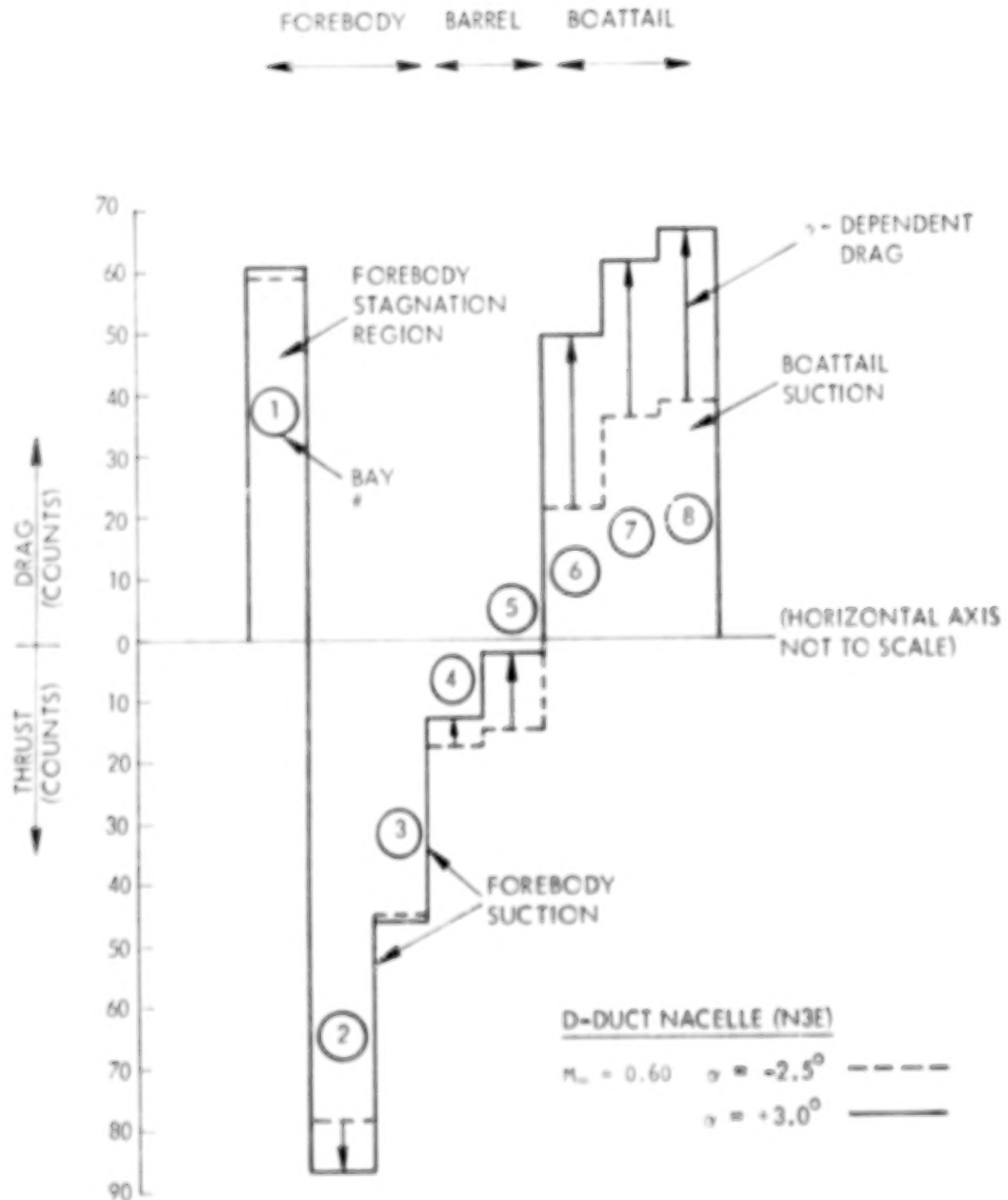


Figure 88. Computed drag count distribution along nacelle axis (Nacelle Surfaces Only).

USB CRUISE PROGRAM

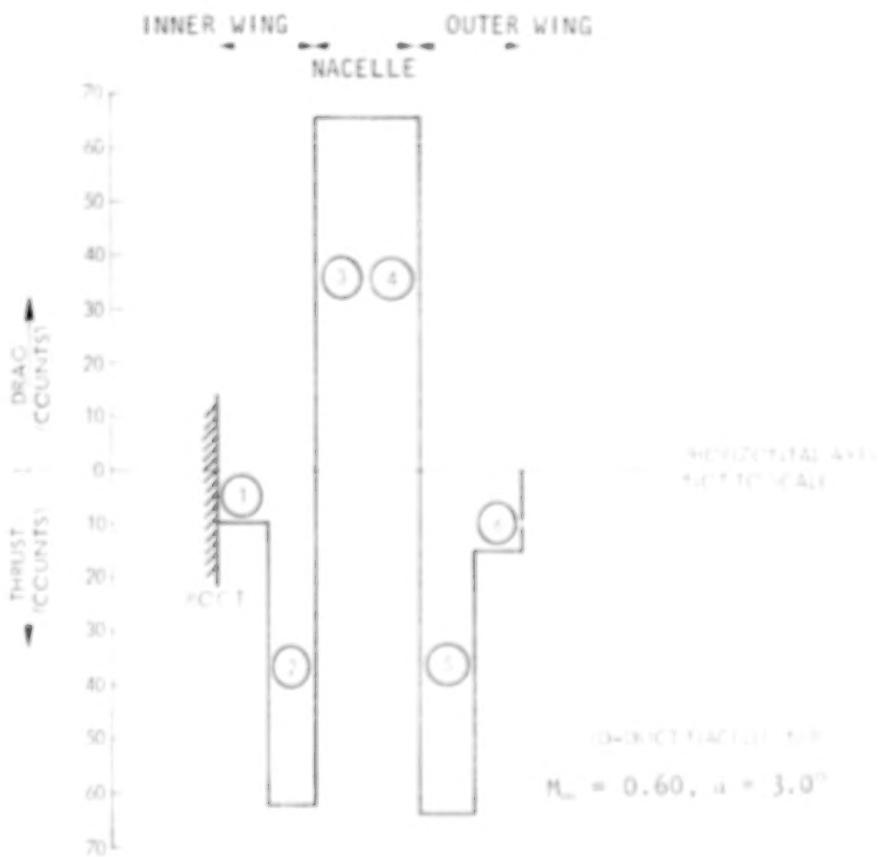


Figure 89. Computed drag count distribution along semi-span (All Surfaces).

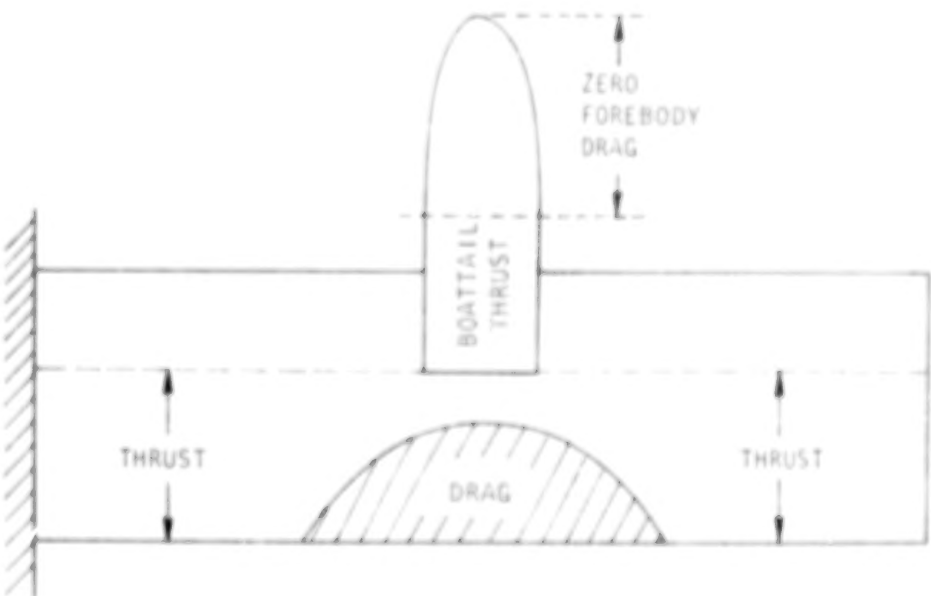


Figure 90. Location of drag-producing and thrust-producing regions due to application of power.

ing the curves. One advantage of this approach was that drag-producing regions could be readily identified (see Figure 90).

4.2.5 Drag correlation. - Figure 91, which is typical of drag correlations across the entire range of test pressure ratios, shows that the anticipated residue between experimental drag increments (relative to clean wing) and theoretical predictions was essentially independent of angle-of-attack. However, Figure 92 shows that the residue has definite trends with pressure ratio.

At approximately flow-through pressure ratio, the residual drag increment lies close to independent estimates of nacelle skin friction, which were based on change of wetted area. As pressure ratio increases towards sonic jet conditions, the drag residue increases at a constant rate, which is consistent with jet scrubbing skin friction estimates. Beyond the sonic point, the residual drag decreases. Inspection of the pressure plots shows reduced aft suction at the higher pressure ratios when shocks in the jet reduce its ability to turn.

The drag correlation, as exemplified by Figure 92, shows not only the expected qualitative agreement, but also far better quantitative results than might reasonably have been expected from the present theoretical model. It seems that the essential features of the flow may have been captured despite both the simplicity of the model and the coarseness of the paneling used.

5.0 COMPATIBILITY STUDIES - TASK III

To further investigate the compatibility of the USB concept with advanced transport aircraft requirements, a detailed design feasibility study was performed in concert with on-going acoustical investigations of USB installations (Noise Characteristics of Upper Surface Blown Configurations, NAS1-13870). This effort, under the present program, is denoted as Task III to the overall data-base study. Basic objectives of the combined Task III study were:

USB CRUISE PROGRAM

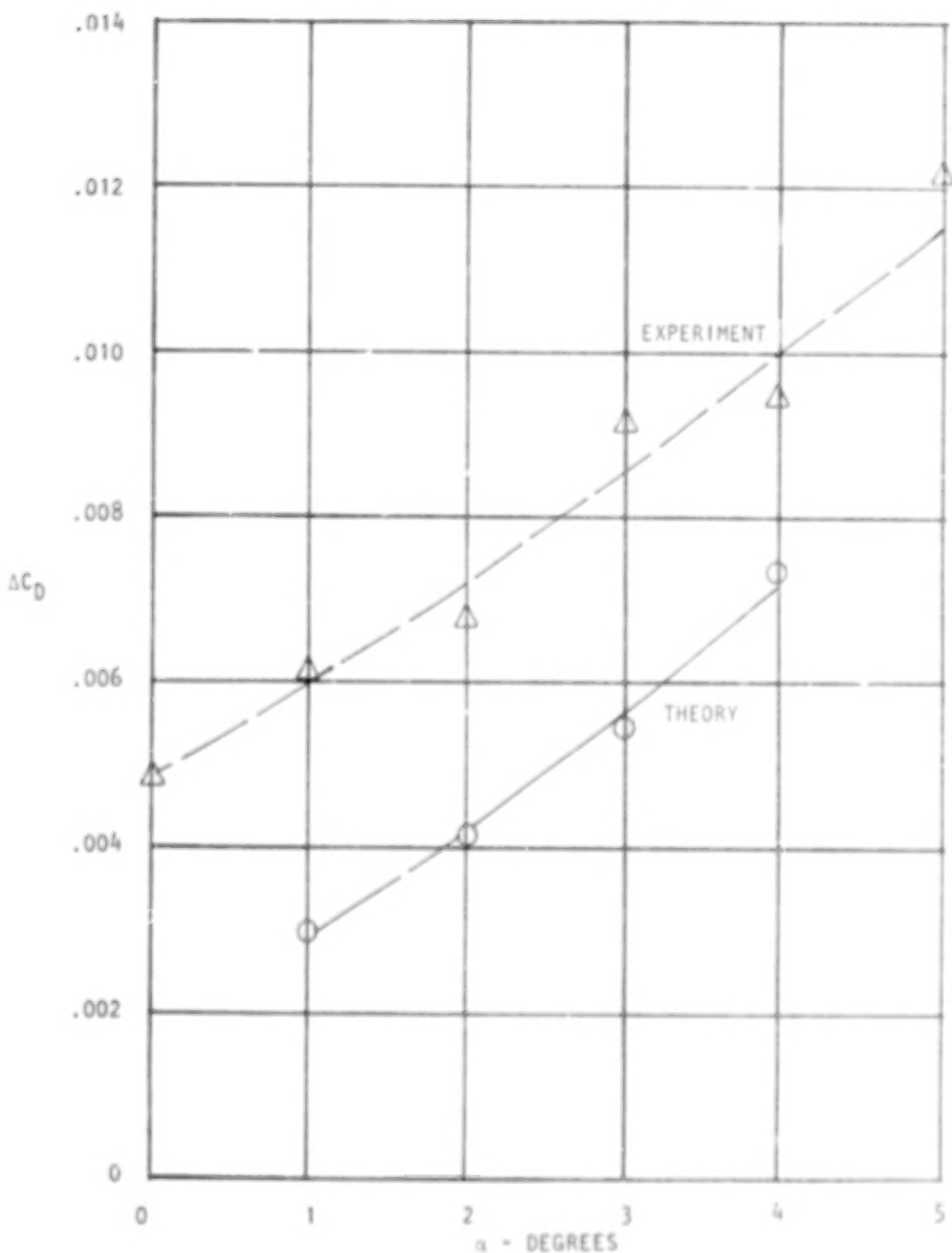


Figure 91. Comparison between predicted and measured drag increments for nacelle N3E (D-Duct), $c^2/A_N = 24$, $M_\infty = 0.60$, $H_1/p_\infty = 2.0$

USB CRUISE PROGRAM

- (1) NACELLE SKIN FRICTION
- (2) JET SCRUBBING DRAG
- (3) REDUCED TURNING/SCRUBBING DRAG AT $M_{JET} > 1.0$

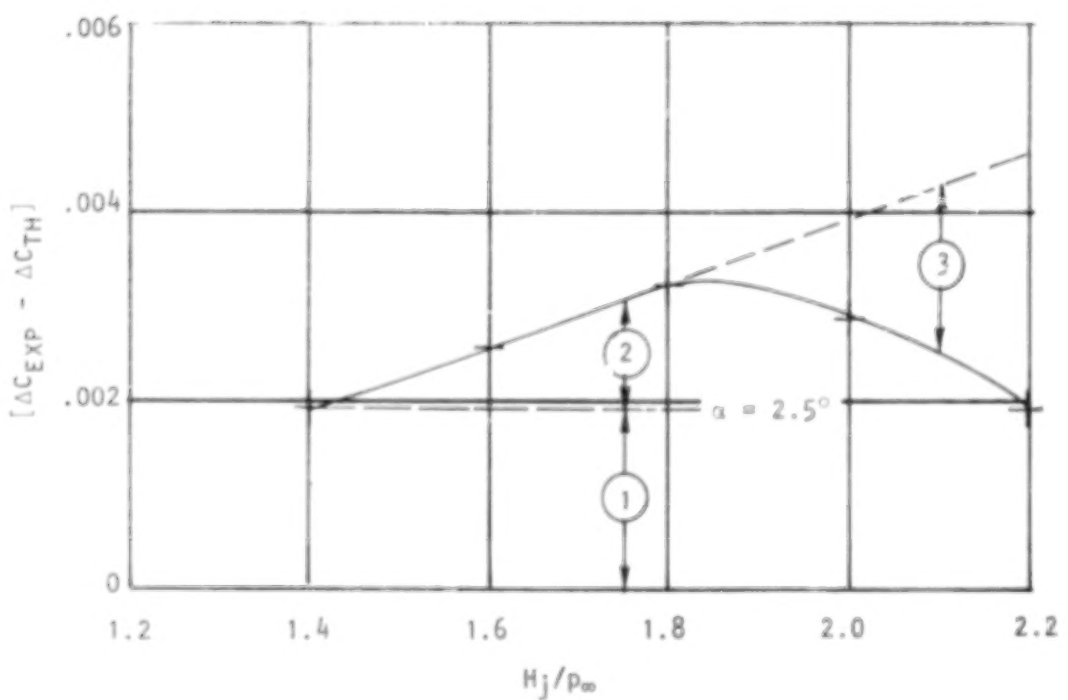


Figure 92. Residual difference between experimental and predicted drag increments for nacelle N_{3E} at $M_{\infty} = 0.60$.

- o Selection of a suitable mission and definition of a nominal baseline configuration
- o Evaluation of the effect of perturbations on the baseline aircraft for final design refinements
- o Perform design feasibility studies of characteristic systems and subsystems on the final configuration

One additional requirement in the present program was an evaluation of the final configuration high-lift system to demonstrate experimental compliance with study-projected airport performance. Throughout the study, basic goals of (1) cruise drag competitive with that of conventional configurations, (2) satisfactory short-field characteristics, and (3) a 90 EPNdB noise footprint area of 2.59 km^2 (1 sq. mil) were considerations.

5.1 Design and Feasibility Studies

Based on earlier NASA short-haul studies, a basic mission around which a candidate baseline could be formulated was selected. The performance requirements were:

- o 148 passengers
- o stage lengths of 527 (500) and 2780 (1500) km (n.m.)
- o field lengths of 610 (2000) and 1219 (4000) m (ft.)

Candidate engines for this preliminary study phase were the Allison PD-287-11 (design fan pressure ratio = 1.35) and the General Electric CFM56 (design fan pressure ratio = 1.47). The selected range of cruise Mach numbers of interest varied from 0.70 - 0.75. From suitable combinations of fan pressure and cruise Mach number, four candidate aircraft with varying cruise speeds were identified for parametric sizing, costing and noise evaluations. Characteristic data for these designs are provided in Figure 93. From these unrefined candidate designs, aircraft 4 (1.47 fan pressure ratio) was deleted because of the relatively high noise level (see Figure 94). The remaining three candidate aircraft (aircraft 1-3, Figure 93), with fan pressure ratios of

USB CRUISE PROGRAM

AIRCRAFT NO.	1	2	3	4
<u>MISSION</u>			↓	
NO. OF PASSENGERS	148			
STAGE LENGTH, KM (N.M.)	27 (560)			
FIELD LENGTH, M (FT)	610 (2000)			
CRUISE MACH NO.	0.70	0.75	0.80	0.75
CRUISE ALTITUDE, M (FT)	9145 (30000)			
<u>PROPELLION SYSTEM</u>				
NOZZLE SHAPE	D (SEMICIRCULAR)			
NACELLE TYPE	BLENDDED			
NO. OF ENGINES	4			
FAN PRESSURE RATIO	1.35			1.47
RATED THRUST, N (LB)	74993 (17984)	83291 (18705)	90753 (20403)	101307 (22777)
NACELLE DIAMETER, M (FT)	2.05 (6.72)	2.09 (6.85)	2.18 (7.15)	2.18 (7.02)
<u>AIRCRAFT</u>				
RAMP WEIGHT, KG (LB)	60264 (136116)	66067 (145678)	68765 (155162)	72561 (160001)
WING AREA, M ² (FT ²)	186.3 (200.1)	189.8 (202.8)	199.0 (211.1)	198.9 (215.2)
WING LOADING, KG/M ² (LB/FT ²)	158 (22.5)	167 (29.2)	170 (26.0)	159 (21.6)
THRUST-TO-WEIGHT RATIO	0.460	0.480	0.504	0.516
ASPECT RATIO	10.6			
SLEEP ANGLE, 0.250, DEGREES	20			
TAPE RATIO	0.1			
THICKNESS RATIO, AVG.	0.141		0.121	0.181
<u>CRUISE DATA</u>				
F _N /MAX CRUISE F _N	0.990			0.600
CL	0.325	0.310	0.304	0.291
CD	0.0271	0.0256	0.0248	0.0208
CD ₀	11.9	12.1	12.1	14.2
NACELLE CD, TOTAL	0.0504	0.0498	0.0496	0.0450
<u>TAKEOFF AND LANDING DATA</u>				
CLIMBOUT ANGLE	18.2	14.8	15.5	18.3
CLIMBOUT SPEED, KM/HR (KT)	184.7 (199.6)	184.7 (199.6)	185.4 (190.0)	187.6 (191.2)
APPROACH ANGLE, DEGREES	5.9	5.9	5.9	6.1
APPROACH SPEED, KM/HR (KT)	160.7 (166.7)	160.2 (166.4)	159.8 (166.0)	153.8 (153.0)
RATE OF DESC, M/S (FT/MIN)	4.57 (900)			
APPROACH F _N /TAKEOFF F _N	0.38	0.42	0.47	0.45
<u> COSTS (1972 \$)</u>				
ENGINES	\$1.598	\$1.668	\$1.758	\$2.838
COMPLETE AIRCRAFT	\$10.588	\$10.928	\$11.348	\$10.368
DOC - 2 X 1972 FULL PRICE (2.7/GAL), 1/SEAT-S.M.	2.33	2.26	2.27	2.27
DOC - 4 X 1972 FUEL PRICE (4.6/GAL), 1/SEAT-S.M.	2.99	2.46	2.89	2.89
<u>NOISE</u>				
TAKOFF FOOTPRINT, 90 EPNdB, KM ² (5.8,7)	2.81 (1.09)	1.93 (1.17)	1.67 (1.18)	9.90 (3.62)
TAKOFF FLYOVER AT 6.49 KM (1.5 N.M.), EPNdB	83.4	83.4	83.7	88.6
TAKOFF, MAXIMUM AT 152.4 M (500 FT), SIDELINE, EPNdB	99.1	99.1	100.3	106.3
LANDING FOOTPRINT, 90 EPNdB, KM ² (5.8,7)	2.17 (0.04)	0.16 (0.07)	0.36 (0.14)	1.16 (0.48)
LANDING FLYOVER AT 1.46 KM (1 N.M.), EPNdB	86.8	86.7	91.1	95.0
TOTAL FOOTPRINT, 90 EPNdB, KM ² (5.8,7)	2.98 (1.13)	1.21 (1.24)	1.81 (1.48)	11.08 (4.26)

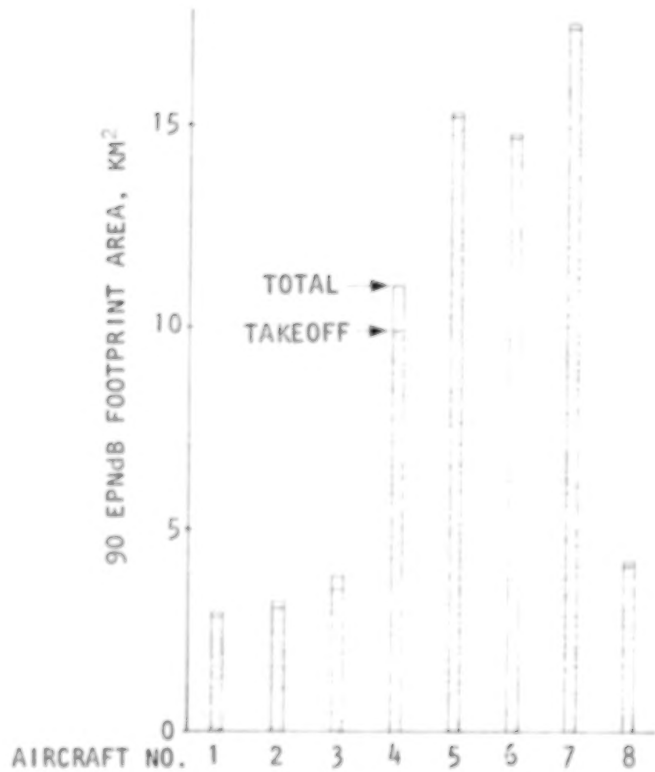
Figure 93. USB Study aircraft.

BLANK

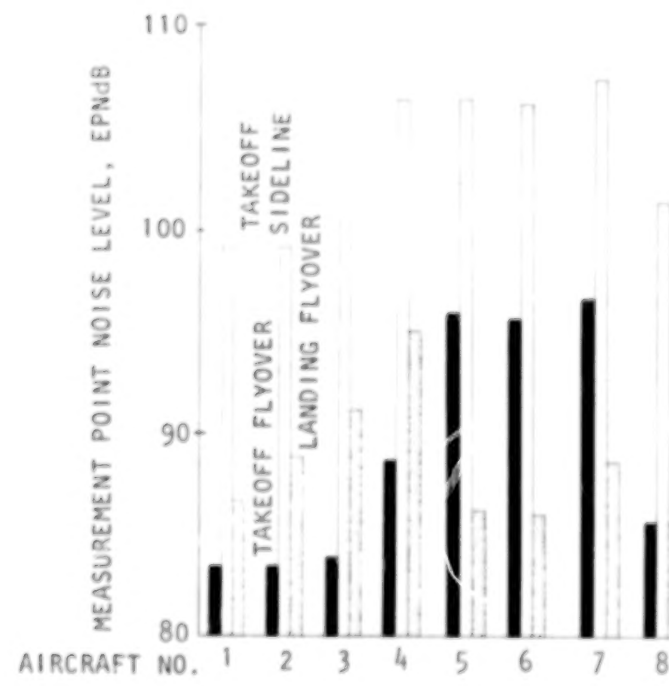
PAGE

132

USB CRUISE PROGRAM



(a) Noise footprint areas



(b) Measurement point noise levels

Figure 94. Noise footprint and measurement point noise levels, USB study aircraft

1.35, appeared to be capable of meeting the 90 EPNdB noise goal as indicated in Figure 94. Further consideration of such variables as cruise speed, block time and direct-operating cost, led to aircraft 2 (Figure 93) as a baseline selection suitable for further design refinement via parameter perturbation studies.

5.1.1 Perturbation studies. - The objective of the parameter perturbation study was to create a second level of aircraft refinement before making a final USB configuration selection. In this study, sensitivity data were used to assess the effects of slight excursions in wing sweep, wing aspect ratio, nacelle or engine size, etc. on weight and direct-operating-cost (DOC) while holding the basic mission constant. The high-speed wind-tunnel data and the experimental acoustical data from NAS1-13870 were employed as the basis for translating geometric variations into aerodynamic and noise effects. The cruise performance parameters varied were nozzle boattail angle, nozzle aspect ratio, relative size and discharge position. Parameters varied as affecting noise included nozzle aspect ratio, wing impingement angle, flap extension, deflection and radius of curvature, fan duct noise treatment and total noise source strength. Also for the noise studies, the effects of a long-chord flap, combined with variations in nozzle aspect ratio and fan-duct noise treatment, were studied. In this phase of the work, only takeoff footprint area and takeoff measurement point flyover noise were considered.

5.1.2 Final design. - The final aircraft design, shown in Figure 95, has about the same dimensional characteristics as the baseline aircraft 2 of Figure 93. It is a high-wing, four-engine aircraft designed for a passenger capacity of 148, field length of 610 m (2000 ft), stage length of 927 km (500 n.m.) and cruise Mach number of 0.75. The ramp weight is 67,067 kg (145,678 lb) and the wing area is 170 m² (1828 ft²) for a wing loading of 387 (79.2 psf). The engines are Allison PD-287-11's scaled to a takeoff-rated thrust of 83,200 N (18,705 lb), giving an installed thrust-to-weight ratio of 0.48. Other features are shown in Figure 93 and 95.

The propulsion and high-lift installations are shown in Figures 95 and 96. The USB-nozzle used with the selected aircraft is "D-shaped", located at 35 percent chord and employs a boattail angle of 16 degrees. These geometric

BLANK

PAGE

USB CRUISE PROGRAM

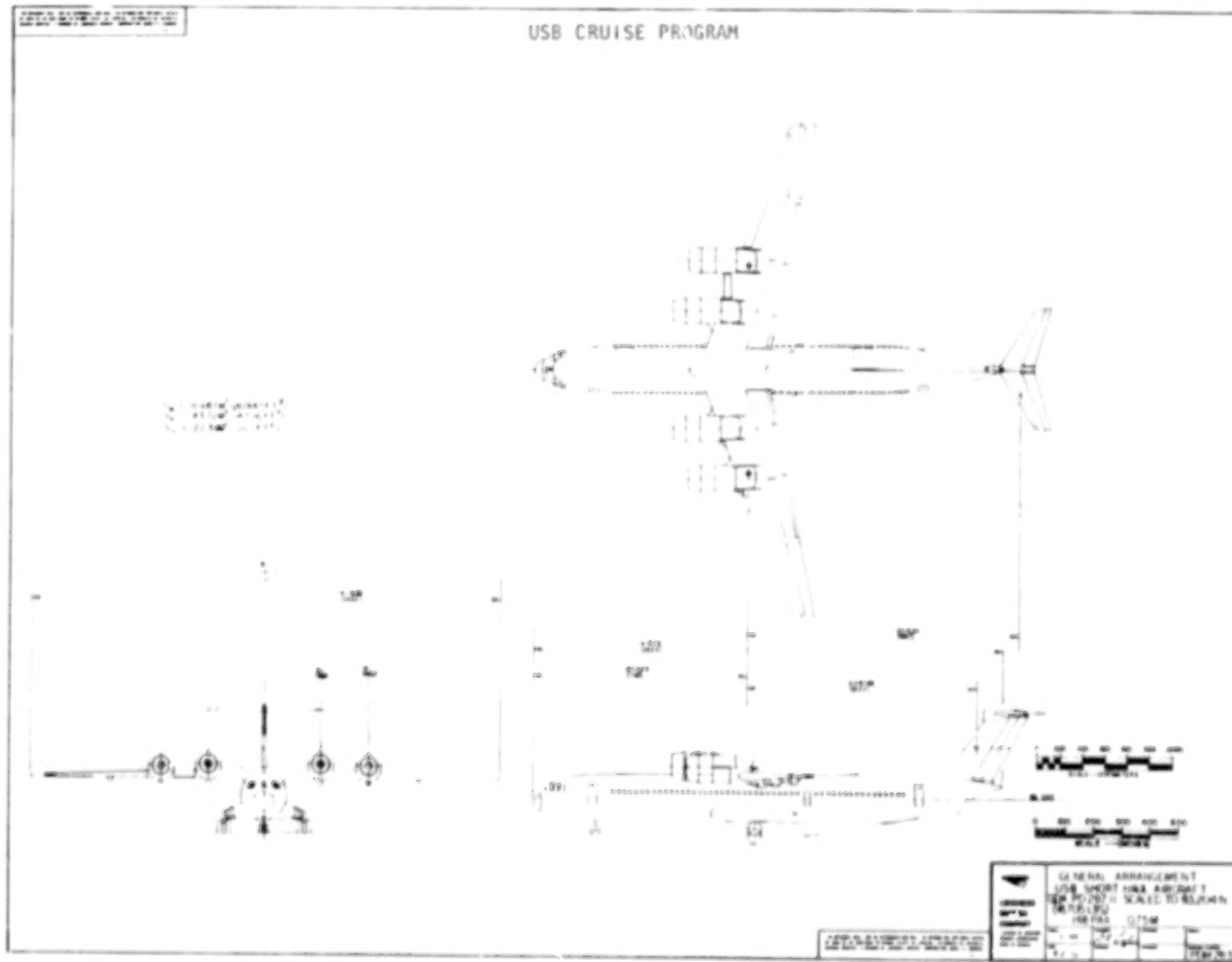


Figure 95. General arrangement, baseline aircraft.

USB CRUISE PROGRAM

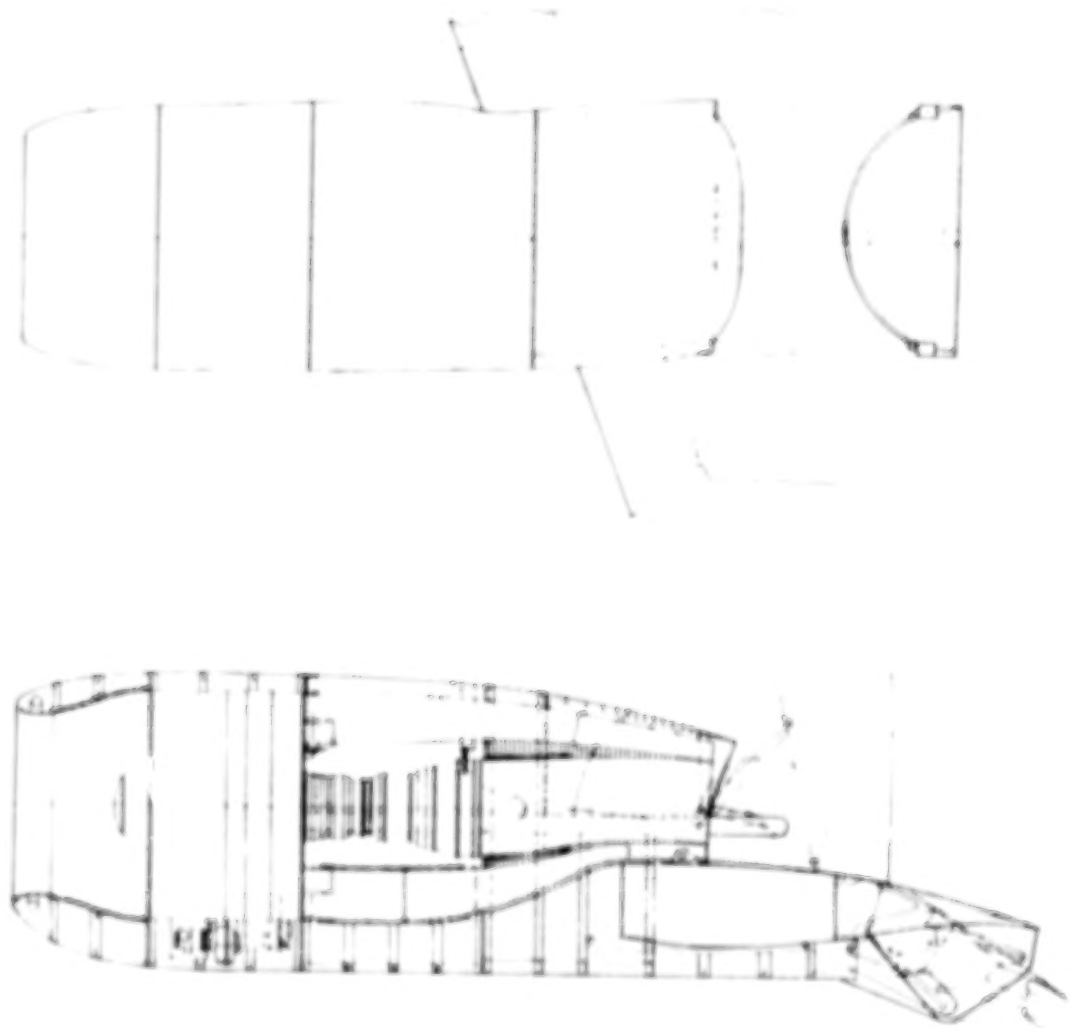


Figure 96. Nacelle inboard profile.

characteristics represent favorable cruise drag alternatives along with some compromise (on nozzle exit shape) to ensure powered-lift capabilities commensurate with the desired field performance. The trailing-edge flap has a sliding-motion with the segments moving rearward on tracks extending the basic wing chord by 36 percent on landing and by about 25 percent on takeoff; the chord-extending flaps provide a substantial noise benefit from the increased flow length from nozzle to flap trailing edge.

The nacelle installation is a standard, short duct arrangement as indicated in Figure 96. The rear upper external contour of the nacelle is formed by the outer surface of a target-reverser door. Extension or retraction of the door is accomplished hydraulically with movable hinge points describing the arcs illustrated in the figure. In the reversing mode, the total jet (primary and secondary) are deflected upward and forward providing a reverse plus downward force on the aircraft. There is also an articulated "eyebrow-shaped" section on the aft-lip of the reverser such that, upon extension, the jet discharge is forced downward toward the wing surface to promote jet attachment and thus increased jet deflection in the high-lift configuration. Provisions have also been made in the forward and aft fan duct to incorporate noise suppression treatment if such is found to be desirable.

The noise characteristics of the final design were calculated based on the following:

- o Aircraft size, weight, and performance as in the baseline
- o 40% chord flap extension at both takeoff and landing
- o Flap deflections and landing thrust setting as in the baseline
- o No internal flap blowing
- o No fan duct noise treatment

The calculated values are:

Takeoff Footprint Area, 90 EPNdB	-	1.76 km ² (0.68 s.m. ²)
Takeoff Flyover at 6.49 Km (3.5 n.m.)	-	79.5 EPNdB
Takeoff, Maximum at 152.4 M (500 ft) Sideline	-	98.4 EPNdB
Landing Footprint Area, 90 EPNdB	-	0.12 km ² (0.05 s.m. ²)
Landing Flyover at 1.86 Km (1 n.m.)	-	86.8 EPNdB
Total Footprint Area, 90 EPNdB	-	1.88 km ² (0.73 s.m. ²)

It can be seen that the calculated total footprint area of 1.88 km² (0.73 s.m.²) betters the 2.59 km² (1 s.m.²) goal by a considerable margin. The area would be further reduced if the overlap of the takeoff area and landing area were subtracted.

The flight path and footprint are shown in Figure 97. The takeoff spectra of the various noise sources considered in the noise prediction program and of the complete aircraft are presented for the flyover location in Figure 98. Even with no fan duct treatment, high-lift system noise is the strongest source, although fan noise exceeds it at the higher frequencies. The PNL directivity pattern at takeoff is shown in Figure 99.

5.2 Supplementary Low-Speed Tests

In the preliminary parametric studies of Task III, estimated high-lift performance was utilized in the initial sizing process. Further geometric refinements to the high-lift system were made during the perturbation studies to reflect more favorable noise, performance and weight guidelines. To validate the capability of the final high-lift system for consistency with a 610 m (2000 ft) design field length, a low-speed test program was undertaken. A description of these tests and the experimental results obtained are summarized in the paragraphs which follow.

5.2.1 Model description. - The test vehicle employed in the high-lift performance study was a short-haul type of aircraft configuration around which numerous high-lift investigations, powered and unpowered, had been previously performed. Figure 100 shows the 216 cm (7-foot) span model mounted in the

TABLE OF CONTENTS

<u>Section</u>	<u>Title</u>	<u>Page</u>
	FOREWORD	iii 1/A6
	LIST OF FIGURES	vii 1/A10
	SUMMARY	1 1/B7
1.0	INTRODUCTION	1 1/B7
2.0	SYMBOLS	3 1/B9
3.0	PROGRAM DEFINITION - TASK I	5 1/B11
4.0	CRUISE PERFORMANCE DATA BASE - TASK II	7 1/C1
	4.1 Exploratory Wind-Tunnel Tests	7 1/C1
	4.1.1 Experimental models	8 1/C2
	4.1.2 Test facilities	16 1/D2
	4.1.3 Experimental data analysis	16 1/D2
	4.1.3.1 Pressure-test results	19 1/D7
	4.1.3.2 Force-test results	34 1/E8
	4.1.3.3 Geometric "effects" data	93 2/D2
	4.2 Math Model Development	114 2/E10
	4.2.1 Representation of wing, nacelle and power unit .	114 2/E10
	4.2.2 Surface pressure	119 2/F3
	4.2.3 Lift	122 2/F8
	4.2.4 Drag prediction methods	122 2/F8
	4.2.5 Drag correlation	127 2/F13
5.0	COMPATIBILITY STUDIES - TASK III	127 2/F13
	5.1 Design and Feasibility Studies	130 2/G2
	5.1.1 Perturbation studies	133 2/G7
	5.1.2 Final design	133 2/G7
	5.2 Supplementary Low-Speed Tests	137 2/G14
	5.2.1 Model description	
	5.2.1.1 Leading-edge device	142 3/A9
	5.2.1.2 Trailing-edge flaps	142 3/A9
	5.2.1.3 Nacelles	142 3/A9
	5.2.1.4 Instrumentation	142 3/A9

TABLE OF CONTENTS (CONT'D)

<u>Section</u>	<u>Title</u>	<u>Page</u>
	5.2.2 Test results	147 3/B2
	5.2.2.1 Static performance	147 3/B2
	5.2.2.2 Wind-on performance	147 3/B2
	5.2.3 Discussion	147 3/B2
	5.2.3.1 Experimental data comparisons	147 3/B2
	5.3 Powered-Lift Analytical Synthesis	157 3/B14
6.0	RECOMMENDATIONS FOR ADDITIONAL DEVELOPMENT - TASK IV	160 3/C3
7.0	PROGRAM CONCLUSIONS	167 3/C13
	7.1 Cruise Performance Data Base - Task II	167 3/C13
	7.1.1 Experimental program	167 3/C13
	7.1.2 Theoretical program	169 3/D1
	7.1.2.1 Vortex lattice studies	169 3/D1
	7.1.2.2 Applications of jet flap theory	171 3/D3
	7.2 Compatibility Studies - Task III	171 3/D3
	7.2.1 Design feasibility studies	172 3/D4
	7.2.2 Supplementary tests	173 3/D5
8.0	REFERENCES	174 3/D6

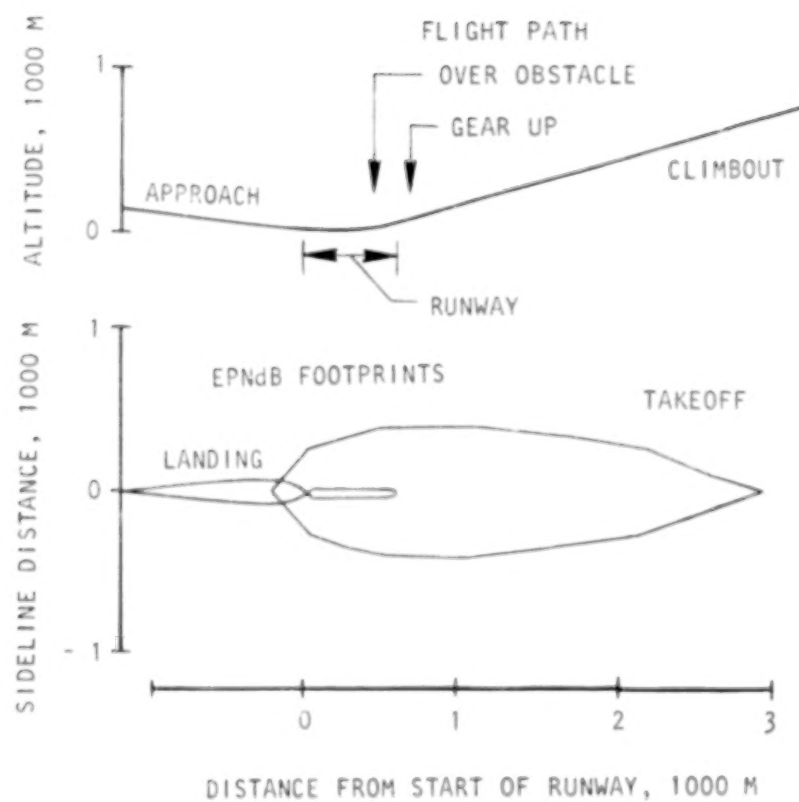


Figure 97. Flight path and noise footprints, final design aircraft

USB CRUISE PROGRAM

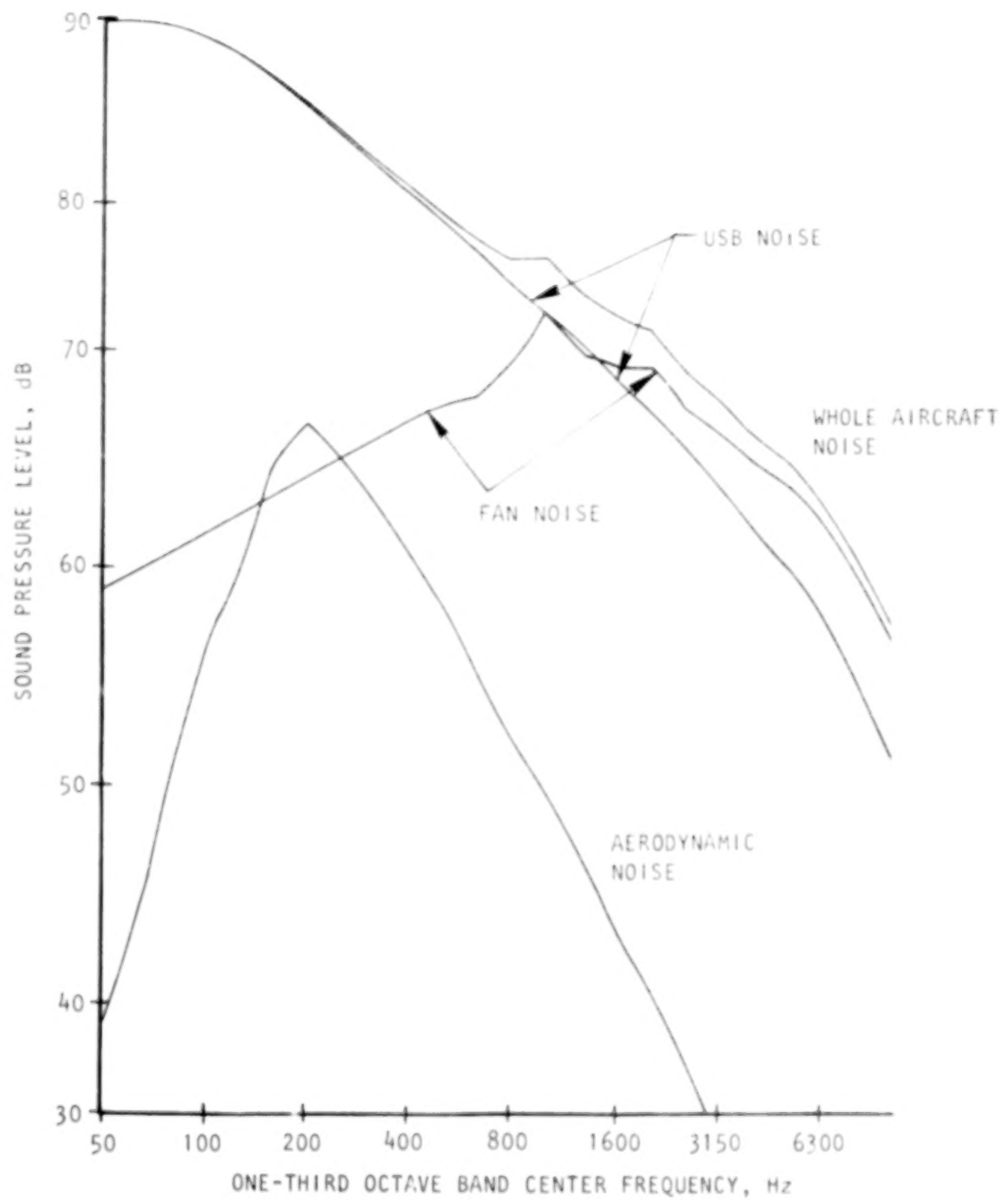


Figure 98. Spectra by source, final design aircraft, takeoff elevation angle = 90°, 152.4 m (500 ft) distance, no ground reflection

USB CRUISE PROGRAM

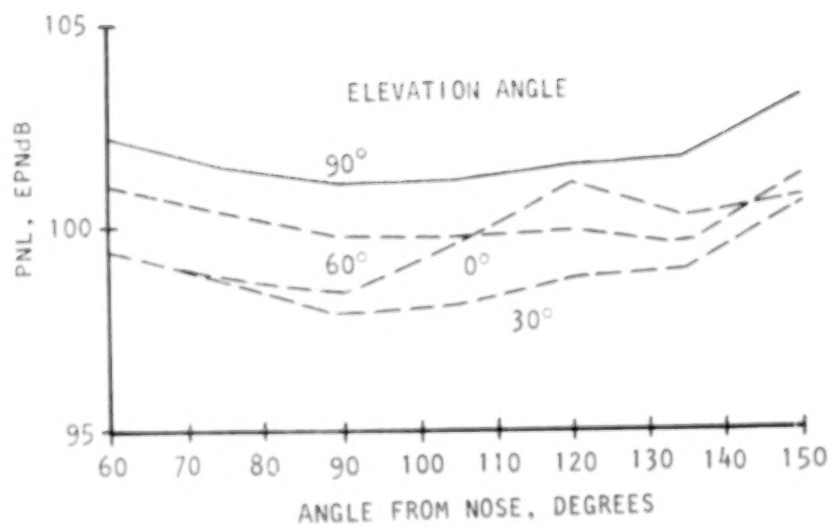


Figure 99. PNL Directivity, final design aircraft, takeoff 152.4 M (500 ft) radius, no ground reflections

BLANK

PAGE

USB CRUISE PROGRAM

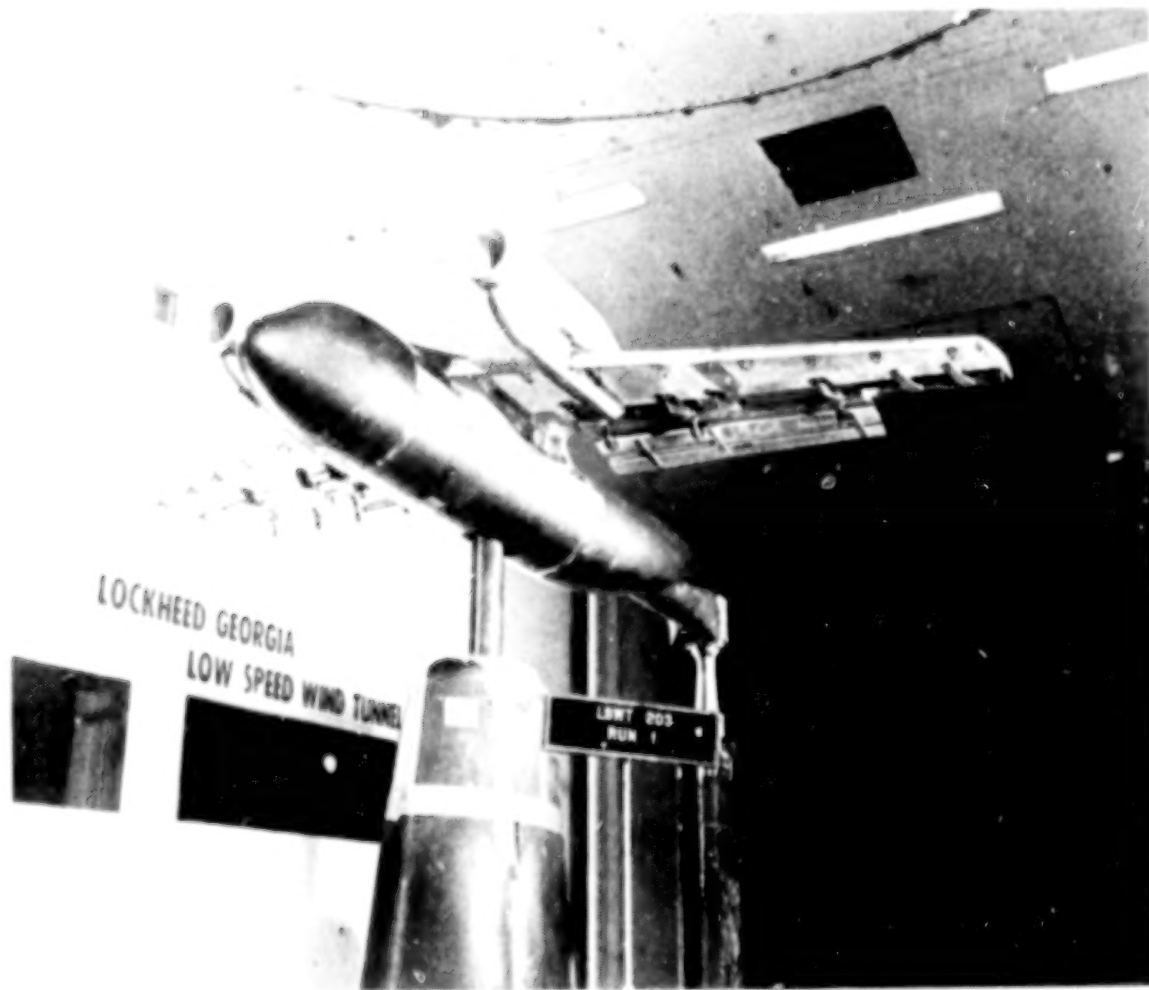


Figure 100. Low-speed, high-lift test model.

Lockheed-Georgia V/STOL wind tunnel. Powered-lift is derived from two ejector-powered nacelles with "D-duct" (semi-circular) nozzles exhausting over Coanda plates attached to the upper surfaces of triple-slotted flaps. A full-span, high-camber Krueger-type flap provides the leading-edge stall protection. Pertinent model dimensions are given in Table I.

5.2.1.1 Leading-Edge Device: The leading-edge device consisted of a high camber, full-span, Krueger-type flap closely fitted at the flap-pylon junction. The flap reference line was deflected downward 50 degrees from the wing chordline and the gap between the flap trailing-edge and wing was sealed. This leading-edge configuration was maintained throughout the tests.

5.2.1.2 Trailing-Edge Flaps: The trailing-edge flap system consisted of 56 percent span, triple-slotted flaps as illustrated in Figure 101. The flap gaps, also given on the figure, were held constant during the course of the investigation. A smooth, Coanda plate covered the upper surface of the flaps immediately behind the nacelle and across a flap span of $\Delta\eta = 0.16$. Three flap deflections were investigated. These were 25° , 42.5° and 52° defined in terms of the flap chord-to-wing chord angle; in terms of the upper-surface angle at the trailing edge, these became 34° , 56.5° and 66° , respectively.

5.2.1.3 Nacelles: Installation of the nacelles on the wing is illustrated in Figure 102 with details of the nozzle design shown in Figure 103. The nacelles were powered by pneumatically driven ejector engine simulators and each had 50.895 cm^2 (7.889 in.^2) nozzle exit area. The nozzle shape employed was a "D-duct" ($AR = 2.5$) with a discharge position at 35% chord. A roof angle of 30° was utilized to ensure jet attachment at the maximum flap angle setting. It was designed to accurately represent the deflector mechanism employed on the baseline design.

5.2.1.4 Instrumentation: The model was mounted on the six-component pyramidal balance system in the 16' x 23' test section of the Lockheed Low Speed Wind Tunnel. Airflow to the nacelles was measured by the wind tunnel air supply orifice system. Inside the nacelles, nozzle pressures were measured by twelve total pressure probes manifolded together and routed to a single pressure transducer inside the model fuselage. Thrust level as a

USB CRUISE PROGRAM

TABLE I. - MODEL DIMENSIONAL DATA

<u>Wing</u>	<u>Dimension</u>
Area, square meters (square feet)	0.6033 (6.494)
Span, centimeters (inches)	216.052 (85.026)
MAC length, centimeters (inches)	28.928 (11.387)
Sweep of c/4, degrees	14.918
Taper ratio	0.509
Aspect ratio	7.731
Incidence, degrees	3.0
Twist, degrees	0
Anhedral, degrees	0
Thickness ratio, % local wing chord	
Root	13.7
Tip	10.5
<u>Leading Edge Flaps (Full Span)</u>	
Chord length, % local wing chord	17
Deflection angle, degrees	50
<u>Trailing Edge Flaps</u>	
Flap span, centimeters (inches)	121.70 (48.0)
Flap chord extension along engine centerline, centimeters (inches)	10.41 (4.1)
Flap chord extension along engine centerline, % local wing chord	32.5
Coanda plate, % semispan	16.3
<u>Fuselage</u>	
Length, centimeters (inches)	206.726 (81.388)
Maximum frontal area, square meters (square feet)	0.0527 (0.567)
Maximum diameter, centimeter (inches)	25.908 (10.200)
<u>Nacelles</u>	
Length, centimeters (inches)	43.43 (17.10)
Diameter, centimeters (inches)	10.92 (4.30)
Exit width, centimeters (inches)	11.384 (4.482)
Nozzle aspect ratio	2.5
Exit area, square centimeters (square inches)	50.90 (7.889)
Spanwise nacelle location, % wing semi-span	28.8
Chordwise nozzle exit location, % local chord	35

USB CRUISE PROGRAM

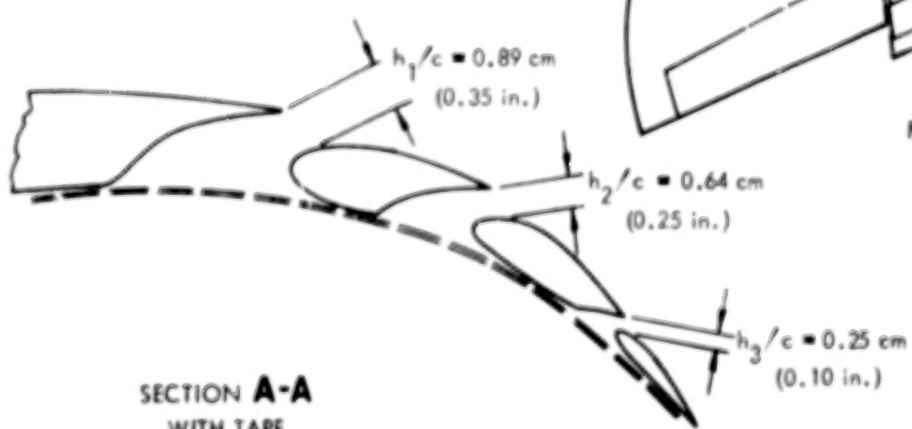
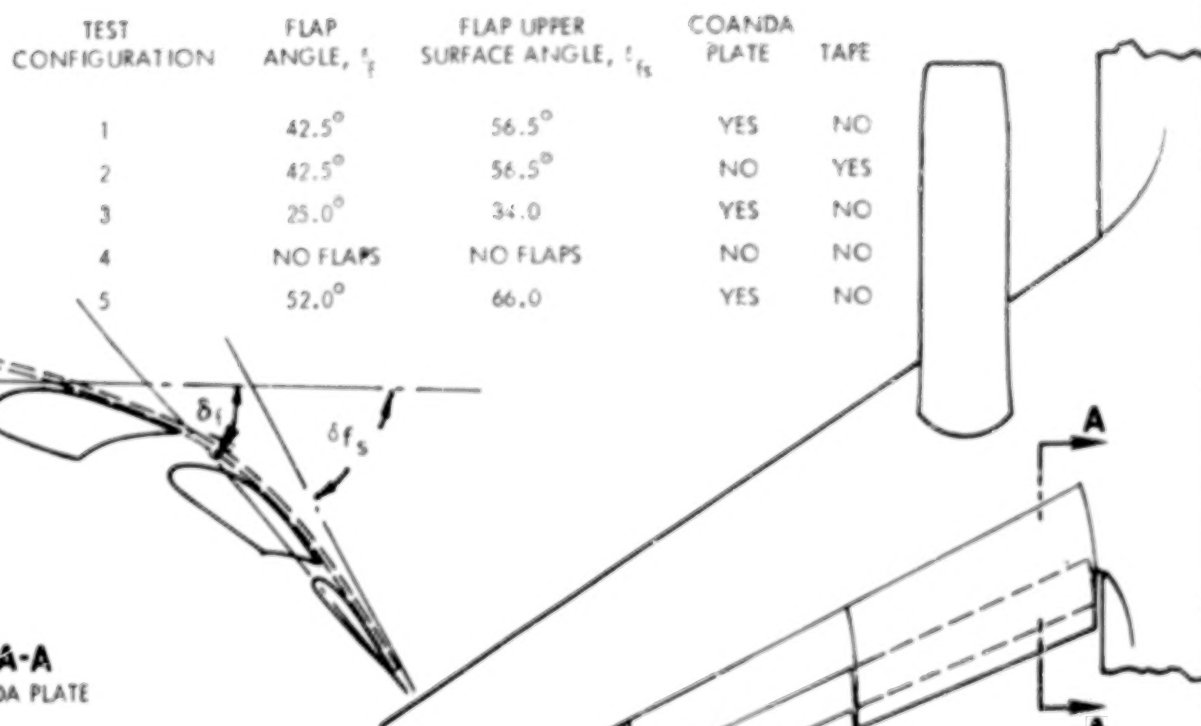


Figure 101. Trailing edge flap system design details, low speed model

USB CRUISE PROGRAM

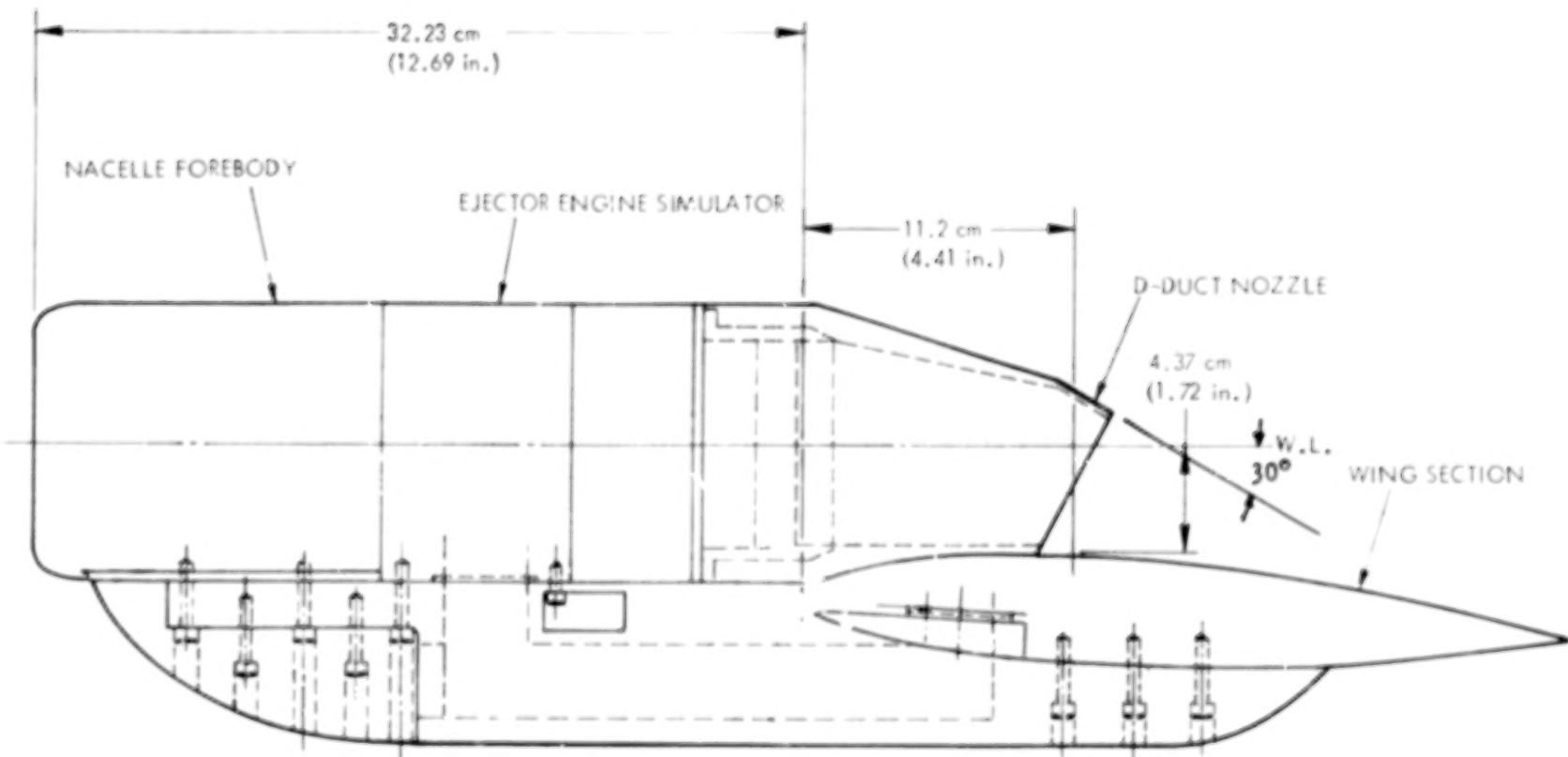


Figure 102. Nacelle installation on the wing

USB CRUISE PROGRAM

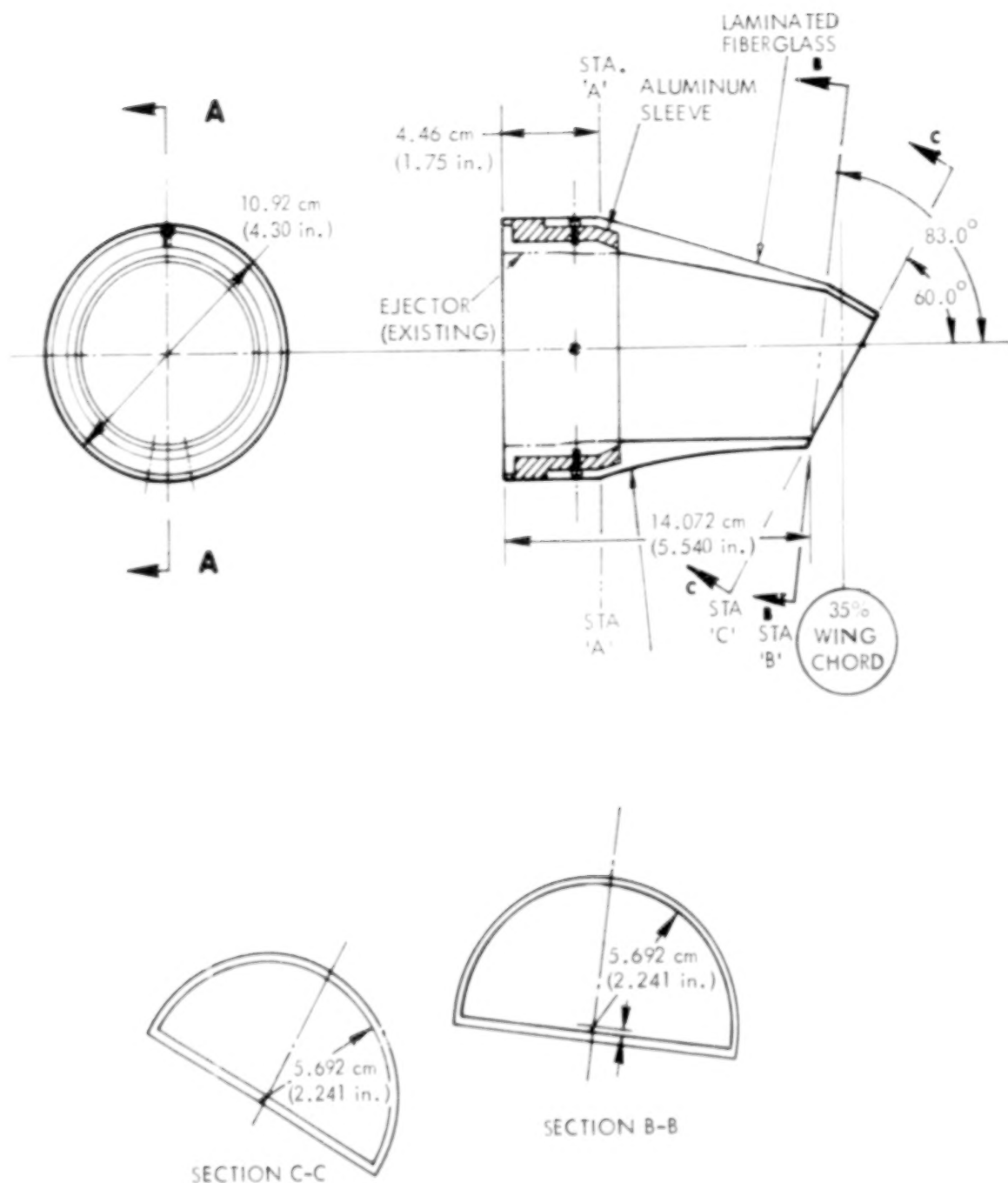


Figure 103. Nozzle design details

function of nozzle pressure ratio was obtained by removing the flaps and operating the nozzles statically.

5.2.2 Test results. -

5.2.2.1 Static Performance: The ejector-powered nacelles were mounted on the wing, with flaps removed, and tested statically. This test provided the thrust calibration data (C_{μ}) shown in Figure 104 where the thrust coefficient is based on a freestream dynamic pressure of 718.2 N/m^2 (15 psf). With the flaps installed at selected angles, and the Coanda plate in place, static tests were also conducted to determine thrust turning efficiency and the effective turning angle, δ_j . These results are given in Figure 105 in polar form and as a function of nozzle pressure ratio in Figure 106.

5.2.2.2 Wind-On Performance: Wind-on high-lift performance for several representative flap angles are shown in Figures 107 through 110. The wind tunnel dynamic pressure was held at 718.2 N/m^2 (15 psf) during these tests providing a Reynolds number of 675,000 based on mean wing chord. The drag data, Figures 108 and 110, have not been corrected for ram drag of the inlet air flow; such a correction would amount to $\Delta C_D \approx 0.10 - 0.2$. An oil flow photograph highlighting the nacelle exhaust/flap region is provided in Figure 111 illustrating a typical case of the flow-visualization studies made during the testing.

5.2.3 Discussion. - The supplementary high-lift test results will be discussed first from the standpoint of data comparisons with other systems and facilities, and secondly, as the means of validating the estimated performance of the USB final design.

5.2.3.1 Experimental Data Comparisons: The model used in the subject tests represented a basic experimental vehicle utilized for studying a variety of powered-lift concepts. Figure 112 compares the two-engine USB test results with data obtained on a four-engine externally-blown flap configuration. The test hardware (i.e., ejector units, trailing-edge flaps, high-camber, leading-edge device) are essentially the same in both instances, except that the EBF data were obtained on a wing with slightly higher sweep (25 degrees) than the

USB CRUISE PROGRAM

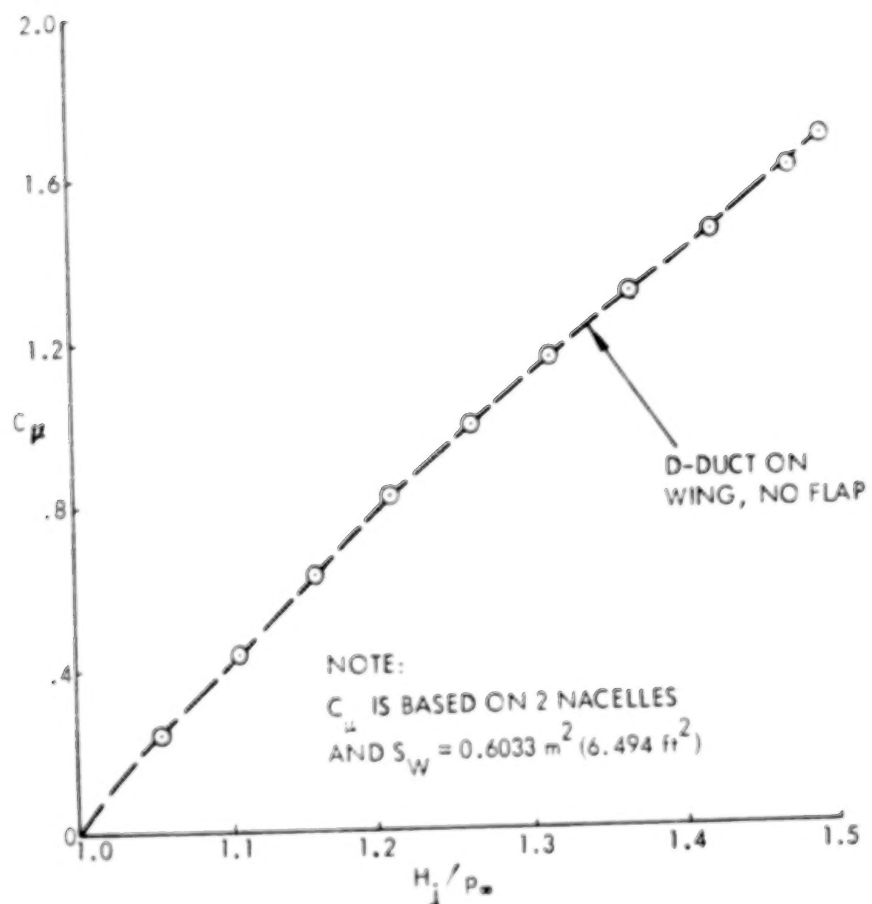


Figure 104. Low speed model thrust coefficient, $q_{\infty} = 718.2 \text{ N/m}^2$
 (15 lb/ft^2)

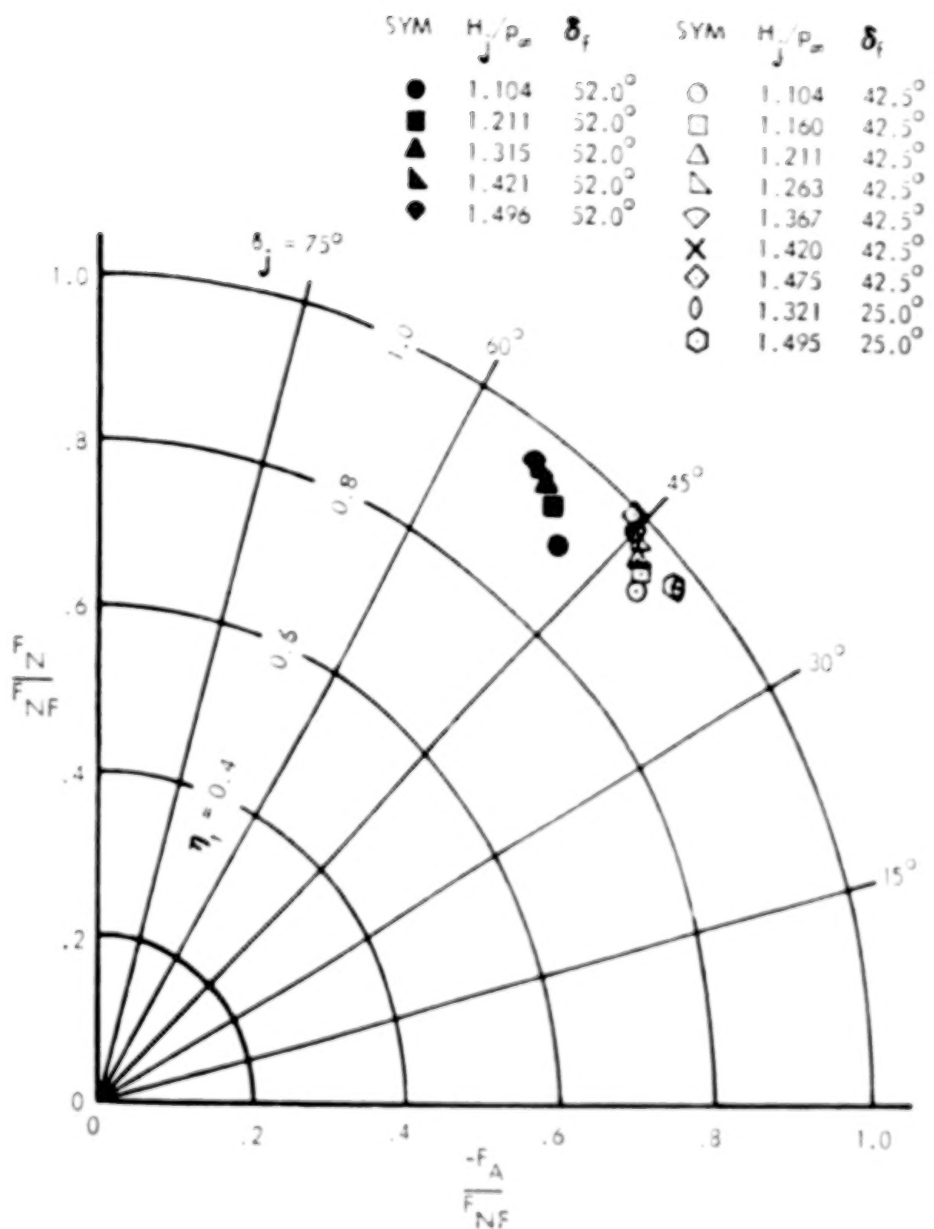


Figure 105. Low speed model static turning characteristics

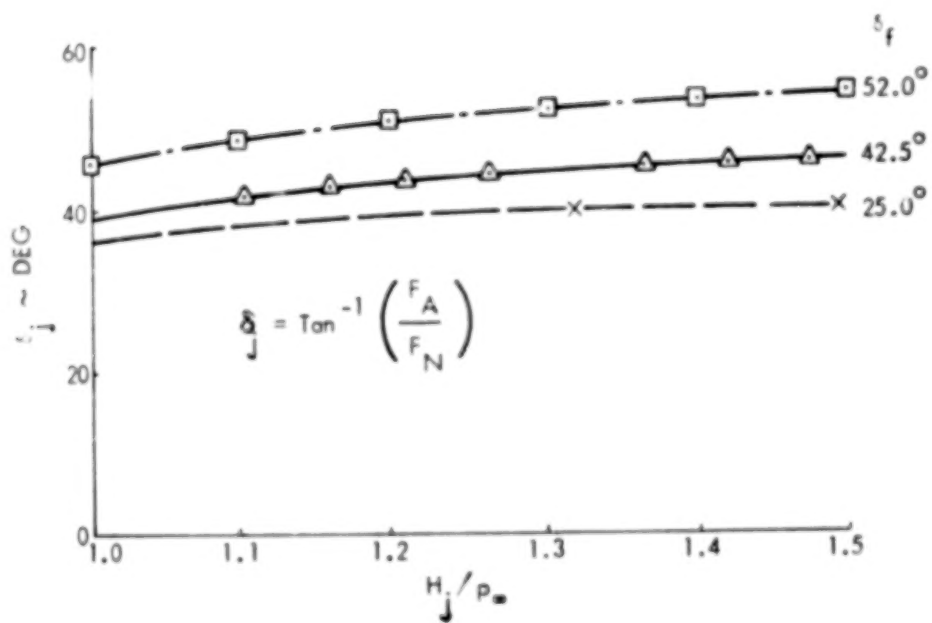
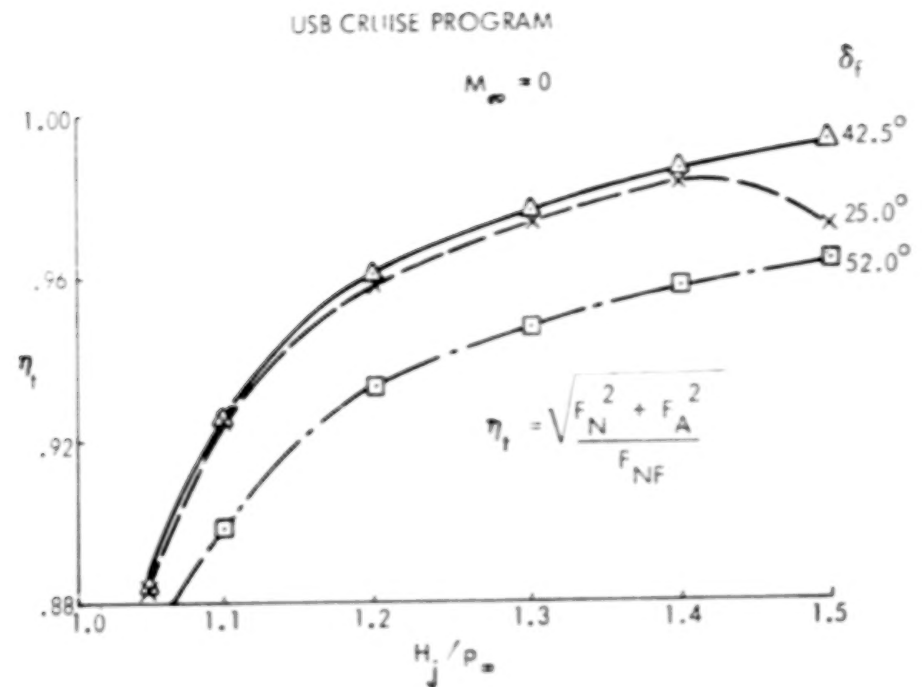


Figure 106. USB low speed model propulsion performance

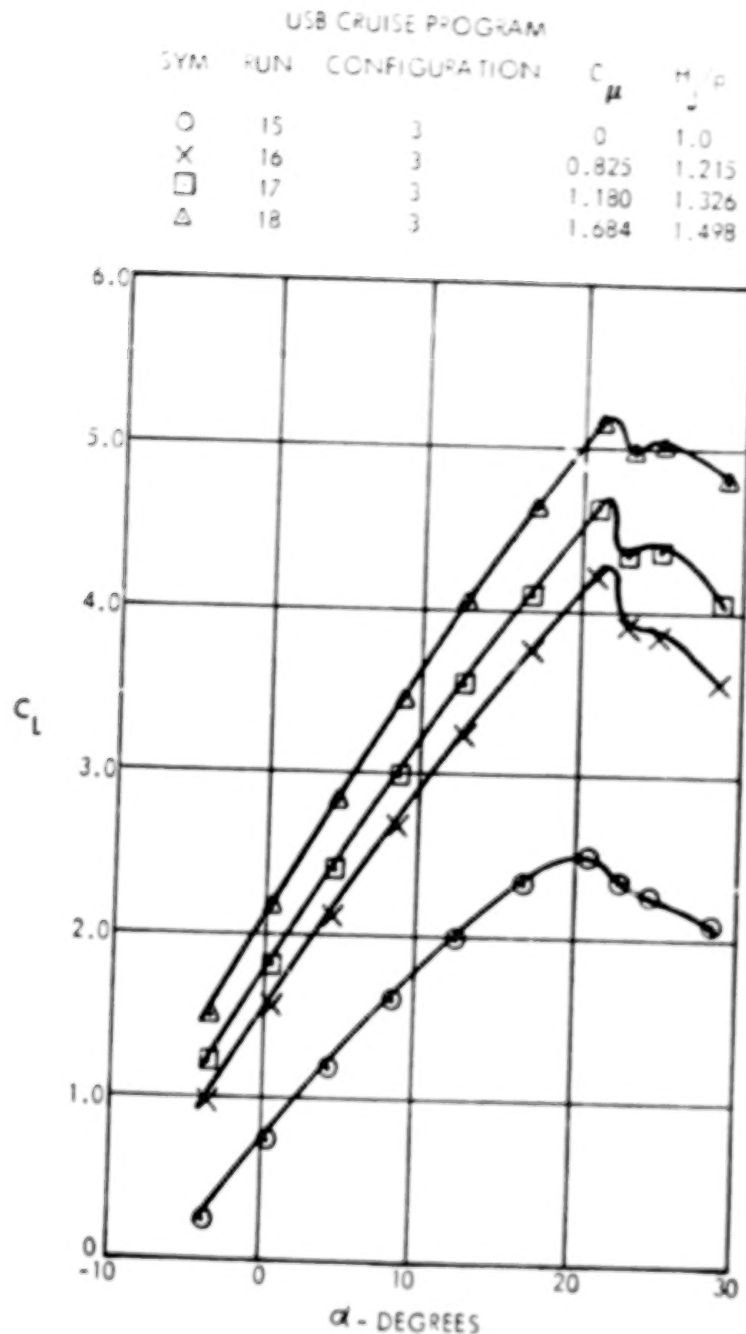


Figure 107. Variation of low speed model lift coefficient with angle of attack, $q_{\infty} = 718.2 \text{ N/m}^2 (15 \text{ lb/ft}^2)$, $\delta_f = 25^\circ$, Coanda plate

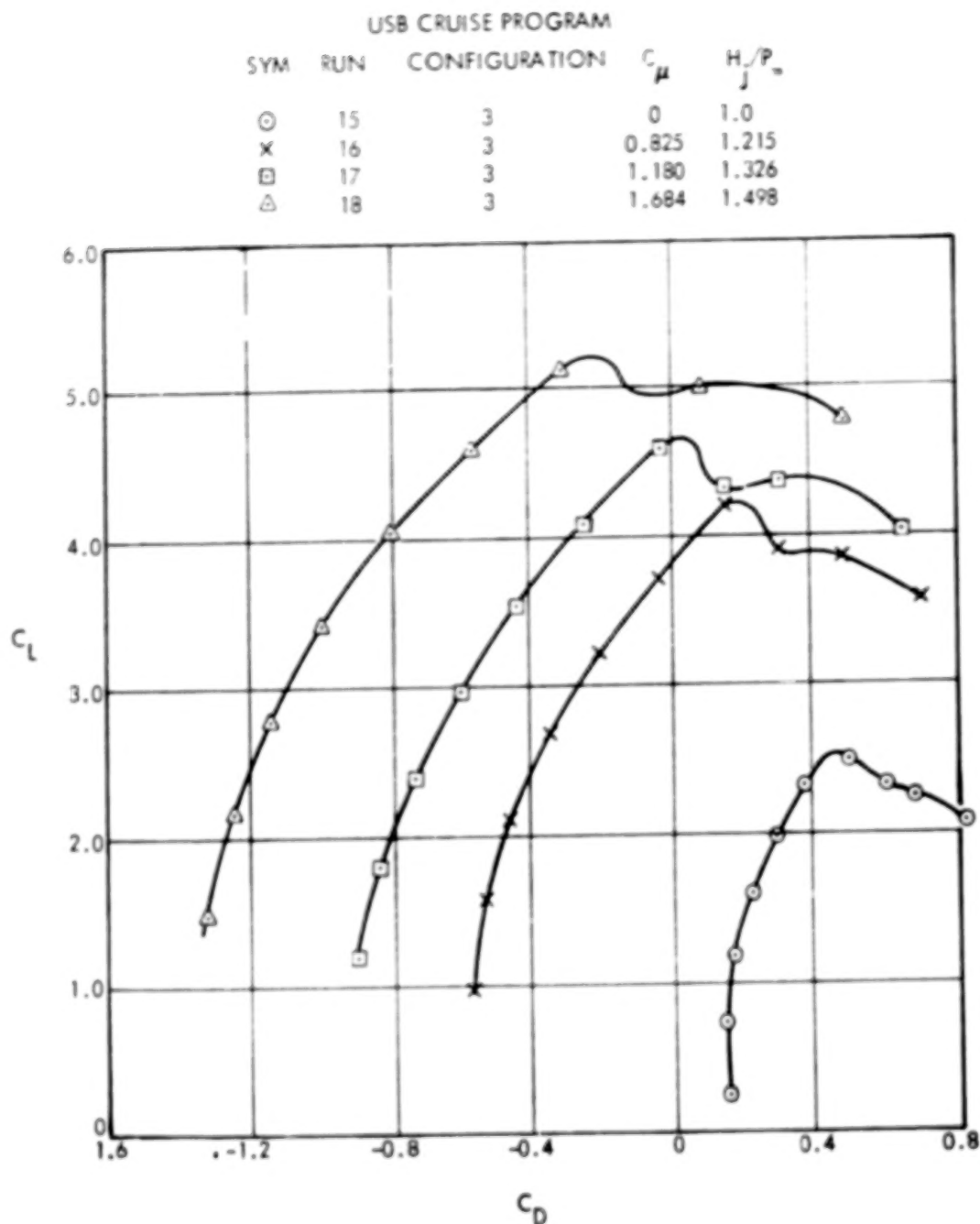


Figure 108. Variation of low speed model lift coefficient with drag coefficient, $q_{\infty} = 718.2 \text{ N/m}^2 (15 \text{ lb/ft}^2)$, $\delta_f = 25^\circ$, Coanda plate

SYM	RUN	CONFIGURATION	C_L	H_j/p_∞
○	20	5	0	1.0
×	21	5	0.810	1.209
□	22	5	1.164	1.322
△	23	5	1.660	1.489

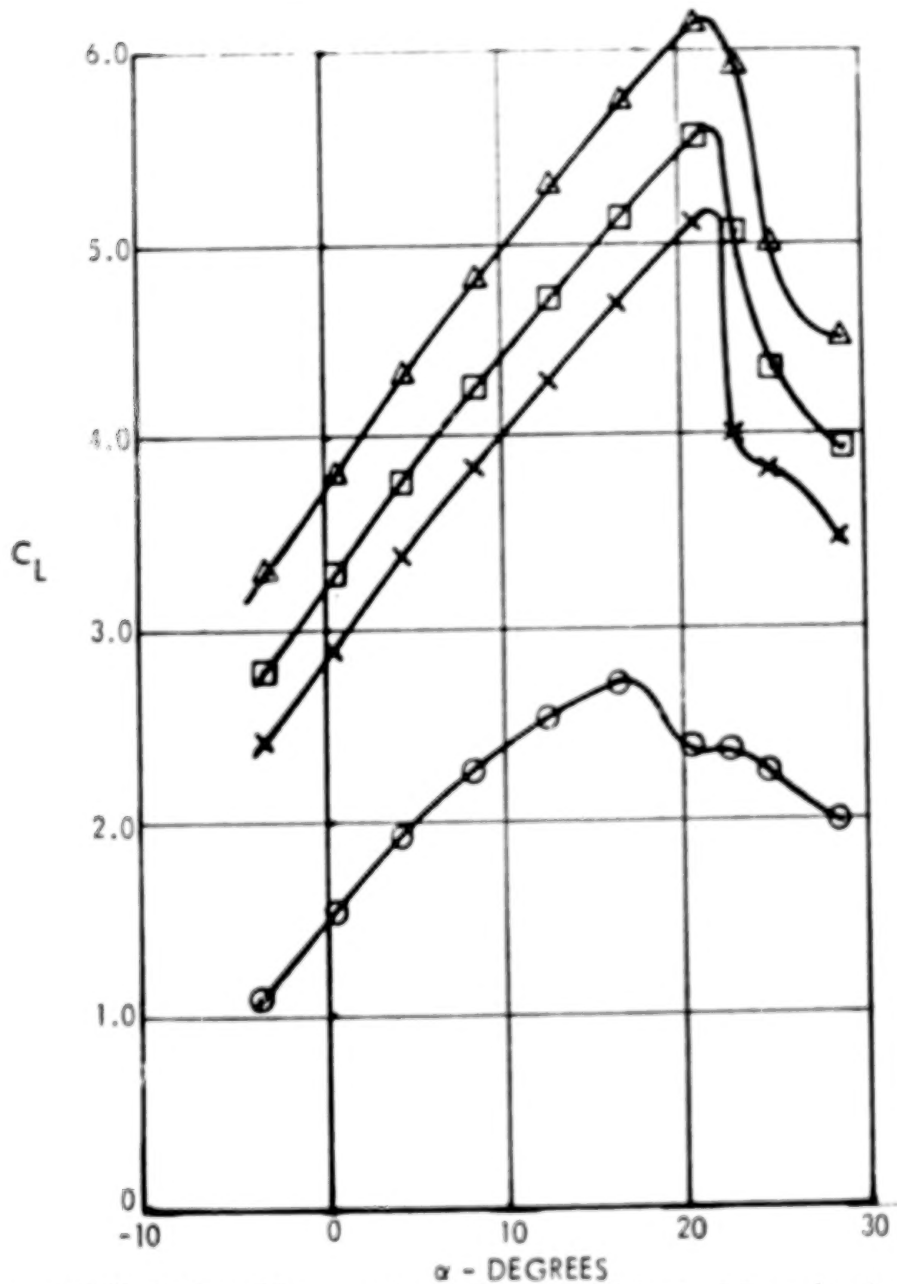


Figure 109. Variation of low speed model lift coefficient with angle of attack,
 $q_\infty = 718.2 \text{ N/m}^2 (15 \text{ lb/ft}^2)$, $\delta_f = 52^\circ$, Coanda plate

SYM	RUN	CONFIGURATION	C_L	H_j/p_∞
○	20	5	0	1.0
×	21	5	0.810	1.209
□	22	5	1.164	1.322
△	23	5	1.660	1.489

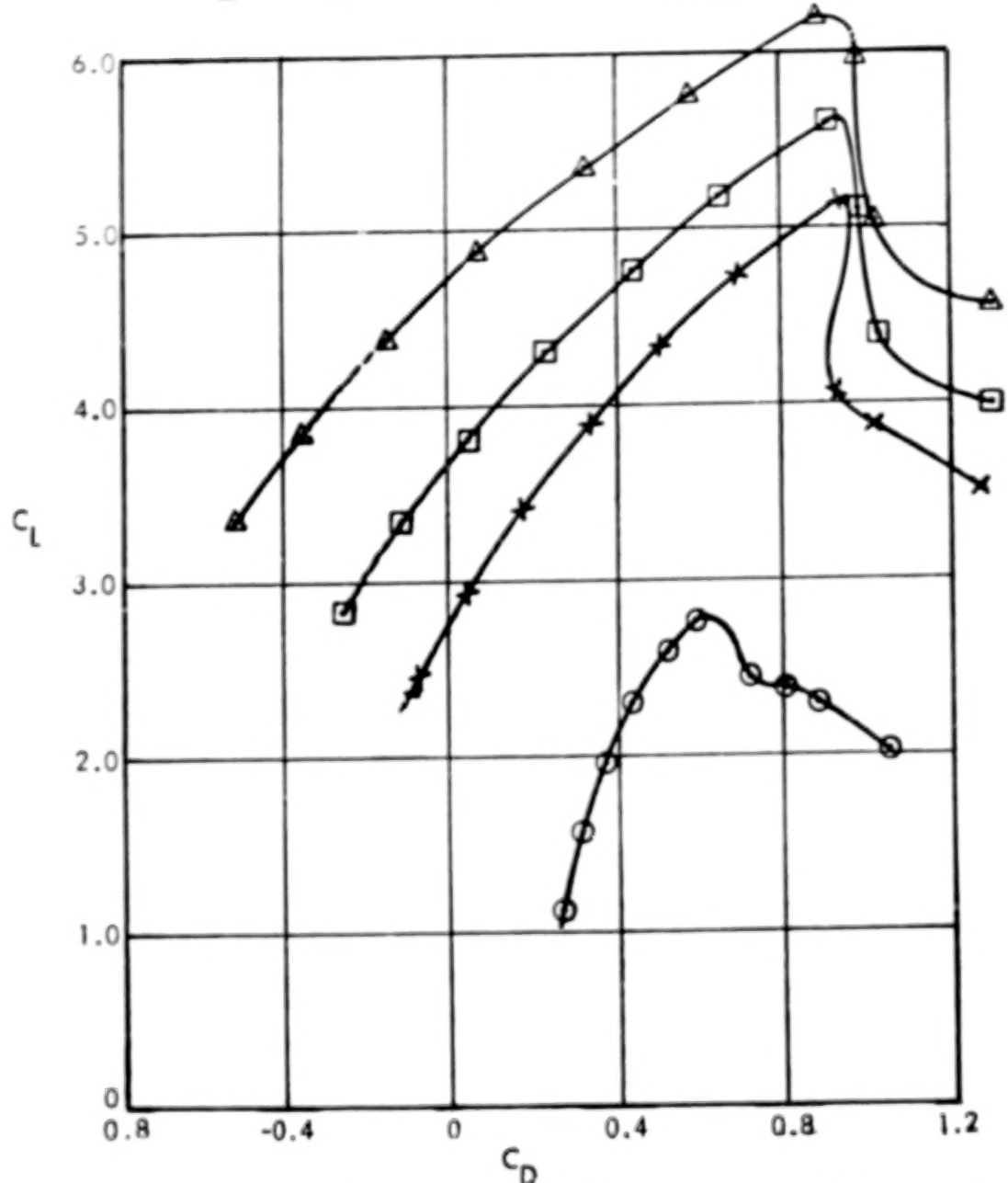


Figure 110. Variation of low speed model lift coefficient with drag coefficient, $q_\infty = 718.2 \text{ N/m}^2 (15 \text{ lb/ft}^2)$, $\delta_f = 52^\circ$, Coanda plate, tail-off

BLANK

PAGE

USB CRUISE PROGRAM

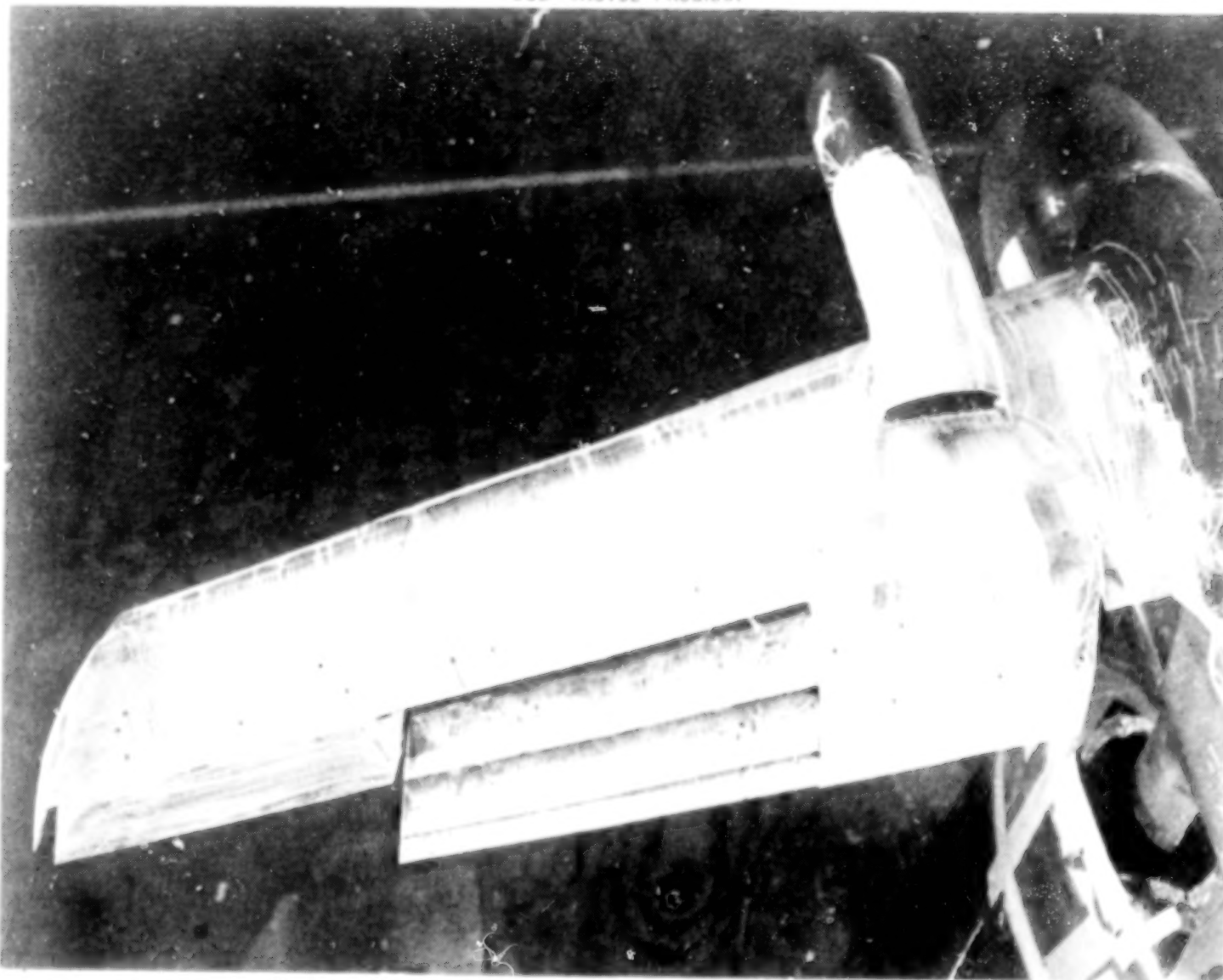


Figure 111. Oil flow photo of nacelle-wing flow pattern,
 $\delta_f = 42.5^\circ$, $C_T = 0.82$, $\alpha = 10^\circ$.

USB CRUISE PROGRAM

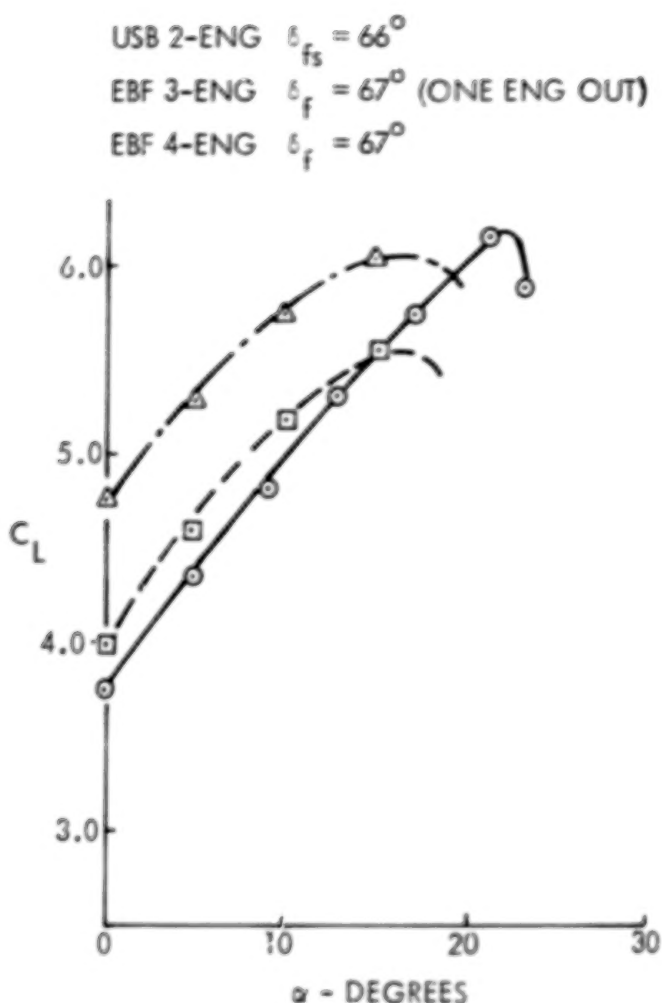


Figure 112. USB/EBF performance comparison, tail-off configuration,
 $C_{\mu} = 1.66$

USB wing (15 degrees). At the lower angles of attack, the four-engine EBF system with the greater span of blown flap produces a higher lift coefficient. The sensitivity of the EBF system to number of engines is illustrated by the three-engine (engine-out) performance which approaches that of the two-engine USB case. In terms of maximum lift, the USB-system provides about the same $C_{L_{MAX}}$ as the four-engine EBF for the thrust coefficient represented ($C_{\mu} = 1.66$). As will be noted in a later paragraph, going to a four-engine USB installation requires a very careful tailoring of the nacelle/wing leading-edge juncture in order to realize the improved performance associated with the better spanwise distribution of the four-engine blowing. The data of Figure 112 do illustrate, however, that the potential of the USB system for powered-lift generation is competitive with that of a similar EBF arrangement. It should also be noted that the USB test article represented an unrefined configuration, in contrast to the EBF model, and, as such, the USB performance should be responsive to additional system refinements.

A comparison of the subject USB high-lift performance data with similar data obtained on a two-engine USB arrangement is shown in Figure 113. The comparative results are taken from reference 5 representing large-scale tests of a USB-system using JT15D-1 turbofan engines. For a typical landing flap case, the present USB test results are shown to compare favorably with the large-scale results, although the referenced results represented a wider nozzle, relative to wing span, than does the present case. Comparisons with the more optimized test results from the referenced investigations are shown in Figure 114. Both maximum lift and lift at $\alpha = 0$ degrees for the present data are shown to be less than that found in the large-scale results by $\Delta C_L \approx 0.5$. This is believed to be indicative of the performance improvements which could be readily obtained from the tested system if similar refinements were made.

5.3 Powered-Lift Analytical Synthesis

For use as a correlation prediction tool, the Lockheed-Georgia powered-lift computer program was employed as an intermediate step between the low-speed test and the full-scale Task III aircraft. This program has been successfully utilized for the design and analysis of a wide variety of powered-lift

USB CRUISE PROGRAM

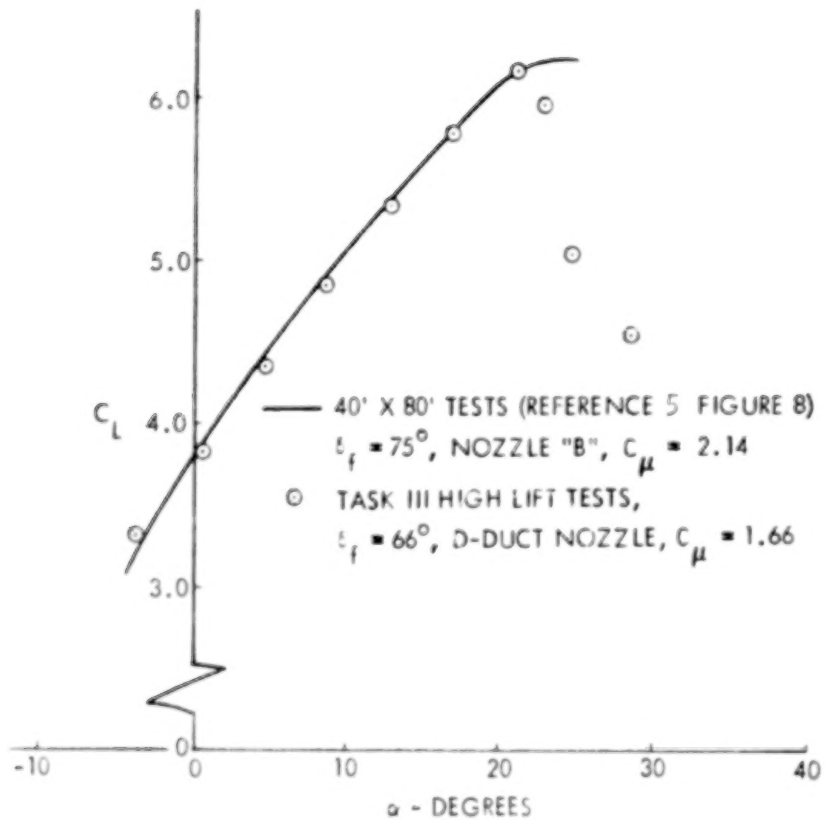


Figure 113. USB performance comparison, two-engine configurations

USB CRUISE PROGRAM

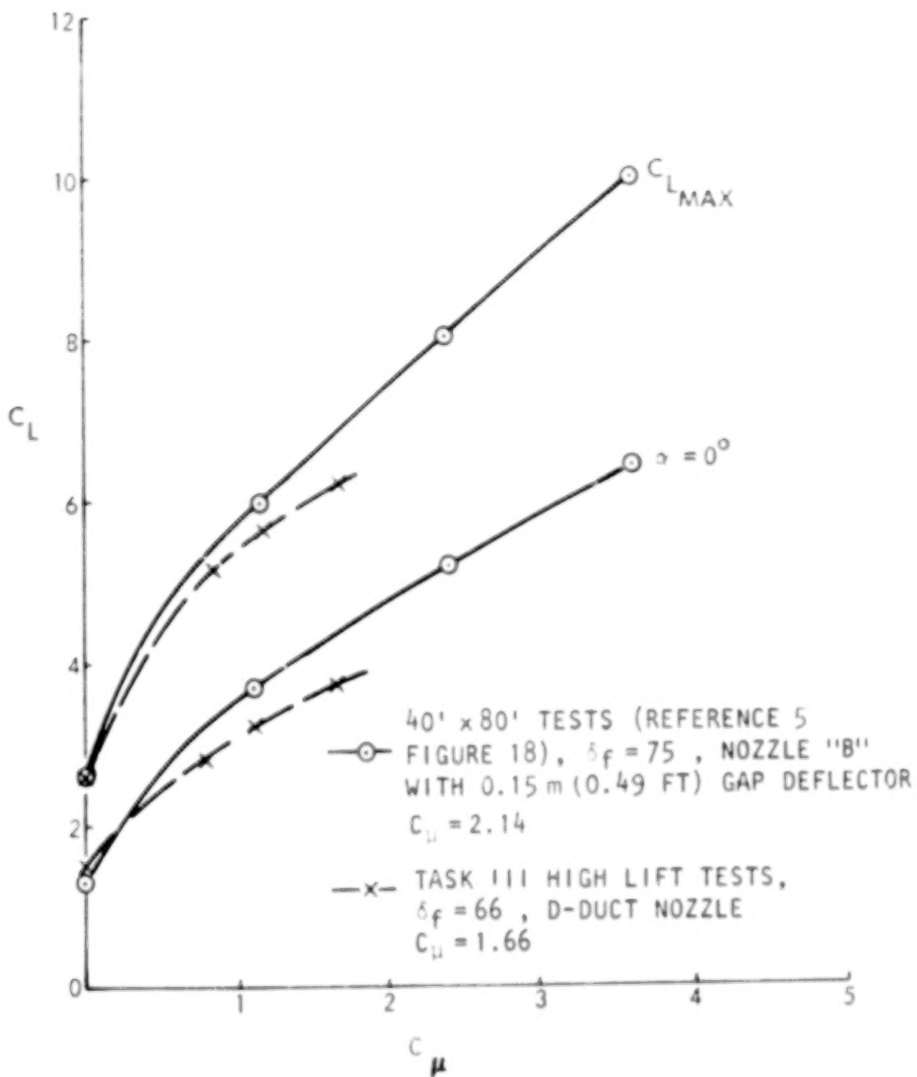


Figure 114. Effect of thrust coefficient on USB performance comparison, two-engine configuration

systems. Figures 115 and 116 show typical examples of this usage and include the reference USB test results. Good correlation is shown for both lift and drag with the experimental results for the various systems. Use of this program to predict the present experimental configuration performance is represented in Figure 117. The lift shows excellent agreement with the test data; the test drag as shown, when corrected for the ram drag of the ejector units ($\Delta C_D \approx 0.10$) also correlates well with the program.

Employing the same computer program for predicting the high-lift performance of the Task III aircraft provides the comparison shown in Figure 118. In formulating the analytical results, several refinements were observed. First, the theoretical data were trimmed according to the calculated pitching moments ($\Delta C_M = -0.23$). Secondly, a lift penalty was imposed as representative of four-engine interference effects found in the Reference 6 investigation. While the referenced documents indicated that local unsweeping of the leading-edge between nacelles and nacelle/fuselage could recover most of this penalty, it was judged that this approach may not be compatible with good cruise performance without highly complex leading-edge deployment devices. Accordingly, this penalty was accepted in view of the preliminary nature of the Task III design. Finally, a lift penalty was imposed ($\Delta C_L \approx 0.3$) to represent a quick-acting, slot-opening device for engine-out conditions. This penalty reflected test results with the Coanda plate removed and with the slot openings behind the nacelles covered on the bottom surface of the flaps (see Figure 101). The data of Figure 118 shows that the initial Task III high-lift performance used in the parametric sizing programs is in basic agreement with the analytical results after the foregoing refinements were made. The indications are that in the lower blowing range ($C_\mu = 0.6$), slightly better performance could have been projected in the parametric program, although the differences, in terms of aircraft size or mission performance, would be negligible.

6.0 RECOMMENDATIONS FOR ADDITIONAL DEVELOPMENT - TASK IV

Task IV of the USB Data Base Program had the objective of identifying previously unforeseen problem areas, potentially attractive cruise concepts or

BLANK

PAGE

USB CRUISE PROGRAM

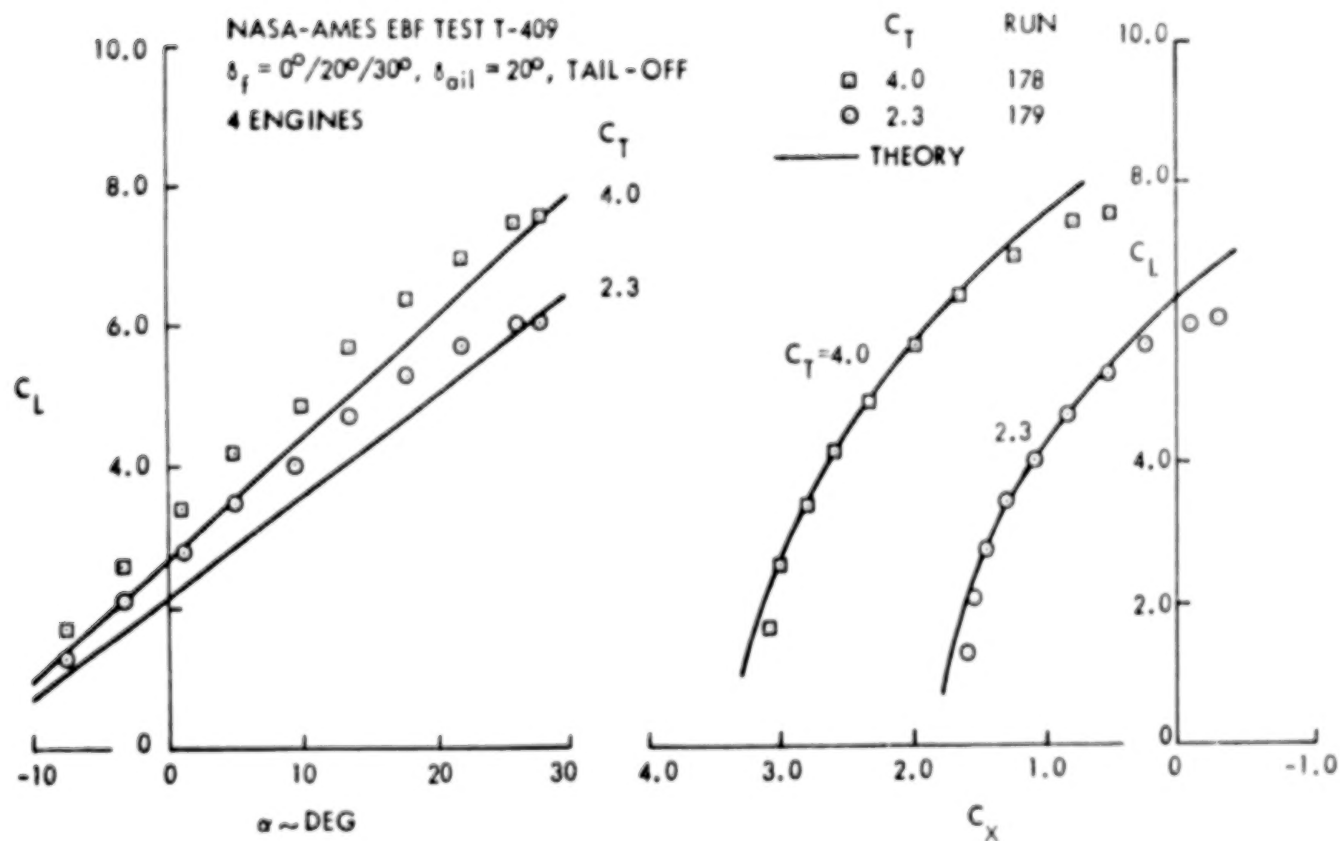


Figure 115. Correlation of theoretical and experimental longitudinal aerodynamic characteristics for a NASA Ames tested high-wing EBF STOL configuration

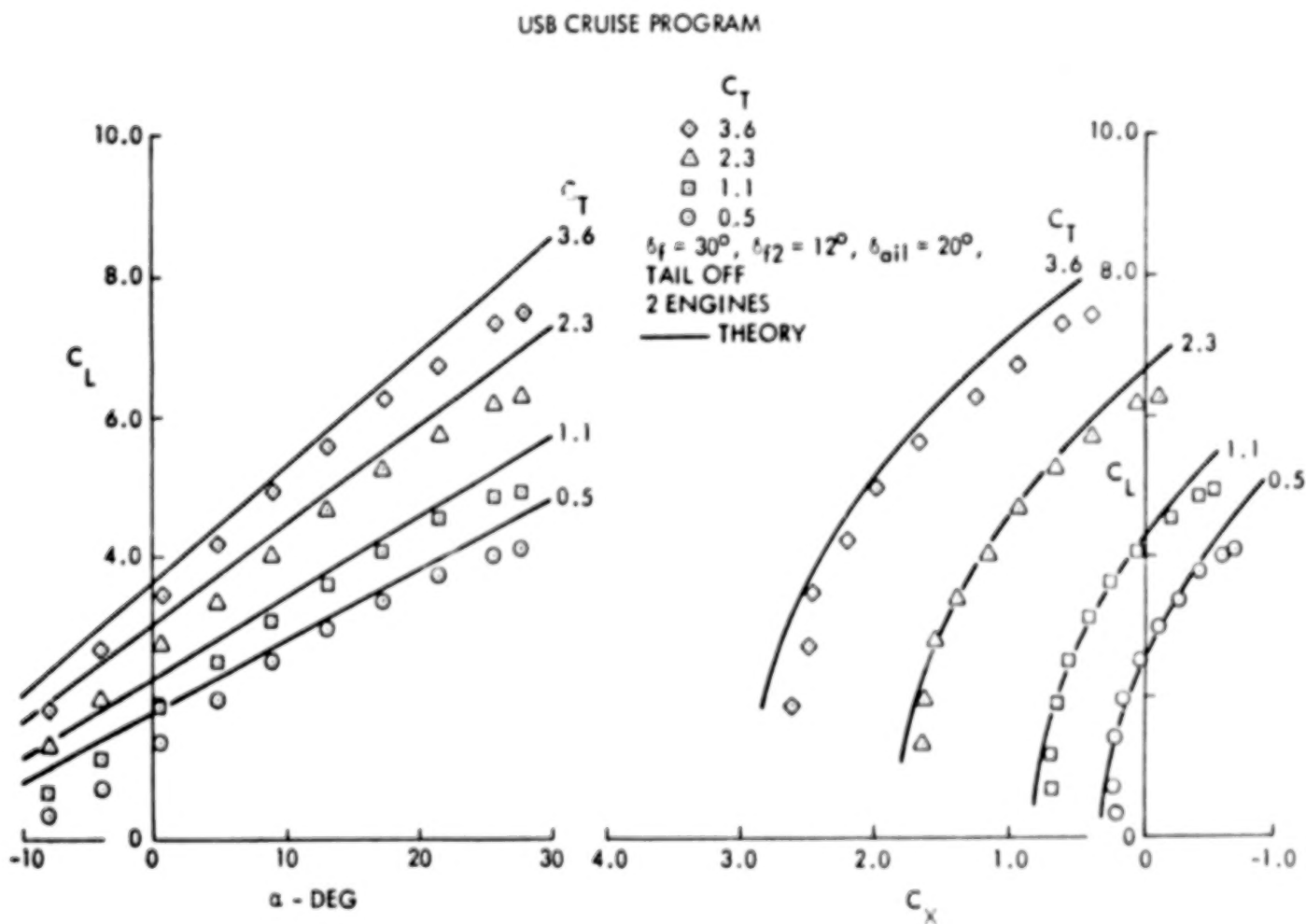


Figure 116. Correlation of theoretical and experimental longitudinal aerodynamic characteristics for a NASA Ames-tested high-wing USB STOL configuration

USB CRUISE PROGRAM

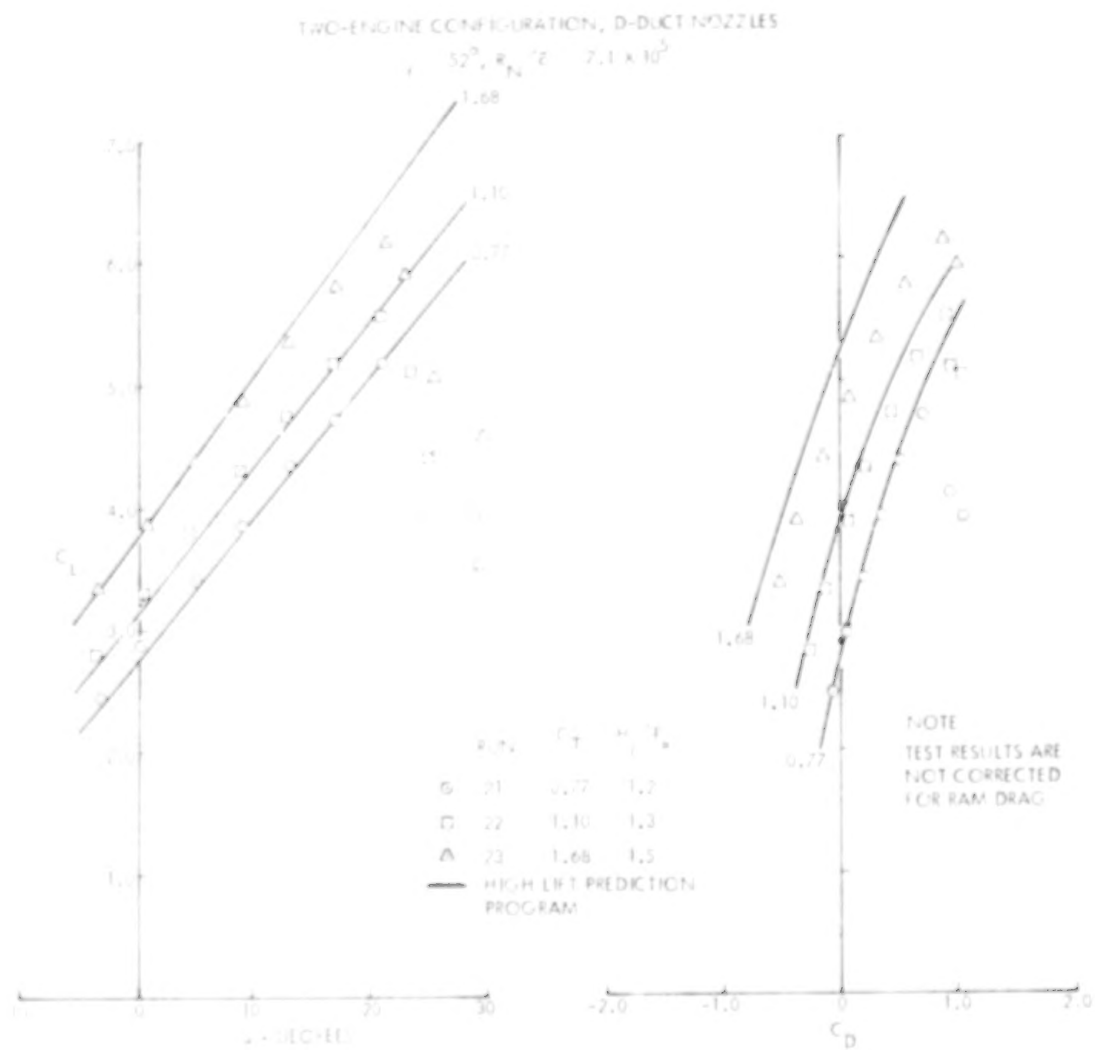


Figure 117. Correlation of theoretical and experimental high-lift performance, USB low speed model, tail off

USB CRUISE PROGRAM

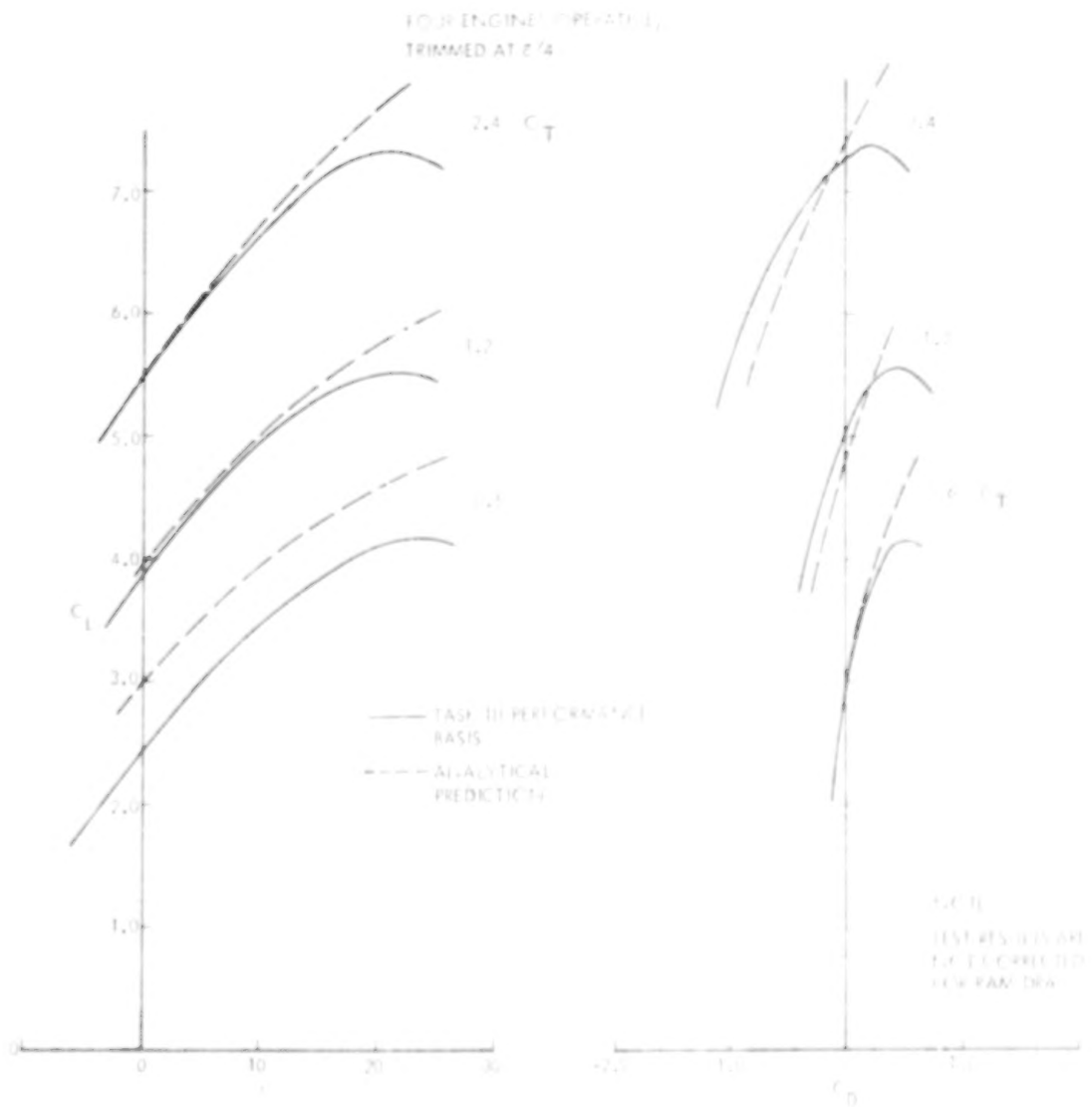


Figure 118. Comparison of Task III USB configuration performance with math model prediction, $T_f = 0.90$, $\dot{\epsilon}_f = 45^\circ$

any area where additional technical effort might be beneficial to the USB-development program. Appropriate recommendations, reflecting the experience gained in performing extensive low- and high-speed USB wind-tunnel testing, math model development and compatibility studies, have been made accordingly. Eight potential areas where additional investigations would be fruitful are:

- (1) High Speed Power Testing of Pylon Mounted (OTW) Nacelles
 - o Compare USB, OTW, and conventional nacelle performance
 - o Make maximum use of existing hardware
- (2) Low Speed Investigations of Powered OTW Nacelles
 - o Investigate effectiveness of eyebrow, Pegasus, and other deflectors
 - o Determine high-lift characteristics of OTW nacelles with deflected jets
 - o Compare performance between OTW and USB - designs
- (3) Integrated Configuration Design Study
 - o Produce optimum nacelle/wing/body design using latest available data and methods
 - o Test model of optimum configuration
- (4) USB-OTW Aircraft Design System Study
 - o Perform trade-off and sensitivity studies to optimize aircraft
 - o Integrate configuration for best compromise on performance and noise
- (5) Jet Plume Boundary Optimization
 - o Provide optimum expansion shape for jet just aft of discharge
 - o Minimize break in spanloading due to nacelle installation
- (6) OTW Variable - Geometry Nozzle Study
 - o Provide for design study of OTW jet - deflection devices
 - o Compare performance and cost of alternative systems
- (7) Powered Vortex Lattice Program Correlation
 - o Predict jet effects on pressure distributions
 - o Correlate preliminary data from USB cruise performance
- (8) Jet Efflux Modeling for USB and OTW Configurations
 - o Predict interactive effects between jet plume and freestream
 - o Combine PVL and "Vorticity Box" programs

Exemplifying recommended studies appropriate to items (3) or (5) above, modification to wing section design would appear to merit further attention. Sketches (b) and (c) of figure 119 provide possible alternative designs which

USB CRUISE PROGRAM

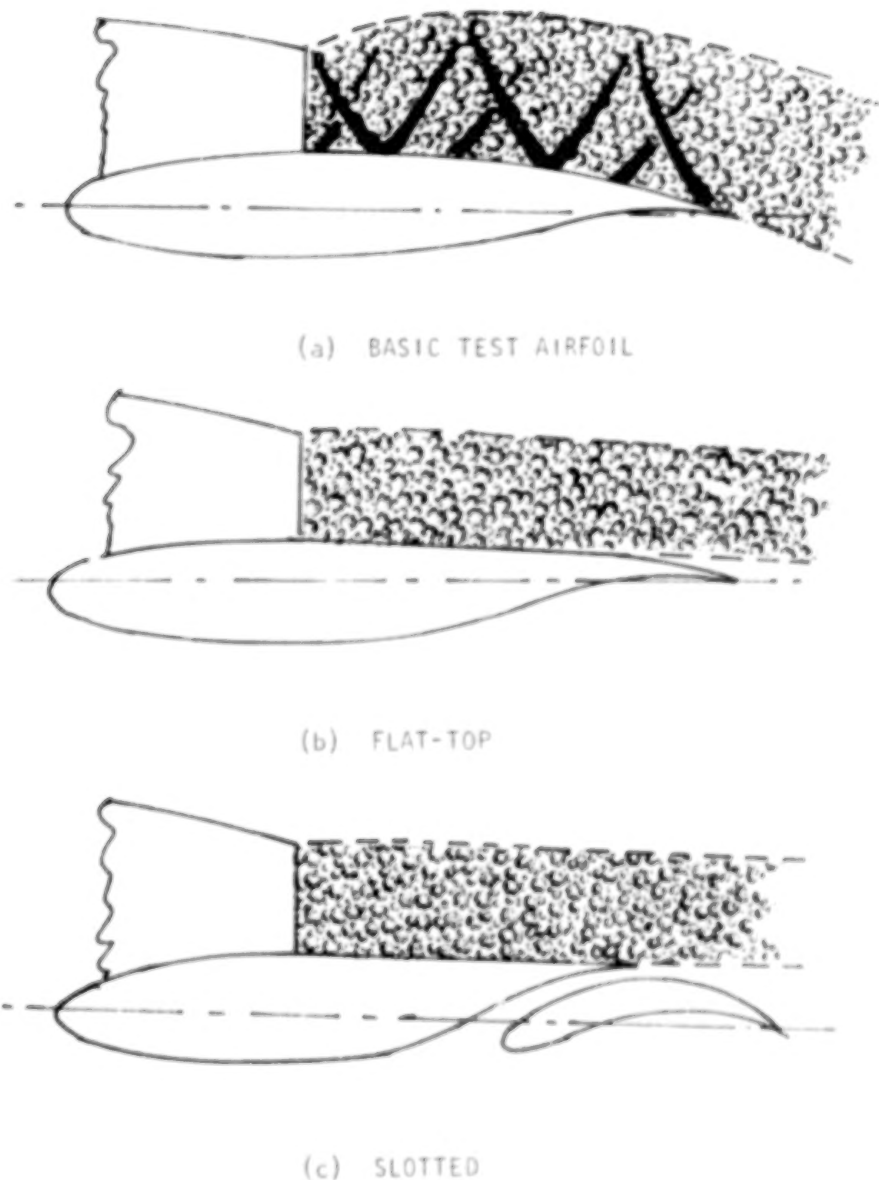


Figure 119. Pressure drag reduction through local modification of airfoil.

could suppress the pressure drag experienced on the present test wings (sketch (a)). Details and justification, along with a preliminary program plan for each of the recommended areas of study have been provided.

7.0 PROGRAM CONCLUSIONS

The USB Data Base Program contained three major tasks for which specific technical conclusions were formulated in the course of the studies. The subject tasks were the high-speed experimental studies, and supporting analytical effort, under Task II, the design compatibility studies of Task III and the follow-on development work as recommended under Task IV. Major conclusions appropriate to Tasks II and III of the program are summarized below.

7.1 Cruise Performance Data Base - Task II

As a result of a detailed experimental/analytical program for the study of the upper-surface blowing concept at cruise, a number of significant conclusions may be identified. Such conclusions, however, must reflect the "data-base" nature of the experimental work in which relatively unrefined models and a broadly-spaced test matrix were necessary features. Within these constraints, it is believed that the aerodynamic and geometric trends developed have general applicability; this has been the major objective of Task II. With particular regard for the levels of cruise drag portrayed, ultimate levels of USB cruise performance, obtained through more highly refined design process, are not necessarily represented by the present data.

7.1.1 Experimental program -

(1) In the unrefined state, the total drag penalty of typical USB-nacelle configurations, under transonic-cruise, powered conditions, were exceptionally high by current standards.

(2) The major drag producing phenomena in the general case, appears to be

- o a jet scrubbing effect on the aft-wing surface
- o the conventional aerodynamic friction drag of the nacelle/nozzle and associated external hardware
- o a pressure-drag component representing deflection of the jet over the aft-wing surface
- o a drag-due-to-lift component inclusive of all lift-related transonic phenomena under powered-model conditions
- o a potential drag penalty reflecting excessive nozzle boattail angles which promote local flow separation.

(3) The major drag components are generally identifiable by force and surface-pressure measurements of powered models tested under both static and wind-on conditions.

(4) For a given nozzle size, scrubbing losses increase with nozzle exit aspect ratio due to the greater span of wing scrubbed and an increased tendency for jet attachment with the thinner jet.

(5) Pressure drag, tending to increase with nozzle width, aft-wing camber, angle-of-attack, and nozzle pressure-ratio can possibly be moderated by the jet shock formations at high nozzle pressure ratios.

(6) Highly three-dimensional jets, such as a circular shape, can also show significant amounts of pressure drag at cruise conditions even under partial jet-attachment conditions.

(7) For moderate nozzle aspect ratios, (AR = 2.5-4) effective jet deflection by the aft wing appears to be within several degrees of the wing upper-surface at the trailing edge.

(8) Total lift performance at constant angle-of-attack is improved by increasing nozzle exit aspect ratio - typical values at a nozzle pressure ratio of 3.0 are $\Delta C_L = .03$ for a circular nozzle and about $\Delta C_L = 0.10$ for an aspect ratio 6.0 nozzle.

(9) A semi-circular ("D-Duct") nozzle (AR = 2.5) represents a reasonable compromise exit nozzle shape between good cruise and potentially-favorable high-lift performance.

(10) Nozzle boattail angles in excess of about 25 degrees may cause significant drag penalties due to local flow separation.

(11) On a multi-jet configuration with nacelles spaced 1.6D apart, both lift and drag increments due to blowing were diminished by an apparent mutual interference between the adjacent jets.

(12) At a flow-through pressure ratio, and at subcritical Mach numbers a faired-over forebody nacelle showed essentially the same drag penalty as that of a flow-through type of forebody.

(13) Cruise drag penalties associated with a pylon-mounted (OTW) nacelle positioned one-half nozzle diameter above the wing surface, compared favorably with a surface-integrated USB-type arrangement under similar test conditions.

(14) A small streamlined USB nacelle, integrated with a straight wing-body combination, showed favorable drag due-to-lift performance when compared to that of a symmetrical design; the effect of streamlining on the total cruise drag penalty showed only a modest benefit due, it is believed, to the straight-wing installation.

7.1.2 Theoretical Program - The USB wing/nacelle/propulsive interactions are complex not only in their viscous aspects, but also with regard to the potential flows involved. Theoretical studies have, therefore, been aimed at understanding the potential flows with minimal representation of viscous effects. The overall philosophy has been to implement the simplest realistic method for simulating the nacelle environment and to embed in this a simplified model of the spreading jet plume.

7.1.2.1 Vortex Lattice Studies - A major effort has been directed towards a vortex lattice representation of the wing/nacelle combination, with sufficient detail to permit comparisons with surface pressure measurements. A

power effects package was developed, for use with the vortex lattice, which comprises vorticity panels which model the jet surface and simulate both its trajectory and its changing cross section. Compressibility effects for the complete model were simulated via geometric transformation according to Goethert's rule.

The vortex lattice study, which was restricted to the N_{3E} 'D-duct' nacelle at $M = 0.60$, leads to the following conclusions:

(1) Where experimental surface pressure measurements were available (i.e., in the scrubbed region, in the aft part of the boattail and on sections just inboard and just outboard of the nacelle), there was generally good correlation between vortex lattice predictions and measured surface pressure coefficients. The correlation was particularly good in the impingement and turning regions. Some differences were noted for supercritical pressure ratios (the theory was for $M_{JET} < 1$) and in small regions inboard and outboard of the nacelle location where the theoretical jet spreading angle was too large towards the trailing edge.

(2) Lift increments in the scrubbed region are small because the upload due to jet turning is almost entirely offset by download in the impingement region. There is an adverse effect on drag because of wing surface curvature which causes the aft-facing suction area in the turning region to be several times greater than the aft facing area in the impingement region and this produces a significant net pressure drag.

(3) A major feature of the flow is a vortex pair which springs from the lifting region on the nacelle boattail. This causes opposing thrust and drag forces in the outer and central regions which are large compared with the net resultant drag increment.

(4) Correlation between the theoretical drag predictions and experiment shows differences which are largely independent of α , but which vary with pressure ratio. At flow-through, this difference agrees well with independent estimates of nacelle skin friction. Thereafter, the difference increases with nozzle pressure ratio at a rate consistent with estimated jet scrubbing drag

effects. At supercritical pressure ratios this trend reverses, possibly due to reduced aft-suction and reduced scrubbing when shocks in the jet reduce its ability to turn.

7.1.2.2 Applications of Jet Flap Theory - Two-dimensional jet-flap theory of Spence, as modified for three-dimensional effects and compressibility, has been applied to the tested USB - configurations. The conclusions appropriate to this limited study were as follows:

(1) Both simplified jet flap theory and the lifting line theory give good predictions of lift increments for nozzle configurations ranging from circular to aspect-ratio four. To achieve this correlations, it was necessary to employ jet deflection angles, which approached the wing upper surface trailing edge angle, in conjunction with measured values of wing sectional lift curve slope.

(2) The simplified jet flap theory also predicted pitching moment increments well for the cases tried, namely the "D-duct" and aspect-ratio four nozzles.

(3) Neither method predicted drag increments which correlated consistently with experiment.

7.2 Compatibility Studies - Task III

The Task III effort was undertaken as a combined effort with the related USB acoustical work of Reference 7. This task consisted of an aero/acoustic assessment of a selected USB configuration in terms of low-speed (high-lift) performance, acoustic footprints, the feasibility of the integrated design and the structural compatibility of the propulsion system and airframe. As a part of this task, supplementary low-speed tests were conducted to validate the estimated airport performance of the selected configuration. Conclusions pertinent to the findings in this phase of the USB program are given below.

7.2.1 Design Feasibility Studies - As a result of experimentally-based design studies of a representative USB-configuration, the following conclusions were made:

- o A practical aircraft system can be formulated for the typical short-haul mission selected [i.e., cruise Mach 0.75, 148 passengers, 527 (500) and 2780 (1500) km (N/m) stage lengths]. Further refinements to the integrated nacelle-design should be the major objective for improving the competitive position of the USB system on longer missions.
- o For a specified thrust loading, two-engine configurations were found to be superior to four-engine versions from a cruise performance standpoint. However, considerations of the engine-out go-around problem on landing led to selection of a four-engine design.
- o The optimum fan pressure ratio found in the USB-cruise design study was high when compared to that for conventional propulsion installations due to the higher nacelle drags used.
- o Powered-lift performance of the USB system is competitive with that of alternate concepts and can be successfully integrated with conventional high-lift devices. Quick-opening slots in a Coanda surface mounted on either the top or bottom of conventional slotted flaps is an effective means of achieving engine-out lift/roll control.
- o From a standpoint of noise suppression, wide, high-aspect ratio nozzles and high-extension flaps were effective geometric arrangements. A "D-duct" nozzle was a reasonable compromise between cruise drag, noise and high-lift performance as a final nacelle design selection.
- o To meet a noise goal of 90 EPNdB for 2.59 km^2 (1 sq. mi.), a design fan pressure ratio of 1.35 or less is needed to minimize jet noise.

- o The USB installation readily lends itself to an excellent thrust reverser design capable of reversing both primary and secondary airstreams with good lift-spoiling and anti-reingestion characteristics. A separately-operating "eyebrow-type" section, integrated with the reverser design, offers a practical means of assuring jet-attachment to the wing and flap in the high-lift mode.

7.2.2 Supplementary tests - Low-speed tests were conducted as a representative USB high-lift configurations featuring:

- o Two USB-type nacelles installed on an aspect ratio 7.7 wing and fuselage
- o 40-percent span triple-slotted, trailing-edge flaps
- o 16-percent span Coanda surfaces aft of the ejector-powered nacelles
- o Full-span leading-edge Krueger-type flaps

Analysis of the test results yielded the following conclusions:

- (1) As tested with the same model hardware, the USB system provided competitive performance with a similar EBF system.
- (2) The subject USB test data compared favorably with test results on a large-scale model of a two-engine USB arrangement.
- (3) A loss in lift up to stall of $\Delta C_L = 0.10$ to 0.15 per nacelle was found with the Coanda plate removed and flap slots blocked on the undersurface of the trailing-edge device.
- (4) Analytical synthesis of the high-lift configuration showed excellent agreement between calculated and tested results.
- (5) Analytical high-lift performance predictions for the Task III, four-engine airplane indicated that parametric estimates of the full-scale

design were reasonably consistent with test results, with the latter conservatively corrected for potential performance penalties.

(6) Additional work is needed to optimally configure the wing leading edge/nacelle junctures for both cruise and high-lift performance when considering four-engine aircraft.

8.0 REFERENCES

1. Bailey, A. B.: Use of Coanda Effect for the Deflection of Jet Sheets Over Smoothly Curved Surfaces, Part I, Institute of Aerophysics, Technical Note No. 49, AD 269128, Aug. 1961.
2. Kettle, D. J.; Kurn, A. G.; and Bagley, J. A.: Exploratory Tests of a Forward-Mounted Over Wing Engine Installation. CP No. 1207, R.A.E., Farnborough, 1972.
3. Lan, C. E.: A Wing-Jet Interaction Theory for USB Configurations. Journal of Aircraft, September 1976, p. 718.
4. Reubush, D. E.: An Investigation of Induced Drag Reductions Through Over-the-Wing Blowing. Paper No. 77-884, AIAA/SAE 13th Propulsion Conf., Orlando, Fla., July 1977.
5. Aoyagi, K., Falanski, M. D., and Koenig, D. G.: "Wind Tunnel Investigation of a Large-Scale Upper Surface Blown-Flap Transport Model Having Two Engines," NASA Ames TMX-62, 296, August 1973.
6. Aoyagi, K., Falanski, M. D., and Koenig, D. G.: "Wind Tunnel Investigation of a Large-Scale Upper Surface Blown-Flap Model Having Four Engines," NASA AMES TMX-62, 419, 1975.
7. Reddy, N. N. and Gibson, J. S.: Noise Characteristics of Upper Surface Blown Configurations - Summary. NASA CR-2918, 1978.

1. Report No. NASA CR-3193	2. Government Accession No.	3. Recipient's Catalog No.	
4. Title and Subtitle EXPLORATORY STUDIES OF THE CRUISE PERFORMANCE OF UPPER SURFACE BLOWN CONFIGURATIONS - Summary Report		5. Report Date July 1980	
6. Performing Organization Code			
7. Author(s) J. A. Braden, J. P. Hancock, J. E. Hackett, K. P. Burdges, and V. Lyman		8. Performing Organization Report No. LG77ER0028	
9. Performing Organization Name and Address Lockheed-Georgia Company 86 South Cobb Drive Marietta, Georgia 30063		10. Work Unit No.	
11. Contract or Grant No. NAS1-13871		12. Sponsoring Agency Name and Address National Aeronautics and Space Administration Washington, DC 20546	
13. Type of Report and Period Covered Contractor Report		14. Sponsoring Agency Code	
15. Supplementary Notes Part of a Series of Reports Covering Various Phases of the USB Program: CR-3193, CR-3192, CR-159134, CR-159135, CR-159136 Langley Technical Monitor: William C. Sleeman, Jr. Final Report			
16. Abstract The present report summarizes the data and major conclusions obtained from an experimental/analytical study of upper-surface blown (USB) configurations at cruise. The high-speed (subsonic) experimental work, studying the aerodynamic effects of wing-nacelle geometric variations, was conducted around semi-span model configurations composed of diversified, interchangeable components. Power simulation was provided by high-pressure air ducted through closed forebody nacelles. Nozzle geometry was varied across size, exit aspect ratio, exit position and boattail angle. Both 3-D force and 2-D pressure measurements were obtained at cruise Mach numbers from 0.5 to 0.8 and at nozzle pressure ratios up to about 3.0. The experimental investigation was supported by an analytical synthesis of the system using a vortex lattice representation with first-order power effects. Results are also presented from a compatibility study in which a short-haul transport is designed on the basis of the aerodynamic findings in the experimental study as well as acoustical data obtained in a concurrent program. High-lift test data are used to substantiate the projected performance of the selected transport design.			
17. Key Words (Suggested by Author(s)) Subsonic cruise performance Propulsion integration High-lift Transport design		18. Distribution Statement Unclassified - Unlimited	
19. Security Classif. (of this report) UNCLASSIFIED			
20. Security Classif. (of this page) UNCLASSIFIED		21. No. of Pages 190	22. Price* \$9.00

* For sale by the National Technical Information Service, Springfield, Virginia 22161

NASA-Langley, 1980

90%

END